Intake Ground Vortex Aerodynamics

John Murphy

Submitted for the Degree of Ph.D.

Department of Aerospace Sciences
Cranfield University
Cranfield, UK

2008

Intake Ground Vortex Aerodynamics

PhD Thesis

John Murphy

December 2008

Cranfield University

School of Engineering

Academic Year: 2008-2009

Supervisor: Dr. David MacManus

Abstract

When an aircraft is operating in static or near static conditions during taxiing or take-off a vortex can form between the ground and the intake. With engine diameters increasing, intakes are moving non-dimensionally closer to the ground and as a consequence the likelihood of vortex formation during the aircraft operating envelope is set to increase. To date there is little quantitative knowledge therefore a greater understanding is required. This research is aimed at providing an extensive quantitative parametric study of vortex formation leading to advanced design rules for future engines.

A $1/30^{th}$ scale generic model intake was operated in the Cranfield University $8' \times 6'$ wind tunnel to examine ground vortex formation under quiescent, headwind and crosswind conditions. Stereoscopic Particle Image Velocimetry and total pressure measurements have been extensively taken to assess the external and internal flowfields. For the first time experiments with a rolling ground plane have been performed to provide insight into the formation and characteristics of ground vortices during take-off.

As the velocity ratio reduces a characteristic trend is established whereby the vortex is initially weak, increases in strength to a local maximum and reduces to zero thereafter. The operating points that generate the strongest vortex for a given configuration have been determined and an empirical model has been developed which can predict the vortex strength and fan face distortion for any configuration. Under headwind conditions a new vortex formation criterion has been established which also includes contours of vortex circulation. An a priori prediction of the vortex strength under headwind conditions has also been developed which considers the approaching and intake induced vorticity sources, the latter of which is determined empirically. Good agreement is found between the model and the experimental dataset. The rolling ground plane experiments demonstrate significant sensitivities illustrating that the correct conditions must be simulated properly.

Acknowledgements

Firstly I would like to thank my supervisor, Dr David MacManus for his endless support, encouragement and direction and in particular for the many hours that he took out of his time to enable me to take the data that is so vital to this thesis. Many thanks must go to Rolls-Royce for their financial and technical assistance and in particular to Chris Sheaf of Installations and Jeff Green of Fan Systems. Thanks to John Thrower of Cranfield University and all the wind tunnel technicians. I would also like to thank Stefan Zantopp and Lauren Rehby for their assistance and discussions.

Thanks to all friends that I have spent my time with at Cranfield University. Special thanks to Ross Chaplin, Peter Thomas, David Estruch, Ben Thornber, Marco Hahn, Macro Kalweit, Sanjay Patel, Sunil Minstry and all those who I have shared the office with over the past three years.

Finally this would not have been possible without the loving support and encouragement of my whole family. Much appreciation goes to my Mum, Dad and sister, Kate. I would like to dedicate this thesis to all of my family and in particular to my grandparents. Without their support, this would have never been possible.

Contents

List of Figures

List of Tables

Nomenclature

English Symbols

A	Area, m^2
b	Empirical constant (Eq. 8.1.4)
b_{fl}	Back focal length, mm
c	Empirical constant (Eq. 8.1.4)
D	Diameter, m
e	Empirical constant
f_a	Focal length of optic A, mm
h	Vertical distance from lowest point of the highlight plane to ground, m
H	Intake centreline height from ground plane, m
I_{max}	The number of radial grid points used in the circular zone for processing
J_{max}	The number of circumferential grid points used in the circular zone for processing
L_q	Length scale of intake capture stream tube, m
$\dot{m}$	Intake mass flow, kgs^{-1}
n	Vatistas vortex model constant
n_{bl}	Boundary layer profile shape factor
p	Static pressure, Pa
P	Total pressure, Pa
p_{str}	Average static pressure from the tunnel rings in the settling chamber of the wind tunnel, Pa
q	Dynamic pressure, Pa
r	Radial distance (or radius), m
t	Time, s
T	Temperature, K
U	Velocity, ms^{-1}
u, v, w	Cartesian velocity components, ms^{-1}
V_θ	Vortex swirl velocity, ms^{-1}

V_r	Radial velocity, ms^{-1}
x, y, z	Cartesian coordinates, m
z_0	Roughness factor, m

Greek Symbols

α	Half-angle between the PIV cameras, $deg(^\circ)$
δ	Boundary layer thickness, m
δ_x	Measurement uncertainty of parameter x (Appendix G)
δ^*	Boundary layer displacement thickness, m
Δt	Pulse separation time in PIV recordings, μs
ΔU	Relative difference in velocity between the ground and free-stream speeds, ms^{-1}
Δz_{LS}	Light sheet thickness, mm
Δ_{rg}	PIV spatial resolution, mm
ϵ	Least squares residual of the experiments with the Vatistas vortex model
ϵ_x	Error of parameter x
ϕ	Relationship between the distortion under headwind and crosswind conditions
ϕ_2	Empirical constant
η	Function which describes vortex strength trend with yaw angle
Γ	Total vortex circulation, $m^2 s^{-1}$
Γ_{id}	Induced circulation, $m^2 s^{-1}$
Γ_∞	Integrated approaching boundary layer circulation within sucked streamtube, $m^2 s^{-1}$
Π_1	Empirical constant
Π_2	Empirical constant
θ	Boundary layer momentum thickness, m
ρ	Density, kgm^{-3}
ω	Vorticity, s^{-1}
ζ	Function which describes DC_{60} trend with yaw angle
ψ	Flow angle between engine centreline and the wind direction, $deg(^\circ)$

Non-dimensional Parameters

DC_{60}	Distortion coefficient based on the lowest average 60 degree sector pressure
H_{bl}	Boundary layer shape factor
M	Mach number
P_L	Pressure loss coefficient
Re_{D_i}	Reynolds number based on the inner diameter
Γ^*	Average non-dimensional vortex strength ($\bar{\Gamma}/U_i D_l$)
U^*	Velocity ratio (U_i/U_∞)
U^{*2}	Velocity ratio based on the area weighted average freestream velocity within sucked streamtube ($U_i/\bar{U}_\infty$)
U^*_{max}	Velocity ratio at which Γ^* or DC_{60} is maximum for a given configuration
U^*_R	Ratio of critical to maximum velocity ratios (U^*_{crit}/U^*_{max})
$U^{\sim}$	Modified velocity ratio (Chapter 8)
ρ^*	Density ratio ($=\rho_\infty/\rho_i$)

Subscripts

amb	Ambient conditions
c	Vortex core
crit	Vortex blowaway condition
f	Fan face
g	Ground (Chapter 6)
i	Intake duct
l	Highlight plane station
L	Laser
max	Maximum value (except for U^*_{max})
min	Minimum value
r	Radial
v	Vortex
w	Wall
ref	Reference value
∞	Free-stream conditions

Superscripts

$\bar{}$	Time average or mean quantity
$+$	Positive value (or positive rotating vortex)
$-$	Negative value (or negative rotating vortex)
$*$	Dimensionless quantity

Abbreviations

FFT	Fast Fourier Transform
SPIV	Stereoscopic Particle Image Velocimetry
TP	Total Pressures

Coordinate Systems

The coordinate system used in this thesis is fixed in tunnel space.

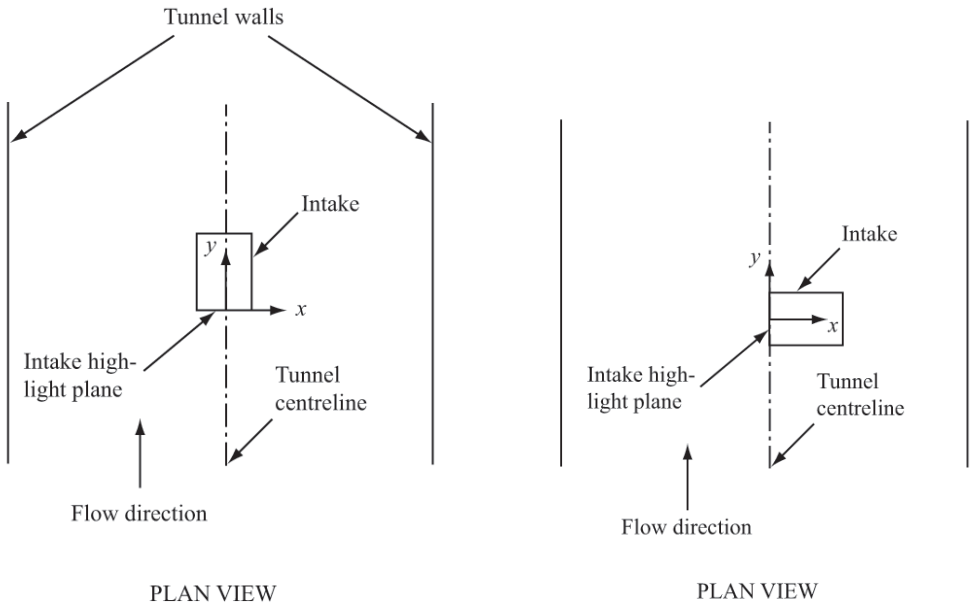

(a) Headwind (b) Crosswind

Figure 0.1: Intake Coordinate System

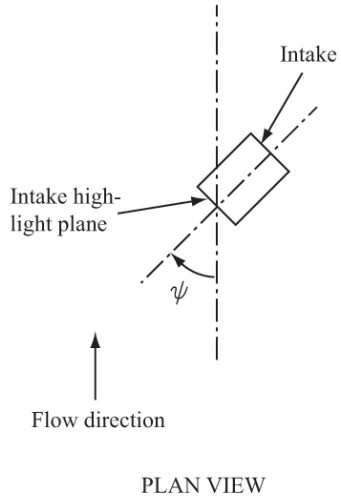

Figure 0.2: Definition of the intake yaw angle, ψ

CHAPTER 1

Introduction

The ever increasing demand for quieter and more fuel efficient engines has lead to the need for higher by-pass ratio turbofans. As a consequence of this ongoing evolution in turbofan configurations, intake diameters are larger than ever before. For conventional wing mounted engines, in particular, this increase has major consequences. When the engine is operating in static or near static conditions close to the ground a strong vortex can be observed between the intake and the solid surface (Fig. 1.1). The ingested vortex is often invisible, however in humid conditions, due to the high velocities within the vortex core, the local flow temperature can decrease below the dew point, promoting condensation of the associated flowfield[8].

Figure 1.1: Visualization of an ingested ground vortex on a Rolls-Royce RB211-524G ©Peter Thomas 2005

This so-called ground (or inlet) vortex can be a major problem. With the advent of large passenger jets in the 1950s ground vortices were quickly identified as a problem because of its ability to ingest large objects into the engine[43,15]. Low pressure in the vortex core can impart an impulsive force onto objects that are present on solid surfaces. Subsequently objects and also particles and dust (referred to as foreign objects) are lifted off the surface, entrained into the inlet flowfield and carried into the engine by the induced velocity field of the intake. The ingested particles and debris

can damage fan blades, erode compressor blades and seals and degrade turbine cooling performance[25].

However not only is the vortex responsible for foreign object ingestion (FOD), but it can also present a severe distortion of the associated intake flow-field[33]. This distorted flow-field can have a major impact on the aircraft performance, such as a reduction on the stall and surge margins and therefore compromising the safety of the aircraft.

With fan diameters becoming increasingly larger, fan vibration has recently been identified as an additional major consequence of ground vortex ingestion[11,16]. The non-uniform flow associated with the ground vortex entering the intake, introduces momentum loss and large velocity gradients, which can significantly alter the local flow angle seen by the fan blade. As a consequence local flow separation can occur which leads to large resonant forces potentially resulting in high cycle fatigue.

1.1 Current Knowledge

It was previously identified that the key to the existence of ground vortices is the formation of a stagnation point on the ground ahead of the intake highlight plane[43]. In order for the aforementioned to exist, the capture streamtube must interact with the ground surface. This has been recognized to fundamentally depend on two key non-dimensional parameters. The first of which is the non-dimensional height of the intake, H/D_i, typically defined in the literature using the centreline height of the intake, H, and the intake inner diameter, D_i. The second dimensionless parameter is the velocity ratio, U_i/U_∞, which characterizes the contraction ratio of the sucked streamtube and is a measure of the size of the streamtube upstream of the intake. This is derived from continuity considerations and is defined as being the intake velocity, U_i, divided by the free-stream velocity, U_∞. In order for the streamtube of the intake to interact with the ground plane the height-to-diameter ratio, H/D_i, must be small and the contraction ratio, U_i/U_∞, must be large.

Current design rules for the avoidance of ground vortex formation relies on the vortex/no-vortex map in which a number of previous researchers have correlated combinations of H/D_i and U_i/U_∞ for both when vortices are observed and when no vortex activity is identified. This lead to the establishment of two distinct regions as a function of ground clearance and velocity ratio; a region of vortex formation and no vortex formation (Fig. 1.2). At present this represents the most advanced designs rules for engine installations and operations. However, this graphic gives no indication of what happens to the quantitative vortex characteristics as the engine operates in different regions of the vortex formation zone (Fig. 1.2).

In terms of alleviating the phenomenon a number of methods, past and present, have been attempted with a number of patents being documented[29,51]. The majority of these measures attempt to remove the stagnation point on the ground plane which is recog-

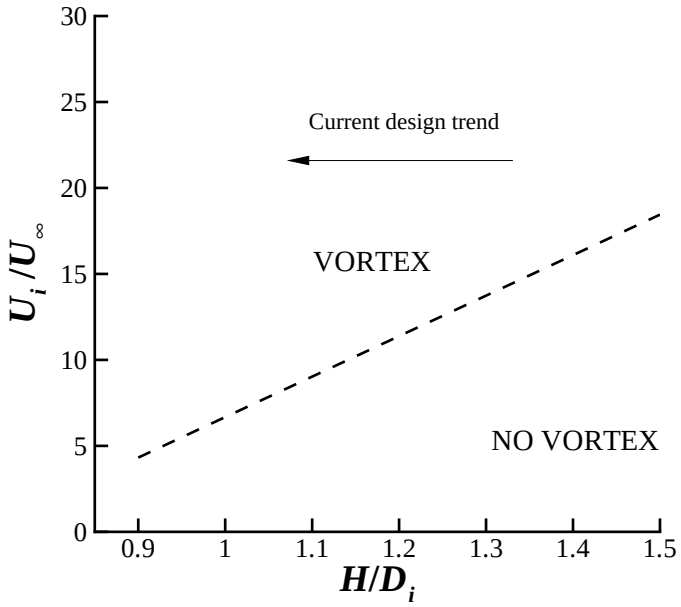

Figure 1.2: Velocity ratio against non-dimensional revealing a region of vortex formation

nized as being a fundamental to the formation of ground vortices. Most mitigation measures use a jet of air, extracted from the compressor, directed on the region of vortex formation on ground, at an aim of removing the FOD issue. A prevention system, of this form, was even put into practice in the late 1950's, and early 1960's, on the DC-8[29,25]. However after reviewing the unscheduled removal of engines due to FOD, the device was found to actually cause more problems by disturbing just as much debris as the vortex itself[25].

Despite a number of flow control methods being developed, the general consensus is that ground vortex formation is unavoidable. With the current design trend of turbofans, intakes are operating further to the left in Fig. 1.2 in which the formation envelope is considerably larger. As a consequence ground vortex formation will occur over a wider range of operating conditions and will potentially be sustained for longer periods during the take-off phase. This significantly increases the number of vortex ingestion events that will occur over the lifespan of the engine. With limited quantitative information available particularly at different height-to-diameter ratios, it is becoming vitally important to further understand the severity of the vortex in different regions of the vortex zone (Fig. 1.2).

1.2 Project Aims and Objectives

The present work primarily aims to provide quantitative information on the ground vortex over a wide range of operating conditions, which encapsulates the potential

changes in turbofan installations. In achieving this aim it is hoped that advanced design rules can be established for future engine designs. A number of key objectives have therefore been established to achieve this target:

1. Design and build a test rig for taking quantitative measurements of the ground vortex, at a representative intake Mach number, in the Cranfield University $8' \times 6'$ wind tunnel.

2. Successfully apply the measurement technique of Stereoscopic Particle Image Velocimetry (SPIV) to the complex flowfield.

3. Conduct an extensive total pressure survey within the intake duct, for supporting analysis, for the majority of SPIV configurations.

4. Quantify the effect of the non-dimensional parameters of primary importance (i.e. the non-dimensional height (h/D_l), the intake yaw angle (ψ) and the velocity ratio (U_i/U_∞) in terms of vortex strength and fan face distortion.

5. Develop an empirical model that can predict the vortex characteristics for a given configuration.

6. Establish a more complex vortex formation map which can indicate not only when a vortex is expected to occur but also how detrimental it is expected to be for a given non-dimensional height and velocity ratio.

7. Provide the vortex characteristics of primary importance with regards to fan vibration (i.e. the vortex size, strength and intake distortion) and to understand how these vary with intake configuration.

8. Quantify and understand the effect of a moving aircraft on the formation and characteristics of the ground vortex using a rolling ground plane in the wind tunnel. This should reveal additional features on the formation mechanism as well as indicating the expected characteristics and lifetime of the vortex during the take-off phase.

9. Interpret the model results with respect to engine application.

CHAPTER 2

Literature Review

A concise review of published work relating to ground vortex formation is presented in this chapter. The first part of the review discusses the criteria for vortex formation based on previous research. This is then followed by a discussion of the formation mechanisms that have been established to date, as well as the generation of ground vortices under reverse thrust operation. The review also includes CFD studies that have been published in the public domain. The chapter concludes by discussing the attempted methods of removing or reducing the impact of ground vortex formation.

2.1 Criteria for Vortex Formation

Within the first published works on ground vortex formation, characteristics, and behaviour, it was quickly identified that a necessary requirement for vortex formation is the existence of a stagnation point on the ground plane[43]. This acts as a focal point for vorticity upstream to be concentrated and stretched into the intake. A prerequisite for this stagnation point to exist is that the sucked streamtube has sufficient interaction with the ground surface. The sucked (or capture) streamtube itself is defined as being a streamtube of air which divides the airstream into an internal flow and an external flow (Fig. 2.1). All flow inside the capture streamtube is ingested, whereas all air outside this boundary travels downstream. The characteristics of the sucked streamtube can be estimated from conservation of mass:

$$\rho_\infty A_\infty U_\infty = \rho_i A_i U_i \tag{2.1.1}$$

$$\frac{A_\infty}{A_i} = \frac{\rho_i}{\rho_\infty}\frac{U_i}{U_\infty} \tag{2.1.2}$$

For an incompressible flow the area ratio, A_∞/A_i, of the sucked streamtube is equal to the operating velocity ratio:

$$\frac{A_\infty}{A_i} = \frac{U_i}{U_\infty} = U^* \tag{2.1.3}$$

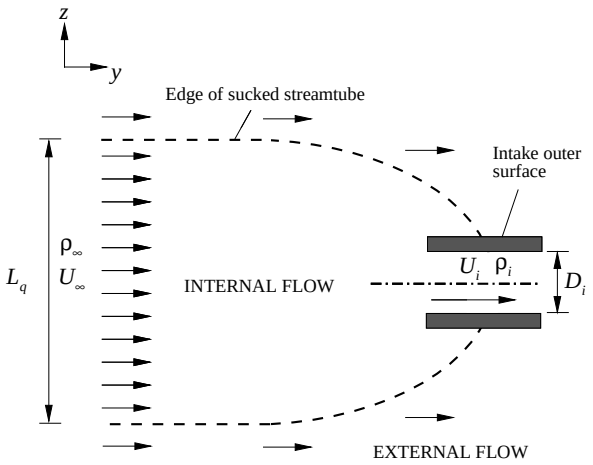

Figure 2.1: Illustration of sucked streamtube of an intake far from the ground

Within the literature on ground vortex formation, the velocity ratio, U^*, is used to define the sucked streamtube size at far field relative to the intake dimension. When the approaching velocity, U_∞, is low (i.e. U^* is large) the engine mass flow demand increases and as a consequence the sucked streamtube size, A_∞, increases to match this demand.

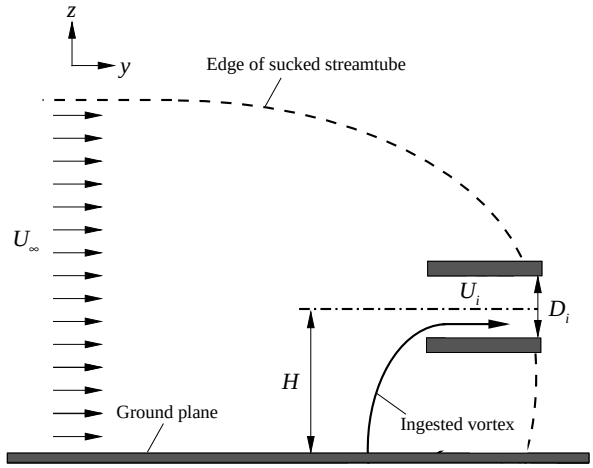

Figure 2.2: Schematic of the sucked streamtube interaction with the ground plane

The primary parameters that dictate whether the capture streamtube interacts with the ground plane depends fundamentally on the height-to-diameter ratio, H/D_i, of the intake (Fig. 2.2) and the velocity ratio, U^* (which determines the size of the capture streamtube at far field). High velocity ratios and low non-dimensional heights lead to an interaction of the streamtube with the ground and therefore vortex formation. The

dependency of these two parameters on the formation of ground vortices was graphically illustrated by Liu et al[31], in which pairs of H/D_i and U^* values were correlated for cases with and without vortices. The vortex/no-vortex map reveals two regions; a vortex formation region and a no vortex zone (Fig. 2.3). Subsequently, in a related study, Shin et al[50] constructed a vortex formation map based around Liu et al's results but also included data from full scale engine visualizations and other researchers. The established threshold has also been indicated in Fig. 2.3. In addition, Nakayama and Jones[37] presented a criterion based on previous research (Eq. 2.1.4). This is also included in Fig. 2.3. All three datasets show excellent agreement, however they all appear to be based on roughly the same data.

$$\frac{U_i}{U_\infty} = 24 \cdot \left(\frac{H}{D_i}\right) - 17 \tag{2.1.4}$$

Nakayama and Jones[37] presented quantitative total pressure measurements at two velocity ratios under headwind conditions with both data points being included in Fig. 2.3. Their results contradicted all the aforementioned thresholds with the data suggesting that a vortex can form at lower than previously reported velocity ratios (Fig. 2.3). At this point it should be noted that both the formation criterions established by Liu et al[31] and Shin et al[50] were based purely on crosswind configurations and were determined from visualizations only and as stated above the boundary presented by Nakayama and Jones appears to be based primarily on the same data.

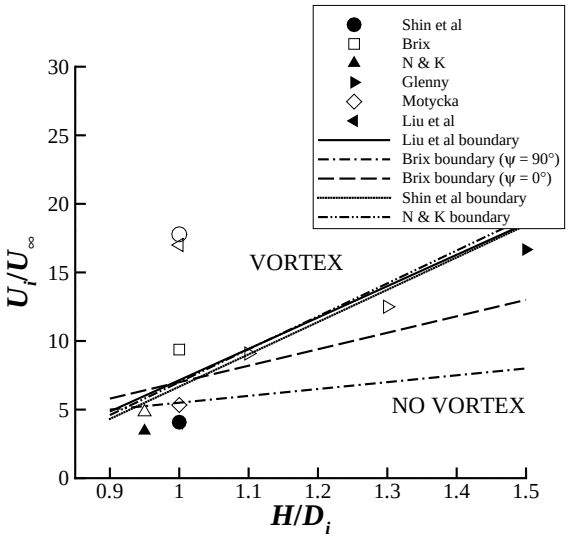

Figure 2.3: Correlation of velocity ratio and non-dimensional height combinations revealing a region of vortex formation and no-vortex formation (filled symbols represents a data point in which no vortex is seen, and unfilled symbols are points in which vortices are observed)

More recently Brix et al[6] presented a vortex formation map with a criterion being established for both headwind and crosswind configurations. Both have been approximately extracted and included in Fig. 2.3. Within Brix et al's[6] work quantitative

measurements were taken within the intake duct using a rotating hot-wire. However it is unknown whether this criterion was based on visualizations or quantitative results. Nonetheless there is a considerable difference between the established boundary under crosswind conditions ($\psi = 90°$) and the previously mentioned vortex avoidance thresholds. This discrepancy can be put down to the different methods used to detect a vortex, as well as potentially different operating conditions (such as boundary layer thickness). However, surprisingly the minimum velocity ratio required to generate a vortex under headwind conditions is higher in comparison to crosswind. No explanation was provided by the author for this observation. A number of possibilities could explain this finding such as different sucked streamtube characteristics between headwind and crosswind configurations, the crosswind vortex being significantly stronger and therefore easier to detect, or that the unsteadiness is larger under headwind conditions, thereby rendering it's presence difficult to determine.

A recent computational study by Jermy and Ho[24] examined the sensitivities of different upstream conditions on the formation boundary under headwind conditions. Within this research different upstream velocity gradients and approaching boundary layer thicknesses were examined. The authors found that 'no discernible vortex' formed when the upstream shear reduced below a certain threshold[24]. However as will be discussed below, previous experiments have shown that vortices can form under quiescent conditions, in which there is no upstream shear or vorticity source at all. In terms of the approaching boundary layer thickness, δ, results showed that as δ increased the vortex formation threshold was found to reduce[24].

The above findings lead to an important point in terms of the observed sensitivities in the formation boundary. The velocity ratio defined by Jermy and Ho[24] and within all previous literature uses the velocity ratio based on the free-stream velocity, U_∞. However Eq. 2.1.3 derived above inherently assumes a uniform velocity profile within the sucked streamtube. If there is an approaching boundary layer present in the capture streamtube the velocity profile is therefore clearly not uniform, and will consequently have an effect on the sucked streamtube size. In order to ingest the same mass flow, the sucked streamtube area must increase. As a consequence, the velocity ratio (U^*) at which the streamtube lifts off the surface will be lower, as observed by Jermy and Ho[24]. Strictly, since the velocity ratio is a measure of the sucked streamtube contraction ratio the area weighted average velocity, $\bar{U}_\infty$, within the sucked streamtube should be used in the definition of the velocity ratio. Using this definition should give the same velocity ratio for any approaching boundary layer thickness. This is believed to be one of the reasons for the discrepancies in the observed formation boundaries*. However since the size of the sucked streamtube is generally not known, it is difficult to determine the $\bar{U}_\infty$, and is why all published literature uses the free-stream velocity.

In addition to the necessary condition that the sucked streamtube interacts with the

*The other main reason for the discrepancies in the formation boundary is the methods used to detect the vortex. As stated above primarily flow visualization techniques have been used, however implementing such methods tend to only identify the strongest vortices. Hence weaker vortices that form just before the vortex is blown-away tend not to be identified

ground plane (thereby forming a stagnation point) all studies state that there must be a vorticity source for the vortex. Within the earliest reported studies a commonly quoted condition was the existence of ambient vorticity in the form of an approaching ground boundary layer[9]. However, as will be discussed in the following section, studies by de Siervi et al[10] and Brix et al[6] have revealed that vorticity can be introduced into the flowfield even with no approaching ambient vorticity source.

2.2 Mechanisms of Ground Vortex Formation

Research to date has identified two formation mechanisms. The first is applicable to an intake under quiescent (no-wind) and headwind conditions and the second relates to an intake in crosswind conditions. The two mechanisms are fundamentally different because of the contrasting dominant vorticity sources for the vortex. Consequently, comparatively different behavioural features and characteristics are observed with each respective mechanism which are described below.

2.2.1 Headwind Mechanism

This mechanism is applicable to an intake with its axis parallel to the flow direction. Many researchers have identified that it is the intensification of ambient vorticity that causes concentrated vortices to form. However it was not until the work of de Sievri et al[10] that proved this theory by conducting extensive water tunnel flow visualization studies using the hydrogen bubble technique. Different approaching vorticity sources and orientations were introduced upstream of the intake including a boundary layer, and clockwise and counter clockwise shear profiles (Fig. 2.4). It was shown that the direction, deformation and convection of the ambient vortex lines associated with the dominant vorticity source dictate the rotation and number of vortices seen at the fan face. This was also verified using potential flow theory in which the primary irrotational potential flow is superimposed linearly with a weak shear flow. Selected material lines were tracked as they approached the intake and the deformation of the vortex lines, where found to agree with the experimental observations. The flow topology for the different boundary layer profiles are discussed below.

Vortex lines are defined as being a line in the fluid whose tangent is everywhere parallel to the local vorticity vector[2]. Hence for a boundary layer type profile (Fig. 2.4a) the vortex lines associated with this flowfield, far upstream of the intake, are parallel to the ground and perpendicular to the flow direction (Fig. 2.5a). As the vortex lines are convected by the mean flow and approach the intake they are stretched and deformed as illustrated in Fig. 2.5 due to the influence of the induced intake flowfield. As a result two counter-rotating vortices are ingested symmetrically placed about the intake axis (Fig. 2.5). The rotation of each respective vortex is directly determined by the rotation of the leg of the vortex line it is associated with (Fig. 2.5a).

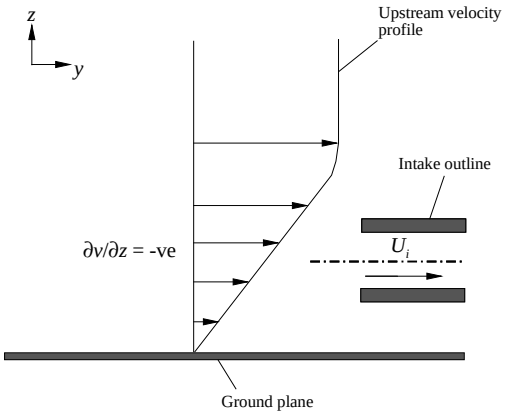

(a) $\partial v/\partial z = -ve$

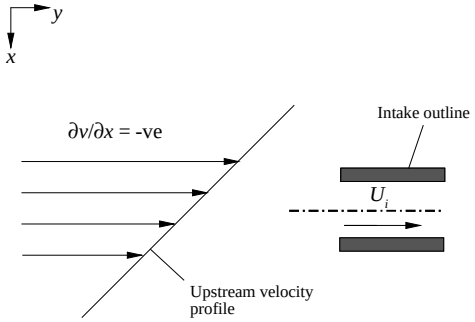

(b) $\partial v/\partial x = -ve$

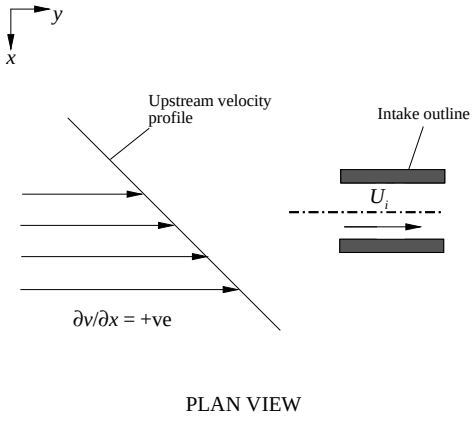

(c) $\partial v/\partial x = +ve$

Figure 2.4: Velocity profiles used in de Siervi et al experiments (diagrams after de Siervi et al[10])

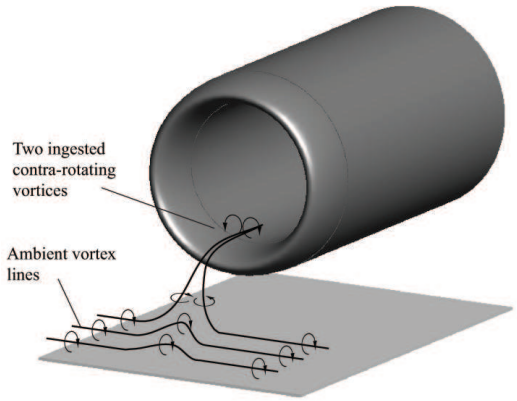

(a) $\partial v/\partial z = +ve$

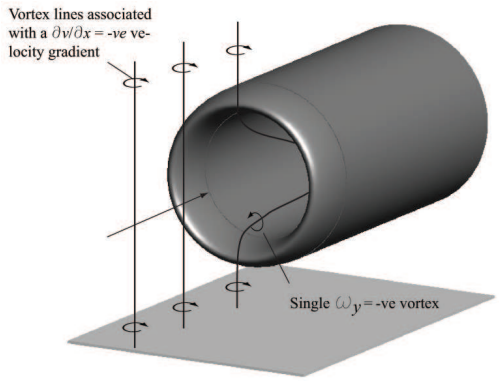

(b) $\partial v/\partial x = -ve$

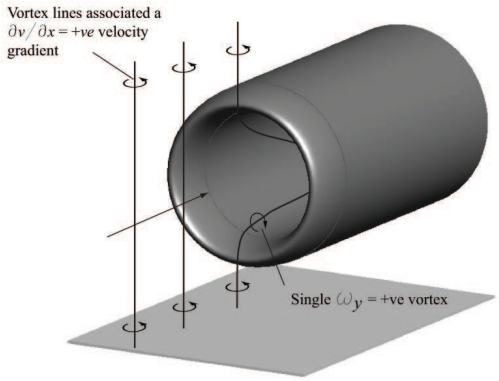

(c) $\partial v/\partial x = +ve$

Figure 2.5: Deformation of the ambient vortex lines as they approach the intake for different upstream velocity gradients

In contrast, for the shear profiles the pattern is quite different. With a negative $\partial v/\partial x$ velocity gradient upstream (Fig. 2.4b) the vortex lines are straight and perpendicular to the ground surface (Fig. 2.5b). As they approach the intake, the high velocities associated with the intake flowfield stretches the vortex filaments resulting in only a single ground vortex being ingested (Fig. 2.5b). The rotation of the vortex is dictated by the corresponding rotation of the dominant vortex lines upstream of the intake. Hence with a negative $\partial v/\partial x$ dominant velocity gradient upstream, the vortex rotates in the intake duct such that it has negative ω_y vorticity (Fig. 2.5b). The converse is true for the positive $\partial v/\partial x$ dominant velocity gradient upstream (Fig. 2.5c) where the ingested vortex rotates with positive ω_y. In addition to the experiments potential flow calculations were performed to verify the experimental observations and to determine the behaviour of the upper legs of the ingested vortex lines. The results showed that the all the lower legs were concentrated at the stagnation point whereas the upper legs fanned out over the top of the intake, with no concentration being observed.

The experiments and theories put forward by De Siervi were instrumental in the understanding on the fundamental mechanisms of vortex formation. However these studies were purely qualitative in nature and no quantitative information of the vortex was provided. In order to determine the scale of the problem, distortion and vortex strength measurements need to be taken.

As a follow on to de Siervi et al's[10] research, Shin et al[49] performed experiments to quantitatively verify the potential flow calculations. A negative $\partial v/\partial x$ velocity gradient was introduced upstream of the intake (Fig. 2.4b) and hot-wire measurements were taken inside the intake for a single configuration. The results confirmed the theory that the orientation and rotational sense of the ambient vertical vortex lines determines the number and rotation of the vortex within the intake. In addition, a first measure of the vortex strength was given for a $H/D = 1.13$ and $U_i/U_\infty = 22$:

$$\frac{\Gamma}{\omega_\infty A_\infty} \approx -2 \tag{2.2.1}$$

However, it was not until the work of Brix[5,6] that significant measurements of the ground vortex were taken. Quantitative data was taken inside the intake duct using two rotating hot-wires. The technique enabled quantitative measurements to be taken within the intake duct without averaging. The results were in agreement with the above observations, with some new findings also being reported. Perhaps the most significant of which was the formation of two contra-rotating vortices under quiescent conditions ($U^* = \infty$), which had never been previously reported. Although no quantitative measurements were presented under such conditions the vortices were observed to rotate in the opposite sense to that in headwind conditions. Brix et al[6] also demonstrated quantitatively under headwind conditions that the vortices rotate in accordance with the quiescent mode if the velocity ratio exceeds a certain threshold. In the following section these flow modes are discussed in more detail.

2.2.1.1 Formation Modes

Under quiescent (no-wind) conditions the engine induces an external flowfield to the intake that emanates from all directions in the near vicinity. The induced velocities immediately adjacent to the ground interact with the surface generating vorticity. This 'induced' vorticity is the source for the vortex and by definition this formation mechanism requires no ambient vorticity. Brix notes that under no-wind conditions it is the flow behind and between the intake and the ground that dominates. As a consequence the vortex lines associated with this dominant flow are stretched and deformed as shown in Fig. 2.6. This situation is very similar to the headwind mode (Fig. 2.5a) except the source of vorticity is associated with flow approaching from the opposite direction and is a direct consequence of the intake induced flowfield rather than the approaching flow. As a consequence the vortices within the intake duct rotate in the opposite direction to that under headwind conditions, as shown in Fig. 2.7a. Since the formation mechanism is largely the same in comparison to headwind conditions, the vortices generated under quiescent conditions can be regarded as a flow mode of the headwind mechanism. This finding, by Brix et al, was purely based on flow visualization studies and no quantitative measurements have been reported under such conditions to date.

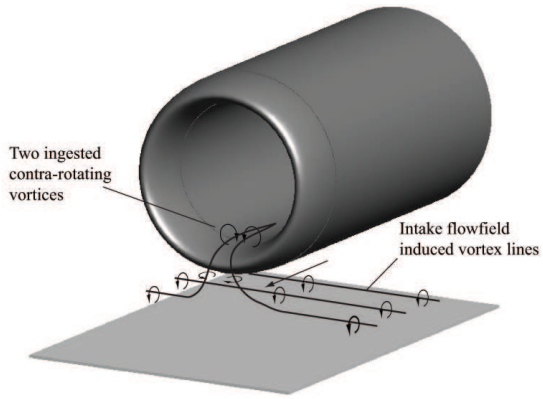

Figure 2.6: Vortex formation under quiescent conditions

Related to the current work Murphy et al[36] have quantitatively verified the findings of Brix. Using Stereoscopic Particle Image Velocimetry (SPIV) the flow under quiescent conditions was quantitatively studied and two contra-rotating vortices were found to form in accord with the flow topology presented in Fig. 2.6. However the flowfield was observed to be highly unsteady and often only a single dominant vortex was observed. For the first time quantitative measurements under quiescent conditions were presented which included fully averaged total pressure distortion measurements at the fan face. The vortices generated under quiescent conditions were observed to be weak but not insignificant.

In addition to the above findings, Brix et al[6] quantitatively demonstrated that even under headwind conditions (i.e. $U^* \neq \infty$), if the velocity ratio is large enough the

(a) No-wind mode (b) Transition phase (c) Headwind mode

Figure 2.7: Flow modes observed under headwind conditions (diagrams after Brix et al[6])

vortices will rotate in agreement with the quiescent mode within the intake duct. This was shown for a configuration in which the intake height, H/D_i, was equal to 1 and the velocity ratio was $U^* = 33$. In contrast, at a velocity ratio of 12 the vortices were found to rotate in the expected fashion for the headwind mechanism (i.e. in accord with the flow topology presented in Fig. 2.5a and Fig. 2.7c). Brix noted that in between this rotation switch there existed a transitional phase in which the influence from the approaching (Fig. 2.5a) and induced vorticity sources (Fig. 2.6) are approximately equal and opposite (Fig. 2.7) leading to an instability in the vortex pair. The exact velocity ratio at which this occurred was not given in Brix et al[6].

2.2.1.2 Additional Observations

Before the works of de Siervi and Brix an intriguing study was provided by Bissenger and Braun[4] in which contrasting observations are reported in comparison to the above findings. Similar to de Siervi et al[10], hydrogen bubble visualization was implemented within a water tunnel but with a considerably smaller intake diameter, D_i, of 16mm constructed from a copper tube. A range of intake configurations were investigated including a single inlet close to the ground as well as two symmetrically placed inlets with no ground plane to examine the influence of the approaching boundary layer.

For the single intake configuration, at low velocity ratios when no ground vortex was present two vortices were ingested into the intake and trailed downstream (Fig. 2.8a). This flow structure has never been reported by any other researchers. As the intake velocity and hence velocity ratio increased a vortex system appeared which comprised of a single ground vortex, a trailing vortex and a number of ground based streamwise vortices (Fig. 2.8b). Bissenger and Braun found that all vortices were non-stationary and often the ground vortex would appear on the other side of the intake with a reversed sense of rotation (with the trailing vortex also reversing its position and rotational sense). Often the vortex system was observed to break down and then reform sporadically without any changes in the test conditions.

As stated above, the observations of Bissenger and Braun[4] are slightly different to previously mentioned experiments. It should be noted that no upstream velocity profile

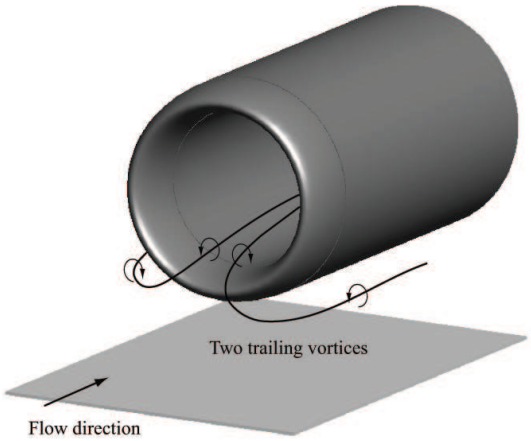

(a) Low velocity ratios

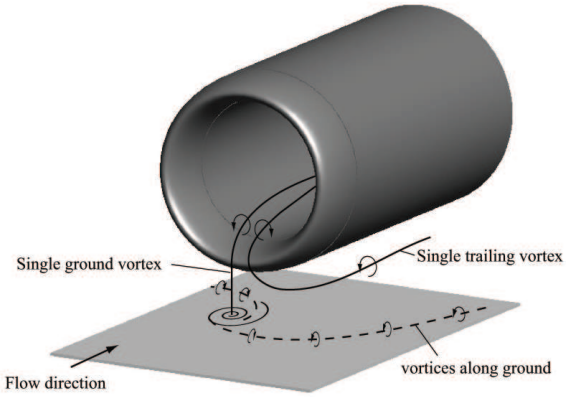

(b) High velocity ratios

Figure 2.8: Flow topology observed by Bissenger and Braun[4] under headwind conditions for (a) two trailing vortices (b) A complex vortex system involving a single ground and trailing vortex, plus vortices on the ground

was prescribed in the tests. It is therefore expected that the vortex lines associated with the boundary layer type profile would dominate, and given the above, one would expect two contra-rotating vortices to be observed. A potential reason for the prevalence of only a single vortex could be due to a slightly asymmetric flowfield or small non-uniformities inherent in the tunnel flow. In addition the hydrogen bubble generator was placed just upstream of the intake and spanned across the test section which may have influenced the flowfield topology. The highly unsteady flowfield observed by Bissenger and Braun may be due to the flow quality in the water tunnel. However the non-dimensional heights investigated were considerably larger compared to other researchers and ranged from 1.5 to 3 (H/D_i). Many workers note that higher ground clearances result in a considerably more unsteady vortex behaviour[35,56].

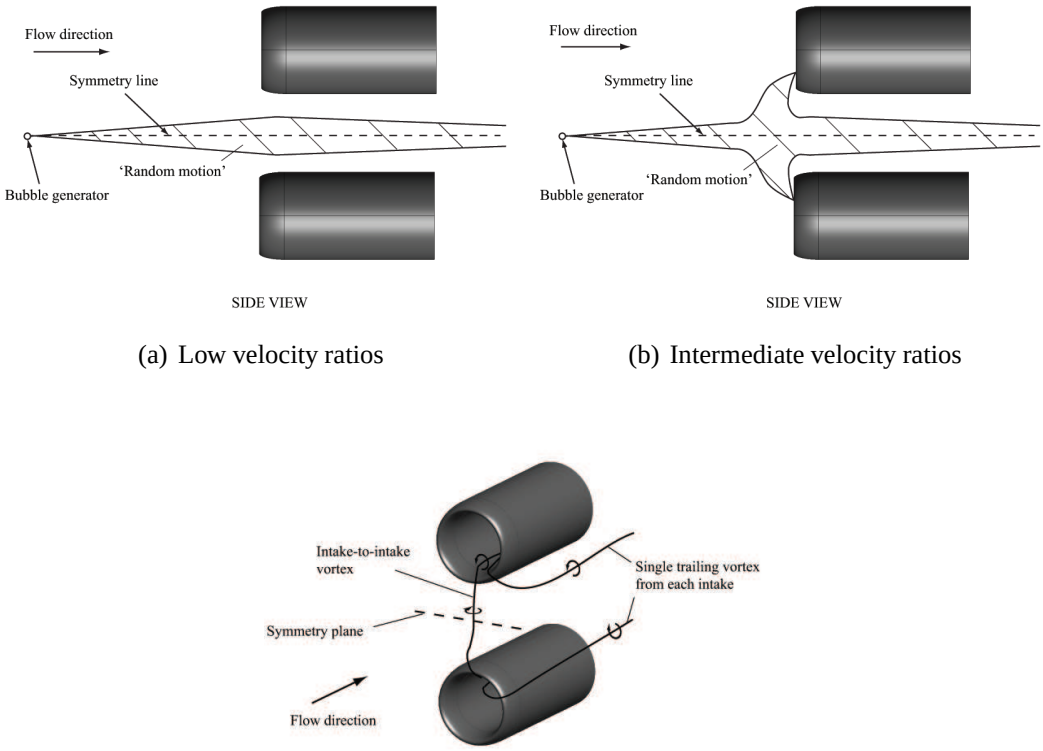

(a) Low velocity ratios

(b) Intermediate velocity ratios

(c) High velocity ratios

Figure 2.9: Formation of the intake vortex system for a twin inlet configuration as observed by Bissenger and Braun[4]

Tests were also conducted with two intakes one above the other with no ground plane (Fig. 2.9). For this configuration the presence of the second intake introduces a symmetry plane that acts as an inviscid ground, hence the influence of the approaching boundary layer vorticity source can be examined. Bissenger and Braun[4] observed at

low velocity ratios a region of 'random motion' formed between the two intakes (Fig. 2.9a). This region extended from the hydrogen bubble generator and as the velocity ratio increased the 'random motion' extended into the two intakes (Fig. 2.9b). With a further increase in the velocity ratio a vortex system appeared which comprised of an intake-to-intake vortex, and a single trailing vortex from each respective inlet (Fig. 2.9c). The authors therefore concluded that the approaching boundary layer is not vital for vortex formation. However it is clear from the diagrams presented in Bissenger and Braun[4] that the presence of the hydrogen bubble generator is introducing a source of vorticity into the flowfield which is seen by the presence of this 'random motion' region.

2.2.2 Crosswind Mechanism

In this section the relevant past research relating to the formation of ground vortices under crosswind conditions is discussed. This section is divided into two parts; the formation mechanism and the quantification of the vortex characteristics.

2.2.2.1 The Formation Mechanism

Within the works of de Siervi et al[10] studies were also conducted to examine the effect of different approaching vorticity sources under pure crosswind conditions ($\psi = 90°$). The experiments under this configuration were aimed at testing the theory of the intensification of ambient vortex lines upstream of the intake to non-zero yaw angles. The experiments gave rise to an additional vortex formation mechanism applicable to intakes in significant crosswinds.

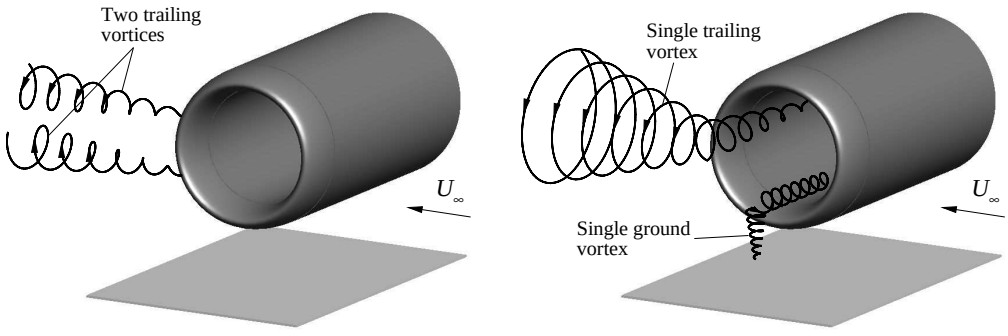

(a) High h/D_l or low U^* (b) Low h/D_l or high U^*

Figure 2.10: Flowfield topology under crosswind conditions (a) two contra-rotating vortices and (b) a single trailing vortex, ground vortex system

The influence of positive and negative $\partial v/\partial x$ velocity gradients (Fig. 2.4b-c) were examined upstream of the intake with its axis 90 degrees to the flow direction. From the results under headwind conditions it was expected that a change in the sense of rotation of the ambient vortex lines would lead to a change in the rotation of the vortex (Fig. 2.5). However, the behaviour of the vortex was observed to be quite different to that in headwind. It was found that for a left to right crossflow, the ground vortex always had positive ω_y vorticity within the intake duct; changing the upstream rotation of the vortex lines therefore lead to no change in the vortex rotation, suggesting an additional mechanism was at play.

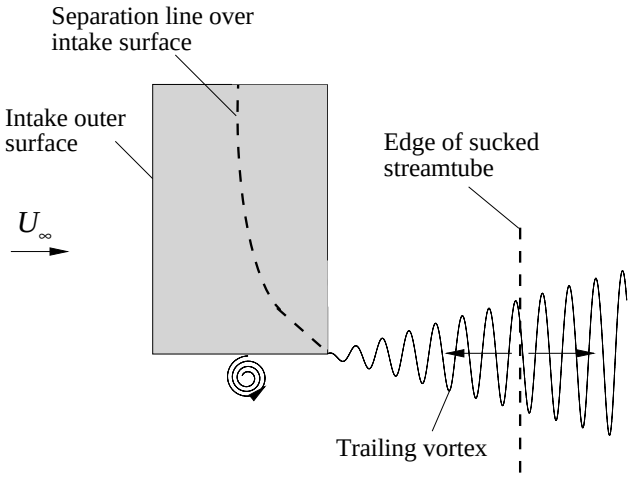

Figure 2.11: Plan view of flowfield under crosswind conditions with a ground vortex showing the separation line over the intake surface (diagram after Shin et al[50])

This prompted further study in which an irrotational flow upstream of an intake at 90 degrees to the flow direction was examined. The experiments revealed the formation of a single ground vortex accompanied by a trailing vortex off the leeward edge of the intake (Fig. 2.10b). The size of the trailing vortex was observed to be approximately that of the intake outer diameter, D. The presence of the trailing vortex was postulated to be due to a variation in the circulation around the intake. This was argued by considering the variation in the circulation at different axial stations along the outer surface of the intake. Several diameters from the lip the flow around the intake is roughly two-dimensional, in which the local flow velocity is of the order of U_∞, hence the local circulation around the intake should scale with $U_\infty D$[10]. In contrast, the circulation around the intake close to the lip is expected to be proportional to $U_i D$ (where U_i is the intake velocity), since at this location the induced intake flowfield has a dominating effect[10]. This variation was qualitatively visualized by the skew in the separation line over the top half of the intake surface (Fig. 2.11) which was later quantitatively verified using static pressure measurements over the intake outer surface at different axial stations[31]. Due to the difference in circulation, it was argued that there must be trailing

vorticity between the two axial locations. de Siervi et al[10] hypothesized, which was later verified by Shin et al[50], that the circulation of the ground vortex is approximately that of the trailing vortex. This hypothesis was based on the theory that the vortex lines associated with the ground vortex and trailing vortex must join at infinity. However Brix et al[6] took measurements of the ground and trailing vortices which indicates that the two are not equal with the trailing vortex being weaker.

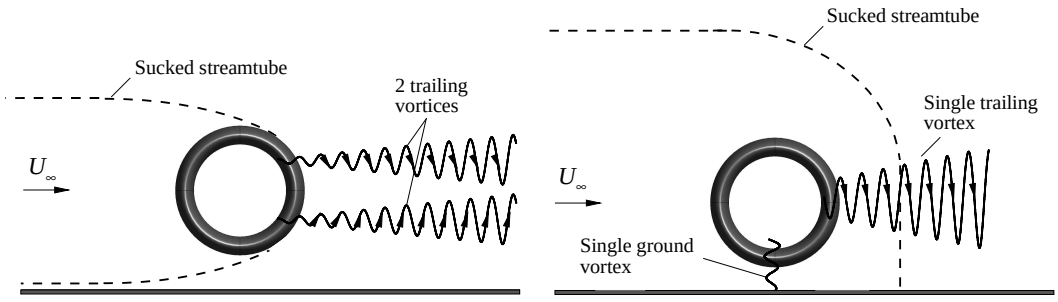

(a) High h/D_l or low U^* (b) Low h/D_l or high U^*

Figure 2.12: Side view showing the flowfield topology under crosswind conditions with and without the sucked streamtube interacting with the ground plane (figure after de Siervi et al[10])

The flow regimes as a function of contraction ratio were also explored using flow visualization studies briefly by de Siervi[10] and in more detail by Shin et al[50]. It was observed at low velocity ratios, when the sucked streamtube has no ground plane contact and no ground vortex was observed, two contra-rotating vortices trailed from the leeward edge of the intake (Fig. 2.10a and 2.12a). As the velocity ratio was gradually increased, the two trailing vortices exhibited considerable lateral, as well as up and down movement, with the lower vortex intermittently attaching to the ground[50]. As the velocity ratio was slightly increased the ground vortex, trailing vortex system abruptly appeared (Fig. 2.10b). This intermittent attachment behaviour of the ground vortex and also the abrupt nature to which the vortex attaches to the ground plane was also observed by Brix et al[6] and can also be seen in the full engine test visualizations presented in Appendix A.

Given the finding that the orientation of the upstream ambient vorticity had no influence on the vortex rotation, the flowfield was further investigated by examining the influence of the ground boundary layer. de Siervi et al[10] conducted experiments using a twin inlet configuration, in which the ground plane is replaced by an inviscid symmetry plane (Fig. 2.13). Flow visualization studies reveal the occurrence of a single intake-to-intake vortex, with a single trailing vortex off each corresponding intake (Fig. 2.13). It was observed that within the core of the intake-to-intake vortex there was a continual convection of vorticity away from the symmetry plane. To examine the source of vorticity for the vortex, the transient formation of the vortex was studied by de Siervi et al[10]. With no approaching vorticity, the only source of vorticity is that associated with the boundary layer over the intake surface. Flow visualizations

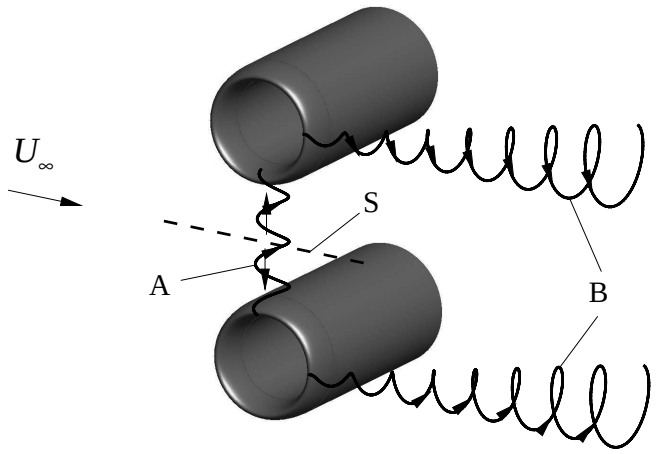

Figure 2.13: Flow topology for a twin inlet configuration (*S* denotes the symmetry plane location, *A* is the intake-to-intake ground vortex and *B* highlights the two trailing vortices) (figure after de Siervi et al[10])

showed that vorticity is shed from the intake during the transient and a vortex forms downstream of the inlets, strengthens and moves upstream to a position between the intake once the steady state is achieved. The formation time scale was quoted to be approximately $10H/U_\infty$. After the transient, de Siervi et al[10] noted that no further convection of vorticity was observed into the core from the surrounding fluid. It was mooted that the convection of vorticity away from the symmetry plane was balanced by the production of vorticity due to stretching of the vortex filaments within the core. Shin et al[50] also provides similar arguments with regards to the trailing vortex.

However, there appears to be inconsistencies in the flowfield as described by de Siervi et al[10] and Shin et al[50] (as well as that in Waitz et al[65]). Firstly stretching of vortex lines is not a production mechanism, it only maintains vorticity that is already present[69]. If there is no continual convection of vorticity into the core of the vortex then ultimately the vortex should dissipate with time which is clearly is not the case. It is clear from de Siervi et al's experiments, however, that the source of vorticity for the vortex is from the separated flow over the intake outer surface. It is therefore possible that vorticity is shed from the intake during the transient and travels a small distance downstream due to the momentum imparted by the free-stream flow. At some point downstream of the intake, a stagnation region exists which marks the edge of the sucked streamtube. At this point the intake induced velocity field convects the vorticity back upstream to be concentrated and stretched to form a ground vortex. During the steady state there must be a continual convection of vorticity emanating from the intake outer surface and the

ground plane that feeds the vortex. For the twin inlet configuration, it is possible that vorticity shed from the lower portion of the intake is convected back upstream along the symmetry plane and enters the core of the vortex. This may be a better and more consistent description.

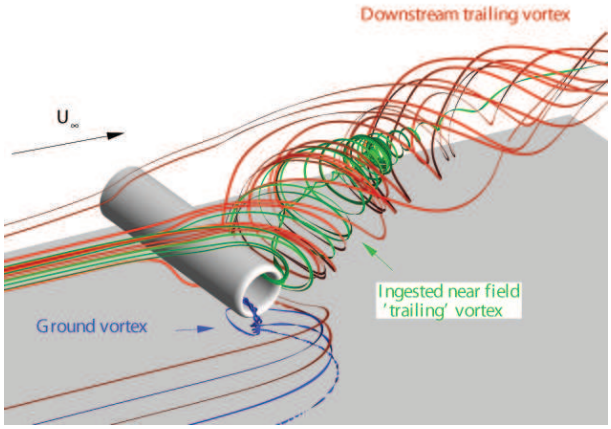

(a) $U^* = 19.8$

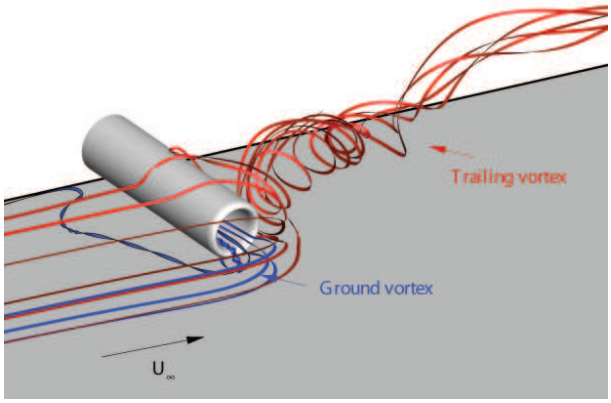

(b) $U^* = 9.9$

Figure 2.14: CFD simulations of the crosswind flowfield topology for a non-dimensional height of 0.25 (h/D_l) and $M_i = 0.58$ at two different velocity ratios[71,32]

In terms of the trailing vortex topology, the diagrams presented in de Siervi et al[10] (and also in related works[50,65]) depict the vortex emanating off the leeward edge of the intake and travelling downstream through the sucked streamtube. However a flow topology such as this seems unlikely since there must be a stagnation point at the edge of the capture surface that the trailing vortex must pass through. CFD simulations by Zantopp[71], however, reveals a slightly different flowfield topology which is more complex but appears to be more believable. For a non-dimensional height of 0.25 (h/D_l) and a velocity ratio (U^*) of 19.8, a single ground vortex forms between the intake and the ground plane (Fig. 2.14a). However, at this velocity ratio there are *two trailing vortices*; one inside (denoted by near field) and one outside the sucked streamtube (Fig. 2.14a). The nearfield trailing vortex is associated with the vorticity

off the intake outer surface. This vorticity initially travels downstream and once the edge of the capture streamtube is reached, is convected back towards the intake. This reverse flow forms the core flow of the trailing vortex. At the same time, fresh vorticity generated over the outer intake surface initially travels downstream and as it does so spirals around the core of the vortex. Once this vorticity reaches the edge of the sucked streamtube it enters the core of the vortex and is reingested into the intake. This can be seen from the near field ribbon streamline patterns in Fig. 2.14a. The second vortex is associated with the flow that travels over the outside of the capture streamtube. This trailing vortex also collects vorticity from the outer intake surface as well as from the ground plane downstream of the intake (Fig. 2.14a) and appears to be weaker than the 'ingested' trailing vortex. Interestingly, computations at a lower velocity ratio of 9.9 reveal just a single trailing vortex that is not ingested into the intake. This is plausible, since at this velocity ratio, the extension of the sucked streamtube downstream of the intake will be smaller therefore inhibiting the formation of an embedded trailing vortex within the capture surface.

2.2.2.2 Quantitative Studies of the Crosswind Ground Vortex

Shin et al[50] perhaps provides some of the first quantitative measurements of the vortex system under crosswind conditions. The primary aim of the study was to verify that the strength of the ground vortex was equal and opposite to the trailing vortex and also to conduct a parametric study of the important non-dimensional parameters (i.e. H/D_i and U^*). Measurements of the average inlet vortex strength were conducted inside the intake using three-hole and five-hole probes by rotating the inlet through 360° to obtain full coverage of the flowfield. Data was also taken external to the intake in a plane parallel to the ground using slanted hot-wire for comparison and were quoted to be 75-80% of the strength within the intake duct. Measurements of the trailing vortex found, as hypothesized, that the strength was equal and opposite to the ground vortex.

In addition to verifying that the ground vortex is roughly the strength of the trailing vortex, a limited parametric study of effects of capture ratio and non-dimensional height were given on the vortex strength and position within the intake. The ground clearance was reduced at a fixed velocity ratio of 44 (U_i/U_∞) from an H/D_i of 2 to 1. The vortex strength was found to monotonically increase with reducing ground clearance (Fig. 2.15). At the largest ground clearances the vortex strength was initially sensitive to changes in non-dimensional height. However for ground clearances between 1 and 1.5 the increase was very moderate. Three contraction ratios were examined to investigate the influence on this parameter on the vortex strength at a fixed ground clearance. The vortex strength was observed to decrease as the velocity ratio was decreased from 44 to 18 with no vortex being observed at a U^* of 4. It is difficult to interpret the results as only one data point has been taken a different velocity ratio when a vortex forms. The presented reduction in vortex strength may be due to the choice of non-dimensionalization.

As mentioned above the most extensive quantitative study to date has been conducted

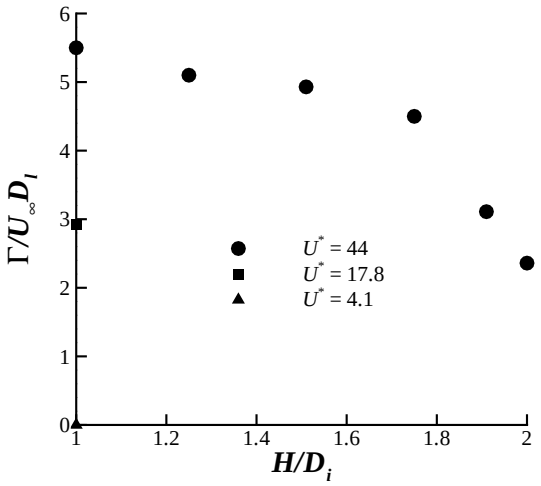

Figure 2.15: Effect of ground clearance and velocity ratio on the non-dimensional vortex strength under crosswind conditions (data extracted from Shin et al[50])

by Brix et al[6]. In crosswind conditions Brix has quantified the strength of the vortex within the intake duct for a range of intake velocities varying from 25 to 100 ms^{-1} and free-stream velocities varying from 2 to 8 ms^{-1}. Within this work maximum tangential velocities are presented for a range of configurations and a measure of the vortex core size is given. Brix found that as the velocity ratio reduced the vortex strength increased with the largest intake velocities producing the strongest vortex. This contradicts the measurements taken by Shin et al[50] (Fig. 2.15). A limitation to Brix et al's work, however, is that quantitative data has only been presented for a single ground clearance and only velocity measurements were taken.

2.3 Vortex Formation under Tailwind and Reverse Thrust Operation

As well as vortex formation under headwind and crosswind conditions, ground vortex formation can also occur under tailwind and during reverse thrust operation. Both situations are similar since in the latter case engine airflow is redirected back upstream toward the intake highlight plane effectively producing a tailwind (Fig. 2.16). An example picture of an ingested vortex under reverse thrust operation is shown in Fig. 2.17. In addition, a sequence of snapshots extracted from a video of a C-17 aircraft moving backwards under the influence of thrust reversal operation just prior to take-off is shown in Appendix A. The set of images illustrate the highly unsteady nature of the vortex and its apparent strength despite the height at which the intake is operating. It is also clear that the vortex is often seen to ingest into the core of engine, which is known to cause significantly greater operating difficulties. Despite these issues, in general, very little research has been conducted under such conditions. This is almost certainly due to the difficulties in simulating such conditions within a wind tunnel environment.

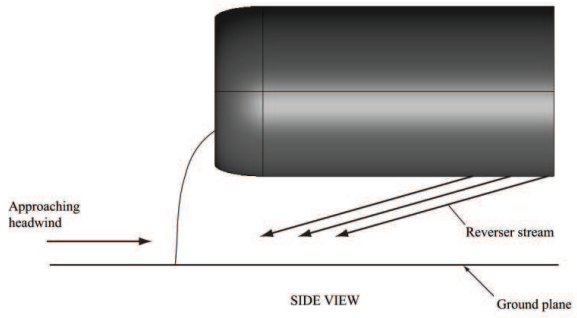

Figure 2.16: Reverse thrust operation introducing an effective tailwind to the intake

Figure 2.17: Ground vortex ingestion under reverse thrust operation, ©Keith Blincow

The only known research to have have covered this aspect experimentally has been conducted by Motycka et al[33,34,35]. This literature is also unique in that it is the only

known work, with the exception of Nakayama and Jones[37], to present distortion measurements induced by ground vortex ingestion at the fan face. Motycka et al conducted scaled model experiments and analytical potential flow calculations to establish the general behaviour and characteristics of ground vortex formation under tail-wind and revere thrust operation. The results of the potential flow calculations, which included swirl effects, are summarized in the following points:

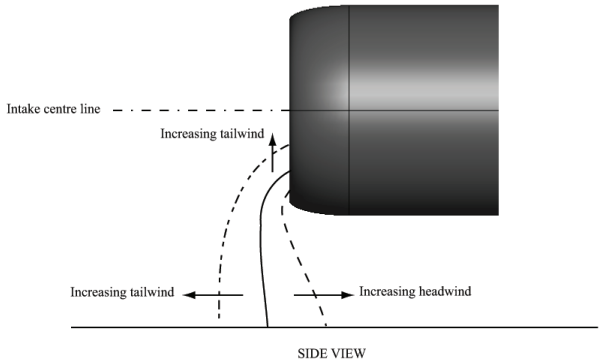

Figure 2.18: Effect of wind direction and strength on the vortex location on the ground plane and its consequent ingestion location (after Motycka[33])

1. Increasing the upstream ambient vorticity reduces the velocity ratio at which the vortex blows away. This is consistent with the discussion provided in §2.1.

2. As the tailwind increases the standoff distance of the vortex foot from the highlight plane increases. Consequently the vortex ingestion location changes with the vortex moving closer to the engine axis (Fig. 2.18).

3. The blowaway velocity required to remove the stagnation point on the ground plane is independent of wind direction except for yaw angles between 0 and 55°.

4. Decreasing the ground clearance of the intake increases the range of wind speeds at which a vortex will form.

5. The region of possible vortex formation on the ground increases as the non-dimensional height is increased (i.e. the unsteadiness is expected to be amplified).

6. The vortex core diameter under 135° tailwind conditions with $U^* = 8.7$ was found to be approximately 3.1% of the intake outer diameter from shadowgraph technique. In addition vortex core size was found to scale with the intake diameter.

Experiments were performed utilizing a $1/11^{th}$ scale model to evaluate the influence of reverser targeting (i.e. the direction in which the flow is redirected away from the

intake), inlet height, headwind speed on ground vortex formation during reverse thrust operation. The main conclusions from this aspect of Motycka et al's research are highlighted in the following:

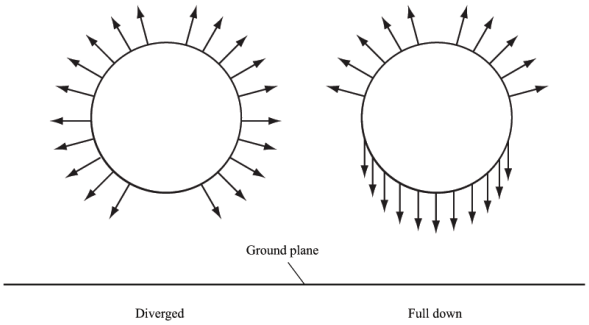

Figure 2.19: Reverser targeting pattern configurations investigated by Motycka (after Motycka[33])

- Two loss cores are identified. This indicates that the mechanism for vortex formation under reverse thrust operation is similar to that in headwind, with the dominant vorticity source being associated with the approaching boundary layer associated with the reverser jet stream.
- Local total pressure recovery within the core of the vortex was typically observed to be around 0.85 (P/P_∞).
- During constant reverser operation, as the headwind speed increases the distortion increases and reaches a maximum at a specific velocity ratio and reduces thereafter. This was attributed to a reduction in the interaction between the reverser and ambient air streams.
- Reducing engine power reduced inlet distortion at all airspeeds.
- Higher ground clearances resulted in significantly reduced levels of distortion.
- The reverser jet configuration appeared to affect the blowaway velocity ratio. With the jets directed vertically downwards (Fig. 2.19) the vortex was observed at higher headwind speeds, in comparison to the reverser configuration in which the jet stream was directed sideways (Fig. 2.19).

In addition to the above Motycka[33] provides perhaps the only study in the public domain to include full scale measurements of ground vortex ingestion. The tests were performed on the JT9D engine installed on a B-52 flying test bed aimed at determining the peak distortion levels just prior to engine surge during reverse thrust operation. Results indicated that ground vortex ingestion was the primary cause of engine surges. This is partly due to the high total pressure distortion induced by the vortex and most importantly the vortex being ingested into the core of the engine, as predicted from the potential flow results.

2.4 CFD Studies

Within the published literature there are relatively few CFD studies on ground vortex formation. However of these studies Karlsson and Fuchs[26,27] present Large Eddy Simulations (LES) of the ground vortex which reveal very interesting phenomena. Computations were performed under headwind conditions at fixed ground clearance of 1 (H/D) at a velocity ratio of 10 with a Reynolds number based on the inner diameter, D_i, of 55000. The results reveal a series of flow modes with time. Analysis of the vortical structures shows the existence of a complex vortex system consisting of multiple ground vortices, traces of horseshoe vortices from the ground, and streamwise vortices (aligned with the intake axis). In the first described flow mode two weak contra-rotating vortices are observed. At a later time a second flow mode appears in which a single dominant vortex prevails. This vortex is approximately aligned with the intake axis, with a clockwise sense of rotation on the ground plane[†]. The authors note that the vortex system and dynamics is similar to that described in Bissenger and Braun[4]. In a related piece of work conducted by Secareanu et al[46], the LES data is validated against LDA and two-dimensional PIV results of the flowfield at the same operating conditions. Despite some difficulties with seeding, the results between the datasets generally show good agreement illustrating that the LES technique has captured the correct flow physics.

As part of a larger study into novel flow control methods, Yadlin et al[70] present RANS computations of ground vortex formation for a range of configurations including a single intake, side-by-side intakes for varying respective positions, and a full scale aircraft model under headwind, tailwind and reverse thrust operation. The results reveal the formation of intake-to-intake vortices, as well as fuselage to intake vortices that agree with general full-scale observations. However, all results remain unvalidated against experimental data. It is hoped that the data presented in this thesis will provide a benchmark for CFD validation in the future.

In a study related to the current work, Rehby[42] and subsequently Zantopp[71] have studied ground vortex formation computationally. In the latter investigation, significant progress was made and a range of configurations were examined and compared with the experimental results presented in this thesis. Computations were performed under headwind and crosswind conditions and the vortex strength and fan face distortion was compared with experiments. In general excellent agreement was found and a comparison between the experiments and computational results is presented in §8.3. With the results being validated against experimental data and showing good agreement, additional configurations were examined that could not be conducted in the experiments. As will be discussed in §8.3 full scale simulations were performed and highlighted that the distortion for the scaled model results was affected by an induced separation that was not present for the higher Reynolds number case.

[†] when viewed from above, facing downstream

2.5 Flow Control Methods

Attempted flow control methods at removing or reducing the ground vortex date back to when vortex formation was first identified as an operational hazard. The majority of mitigation devices to date recognize that a fundamental requirement for vortex formation is the existence of a ground stagnation point ahead of the highlight plane. This stagnation point acts as focal point for ambient vorticity upstream to be concentrated, stretched and intensified, to form a ground vortex, as it is ingested into the intake. Klein[29] recognized this requirement and proposed a device which directs a jet of air directly onto the ground plane formation region to disturb the stagnation point (Fig. 2.20). This contraption, known as the 'blow-away' jet, was put into commercial service on the DC-8 aircraft in the late 1950's early 1960's[25]. However after review of unscheduled engine removals due to FOD the blow-away jet appeared to cause just as many problems as the vortex itself[25].

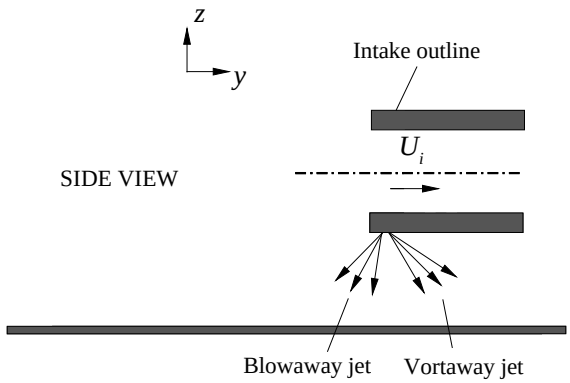

Figure 2.20: Schematic of two different concepts that have been invented for ground vortex prevention

Despite this unsuccessful attempt a number of vortex prevention systems have subsequently been proposed[62,14,51,54] all of which implement a similar technique in slightly contrasting forms. Vanfleet[62], identifies the reverse flow behind and underneath the intake between the ground plane as being the key ingredient to the formation of a stagnation point. A jet of air is directed aft underneath the intake, introducing an effective headwind, to counteract this reverse flow (Fig. 2.20). Johns notes that this 'vortaway' jet has had no commercial interest[25]. More recently related works by Smith and Dorris[54] and Funk et al[14] highlights the difficulties in implementing such counter measures in practice as being the major reason behind the aforementioned failures. Instead of a constant stream of air, a pulsed, nacelle integrated, blowing system is proposed which demands less mass flow for operation. This study uses two dimensional Particle Image Velocimetry (PIV) technique to demonstrate the effectiveness of different blowing

configurations[‡]. The PIV results revealed a highly unsteady vortex, under crosswind conditions, and blowing was found to be effective at disturbing the formation of the vortex.

The latest attempts offered by Shmilovich, in which a series of related papers have been published[51,53,52], considers the vortex unsteadiness as being an additional cause for the lack of success in removing the ground vortex phenomenon. Again a similar concept is proposed which uses a jet of air to remove the stagnation point, however this so-called 'sprinkler-system' implements a swivelling nozzle concept directed ahead of the highlight plane onto the ground to disrupt the vortex at any location that it may form. CFD analysis was used to characterize its effectiveness for both an isolated intake and full aircraft configuration. Simulations were primarily focused on vortex formation under tailwind conditions, due to its reputation for initiating engine surge as well as the increased likelihood of vortex formation under such conditions.

It should be noted that all of the above methods are motivated to circumvent the inherent ability of the ground vortex to ingest foreign objects. All inventions and the success thereof have been based on this specific consequence. As far as the author is aware no research has been conducted to evaluate the effectiveness of such concepts in reducing fan face distortion for example. Brix et al[6] explored a number of ground vortex counter measures, including vortex generators inside the intake. Extensive tests were conducted using fins of differing geometry, size and quantities with all being unsuccessful. The only device reported to prevent vortex formation was to place a barrier between the lower inlet lip and the ground plane, which splits the approaching flow and the flow underneath the inlet travelling toward the highlight plane. This device guarantees that the stagnation point does not form, however, as noted by the author, the practicality of such an instrument is very limited.

2.6 Summary

The relevant literature relating to the formation of ground vortices within intakes close to the ground has been reviewed. The main findings within previous research are stated below which is then followed by a summary of the deficiencies and gaps within current understanding and areas requiring further work.

2.6.1 Current Knowledge

1. Two fundamental requirements have been established for the formation of ground vortices; a ground plane stagnation point ahead of the intake and a source of vorticity.

[‡]As far as the author is aware this was the first known PIV study of ground vortex ingestion. However the results were severely compromised by poor seeding and no significant quantitative data was presented

2. Current knowledge highlights the dependency of the non-dimensional height and velocity ratio on the formation of ground vortices.

3. Two vortex formation mechanisms have been established; the headwind and crosswind mechanisms.

4. The headwind formation mechanism relates the stretching and intensification of the dominant source of ambient vorticity within the sucked streamtube upstream of the intake. The relative orientation and direction determines the number of vortices observed and the respective rotations.

5. Under crosswind conditions the vortex system comprises of a strong ground vortex and a trailing vortex off the leeward edge of the intake. The dominant vorticity source for the vortex system is associated with the flow over the outer intake surface rather than the ground plane.

6. Vortex formation can also occur under quiescent conditions producing two contra-vortices which rotate in the opposite sense to the headwind mode.

7. All prevention systems to date have been aimed at removing the stagnation point on the ground plane which has been identified by many researchers as a fundamental requirement.

2.6.2 Deficiencies in Current Understanding

1. The majority of work is based on flow visualization studies.

2. Two dimensional Particle Image Velocimetry has been implemented on two different occasions and both report difficulties with seeding the flowfield.

3. No three component PIV measurements have been taken of the ground vortex flowfield.

4. There are some discrepancies in literature relating to the vortex formation boundary.

5. Although Brix[5] has provided significant quantitative measurements, the data was taken at a fixed height. Only Shin et al[50] has quantified the effect of ground clearance, however this was only under crosswind conditions.

6. The effect of the approaching boundary layer has not been experimentally investigated. This aspect is important since a full-scale intake in practice is immersed in an atmospheric boundary layer, which is likely to influence the flowfield features and characteristics. As a consequence it is of interest to understand the sensitivity of this parameter.

7. Vortex strength measurements have only been taken over a limited range of free-stream velocities. To establish the characteristics of the vortex during take-off, it is important to understand the behaviour of the vortex to its blow-away condition.

8. In addition to this, no research has been conducted using a rolling ground plane. Implementing such a technique will provide a significant insight into the ground vortex formation characteristics for a moving aircraft.

9. There is no quantitative data of the ground vortex available under quiescent conditions.

10. There is very little measurements of the total pressure distortion induced by ground vortex formation. There are no distortion measurements available under both headwind and crosswind conditions over a wide range of configurations. This is surprising since this parameter is important to the stability of the engine.

11. Finally, to date there has been no extensive parametric study of ground vortex formation examining the effect of non-dimensional height, boundary layer thickness, intake Mach number, velocity ratio and intake yaw angle using both velocity and total pressure measurements.

CHAPTER 3

Experiment Approach and Methodology

In this chapter the methods used to quantitatively measure the formation of ground vortices between the ground and a model intake are discussed. First the non-dimensional groups that are expected to be of primary importance to the vortex strength and fan face distortion are introduced. Attention is then given to the design of the model rig, the wind tunnel and the experimental techniques used to investigate the flowfield. The methods used to post-process the results are outlined and finally an uncertainty analysis of the results is presented.

3.1 Experiment Variables

This section derives the relevant non-dimensional groups for that are important with regards to the vortex strength (Γ). This parameter is the primary descriptor used to characterize the vortex and to establish the sensitivity of the non-dimensional groups discussed below. This is then followed by a discussion of the variables and the techniques applied to control them are discussed.

3.1.1 Dimensional Analysis

Dimensional analysis shows that the vortex strength is primarily a function of the Reynolds number, Re_{D_l}, the non-dimensional height of the intake, h/D_l, the operating velocity ratio, U_i/U_∞, the angle of the intake centreline relative to the flow direction, ψ, the intake Mach number, M_i, based on the intake velocity, U_i and the approaching boundary layer thickness, δ^*/D_l (Eq. 3.1.1). The variables are discussed in the following sections.

$$\frac{\Gamma}{D_l U_i} = f\left\{Re_{D_l}, \frac{h}{D_l}, \frac{U_i}{U_\infty}, \psi, \frac{\omega D_l}{U_i}, M_i, \frac{\delta^*}{D_l}\right\} \tag{3.1.1}$$

3.1.2 Non-dimensional Vortex Strength

In this study the total average vortex strength, $\bar{\Gamma}$, is non-dimensionalized by the intake velocity, U_i and the intake highlight diameter, D_l. Throughout this thesis the total non-dimensional vortex strength of the vortex system is denoted by Γ^* (Eq. 3.1.2).

$$\Gamma^* = \frac{\bar{\Gamma}}{D_l U_i} \tag{3.1.2}$$

It is expected that by non-dimensionalizing the circulation in this form, Γ^* will remain constant if the intake velocity, U_i, or the intake diameter, D_l, is altered. The dependency of U_i on the vortex characteristics will be investigated throughout this study under various operating conditions (i.e. under quiescent, headwind and crosswind conditions).

3.1.3 Reynolds Number

The intake Reynolds number is defined using the conditions inside the intake duct. The definition uses the intake velocity and inner intake diameter (Eq. 3.1.3). The variation in intake Reynolds has not been investigated by varying the intake diameter. However a discussion of this parameter is given in §8.3.

$$Re_{D_i} = \frac{\rho_i U_i D_i}{\mu_i} \tag{3.1.3}$$

3.1.4 Ground Clearance

In this thesis the ground clearance is defined as being the vertical distance from the lowest point of the highlight plane to the ground, h, normalized by the intake highlight diameter, D_l (Fig. 3.5a). This definition has been used because it is commonly implemented in industry. Typically within the literature an alternative definition is used which is based on the centre-line height of the intake, H, divided by the inner intake diameter, D_i. Both definitions are related via Eq. 3.1.4.

$$\frac{H}{D_i} = \left(\frac{D_l}{D_i}\right)\left(\frac{h}{D_l}\right) + \frac{D_l}{2D_i} \tag{3.1.4}$$

This parameter is of key importance to this project. As explained in the introduction, due to current design trends of high-by-pass ratio turbofans the non-dimensional height of the intake is reducing. One of the major consequences is an increased probability of ground vortex formation over a broader range of operating conditions. As will be discussed in the following chapter, the effect of reducing the ground clearance has received very little attention in the past. Hence one of the primary objectives within

this project is to understand the effect of varying the ground clearance on the vortex characteristics.

3.1.5 Velocity Ratio

The velocity ratio, U_i/U_∞, is derived from conservation of mass and is defined below (for the definition of the symbols see §2.1):

$$\frac{U_i}{U_\infty} = \frac{\rho_\infty}{\rho_i}\frac{A_\infty}{A_i} \tag{3.1.5}$$

This parameter, sometimes referred to as the streamtube contraction ratio, is equally as important as the non-dimensional height of the intake. The higher the contraction ratio, for a given h/D_l, the larger the sucked streamtube will be and the more likely it will interact with the ground, thereby promoting vortex formation. In this thesis the velocity ratio will be reduced primarily by increasing the free-stream speed, U_∞, until the vortex disappears or until the tunnel speed, U_∞, cannot be increased any further.

3.1.6 Yaw Angle

The literature review has shown that the yaw angle of the intake centreline relative to the flow direction, ψ, is a key parameter to the characteristics of vortex formation. This parameter determines the primary vorticity source for the vortex, which in turn determines the vortex strength and rotational sense within the intake duct. Due to the set-up of the experimental rig, data can only be taken at yaw angles between 0 and 90°. These two extremities will be the primary focus in this thesis. The former is important from the point of view of an aircraft take-off, whereas the latter is important because this is known to produce the strongest vortex and it also represents the design limit of current intakes.

3.1.7 Intake Mach Number

The majority of experiments performed were conducted at a representative intake Mach number to that of full scale engines. This is at an M_i of 0.58. Due to the different ducting set-up within the tunnel working section between the headwind and crosswind configurations the intake Mach number varied between 0.55 (for crosswind) and 0.58 (for headwind). To establish the sensitivity of this parameter limited measurements were taken at a lower intake Mach number of 0.43. Under quiescent conditions data was also taken at an $M_i = 0.14$.

3.1.8 Approaching Boundary Layer Thickness

The full scale in-service intake is immersed in an atmospheric boundary layer that is an order of magnitude larger than the intake dimension. An atmospheric boundary layer is not simulated in this thesis, however to establish the sensitivity a number of approaching boundary layer thicknesses have been investigated. As noted in the literature survey no previous workers have quantified the sensitivity of this parameter experimentally. As discussed in §2, the primary influence will be to effect the average velocity within the sucked streamtube, thereby altering the streamtube size at far-field and therefore changing the velocity ratio at which the capture streamtube lifts of the surface. The thickness is characterized using the displacement thickness, δ^*, normalized by the intake highlight diameter, D_l.

3.2 Intake Model

A schematic of the model is given in Fig. 3.1a. The intake is axi-symmetric and cylindrical in shape of approximately $1/30^{th}$ scale. The model did not include a central hub or rotating fan. The lip geometry was modified relative to a large-scale intake and consisted of elliptical elements with an axis ratio of 2. The inner diameter, D_i, of the model was equal to 0.1 m with the ratio of outer to inner diameter (D/D_i) equal to 1.4 (Fig. 3.1a). The intake Reynolds number ranged from between 0.3 - 1.26×10^6 based on the inner diameter and average intake velocity. Due to the low Reynolds number transition strips were placed on both the inside and outside of the intake lip to promote transition and to avoid premature laminar separations (Fig. 3.1b).

The intake is equipped with a total of 12 total pressure rake ports equi-spaced around the circumference. With the pressure rakes installed, the front face of the pressure probes were at a distance of $0.7D_i$ from the intake highlight plane (Fig. 3.1a) which is at an equivalent location to the aerodynamic interface plane[68]. Installation of the total pressure rakes inside the intake is shown in Fig. 3.1b. In addition, 36 static pressure ports are located equi-spaced around the circumference, inside the intake duct. All ports are at a location of $0.65D_i$ from the intake highlight plane (Fig. 3.1a). These were used to determine the mass flow in the intake.

3.2.1 Intake Suction System

A full account of the intake suction system is given in Appendix B. A short description is given below. The intake mass-flow was provided by a large vacuum tank situated outside the tunnel which has a capacity of approximately 60 m^3. A network of large bore ducting, with a total length of approximately 40 m, connects the vacuum tank to a diffuser located immediately above the tunnel ceiling. The diffuser brought the duct diameter down to approximately that of the intake diameter. Flexible tubing connected the diffuser to either a sonic throat designed for an intake Mach number, M_i, of 0.43 or

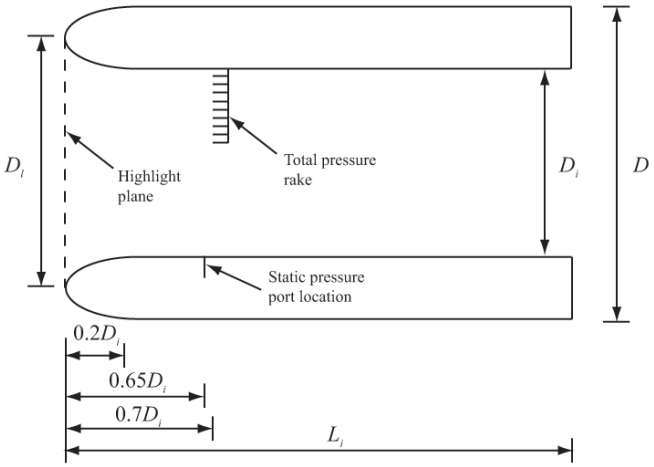

(a)

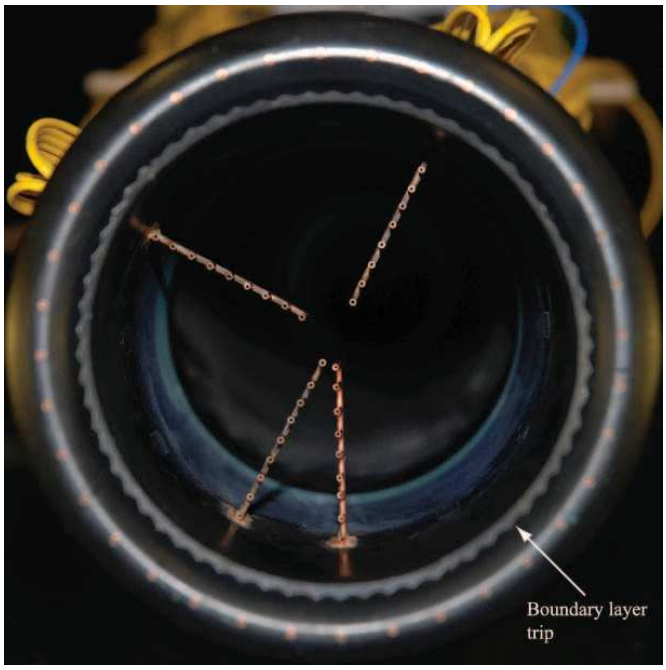

(b)

Figure 3.1: (a) Schematic of intake illustrating the model dimensions and (b) Front view picture of intake model, with the total pressure rakes installed

a straight through duct section that enabled the maximum mass flow of the suction system to be achieved ($M_i = 0.58$) (see Appendix B). The sonic throat or straight through duct itself was connected to a length of rigid ducting on which the intake model was attached. The flow was controlled using a quick release shutter valve installed near the suction tank that was pneumatically driven. When a voltage was supplied to the valve, from the tunnel control room, the shutter released within approximately 0.1 *s* and air

was sucked through the intake model into the 60 m^3 chamber. The required steady mass flow was achieved approximately one second after initiation. A run time of approximately 22 seconds was achieved at a constant maximum mass flow of approximately 1.49 kgs^{-1} ($M_i = 0.58$) until the tank was filled with air. The mass flow was monitored for the duration of the experiments using static pressure measurements in the intake and was found to be steady throughout. For the crosswind experiments, due to the slightly different ducting set-up within the tunnel working section (Fig. 3.2c), a maximum mass flow of 1.46 kgs^{-1} was achieved corresponding to an intake Mach number of 0.55.

3.3 The $8' \times 6'$ Wind Tunnel

The experiments were conducted in the Cranfield University low-speed wind tunnel which has a 2.4 $m \times 1.8$ m working section. The tunnel is of conventional closed circuit return type design. The speed in the working section can be varied between 10 and 50 ms^{-1}, however during some specific tests presented in this thesis the tunnel was limited to an operational speed of 40 ms^{-1}. Throughout the experiments the wind velocity was measured using a pitot-static tube in the working section. Details of the pressure transducers used to measure the velocity is given in Appendix G.

The intake model was supported via two ring mounts connected to the rigid section of ducting which was attached to the intake model. The ring mounts themselves were connected to a variable height strut extension which enabled the ground clearance of the model to be varied. The variable height strut was connected to a primary strut that was attached to the tunnel mounting plate above the ceiling. The mounting plate could be rotated through 360° in steps of approximately 1°. For the headwind experiments the mounting plate was orientated in-line with the flow direction whereas under crosswind conditions the mounting plate was rotated through ninety degrees. As explained above, for the crosswind configuration an extra ninety degree bend was used in the ducting set-up to enable the intake to be orientated at 90° to the flow direction.

The size of the boundary layer upstream of the intake was controlled using suction slots (Fig. 3.2a) upstream of the intake. The primary boundary layer suction (BLS1) is located just upstream of the working section approximately $20D_i$ in distance from intake highlight plane position. The secondary suction (BLS2) consists of a perforated plate approximately 1.2 m in width and 0.2 m in length situated roughly $10D_i$ from the intake (Fig. 3.2a). Combining the different suction options led to three different boundary layer thickness configurations being investigated and are summarized in Table 3.1. The boundary layer profiles and characteristics for each tunnel speed is presented in Appendix C.1. Boundary layer measurements were also taken without the PIV seeding rake in place (see Fig. 3.2a) to quantify its influence and are also presented in Appendix C.1.

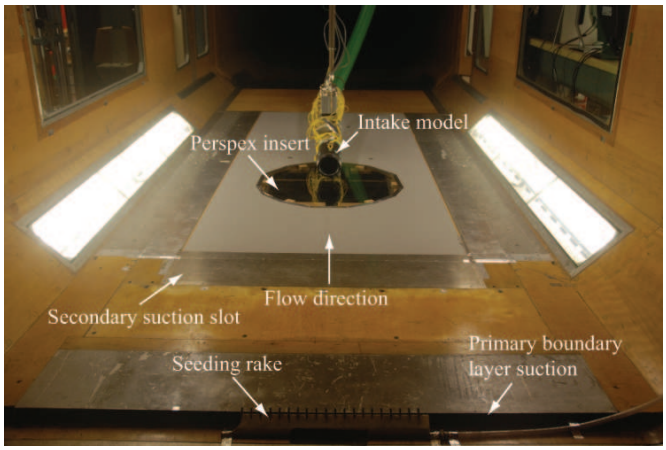

(a)

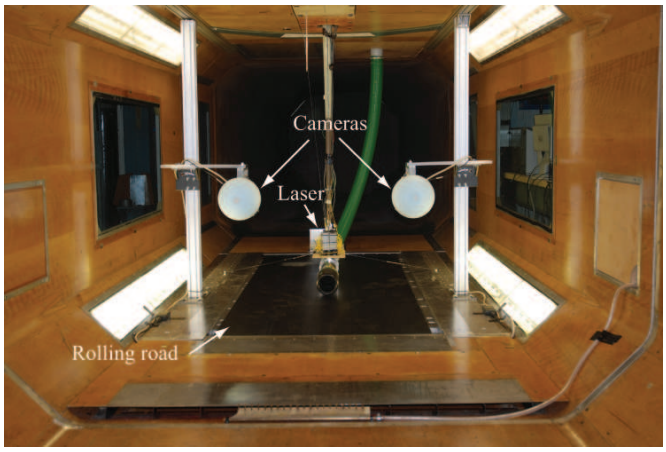

(b)

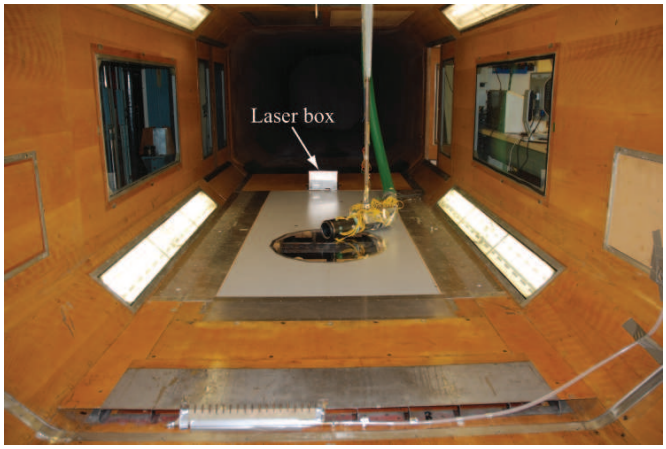

(c)

Figure 3.2: Tunnel configurations under (a) quiescent and headwind and (b) crosswind and (c) rolling ground experiments

Configuration				
BLS1	**BLS2**	δ/D_l	δ^*/D_1	$1/n_{bl}$
×	×	1.03	0.11	0.11
✓	×	0.45	0.07	0.14
✓	✓	0.12	0.03	0.15

Table 3.1: Approaching boundary layer configurations used in the experiments (values represent the average across all tunnel speeds)

3.3.1 Tunnel Configurations

The wind tunnel has the capability of changing its floor and a rolling ground plane can be installed. Measurements of the ground vortex were taken under both headwind (§5), crosswind (§7) configurations and also under headwind conditions with a rolling road in operation (§6). Hence there were three different tunnel configurations implemented and a picture of each set-up is given in Fig. 3.2. Measurements of the ground vortex under quiescent (no-wind) conditions were taken using the headwind tunnel configuration (Fig. 3.2a). As will be discussed below, for the headwind and crosswind experiments the cameras for the PIV system were located underneath the tunnel floor and were directed through a circular perspex insert. With the rolling road installed the cameras could not be positioned underneath the floor, and so were placed inside the tunnel working section (Fig. 3.2). A significant difficulty was to ensure that the cameras did not experience any vibrations from operating the rolling road and also the tunnel at high speeds. Therefore for this configuration the cameras were bolted to slotted pillars which were securely attached to the ground and the tunnel ceiling. This ensured that vibrations were kept to a minimum. During tests no significant problems were encountered with this set-up. In addition, given the range of streamtube contraction ratios tested with the tunnel in operation, the cameras and associated mounting system is expected to have had no notable difference on the ingested flow.

3.4 Measurement Techniques

This section describes the techniques used to acquire the quantitative experimental data of the ground vortex. Two measurement techniques are used; Stereoscopic Particle Image Velocimetry (SPIV) and total pressure measurements. The following two sections describe the techniques and the particular configurations used in the experiments.

3.4.1 Stereoscopic Particle Image Velocimetry

Stereoscopic Particle Image Velocimetry (SPIV) is a non-intrusive, global flowfield, optical, quantitative flow visualization technique, which provides three components of velocity (u,v,w) in a plane of interest. The technique is widely implemented within fluid dynamics research and there is plenty of documentation which gives a detailed description of the method (see Raffel et al[41] or Tropea et al[60] for example). A brief outline of the technique is given which applies to two component PIV. Then the more advanced method of SPIV is discussed.

Seeding is introduced into the flowfield, usually in the form of oil particles. The particles must have good light scattering qualities and must be small enough to faithfully follow the flow. A high powered, double pulsed, laser is used with a set of optics, typically in the form of a cylindrical lens, to diverge the laser beam in one direction. This creates a thin sheet of light which is directed in a region of interest to illuminate the particles. A camera is positioned at ninety degrees to the light sheet and is focused on the illuminated seeding particles. When triggered the camera will take pictures of the particles. To acquire one vector snapshot of the flowfield, the light sheet is pulsed twice with the time between pulses, Δt, defined by the user. The camera is synchronized with the laser and takes a picture of the illuminated particles at each pulse. The movement of the flowfield is given by the difference between the two particle pictures.

To determine the velocity field across the whole image, both frames are sub-divided into small areas called interrogation regions or spots. The particle pattern in the same region of both frames is compared to determine the instantaneous velocity within that sub-region. This is performed using correlation techniques in which the spot from the first frame is placed over the top of the equivalent spot in the second frame. The region from the first image is then shifted in all possible positions and the intensities of the overlapping pixels are compared. The shift that gives the best comparison is assumed to be the average displacement of the particles within that region. With the time between the acquired frames being known the local instantaneous velocity can be determined. This technique is performed for all interrogation regions to give a complete velocity vector map of the flowfield.

The above method gives the in-plane velocities of the particles. However, if there is strong out-of-plane motion in the region of the interest and the particles are not located directly on the camera axis, large errors can be experienced due to perspective error[39]. This is because the 2D method is only capable of recording the projection of the velocity vector onto the plane of the light sheet. Therefore the out-of-plane velocity is lost and the in-plane velocities are also affected by this error[41]. Stereoscopic Particle Image Velocimetry (SPIV) circumvents this problem by using an additional camera and is the main advantage over the 2D method. Both cameras are used to measure a common region of interest and the velocities from each camera can be reconstructed to determine the out-of-plane velocity component. For this more advanced PIV technique, commonly the cameras are placed at angles to the light sheet for practical purposes and also to enable a larger common area of interest as well to minimize lens aberra-

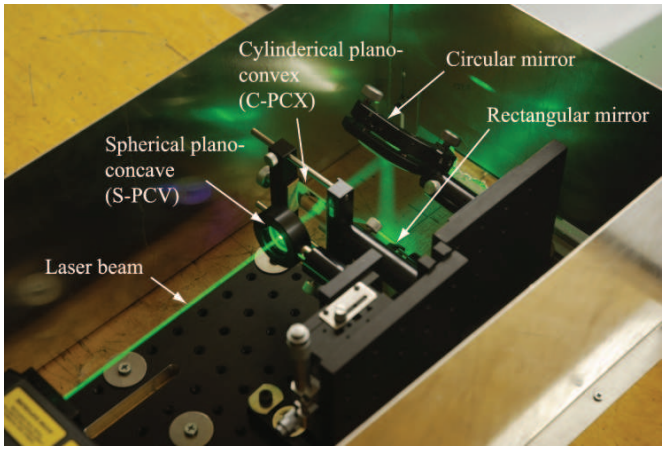

(a)

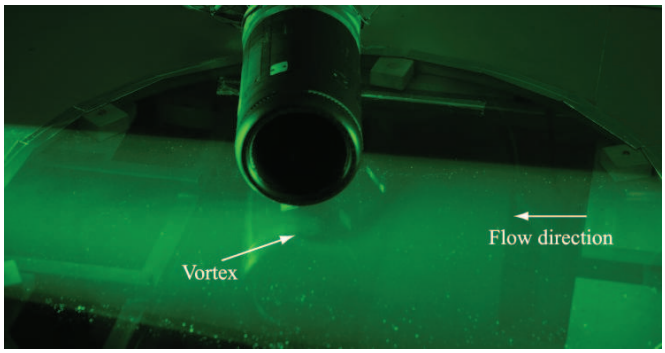

(b)

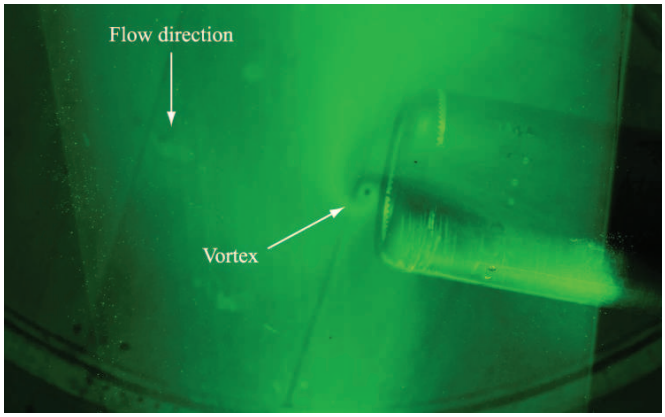

(c)

Figure 3.3: Example application of SPIV to the ground vortex flowfield

tions. This adds an additional problem because the magnification factor is no longer constant across the measurement area, hence rendering the need for a means of calibration. With low f-numbers having to be implemented to image small particles with a finite laser power, the depth of field is also too small to achieve good focus across the whole image width. The back plane of the camera must therefore be tilted according to the Scheimpflug condition to achieve focus across the whole image plane. This is where the image, lens and the measurement plane all intersect in a common line[66].

With regards to measuring the ground vortex flowfield SPIV is advantageous for three reasons. Firstly the measurement technique is non-intrusive which is vital for measuring a very sensitive flow. Secondly the flowfield is observed to be highly unsteady hence with the ability of SPIV to take measurements within a finite area simultaneously, enables the vortex movement to be captured without compromising the results. Finally, significant out-of-plane velocities will be experienced, which therefore will cause significant errors using the two component technique.

3.4.1.1 The SPIV System and Data Acquisition

For the experiments conducted in this thesis, a TSI stereoscopic PIV system was used to acquire the three-components of velocity on a plane. The PIV system consists of two four-mega pixel, 12-bit cameras used primarily with 60 *mm* focal length Nikor lens*. The Scheimpflug condition was satisfied using specially made camera mounts which allow the camera back plane to be rotated in two axes (see Fig. B.5 for picture). For the tests presented in §4-5 & 7 the cameras were positioned underneath the wind tunnel floor and were orientated at ± 45° to the measurement plane with both operating in partial scatter with respect to the laser. A New Wave Solo 120XT Nd:Yag laser with a wave length of 532 *nm* and pulse energy of 120 *mJ* was used. A 1.5 *mm* thick light sheet was generated using a combination of a spherical plano-concave and a cylindrical plano-convex lenses (Fig. 3.3a). For all tests the light sheet was orientated in a plane parallel to the ground (*x-y* plane)(Fig. 3.3b-c). The light sheet height from the ground, h_L, was fixed at 10 *mm* or $0.083 h_L/D_l$ as shown in Figs. 3.4 and 3.5.

A TSI hyperstreaming system was used to acquire the images. This system enables the flow-field snapshots to be captured at the full frame rate of the cameras with a known uniform time separation between each frame. The maximum frame rate of the cameras is 15 *Hz*. A single flowfield snapshot comprises of two images from each camera, hence the resulting flowfield realizations were acquired at a rate of 7.5 *Hz*.

The flowfield was seeded using a Laskin-type seeder using Di-2-Ethylhexyl-Sebacat (DEHS) oil which delivered a mean particle diameter of 1 μm. The seeding rake was placed upstream of the working section ahead of the wind tunnel boundary layer suction slots (Fig. 3.2). The effect of the seeding rake position on the boundary layer thickness and profile is quantified in Appendix C.1.

*105 *mm* focal length lens were used for the rolling ground plane experiments presented in §6

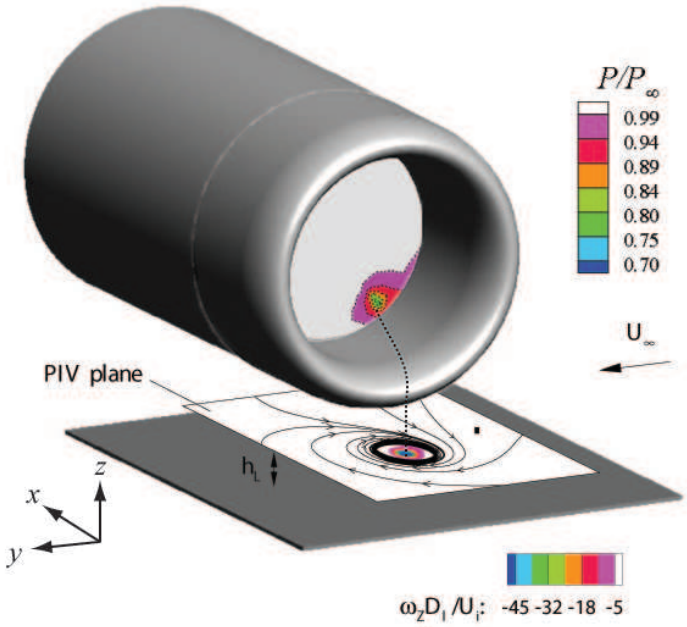

Figure 3.4: Measurement planes used in the experiments

3.4.1.2 PIV Post-Processing

The PIV images were post-processed using TSI Insight3G software version 8.0.5. It was found that the deformation grid, along with the FFT algorithm, was the best method to use for this flow-field. This processing technique was chosen after a number of trails in which different processing permutations were tested for a range of configurations. The best method was identified by inspecting a line plot of the vorticity distribution through the centre of the vortex. The method with the least noise in the signature (i.e. the smoothest distribution) was deemed most appropriate. The general procedure for the deformation grid algorithm is as follows[21]; on the first pass, an estimate of the displacement field is computed using standard correlation with no window offsets. On the second pass, the displacement field is used to offset the windows to improve the correlation peak and hence the signal to noise ratio. The third pass uses the four neighbouring vectors to deform the grid in order to improve the number of image pairs in regions of high velocity gradient. This will again improve the signal to noise ratio. This interrogation algorithm is a widely favoured method for vortical flows[44]. The method allows the procedure to be recursively implemented so that a multi-grid approach can be used to further increase the signal-to-noise ratio[45]. A 64×64 interrogation spot was used initially with 50% overlap to maximise the correlation peak and ensure good sub-pixel accuracy in the displacement estimate for the windows off-sets. A pass validation was also implemented which included a range and median filter to remove spurious vectors and 3×3 smoothing to remove any small scale noise present. The final iteration used a 32×32 (with 50% overlap) spot area to improve the

resolution. This resulted in a measurement resolution of typically between 0.8-0.9 *mm* across all configurations.

3.4.2 Total Pressure Measurement System

The intake was fitted with four total pressure rakes, each comprising nine total pressure probes with a head diameter of 1.5 *mm* (Fig. 3.1b). Total pressure measurements were taken at a location equivalent to a nominal aerodynamic interface plane $0.7D_i$ from the highlight plane. A set of 36 equi-spaced static pressure ports are also positioned around the inner circumference at an axial location in-line with the total pressure measurement plane.

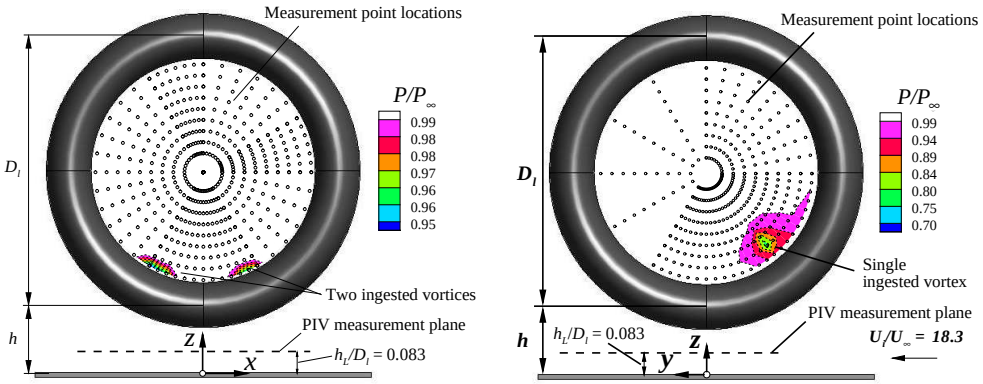

(a) (b)

Figure 3.5: Measurement point coverage within the intake duct for (a) Headwind and quiescent conditions and (b) crosswind conditions

The intake static and total pressure measurements were taken using a set of 40 PX139-005D4V differential pressure transducers. Each pressure transducer has a range of $+/-$ 5 *psi* with typical repeatability of 0.1% full-scale. The measurements were acquired using Labview version 8.5. The analogue signal was converted to digital using a National Instruments PCI-6255 16-bit DAQ card. For each configuration, an acquisition time of 5 seconds was used with a sampling frequency of $600Hz$. A total of 432 measurement points were obtained for each headwind configuration by rotating the model around its axis (Fig. 3.5a). For the crosswind experiments 342 measurement points were taken inside the intake duct (Fig. 3.5b).

For the PX139-005D4V transducers measurements were referenced against the average static pressure in the tunnel contraction, p_{str}. A Furness FC-044 pressure transducer, which had a range of 100 mmH_20, was also used to measure the reference pressure against ambient conditions, P_{amb}. The ambient pressure was recorded for each run to determine the absolute pressure from each pressure transducer. The calibrations and additional details of the pressure system is given within Appendix G.

3.5 Test Matrix

The full test matrix for headwind, crosswind and rolling road experiments is given in tabular format in Appendix D. A summary of the configurations investigated is provided below and the primary data points for the headwind and crosswind configurations are also shown graphically in the vortex formation map in Fig. 3.6. Both formation mechanisms were investigated by varying the velocity ratio, U^*, the non-dimensional height, h/D_l, the approaching boundary layer thickness, δ^*/D_l and the intake Mach number, M_i.

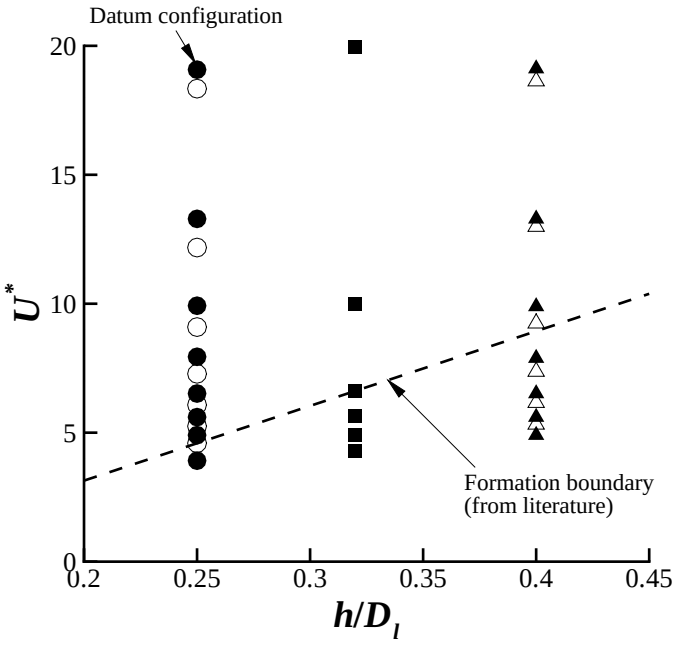

Figure 3.6: Primary data points investigated for both headwind (filled symbols) and crosswind (unfilled symbols) configurations

Under headwind conditions measurements were taken at three height-to-diameter ratios (h/D_l) of 0.40, 0.32 and 0.25 which are typical of possible high bypass ratio engine installations. The approaching wind speed ranged from 10 ms^{-1} up to 50 ms^{-1} typically in steps of 5 ms^{-1} (Fig. 3.6) or until the vortex disappeared. The impact of the approaching ground boundary layer thicknesses, as described above, was examined by controlling the boundary layer using suction slots upstream of the wind tunnel working section. This resulted in three different boundary layer configurations of δ^*/D_l = 0.03, 0.07 and 0.11 which were examined at the two extreme non-dimensional heights of 0.25 and 0.4 (h/D_l). All measurements were primarily taken at an intake Mach number of 0.58, but limited measurements were also taken at a lower M_i of 0.43.

Under crosswind conditions two height-to-diameter ratios were examined equal to 0.25 and 0.4 (h/D_l). For this mechanism, the tunnel speeds investigated ranged from 10 to 40 ms^{-1}. Higher speeds could not be examined due to tunnel limitations. The two

extreme approaching boundary layer thicknesses of $\delta^*/D_l = 0.03$ and 0.11 were investigated under crosswind conditions. As for the headwind configuration measurements were primarily taken at the intake Mach number of 0.55[†], however additional data was also taken at an $M_i = 0.43$.

Rolling ground plane experiments were performed primarily at the datum height configuration ($h/D_l = 0.25$), however a limited set of measurements was taken at the higher ground clearance of 0.4. All measurements were taken at an $M_i = 0.58$. Full details of the configurations tested using the rolling ground plane is given in §6.

3.6 Vortex Characteristics Determination

This section describes the primary descriptors used to characterize the flowfield for both the PIV velocity field measurements and the in-duct total pressure measurements.

3.6.1 Velocity Measurements

A full description of the methods used, with examples, is given in Appendix E, a summary of which is provided below. Following the initial processing of the raw PIV data to determine the three components of velocity, as described above, each flowfield snapshot was loaded into Tecplot 360 for further analysis.

The vortex core size, r_c, and Vatistas shape factor, n, were identified using the vorticity disk method[7], where n effectively represents the potential flowfield decay factor of the vortex. The output of this method is a circumferentially averaged swirl velocity distribution as a function of radial distance, r, from the centre of the vortex. The method is applied by first identifying the vortex centre location within Tecplot 360 using a macro function. This was successfully achieved by locating the maximum out-of-plane vorticity, ω_z. Although there are caveats with using vorticity for this purpose, due to its low signal-to-noise ratio, ω_z was preferred because it can discriminate between positive (anti-clockwise) and negative (clockwise) rotating vortices. Other more advanced vortex identification parameters such as the swirling strength, Q, and the eigenvalues of the velocity gradient tensor, λ_2 [23], are less affected by noise, but cannot distinguish between vortices of differing rotational sense. Nonetheless, ω_z, worked very well for this purpose. Using the vorticity therefore enables both positive and negative vortices to be identified and for their respective characteristics (such as circulation, Γ and core size, r_c) to be determined individually.

With the vortex centre identified, the data was linearly interpolated onto a circular grid with its centre positioned on the vorticity peak. The interpolation process was also performed in Tecplot 360 and the domain size was fixed for all configurations with its radius, r_{max}, equal to 0.5 r_{max}/r_i. The resolution of the circular zone was also constant

[†]The Mach number is slightly lower under crosswind conditions due to the different ducting set-up within the tunnel working section. See §B for further details.

for all configurations with each domain having 150 radial and 261 circumferential grid points. The effect of the domain size and resolution is discussed in Appendix E. After the interpolation process, each circular zone for every vortex snapshot, is then exported from Tecplot 360 in ASCII file format and is loaded into Matlab 2007a to determine the vortex characteristics.

$$\Gamma = \int \omega_z dA \tag{3.6.1}$$

Following the method of Burley et al[7], the vorticity was integrated over circular areas with increasing radial distance, r, from the centre of the vortex. However, because of the complication of an additional vortex being present in the integration area for some configurations, only vorticity of the same sign as that of the vortex of interest was integrated for all configurations (see Appendix E for further details). The total individual vortex strength is obtained by integrating vorticity over the whole circular domain (Eq. 3.6.1). The swirl velocity distribution is then obtained by dividing the local circulation, Γ_i at each radial position by $2\pi r$ (Eq. 3.6.2).

$$V_\theta = \frac{\Gamma_i}{2\pi r_i} \tag{3.6.2}$$

The radial position of peak swirl velocity, $V_{\theta,max}$, gives the vortex core size, r_c. Non-dimensionalizing the swirl velocity distribution by the peak value, and the radial distance by the vortex core size enables the Vatistas shape factor, n, to be calculated using a least squares fit of the velocity distribution (Eq. 3.6.3)[63].

$$\frac{V_\theta}{V_{\theta,max}} = 2^{1/n}\left[\frac{r^*}{(1+r^{*2n})^{1/n}}\right] \tag{3.6.3}$$

The vortex strength, Γ, core size, r_c and Vatistas shape factor, n, was determined for both positive and negative vortices (if both are present) for all flowfield snapshots (i.e. 300). The total average strength of the vortex system, $\bar{\Gamma}$, is determined by computing the average of all positive vortex strengths, $\bar{\Gamma}^+$, and all negative vortex strengths, $\bar{\Gamma}^-$, over all 300 vortex snapshots and summing the absolute magnitudes of both (Eq. 3.6.4).

$$\bar{\Gamma} = \left|\bar{\Gamma}^+\right| + \left|\bar{\Gamma}^-\right| \tag{3.6.4}$$

3.6.2 Total Pressure Measurements

The primary parameter used in conjunction with the total pressure measurements was the distortion coefficient, DC_{60}. This distortion descriptor is based on the difference between the area weighted average fan face pressure, $\bar{P}_f$ and the worst average 60° sector total pressure, $\bar{P}_{60}$, divided by the average dynamic head at the aerodynamic

interface plane, $\bar{q}_f$ (Eq. 3.6.5)[47] (sometimes referred to as the fan face in the text of this thesis).

$$DC_{60} = \frac{\bar{P}_f - \bar{P}_{60}}{\bar{q}_f} \tag{3.6.5}$$

A full description of this descriptor is given in Appendix F and as well as other parameters that were also examined but not presented in the main text.

3.7 Uncertainty Analysis

The uncertainties in the presented measurements comprise of a combination of sources such as those due the model location, transducers, random errors and the data acquisition system. Following the method of Taylor[57], these elements have been assessed to provide an estimate of the overall uncertainty for each measurement type. Full details of the uncertainty analysis in given Appendix G.

The non-dimensional height was set with an uncertainty of $h/D_l = 0.25 \pm 3.6\%$. The free-stream velocity ranged from 10 to 50 ms^{-1} with a typical overall uncertainty of ± 1.1%. The intake velocity was found to be reasonably constant throughout and was at an average value of 192 ms^{-1} ± 2.4%. The velocity ratio ranged from ∞ to 3.9 and for a typical median velocity ratio of 6.6 the uncertainty was ± 2.6%.

For the PIV velocity measurements an uncertainty band was estimated following the analysis presented by Raffel et al[41] based on synthetic images (see Appendix G.3). The analysis used an FFT correlation engine and a three point Gaussian peak fit algorithm which is relevant to this research. The correlation peak was estimated to be measured to within ± 0.06 pixels for each camera. Misalignment of the light sheet with the calibration plate is expected to be the largest source of error, with the centre of the light sheet being, at worst ± 0.25 *mm* off centre. Using error estimates from Petracci et al[38] this is expected to result in a maximum error of 0.13 pixels. The total error is expected to be no worse than ± 0.15 pixels. This equates to an in plane velocity error of 1.61 ms^{-1} or a typical error of ± 3.2%. Since the half-angle between the cameras was at 45°, the out of plane velocity error is equal to the in-plane error[39]. Based on a typical velocity uncertainty the vorticity uncertainty is estimated to be within ± 1875 s^{-1} which leads to an error in the circulation of approximately ± 0.3 $m^2 s^{-1}$.

3.8 Summary

In this chapter the experiment variables that are of primary importance to the vortex strength and fan face distortion have been identified and discussed. Subsequently the model used and the experimental measurement techniques that will be implemented to examine these parameters have been described.

CHAPTER 4

Quiescent Conditions

Vortex formation under quiescent (no-wind) conditions has only recently been reported[6] and there is little or no knowledge of its characteristics and behaviour within the public domain. As discussed in §2 the formation mechanism is largely the same as the headwind mechanism, however due to the different orientation of the dominant vorticity source the rotation of the vortices is opposite to that in headwind. Nevertheless, ground vortex formation under no-wind ($U^* = \infty$) conditions is regarded as being a flow mode of the headwind mechanism. In this chapter, for the first time, quantitative measurements of the no-wind ground vortex are presented. Stereoscopic Particle Image Velocimetry (SPIV) measurements of the flowfield, external to the intake and parallel to the ground are presented, along with in-duct total pressure measurements for supporting analysis.

At the beginning of this chapter the principle features of the flowfield are discussed under quiescent conditions. First the flowfield is compared with expectations and then new observations are presented and discussed. This section forms the main part of this chapter. Subsequently, the effect of ground clearance (h/D_l) and intake Mach number (M_i) are discussed with particular focus on the average vortex strength and in-duct distortion. The results from this chapter provide a reference for the data presented in the following chapter relating to the experiments performed under headwind conditions, which possesses the same formation mechanism.

4.1 Flow Topology

Under quiescent conditions ($U_i/U_\infty = \infty$) a pair of contra-rotating vortices form ahead of the intake highlight plane as illustrated in Fig. 4.1 which shows an example snapshot of the in-plane $u - v$ velocity vectors. This is in agreement with previous quantitative measurements for this type of configuration[6] and shows that the vortex topology is such that the right hand vortex has negative vorticity (-ve ω_Z). This is due to the flow being dominated by the vorticity bound in the flowfield induced by the suction between the intake and the ground (see Fig. 2.6). Fig. 4.1 shows that the vortices are not symmetric relative to the intake axis and is expected to be a result of small asymmetries present

in the intake flowfield.

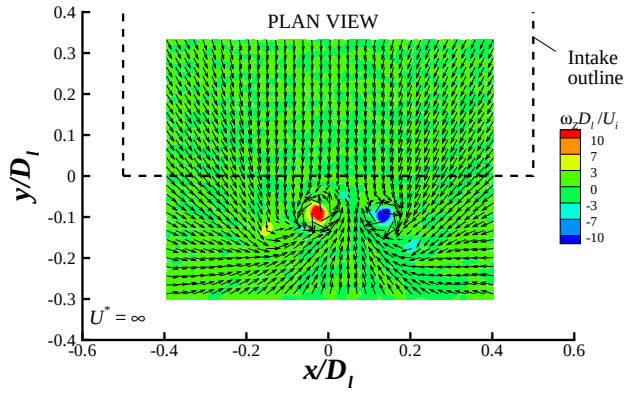

Figure 4.1: Example snap-shot of the in-plane $u - v$ velocity vectors (every 3^{rd} vector shown) and out-of-plane vorticity contours, ω_z, under quiescent conditions for an $h/D_l = 0.25$, $\delta^*/D_l = 0.00$, $U^* = \infty$ and $M_i = 0.58$

The corresponding in-duct total pressure measurements for a height-to-diameter ratio (h/D_l) of 0.25, under quiescent conditions, is shown Fig. 4.2. Two loss regions are clearly identified at the 155 and 205° positions (measured top dead centre clockwise) which indicates ingestion of two contra-rotating vortices. For this configuration the vortices are clearly ingested very close to the intake wall ($r_v/r_i = 0.94$), with the highest total pressure loss being measured at the closest point to the duct surface. As will be discussed later, this has additional consequences on the overall intake aerodynamics. What is interesting, in comparison to the PIV measurements, is that the vortices are now symmetrically placed relative to the intake centre line. This indicates that the vortex position relative to the intake axis has changed between the PIV plane and the fan face. For all three sets of experiments performed under nowind and headwind conditions the position of the vortices was asymmetric relative to the intake centre line.

4.1.1 Unsteady Behaviour

The PIV measurements under quiescent conditions reveal interesting flowfield features. As mentioned above (and in §2.2.1), the flowfield under quiescent conditions is dominated by vorticity bound in the flow travelling in the negative y-direction between the intake and ground plane (i.e. the gap flow). However, there is also a strong induced velocity field in the positive y direction, which is expected have a near equal, but weaker, source of opposite sign vorticity (Fig. 4.4). Since both flows are of near equal strength, travelling in opposition to each other, there is expected to be a strong interaction between the two vorticity sources. This results in a flowfield that is considerably unsteady in time as illustrated in Fig. 4.3 which shows example snapshots for the datum height configuration ($h/D_l = 0.25$) that have been consecutively taken, equi-spaced by $1/7.5$ seconds. During this particular sequence, the flowfield initially

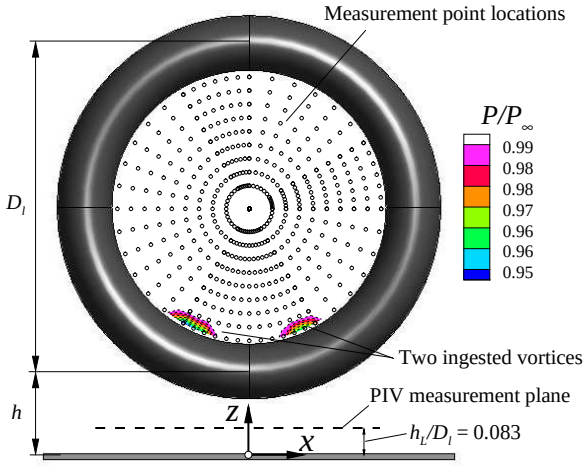

Figure 4.2: Fan face total pressure measurements for an $h/D_l = 0.25$ and $M_i = 0.58$. Also included in the figure are the measurement point locations, PIV measurement plane position relative to the intake and the height-to-diameter ratio definition

contains two contra-rotating vortices (Fig. 4.3a) as expected. However due to the strong interaction there are pockets of both positive and negative vorticity surrounding the two dominant vortices which can be seen in Fig. 4.3b. In the next snap-shot, 0.13*s* later, four vortices are observed in the PIV plane (Fig. 4.3c); two dominant vortices associated with the negative *y*-direction flow and two weaker vortices rotating in the opposite direction associated with the approaching flowfield (positive *y*-direction) (Fig. 4.4). In the following frame (Fig. 4.3d) the positive dominant vortex appears to have strengthened from inspection of the vorticity levels, whilst the dominant negative vortex has split into two smaller regions of high vorticity. Just 0.13 seconds later, the dominant positive vortex has completely broken down with its past existence being inferred from a long thin region of smeared out vorticity (Fig. 4.3e). Further advances in time see the anti-clockwise vortex reappearing, but weaker with now the negative vortex appearing stronger (Fig. 4.3f-g). Finally, in the last flowfield snap-shot, no clear vortex structure can be seen, however there are multiple regions of relatively weaker positive and negative vorticity present. The sequence of snapshots shown in Fig. 4.3 demonstrates the severe complexity of the flowfield.

The highly unsteady, time variant behaviour described above has not been observed to the same level under any other conditions (i.e. headwind and particularly crosswind conditions). As will be discussed in §5 the ground vortex under headwind conditions, which essentially possesses the same formation mechanism as under quiescent conditions, does contain similar unsteady features, however a clear vortex in general can always be detected within the measurement domain.

To quantify the spatial unsteadiness of the nowind ground vortex the time average flowfield is displayed for all three non dimensional heights (Fig. 4.5) along with the locus of both positive (i.e. +ve ω_z) and negative (i.e. -ve ω_z) vortex core locations over all

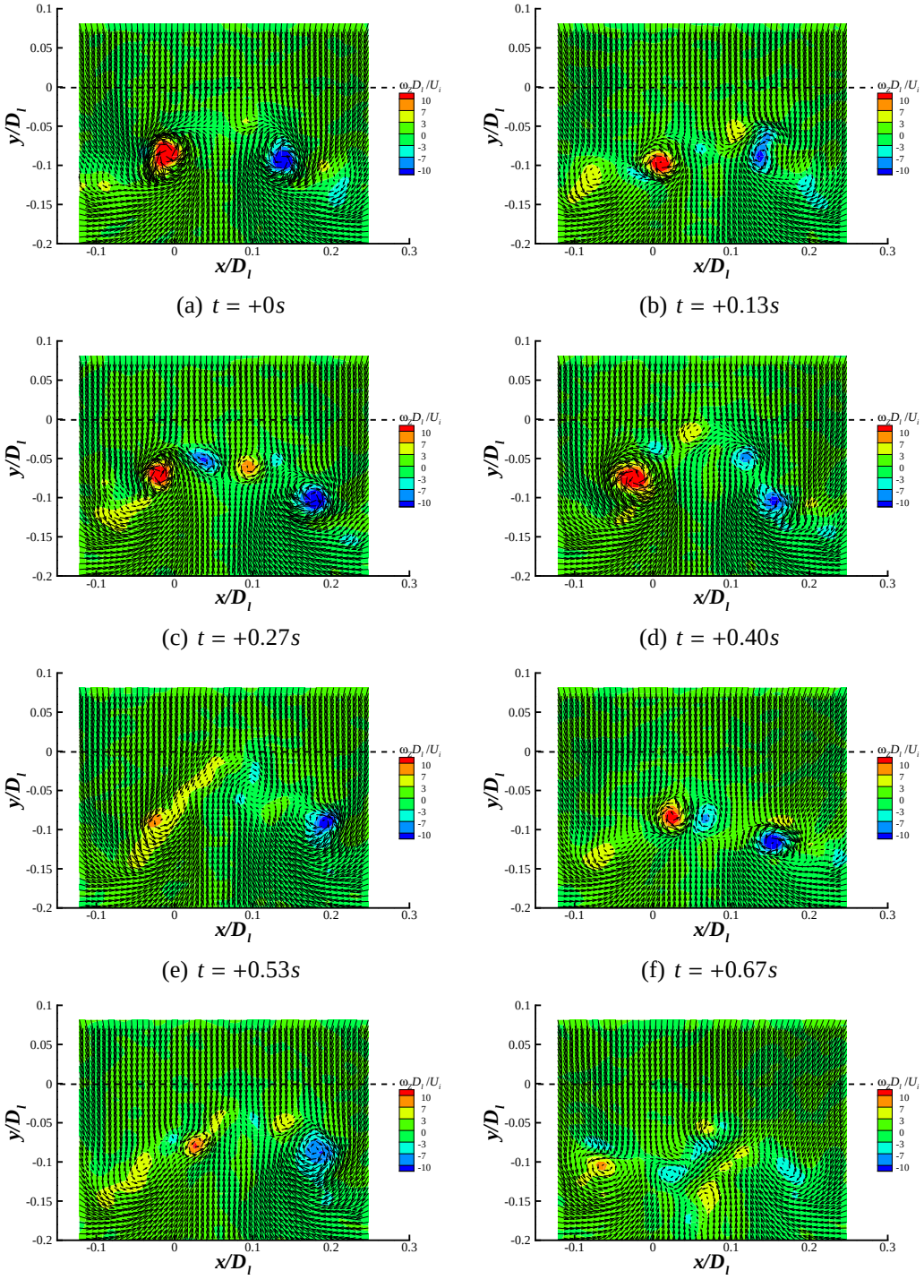

(a) $t = +0s$ (b) $t = +0.13s$

(c) $t = +0.27s$ (d) $t = +0.40s$

(e) $t = +0.53s$ (f) $t = +0.67s$

(g) $t = +0.80s$ (h) $t = +0.93s$

Figure 4.3: Example flowfield snapshots of the ground vortex under quiescent conditions taken consecutively at a $h/D_l = 0.25$, $\delta^*/D_l = 0$, $U^* = \infty$ and $M_i = 0.58$ illustrating the unsteady behaviour

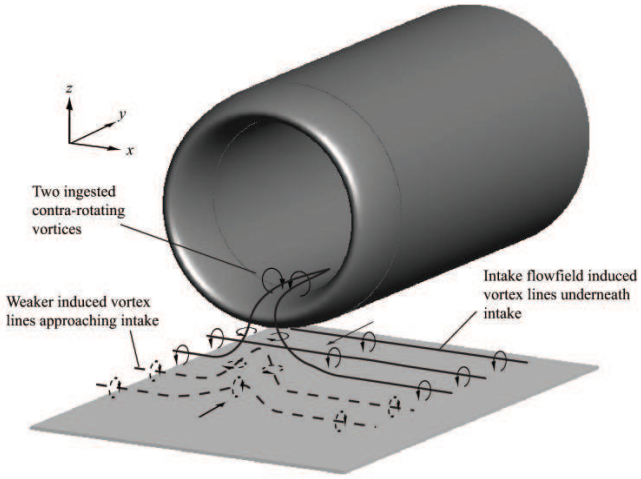

Figure 4.4: Vortex formation under quiescent conditions showing the induced vortex lines approaching the intake in both the positive and negative *y* directions

flowfield snapshots. At the lowest height-to-diameter ratio ($h/D_l = 0.25$) two regions of relatively high vorticity is seen (one positive and one negative) (Fig. 4.5a). Both regions are small with a radius of approximately $0.05D_l$. Inspection of the vortex core positions (Fig. 4.5b) show that the two regions of high vorticity encapsulate the movement of the vortex, as expected. An increase in the ground clearance to 0.32 (h/D_l) leads to an reduction in the peak vorticity levels (Fig. 4.5c). The core locations show that this reduction in partly due to a small increase in the spatial unsteadiness. However the unsteadiness is not notably different from the lower ground clearance configuration suggesting that the average vortex strength has also reduced. With a further increase to 0.4 (h/D_l) similar observations are seen, however the negative region of vorticity is now significantly smaller. The vortex centre locations for this configuration show that this is due to an increase in the unsteadiness of the clockwise rotating vortex as well as an expected reduction in the strength.

4.1.2 Flow Modes

Perhaps the most interesting observation from the experiments under quiescent conditions is the various flow modes that have been captured at the PIV plane. As illustrated in Fig. 4.1 two contra-rotating vortices form at the PIV measurement plane, which agrees with previous qualitative observations (Fig. 4.6a). As mentioned above, the vortices that form are highly unsteady which is expected to be a result of a strong interaction between the gap and the approaching flowfields. However, two vortices are not always observed at the PIV plane. In this case the flowfield modulates with a single dominant vortex being observed which is found to switch from port (Fig. 4.6b) to starboard (Fig. 4.6c) sides. As the vortex switches from side to side the sense of rotation of the dominant vortex changes with a contra-rotating vortex pair generally always ex-

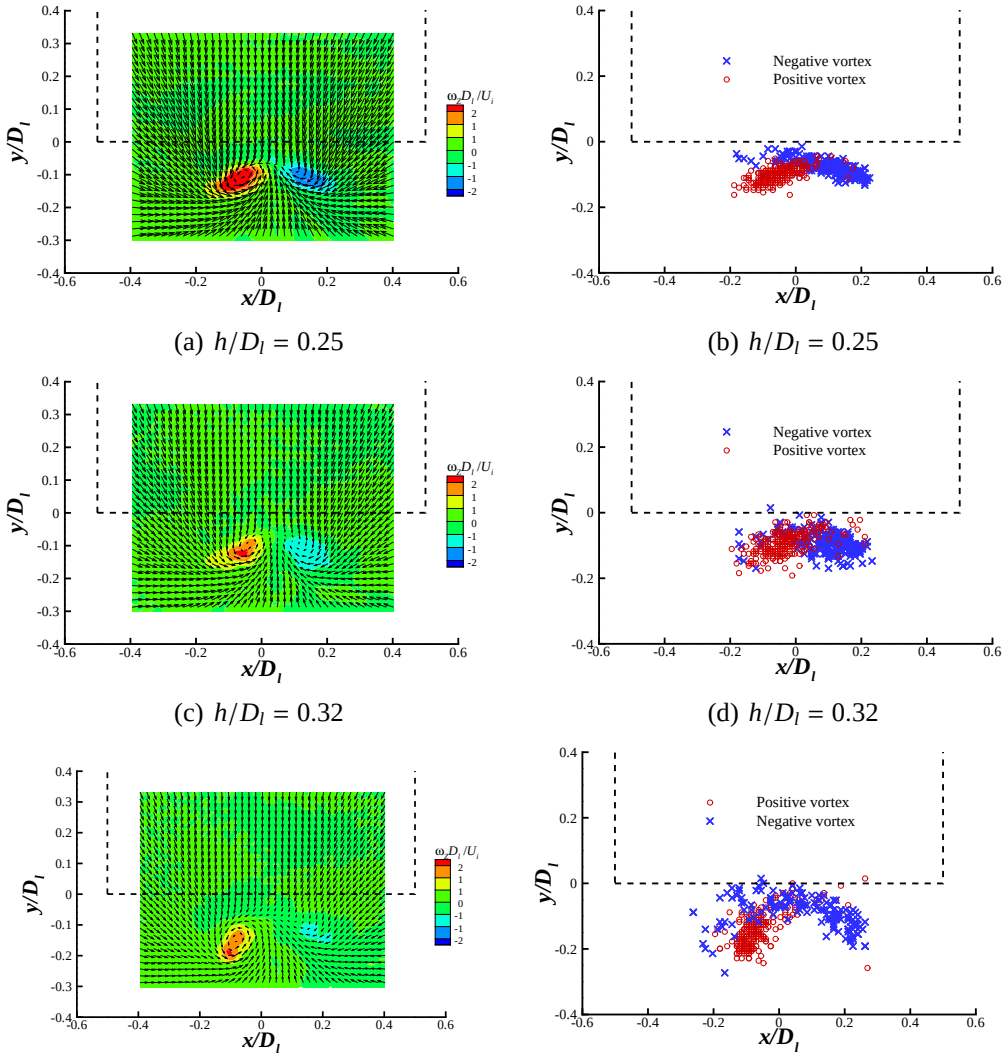

(a) $h/D_l = 0.25$ (b) $h/D_l = 0.25$

(c) $h/D_l = 0.32$ (d) $h/D_l = 0.32$

(e) $h/D_l = 0.40$ (f) $h/D_l = 0.40$

Figure 4.5: Time average flow-field for increasing ground clearance under quiescent conditions with corresponding locus of vortex core positions ($U^* = \infty$, $\delta^*/D_l = 0$ and $M_i = 0.58$)

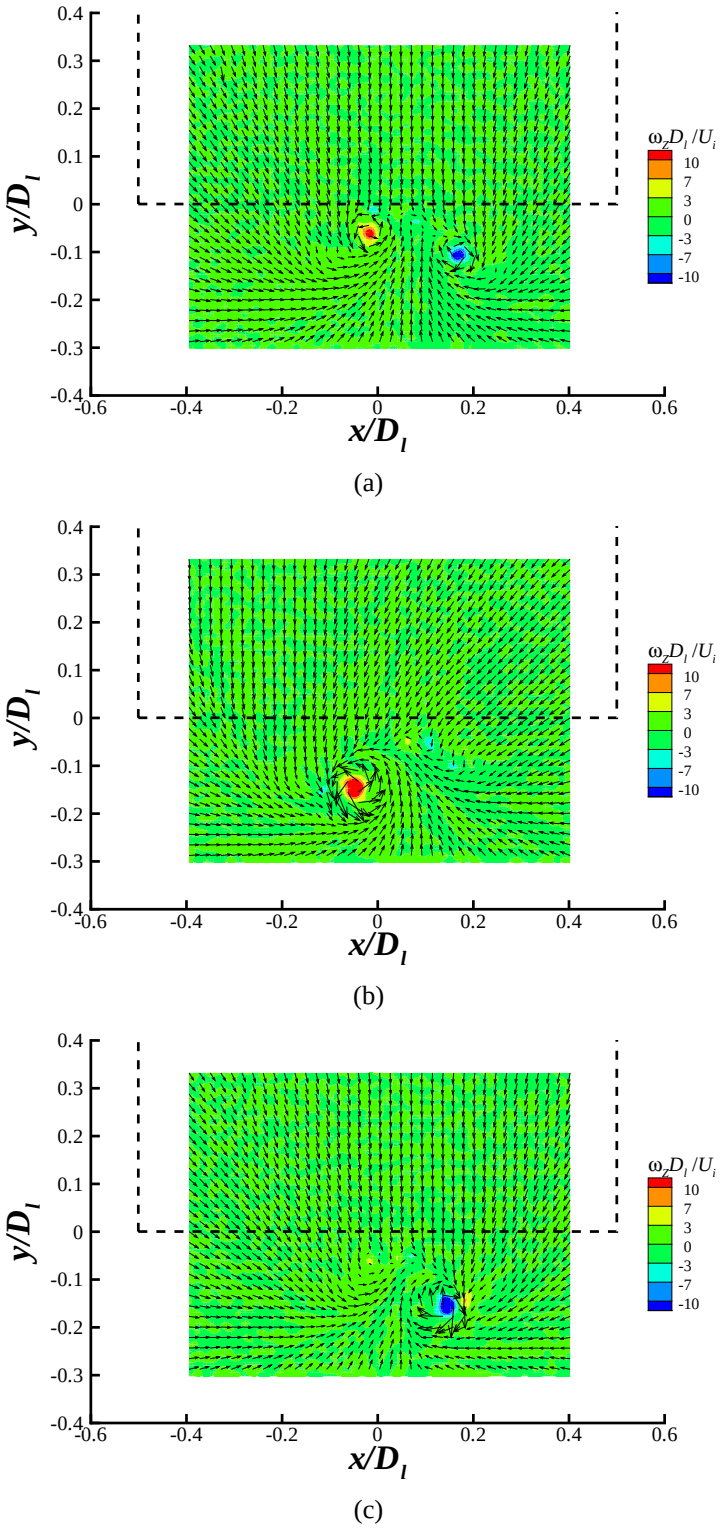

(a)

(b)

(c)

Figure 4.6: Flow modes observed under quiescent conditions ($h/D_l = 0.32$, $M_i = 0.58$, $U^* = \infty$, and $\delta^*/D_l = 0$)

isting between the flow mode change (Fig. 4.6a). As one dominant vortex appears it increases in size and strength, with the other diminishing until it disappears. Full scale engine test visualizations of ground vortex ingestion under no-wind* conditions also show a similar characteristic behaviour, as shown in Appendix A.1. The condensation induced by the high velocity gradients within the vortex core, give a clear indication of the vortex rotation. Fig. A.1 shows two example flowfield snap-shots taken from the same engine test run. A dominant vortex is clearly observed which is found to switch from side to side with a corresponding change in the rotation of the vortex. Similar to that in the scaled model experiments, the vortex system for the full scale visualizations was also found to favour one side of the intake. This of course may be a result of asymmetries in the flowfield, particularly for the full scale tests, which were conducted outside in an uncontrolled environment where the exact 'ambient' conditions are unknown.

4.1.3 Vortex Characteristics Quantification

As explained in §3.4.1.1 for each configuration two runs of approximately 20 s in duration were performed to obtain 300 flowfield samples of the velocity field. For each snapshot the vortex is identified from the location of peak out-of-plane vorticity, ω_z. Using this parameter allows both positive and negative vortices to be identified individually. The vortex strength (Γ), core size (r_c), and Vatistas shape factor (n) are then determined using the methods outlined in Appendix E for both clockwise and counter-clockwise vortices. As explained above, the flowfield under quiescent conditions varies considerably with time and often no clear vortex structure is observed in the PIV plane. For this reason outliers were present in the calculated vortex characteristics data which had to be removed prior to averaging the results. These manifested themselves in a number of ways, such as the 'identified' vortex being at the edge of the measurement domain underneath the intake or possessing an unrealistically large vortex core size (see Appendix E.5 for further details of how the outliers were removed). As a result, under no-wind conditions, typically 25% of the data points was removed prior to averaging. The resulting variation for all three parameters under quiescent conditions at a ground clearance of 0.32 (h/D_l) for the positive vortex is displayed in Fig. 4.7.

Initial inspection of Fig. 4.7a would indicate a long wavelength oscillation associated with the variation in the vortex strength. However as explained above the data was taken over two acquisition runs and the variation in both has been included in Fig. 4.7. The first 120 data points are associated with the first run with the rest being associated with the second (Fig. 4.7). Nevertheless, it is clear that there is some form of unsteadiness present which is resulting in gradual growth in the vortex strength

*For the engine test visualizations pictures shown in this thesis the tests are performed on an outdoor test bed. A large scale blower is used to simulate different wind speeds at the test site. The visualizations shown in §A.1 are with no external blower in operation. However since the tests are performed outdoors, there may be a small level of ambient wind present, hence the snap-shots shown may not be strictly under no-wind conditions. The rotation of the left and right vortices however indicates that the intake is operating in the no-wind mode.

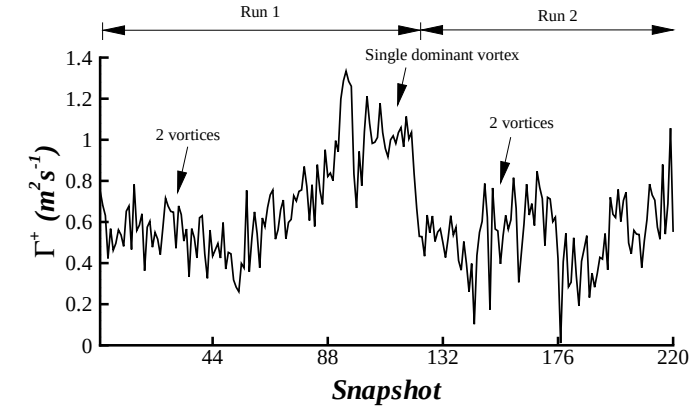

(a)

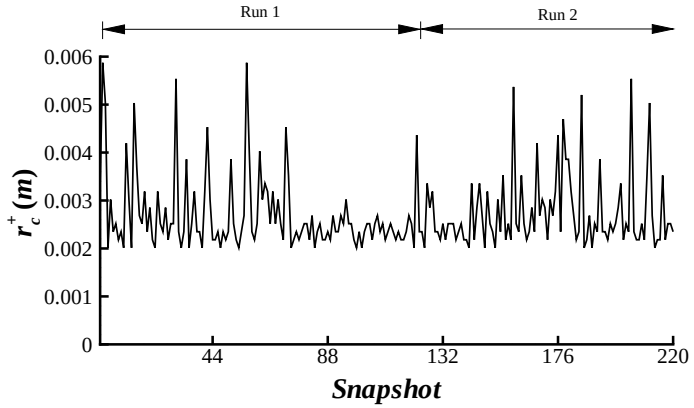

(b)

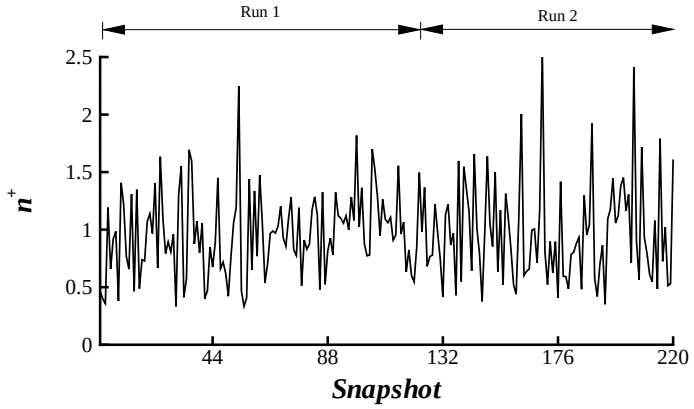

(c)

Figure 4.7: Variation in the positive rotating individual (a) vortex strength, Γ^+ (b) vortex core size, r_c^+, and (c) the Vatistas shape factor, n^+ for an $h/D_l = 0.32$, $M_i = 0.58$ and $\delta^*/D_l = 0$ (subsequent to data filtering, see §E.5 for further details)

for the first data acquisition run. Although no further analysis has been conducted, a discussion of the different unsteady sources is provided below in §4.2.2.1.

The characteristic behaviour in the vortex strength, ilustrated in Fig. 4.7a, has only been observed under quiescent conditions and relates back to the previous section regarding the flow modes observed. Typically, under quiescent conditions, two contra-rotating vortices where always observed at the start of each data acquisition run. This can be inferred from the relatively low vortex strength for the positive vortex for the first 50 or so data points[†] in Fig. 4.7a. Taking into account the amount of data that was filtered in this region, this equates to a time scale of approximately 7 s. Between the data points of 50 and 80 a steady growth in the vortex strength is observed (Fig. 4.7a). A corresponding reduction in the negative vortex is also seen (although not shown in the figure). At approximately the 100^{th} data point, the vortex strength has reached a maximum and fluctuates around $\Gamma = 1\ m^2 s^{-1}$. This is approximately double the vortex strength observed during the first 50 data points, where two contra-rotating vortices were present. In this region, where the vortex has reached a maximum strength, a single dominant vortex was seen for all flowfield snapshots. The flowfield has essentially 'locked' into a specific flow mode, and became very steady in space and magnitude. This is considerably different from the initial phase of the run where two contra-rotating vortices formed which were considerably unsteady in time.

In general this characteristic behaviour was observed for all investigated configurations under quiescent conditions (Fig. 4.8), although it is most evident at a height-to-diameter ratio of 0.32 (h/D_l). The flowfield initially begins with two contra-rotating vortices and with time a dominant vortex appears which eventually becomes prevalent in all snapshots. The transition between the first and second runs is clearly visible for all configurations (Fig. 4.8) which is evidence of this behaviour. It is also worth noting that the dominant vortex was always found to be the vortex closest to the engine centreline (the positive vortex) for all configurations. This perhaps suggests that these observations are a result of the initial asymmetries present in the flowfield (i.e. the occurrence of two contra-rotating vortices asymmetrically placed relative to the intake centreline).

In addition to the vortex circulation, the corresponding vortex core size (r_c) and Vatistas shape factor (n) variations are also displayed in Fig. 4.7. Some sensitivity with snapshot is observed in the r_c trend (Fig. 4.7b), where a drop in the average core size is seen in the region of the single dominant vortex. During this phase the vortex core size is small, approximately equal to 2.4 mm. However for all other snapshots, a relatively large variation is experienced. This is attributed to the interactions associated with the opposite sign vorticity of the second vortex. The average vortex core size across all snapshots for this configuration ($h/D_l = 0.25$, $M_i = 0.58$) was found to be 2.7 mm.

[†]In quiescent conditions the engine induces a flow-field and vorticity created within this flow-field, along the ground, is the source of vorticity for the vortex system. Hence when two vortices are present the sum of the vorticity levels within the vortices is expected to be approximately equal to that for the single vortex case. For example, in Fig. 4.7a, the vortex strength at the start of the run, when two vortices are present, is approximately half that when a single dominant vortex is observed

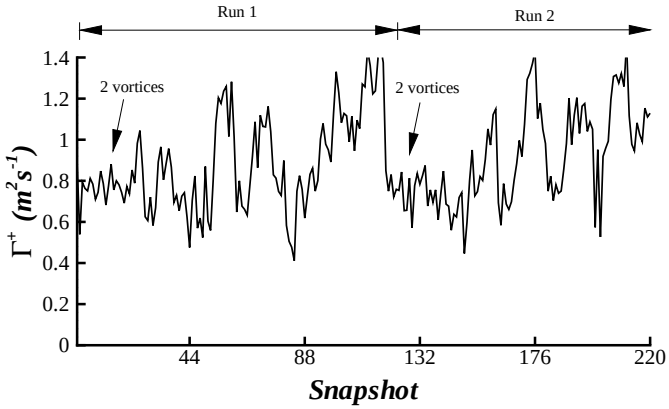

(a) $h/D_l = 0.25$

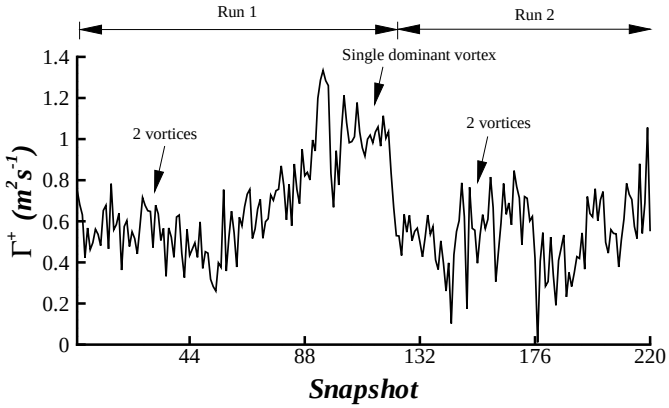

(b) $h/D_l = 0.32$

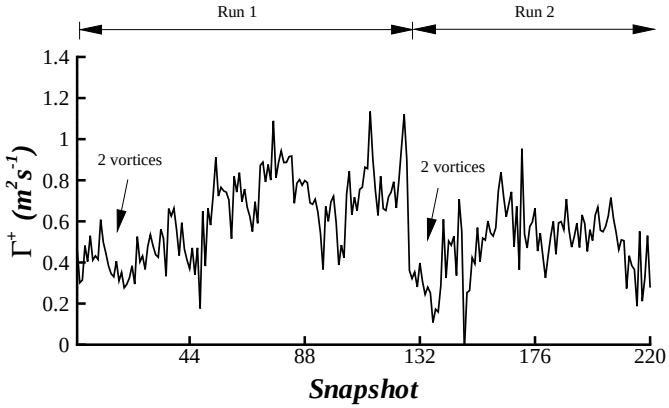

(c) $h/D_l = 0.40$

Figure 4.8: Variation in vortex circulation for the positive vortex, Γ^+, for increasing ground clearance ($M_i = 0.58$, $U^* = \infty$ and $\delta^*/D_l = 0$) (subsequent to data filtering)

In contrast, the Vatistas shape factor shows a fairly consistent trend for all flowfield samples (Fig. 4.7c) with a mean value of 0.97. Generally, the average Vatistas vortex model constant and vortex core size were unchanged for all quiescent configurations and were equal to approximately 1 and 3 *mm* respectively.

4.2 Effect of Non-dimensional Parameters

In this section the affect of varying the ground clearance, h/D_l, and the intake Mach number, M_i, on the average non-dimensional vortex strength, Γ^* and fan face distortion, DC_{60}, is shown. From the dimensional analysis presented in §3.1.1 the appropriate parameters for non-dimensionalising the vortex strength are the intake highlight diameter, D_l and the intake velocity, U_i (Eq. 4.2.1). As explained in §3.6 the average total vortex strength, $\bar{\Gamma}$, is the absolute sum of the average vortex strengths (Eq. 4.2.2). It is expected that non-dimensionalising the circulation in the fashion shown in Eq. 4.2.1 should give the same non-dimensional vortex strength for any given Mach number and intake diameter combination. This hypothesis will be tested with regards to the intake Mach number throughout this thesis for all investigated ground vortex formation mechanisms. The affect of D_l has not been experimentally investigated in this thesis, however a discussion of this parameter on the vortex strength is given in §8.3, with use of supporting CFD studies conducted in conjunction with this project.

$$\Gamma^* = \frac{\bar{\Gamma}}{U_i D_l} \tag{4.2.1}$$

where

$$\bar{\Gamma} = \left|\bar{\Gamma}^+\right| + \left|\bar{\Gamma}^-\right| \tag{4.2.2}$$

4.2.1 Ground Clearance

Although the effect of ground clearance has already been discussed in terms of the vortex topology and unsteadiness, this section discusses the influence of h/D_l on the non-dimensional vortex strength, Γ^* and fan face distortion parameter, DC_{60}. Fig. 4.9 illustrates the effect of reducing the ground clearance on Γ^*, for an intake Mach number, M_i, of 0.58. The lowest ground clearances are associated with the strongest vortex. This is expected given the mechanism of vorticity generation under quiescent conditions. As mentioned above, the intake velocity field induces a flowfield external to the intake. This flowfield interacts with the ground which consequently forms an induced boundary layer along the ground plane. The higher the velocities close to the ground, the higher the level of induced vorticity generation. Hence for a given mass flow, if the intake is closer to the surface, the velocities are expected to be larger

immediately adjacent to the boundary and therefore the vorticity in the flow is expected to increase. This is the reason for the higher vortex strength at lower ground clearances.

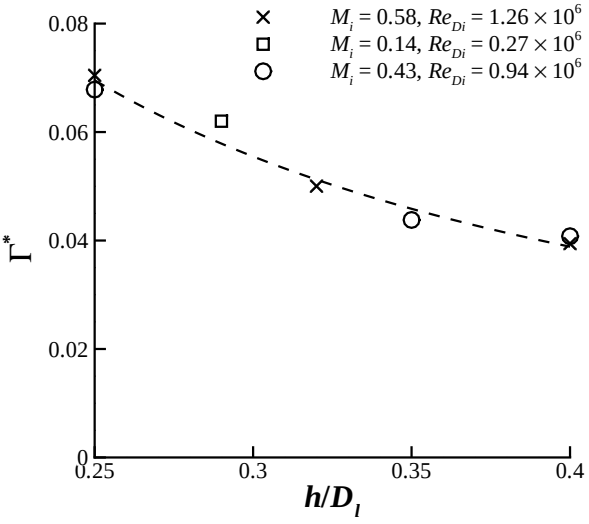

Figure 4.9: Effect of ground clearance on the average non-dimensional vortex strength under no-wind conditions ($U^* = \infty$)

The corresponding in-duct total pressure contours plots for all investigated non dimensional heights are displayed in Fig. 4.10. The distortion coefficient, DC_{60}, for each respective configuration is used to characterize the level of distortion at the nominal aerodynamic interface plane (AIP) and is plotted in Fig. 4.11. The DC_{60} parameter is used extensively in this thesis and is defined as being the area weighted average fan face total pressure, $\bar{P}_f$, subtracted by the worst area averaged 60 degree sector pressure, $\bar{P}_{60}$, divided by the dynamic head at the AIP, q_f (Eq. 4.2.3). For further details on this parameter see Appendix F which also includes other distortion descriptors that have been examined but not included in the main text.

$$DC_{60} = \frac{\bar{P}_f - \bar{P}_{60}}{q_f} \tag{4.2.3}$$

At the highest intake Mach number (M_i) of 0.58, a change in the ground clearance, h/D_l, from 0.25 to 0.4 has no noticeable impact on the total pressure pattern (Fig. 4.10a-b). This is also evident from the DC_{60} trend (Fig. 4.11) which does not alter significantly. As explained above two regions of high local total pressure loss is seen immediately adjacent to the intake wall, which is a clear indication of two ingested vortices. This is seen at both height-to-diameter ratios (Fig. 4.10a-b). The run time for the total pressure measurements was 5 *s*, which is not long enough to see the change in the flow mode from two contra-rotating vortices to a single relatively stronger vortex, as observed in the PIV measurements. At the lower intake Mach number of 0.43 (Fig. 4.10c-d) there is also no clear change in the loss footprint between the ground

clearances, although the vortex closer to the intake axis appears to have strengthened with a corresponding reduction in the low pressure region close to the duct surface. The largest change in the loss footprint is seen at the lowest investigated intake Mach number of 0.14. At a $h/D_l = 0.29$ two loss cores are observed (Fig. 4.10e) but with a change to 0.5 (h/D_l) leads a larger single loss region which is closer to the intake centre line (Fig. 4.10f).

The change from two loss cores to a larger single loss core is a direct result of a change in the flow topology from a flowfield that is dominated by two contra-rotating vortices to a flowfield where only a single vortex is observed. Only a single vortex is seen at the larger h/D_l, due to the increase in ground clearance amplifying the unsteadiness of the ground vortex. Consequently a relatively larger loss core is seen at the fan face due to the increased vortex movement. The change in the vortex ingestion is expected to be due to a 'biasing' effect introduced by increasing proximity to the ground. When an intake is far from the ground the sucked streamtube is symmetrical relative to the engine axis; air is drawn in equally above and below. As the intake is brought to within close proximity of the ground, the capture streamtube becomes considerably asymmetric. Air drawn in between the ground and the intake (the 'gap-flow') reduces, causing more air to be drawn in from above. As the ground clearance gets smaller, the gap flow gets weaker. Consequently the vortex horizontal locus position (in plane stagnation point) moves closer to the highlight plane of the intake which forces the vortex to take a sharper trajectory into the intake and is therefore ingested closer to the intake wall (Fig 4.10e). At high Mach numbers the vortex is much less sensitive to changes in the horizontal locus position, whereas a low Mach numbers ($M_i = 0.14$) there is a clear sensitivity to changes in ground clearance.

4.2.2 Intake Mach Number and Reynolds Number

Due to the nature of the experiments it was impossible to vary the intake Mach number whilst keeping the intake Reynolds number fixed since only a single intake model was constructed. The effect of varying the intake velocity, U_i, and consequently the intake Mach number and Reynolds number, on the non-dimensional vortex strength is also included in Fig. 4.9. By non-dimensionalising the vortex strength data by the intake velocity and intake diameter, no notable difference is seen in the trend with non-dimensional height. This indicates that vorticity generation on the ground plane directly scales with the intake velocity, and is an appropriate scaling parameter.

However in terms of the total pressure contours at the fan face, there is some sensitivity with the average fan face ingestion location (as explained above) (Fig. 4.10) and a significant sensitivity with DC_{60} (Fig. 4.11). A change in the M_i from 0.58 to 0.43 and a corresponding change in the intake Reynolds number from 1.26 to 0.94×10^6 leads to a considerable change in the right of the two vortices (Fig. 4.10c) where the vortex has moved from 0.97 to 0.64 (r_v/r_i). In tandem a marked reduction in the distortion coefficient is observed (Fig. 4.11). At the lower intake Mach number of 0.43 (M_i) the DC_{60} is approximately three times smaller in magnitude. However a further significant

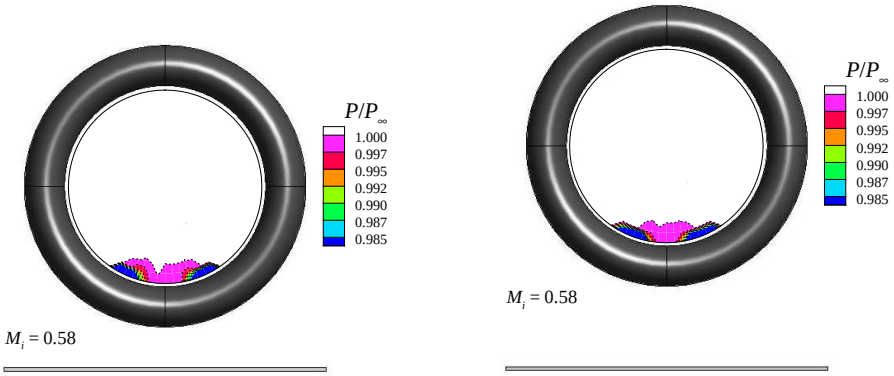

(a) $h/D_l = 0.25$

(b) $h/D_l = 0.40$

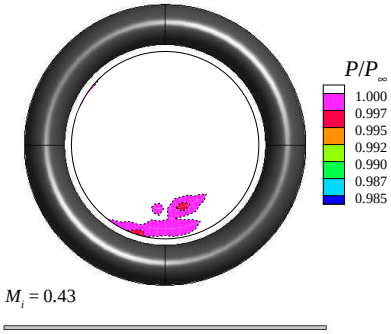

(c) $h/D_l = 0.25$

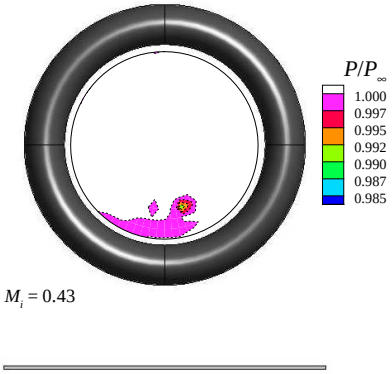

(d) $h/D_l = 0.40$

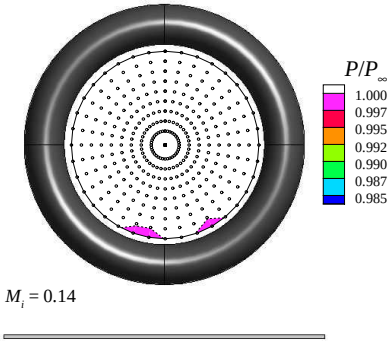

(e) $h/D_l = 0.29$

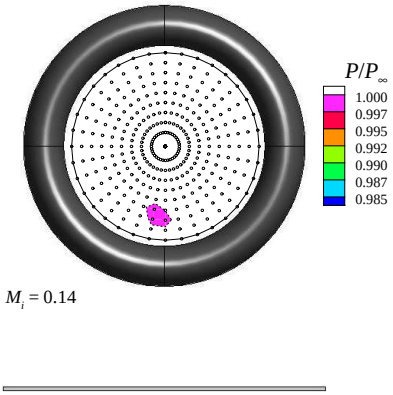

(f) $h/D_l = 0.50$

Figure 4.10: Effect of ground clearance, h/D_l, and intake Mach number, M_i on the total pressure contours within the intake duct under quiescent conditions

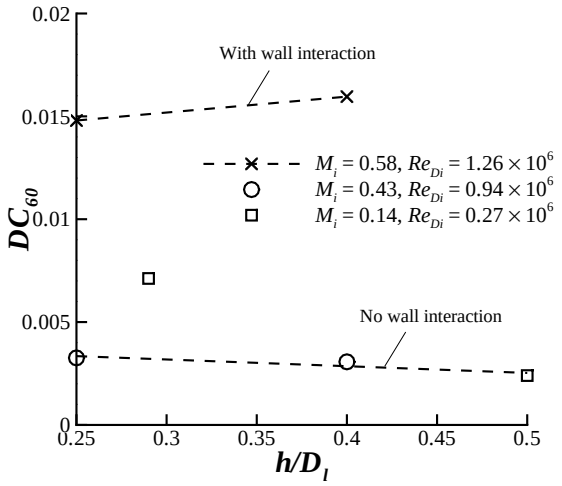

Figure 4.11: Effect of ground clearance on the distortion coefficient under no-wind conditions ($U^* = \infty$) for various intake Mach numbers

reduction in the intake Mach number to 0.14 (at a slightly higher ground clearance, h/D_l, of 0.29) sees both vortices being ingested very close to the intake wall again with the radial position again being equal to 0.94[‡] (r_i/r_v). It is unclear whether the sensitivity in the ingestion location is an intake Mach number or Reynolds number feature.

The sensitivity in the DC_{60} trend, however, appears to be linked to the ingestion location. As highlighted in Fig. 4.11, for the configurations in which the lowest pressure loss region is not in contact with the intake wall (i.e. Fig. 4.10c-d & f) the DC_{60} is relatively lower in comparison to the cases when the minimum pressure region is interacting with the duct surface (i.e. Fig. 4.10a-b & e). This indicates that when the vortex is ingested close to the duct surface the vortex interacts with the wall such that it induces local separation thereby increasing the overall pressure loss in that region. With no wall interaction the DC_{60} trend with ground clearance is similar to the circulation measurements (Fig. 4.9) in that lower ground clearances produce a stronger vortex and therefore higher fan face distortion value (Fig. 4.11). However, with the minimum loss region in contact with the wall the trend with h/D_l is slightly different with the higher ground clearance exhibiting a larger DC_{60}. These differences are a testament to the added complication of the vortex-wall interaction. The data point at an intake Mach number of 0.14 is expected to be different to the $M_i = 0.58$ data points because, for the latter case, measurements were taken as close as $0.97r_v/r_i$ to wall whereas in for the former the closest data point to the duct surface was at $0.94r_v/r_i$. As a consequence, the distortion observed is not just due to the vortex but also a result of local separation. This will be discussed in further detail in §5 and will be clarified in §8.

[‡]This is slightly different to the $M_i = 0.58$ case as the measurement point locations are not the same (see Figs. 4.2 and 4.10e).

4.2.2.1 Sources of Unsteadiness

It is clear from the data presented in this chapter that there are some unsteady features (see Fig. 4.7a), however the source of this unsteadiness is unclear. For the experiments presented in this thesis there are four primary sources of unsteadiness. The first is the start-up transient associated with the non-continuous nature of the experiment run. The second source is associated with the broadband turbulent unsteadiness with the third being associated with the characteristic unsteadiness caused by the interaction of the flow with the physical features of the rig. The most obvious example of this is under crosswind conditions where there is vortex shedding from the outer surface of the intake. Finally there is the inherent unsteadiness of the ground vortex itself.

With regards to the first unsteadiness source, quantitative studies conducted in this thesis (see §7.1.1), reveal that the ground vortex start-up transient lasts for a period of approximately 1 s. For all configurations, data acquisition did not commence until approximately 2 s after the intake suction was initiated, hence the initial transient has been avoided. Given the results in §7.1.1), is known that the during the transient the vortex is relatively weak and rapidly increases in strength to a quasi-steady state magnitude. For all configurations, where the transient has been purposely avoided there has been no evidence of this behaviour at the start of each data acquisition run.

Before discussing the other two sources individually the experiment set-up and data acquisition methodology for the PIV experiments is revisited. Due to the nature of the intake suction system the maximum permissible run time, at a constant maximum mass flow rate of 1.49 kgs^{-1}, is approximately 22 s. The SPIV system implemented in this thesis allows a data acquisition rate of 7.5 Hz. Hence avoiding the initial transient of the ground vortex start-up, each run allows 150 data samples to be acquired. In order to obtain a good statistical representation of the flowfield two runs were performed for each configuration giving a total of 300 flowfield snapshots. Therefore although 40 s of data has been taken, only 20 s of continuous data has been acquired and it is this that determines the lowest frequency oscillation that can be captured.

The broadband turbulent unsteadiness is associated with the turbulence within the free-stream of the tunnel, the approaching boundary layer, the intake boundary layer and also the near wake of the intake for crosswind conditions. With regards to the tunnel, the free-stream turbulence is 0.1% (v'/U_∞) which is very low and is therefore not expected to affect the flowfield significantly. However for most cases the intake is partially submerged in an approaching boundary layer which is expected to cause high frequency variations in the vortex strength.

In terms of the natural frequency of the ground vortex, Karlsson and Fuchs[26] present Large Eddy Simulations which provides frequency data of the ground vortex. Simulations were performed under headwind conditions at a low Reynolds number, Re_{D_i}, of 5.5×10^4, based on the intake velocity, U_i, and intake inner diameter, D_i. Non-dimensional frequencies of between 0.009 and 0.045 were observed (normalised by U_i and D). Scaled to the current experiments, indicates a frequency range of between 12 and 63 Hz. Despite the large difference in Reynolds number, this frequency range

agrees well with the Unsteady RANS simulations conducted by Zantopp[71] which were performed to simulate the current model and Reynolds number (i.e. $Re_{D_i} = 1.3 \times 10^6$).

Given that the SPIV data acquisition frequency is 7.5 *Hz* this is not large enough to resolve the smallest frequencies associated with the ground vortex, as observed by Karlsson and Fuchs[26]. However the intention is to obtain an accurate representation of the average vortex strength. Given that the run time is 20 *s*, this is enough time to capture frequencies down to 0.05 *Hz*.

Under quiescent conditions the flowfield was occasionally observed to gradually lock into a single vortex flow mode (Fig. 4.7a) which perhaps indicated that a low frequency oscillation was dominant. However the analysis of Karlsson and Fuchs indicate that the lowest frequency observed is 12 *Hz*, which can easily be captured in the run time that has been implemented. In addition, it should be stated that the primary aim of this research is to characterize the total circulation of the vortex system. Hence although in Fig. 4.7a the vortex strength of the positive vortex gradually increases, there is also a corresponding reduction in the negative vortex strength. Consequently the variation in the total vortex strength does not show any indication of a low wavelength oscillation. This feature will only have an impact on the time average flowfield which is not used quantitatively in this thesis.

4.3 Summary

Ground vortex formation under quiescent (no-wind) conditions has been quantitatively examined for the first time. PIV measurements external to the intake and in-duct total pressure measurements have been taken to assess the flowfield. The results are in-line with previous qualitative observations for this formation mechanism. The velocity measurements reveal a flowfield which is rich in features and unsteady, time dependent, characteristics. The effect of intake ground clearance (h/D_i) and Mach number (M_i) have been studied. The main features of the flowfield and the most important conclusions are outlined below.

- Under no-wind conditions the intake velocity field induces a flowfield which emanates from all directions in the external vicinity of the intake. With the ground plane in close proximity, this induced velocity field interacts with the surface generating vorticity.
- This induced velocity field is strongest between the intake and the ground plane resulting in two ingested contra-rotating vortices that rotate such that the left vortex has positive ω_z vorticity at the PIV plane. However there is also a relatively strong source of induced vorticity approaching the intake travelling in the opposite direction.
- The interaction of the two vorticity sources is the expected reason for the unsteady formation of two contra-rotating vortices.

- A number of flow modes are observed at the PIV measurement plane; two contra-rotating vortices, and a single clockwise and counter-clockwise vortex.
- With time the flowfield eventually falls into a specific flow mode in which only a single vortex prevails. This vortex is now both steady in time and space. With no external disturbances the flowfield does not recover its initial state and appears to be locked into this specific flow mode.
- Low ground clearances generate a stronger vortex due to the higher induced velocities close to the ground plane.
- The vortex strength under quiescent conditions scales with the intake velocity.
- The vortex ingestion location was found to be sensitive to the intake velocity, but it cannot be determined whether this is a intake Mach number or Reynolds number feature.
- When the vortex is ingested immediately adjacent to the duct surface a higher distortion is observed which is expected to be caused by an induced separation.

CHAPTER 5

Headwind Conditions

The aerodynamic features and characteristics of ground vortex formation under headwind conditions is presented in this chapter. The experiments under quiescent conditions ($U^* = \infty$) provide a reference point for the results presented here. The velocity ratio is reduced from ∞, by introducing a non-zero headwind speed with PIV and induct total pressure measurements being taken at selected freestream velocities, ranging from 10 to 50 ms^{-1} ($U^* = 20$ to 3.5). As well as the effect of velocity ratio, the important geometric and aerodynamic parameters are also investigated. Three height-to-diameter ratios have been studied ($h/D_l = 0.25$, 0.32 and 0.4) which are applicable to current and future conventional wing mounted engine installations. In addition, three approaching boundary layer configurations have been explored to establish its sensitivity, which to the authors' knowledge has not been investigated experimentally to date. From this dataset a new vortex formation criterion is established, which includes quantitative information to provide greater understanding of regions of strong vortex magnitude.

The first section of this chapter discusses the flow topology with particular focus on its sensitivity to reductions in velocity ratio from ∞. Both PIV and total pressure measurements are used to describe the key flowfield features. The effects of the non-dimensional parameters are then discussed primarily in terms of the vortex strength and flow distortion parameter.

5.1 Flow Topology

With an intake operating under quiescent conditions ($U^* = \infty$) a pair of contra-rotating vortices form ahead of the highlight plane (Fig. 5.1a). As explained in the preceding chapter, at a velocity ratio at $U^* = \infty$, the flowfield is dominated by vorticity generated by the induced intake velocity field along the ground plane travelling in the negative y direction (between the intake and the ground). With the dominant vorticity source emanating from this direction the left vortex rotates anti-clockwise at the PIV plane (i.e. has positive ω_z vorticity)(Fig. 5.1a). As discussed in §4.1.3 for all investigated non-dimensional heights under quiescent conditions with sufficient time

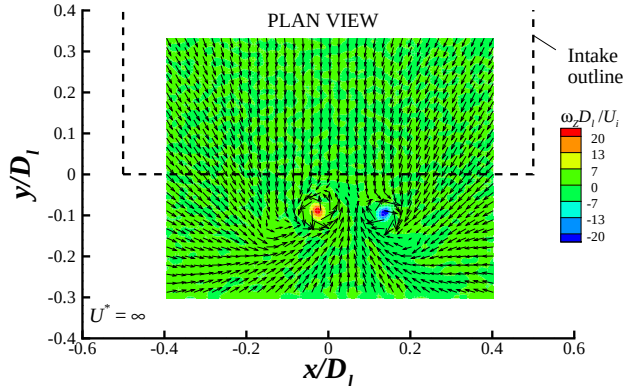

(a) $U^* = \infty$

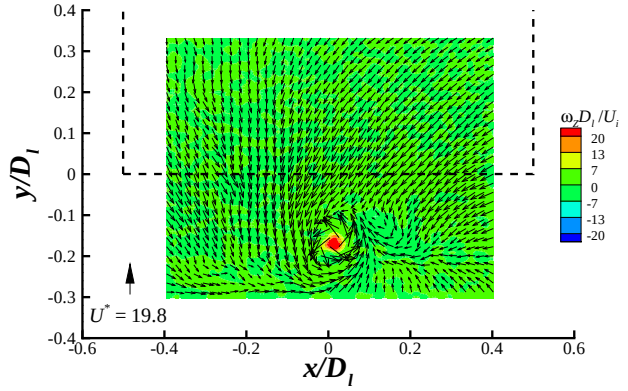

(b) $U^* = 19.8$

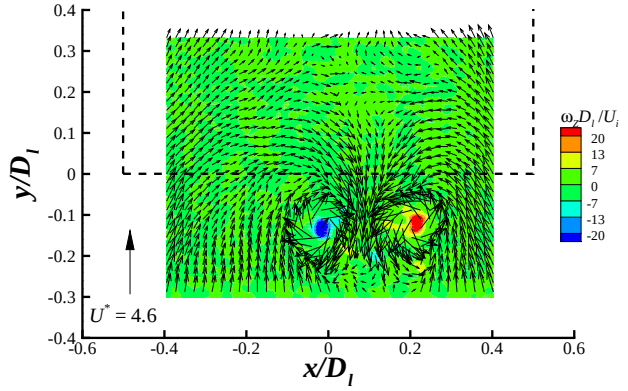

(c) $U^* = 4.6$

Figure 5.1: Typical vortex snapshots showing the effect of velocity ratio on the flowfield topology which shows the in-plane velocity vectors (only every 3^{rd} vector shown) and the out-of-plane vorticity contours, ω_z, at an $h/D_l = 0.25$, $M_i = 0.58$ and $\delta^*/D_l = 0.11$

the flowfield eventually develops into a specific flow mode where only a single dominant vortex prevails. This dominant vortex was always found to be the vortex closest to the intake centreline and always had positive vorticity (+ve ω_z). When a small non-zero approaching wind speed is introduced the flow field immediately enters this flow mode (Fig. 5.1b). At a velocity ratio, U^*, of 19.8 and a non-dimensional height of $h/D_l = 0.25$ a contra-rotating vortex pair almost never forms with a positive rotating vortex prevailing for all flowfield snapshots. The single vortex created under such conditions is found to be steady in space, as illustrated in Fig. 5.2a, which shows the locus of vortex core positions over all flowfield snapshots.

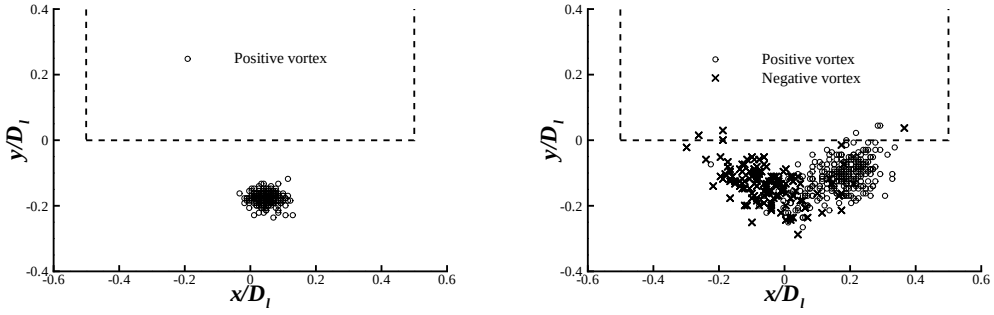

(a) $U^* = 19.8$ (b) $U^* = 4.6$

Figure 5.2: Effect of velocity ratio on the vortex core positions over all flowfield snapshots ($h/D_l = 0.25$, $M_i = 0.58$, $\delta^*/D_l = 0.11$)

Careful inspection of the flowfield suggests that the dominant vorticity source is still associated with the gap-flow (i.e. negative y direction), despite the introduction of an additional approaching vorticity source in the positive y direction. This can be seen in Fig. 5.3 which shows an example snapshot at a $U^* = 19.8$ where a very weak clockwise ($-ve\ \omega_z$) vortex is seen to the right of the dominant anti-clockwise vortex. With the vortices in such positions with respect to each other the flowfield topology is in agreement with the no-wind formation mode (Fig. 5.1a). The snapshot shown in Fig. 5.3, however, is perhaps the only example where arguably two vortices are observed at the PIV plane for this particular configuration ($U^* = 19.8$ and $h/D_l = 0.25$). Given these findings it is expected that the flowfield, at this particular velocity ratio and non-dimensional height ($U^* = 19.8$ and $h/D_l = 0.25$), is on the verge of a change in the dominant vorticity source from that associated with the induced flowfield to the approaching vorticity source. This will be discussed further below.

With a further increase in the headwind velocity, at the datum height of 0.25 (h/D_l), to a velocity ratio of 13.3 still only a single dominant vortex is observed at the PIV plane (Fig. 5.4c). However, as the approaching wind speed increases further the flow topology changes again with the return of a pair of contra-rotating vortices (Fig. 5.1c and also Fig. 5.4e). In comparison with the vortex pair generated under quiescent conditions (Fig. 5.1a) the vortices are stronger and with a reversed sense of rotation. This is in line with expectation and the change in rotation is as a result of the source vorticity now being associated with the approaching flow field[10] (see Fig. 2.5a). This vortex

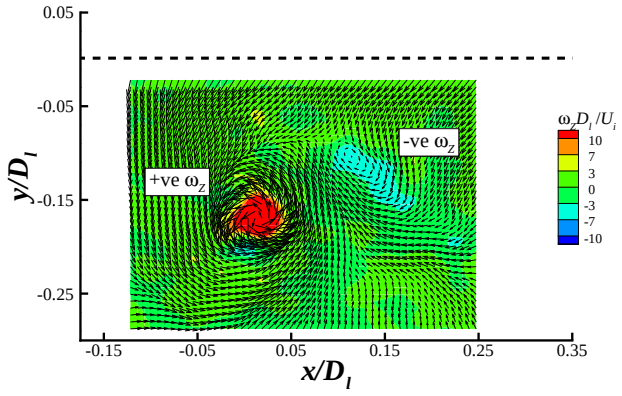

Figure 5.3: Example snap-shot of the in-plane velocity vectors and vorticity field under headwind conditions (h/D_l = 0.25, U^* = 19.8, M_i = 0.58, δ^*/D_l = 0.11)

structure increases in strength and symmetry with further increases in the approaching wind speed. In addition, as the velocity ratio reduces the spatial unsteadiness of the vortex system significantly increases. This is illustrated in Fig. 5.2b which shows the vortex core locations at a velocity ratio of 4.6. In comparison to the single vortex generated at the higher velocity ratio (U^* = 19.8) the vortex movement of the positive vortex, at the PIV plane, has increased by approximately three times.

With regards to the vortex rotation switch boundary, Brix et al[6] had also shown that the rotation of the vortices under headwind conditions was still in the same fashion as the no-wind mode but at a much higher velocity ratio of 33 (see §2.2.1). It was shown that when the velocity ratio was reduced to 12 the vortex pair had changed its sense of rotation and was now rotating in accordance with the headwind mode. Although the exact velocity ratio at which the mode change occurs was not given, Brix et al noted that during this change the vortex pair became unstable. This is a possible reason for only a single vortex being observed at intermediate velocity ratios. In the current study, at the higher ground clearance of 0.4 (h/D_l) where the induced vorticity is lower (see §4.2.1), again only a single vortex was observed at the highest headwind velocity ratio of 19.1 (Fig. 5.4b). At this intake height it could not be determined whether the flowfield was still dominated by the induced vorticity. However, with a reduction in the velocity ratio to 12.1 (Fig. 5.4d), the occurrence of two contra-rotating headwind vortices appeared. This compares to a velocity ratio of 9.1 for the lower ground clearance of 0.25 (h/D_l) (Fig. 5.4e). This perhaps demonstrates that the switch in the flow mode is height dependant and depends on the relative strength of the induced vorticity. This theory will be further explored in the theoretical headwind model presented in §8.2.

An explanation for the observation of just a single vortex, at the datum height configuration for intermediate velocity ratios, can also be given by considering the two dimensional flow topology in the PIV measurement plane. For a typical headwind configuration (U^* = 4.6) the time averaged in-plane vector flowfield clearly shows a contra-rotating vortex system (Fig. 5.5a). The basic flow topology is further high-

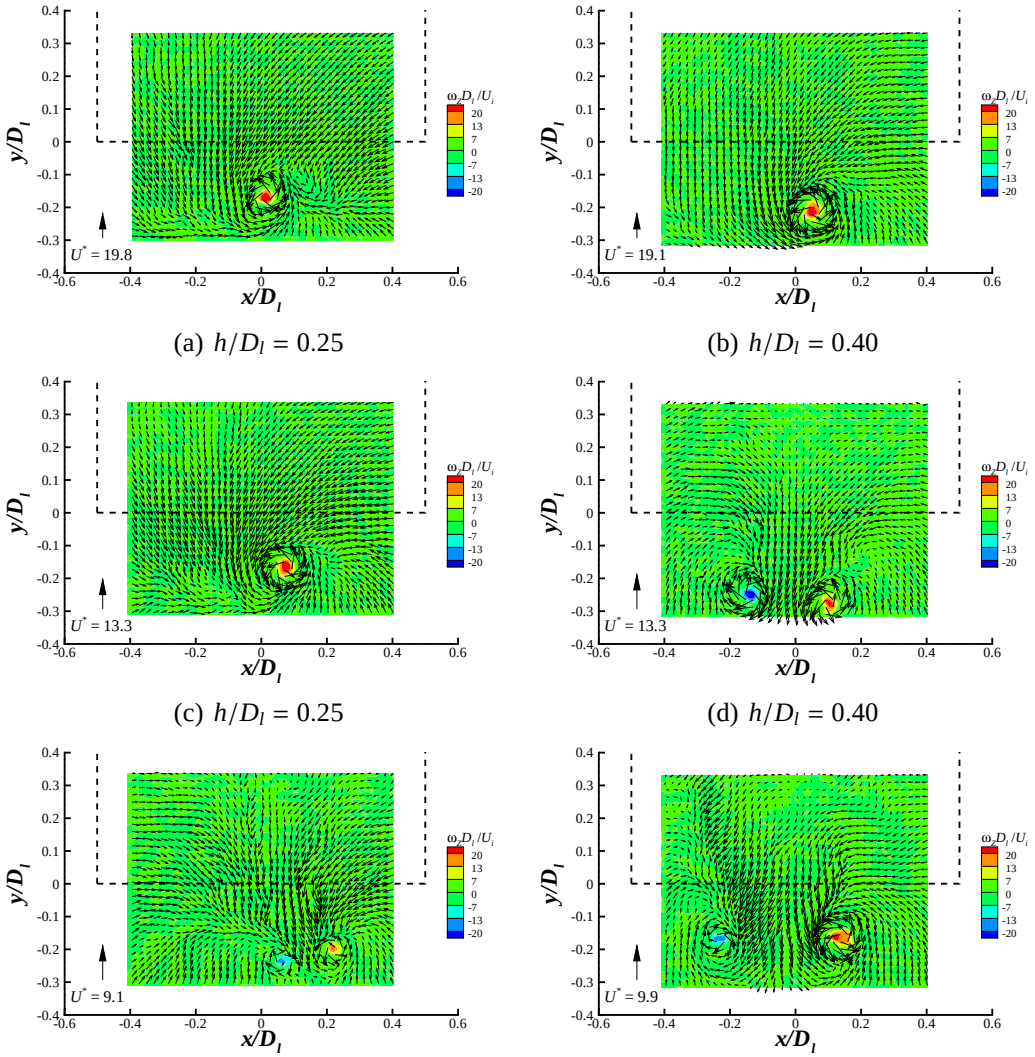

(a) $h/D_l = 0.25$ (b) $h/D_l = 0.40$

(c) $h/D_l = 0.25$ (d) $h/D_l = 0.40$

(e) $h/D_l = 0.25$ (f) $h/D_l = 0.40$

Figure 5.4: Example snap-shots under headwind conditions for an $M_i = 0.58$ and $\delta^*/D_l = 0.11$

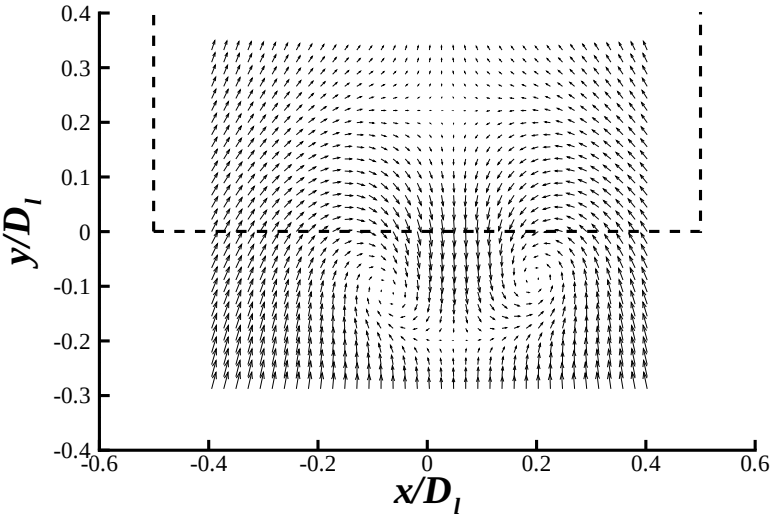

(a)

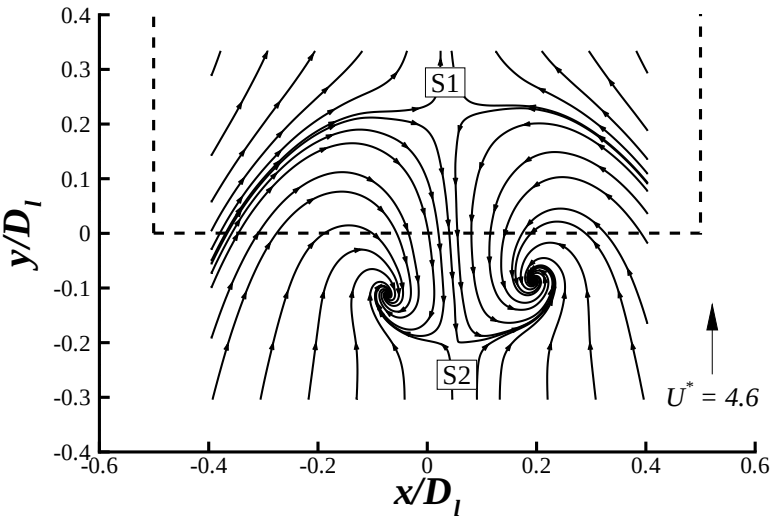

(b)

Figure 5.5: Average (a) vector field with every (3^{rd} vector shown) and (b) in-plane 'streakline' patterns over 300 snapshots for an $h/D_l = 0.25$, $U_i/U_\infty = 4.6$, $M_i = 0.58$, $\delta^*/D_l = 0.11$

lighted by considering the in-plane flow streaklines and although there are caveats with applying this technique off-surface[59], in this case it serves to clarify the flow structure. The topology is characterized by two saddle points which are connected to each other, denoted by **S1** and **S2** in Fig. 5.5b. Saddle point **S1** defines the edge of the capture stream-tube and saddle point **S2** forms just upstream of the intake highlight plane and forms part of the vortex system. The existence of this second saddle point is vital for two vortices to form. Furthermore, the saddle to saddle point connection (**S1-S2)** is indicative of an inherently unstable flow topology[59]. Therefore small changes in the flow field (such as the flow angle), could result in significant changes in the flow structure (twin vortex to single vortex flow-field). At high velocity ratios the flowfield is characterized by lower headwind speeds and is more sensitive to a reduced tunnel flow quality. In addition, the flowfield maybe more sensitive to the seeding rake positioned upstream of the intake at these low headwind speeds (Fig. 3.2a). This may also explain why only a single vortex is seen at high headwind velocity ratios.

5.1.1 In-duct Total Pressure Patterns

In conjunction with the external velocity field measurements, an in-duct total pressure survey was conducted for the majority of configurations examined using the PIV technique (see Appendix D). The measurement coverage within the intake is identical to that in quiescent conditions. A total of 432 data points were taken for each configuration over a number of runs by rotating the intake (Fig. 4.2). As explained in §4.1, the total pressure flow topology under quiescent conditions is characterized by two regions of high local total pressure loss immediately adjacent to the duct surface. This plot is again shown in Fig. 5.6a for an intake Mach number (M_i) of 0.58. It was concluded in §4.1 that the loss seen under quiescent conditions at the highest intake Mach number and Reynolds number is not only due to the vortex, but also due to the interaction of the vortex with the duct surface. As will be discussed in §8.3, Zantopp[71] has shown that the vortices induce local separation within the intake. With the vortices rotating as shown in Fig. 5.6b this will result in two regions of induced separation. With the addition of a modest approaching wind speed of 10 ms^{-1} ($U^* = 19.8$), the loss pattern changes at the fan face with the two loss regions moving towards each other (Fig. 5.6c). However two regions of high total pressure distortion can still be identified. It is expected at this velocity ratio the flowfield is in a transitional state, as interpreted by Brix et al[6], in which the effect of the approaching vorticity source is starting to become dominant. This is signified by the two vortex core locations moving towards each other, which is expected to be due to the influence of the approaching vorticity source, as depicted in Fig. 5.6d. However, since the two loss cores can still be identified, the flowfield is still expected to be dominated by the induced vorticity bound in the flow travelling in the negative y-direction underneath the intake. This agrees with the PIV measurements described above. With a further increase in the approaching wind velocity and a corresponding reduction in the velocity ratio to 10 (U^*), only a

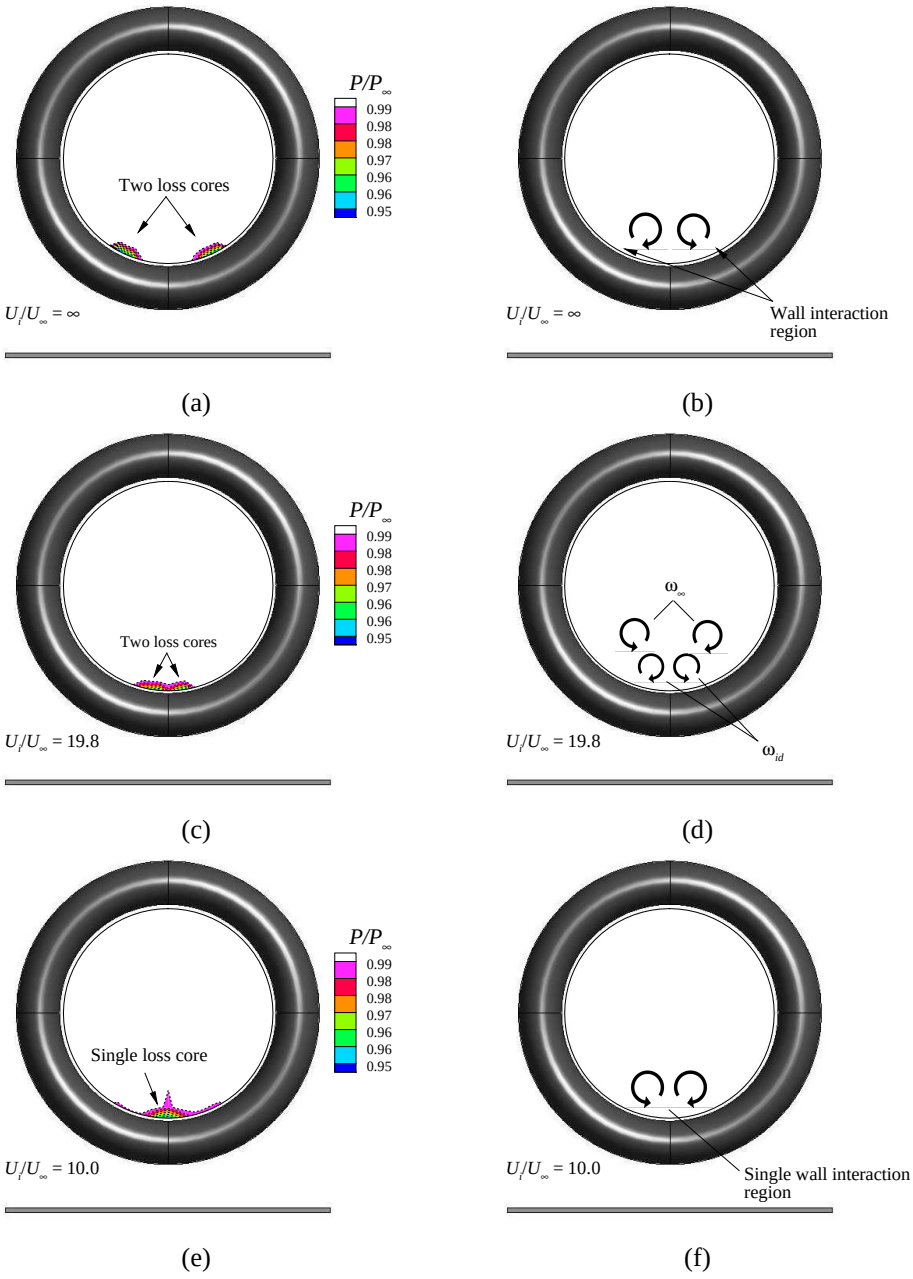

Figure 5.6: Fan face total pressure contours under (a)-(b) quiescent conditions ($U^* = \infty$) and (c)-(d) headwind conditions ($U^* = 19.8$), (e)-(f) headwind conditions ($U^* = 10.1$) with $\delta^*/D_l = 0.11$ at an intake Mach number of $M_i = 0.58$

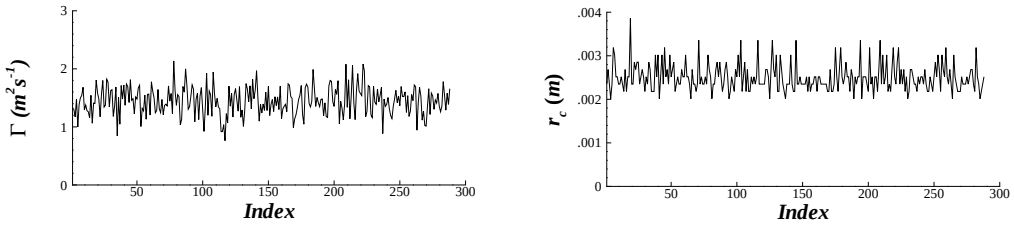

(a) (b)

Figure 5.7: Variations in (a) vortex circulation, Γ, and (b) vortex core size radius, r_c, for an $h/D_l = 0.25$, $U^* = 19.8$, $\delta^*/D_l = 0.11$ both at an intake Mach number of $M_i = 0.58$

single loss core can now be identified at the 180° circumferential location* (Fig. 5.6e). For this configuration only the approaching vorticity dominates with the vortices rotating in the intake duct as shown in Fig. 5.6f. Due to the sense of rotation of the vortices for this velocity ratio only a single region of induced separation is observed.

5.1.2 Snapshot Variations

As explained in the previous chapter and in §3.6, for each PIV configuration 300 flowfield snapshots have been acquired. Each vortex snapshot has been analysed to determine the vortex parameters such as circulation, core size and Vatistas shape factor, *n*. When both positive and negative vortices are present in the measurement domain the vortex characteristics are determined for both individual vortices.

Fig. 5.7 displays typical signatures of vortex strength and core size over 300 vortex snapshots for a single configuration in which only a single vortex is present at the PIV plane. For this example the average vortex strength, $\overline{\Gamma}$ was found to be 1.4 m^2s^{-1} with a standard deviation, σ_Γ, of 0.2 m^2s^{-1}. For most configurations the vortex strength was found to exhibit a near normal statistical distribution and the standard deviation was typically around 15-30% for the $\delta/D_l = 0.11$ approaching boundary layer. This variation in vortex strength is expected to be primarily due to the level of fluctuations within the boundary layer. For a much thinner approaching boundary layer ($\delta/D_l = 0.03$), the standard deviation in the circulation, $\sigma_\Gamma/\overline{\Gamma}$ was typically around 10-15%. Since the measurement plane is fixed relative to the tunnel coordinate system, it is closer to the edge of the boundary layer for this configuration; hence the level of turbulent fluctuations in this region will be lower. In contrast to the vortex strength, the vortex core radius, r_c reveals a positively skewed statistical distribution (Fig. 5.7b). The average vortex core radius size is 2.5 *mm* ($0.05D_i$) with a standard deviation of 0.3 *mm*. As with quiescent conditions, the average vortex core size was found to fluctuate around a value of 3.0 *mm* ($0.06D_i$) for all configurations.

Further to the basic flow topology understanding, it is of interest to assess the characteristics of the vortices relative to existing vortex models which usually parameterise

*measured top dead centre clockwise

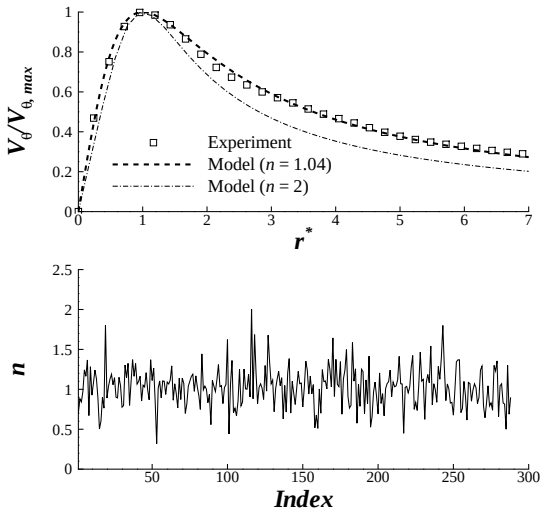

Figure 5.8: Typical (a) plot of non-dimensional swirl velocity against non-dimensional radial distance ($r^* = r/r_c$) and (b) variation in the Vatistas vortex model, n, over all flowfield snapshots for a single configuration ($h/D_l = 0.25$, $U^* = 19.8$, $\delta^*/D_l = 0.11$ and $M_i = 0.58$)

the vortex based on a non-dimensionalised core size, peak swirl velocity ratio and potential field decay factor[64]. The measured velocity flow field snapshots provide sufficient data to enable the vortices to be evaluated against such vortex models. An example distribution of the non-dimensional swirl velocity against radial distance from the centre for a single vortex snapshot is given in Fig. 5.8. A least squares fit of the non-dimensionalised swirl velocity distribution shows that at the PIV plane the ground vortex has a Vatistas shape factor of 1.04 for this example snapshot. The commonly quoted general vortex distribution of n=2 has also been added for comparison. The variation of the Vatistas vortex model constant with the individual snapshots is also shown in Fig. 5.8. Outliers were removed if the least squares residual of the velocity distribution was greater than 0.3 (see Appendix E.5 for further details). This typically led to 5% of the results being removed. For the configuration in Fig. 5.8 the average shape factor, $\overline{n}$, was found to be 1.03. Across all configurations $\overline{n}$ was approximately 1.0 and indicates that the ground vortex best fits the Scully vortex model[30,3] (n=1) from the measured data that has been taken. This result is in contrast to the previous experimental research by Brix et al[6] which found that the ground vortex was best approximated by the Vatistas (n=2) vortex model. It should be noted however, since the spatial measurement resolution is low relative to the vortex core size, measurements will tend to under-predict the model constant (bias towards lower values) as determination of this parameter strongly depends on the measured peak tangential velocity. Using an n=1 vortex model to investigate the effects of this low spatial resolution, it is expected that this would introduce a +0.2 and -0.15 uncertainty in the Vatistas shape factor.

5.2 Effect of Principal Parameters

In this section the effect of the important non-dimensional parameters are presented and discussed in terms of the average non-dimensional vortex strength (Γ^*) and fan face distortion (DC_{60}). As explained in the previous chapter (§4.2) the vortex strength, Γ is determined for each individual vortex snap-shot for both positive and negative vortices. The average circulation of the vortex system, $\overline{\Gamma}$, is then determined by taking the sum of the absolute mean values of the clockwise (negative) and counter-clockwise (positive) vortices. $\overline{\Gamma}$ is then non-dimensionalised by the intake velocity, U_i, and intake highlight diameter, D_l to give Γ^*. In §4 it was shown that non-dimensionalizing the vortex strength in this fashion leads to an invariant parameter with changes in Mach number. This will again be tested under headwind conditions.

5.2.1 Contraction Ratio

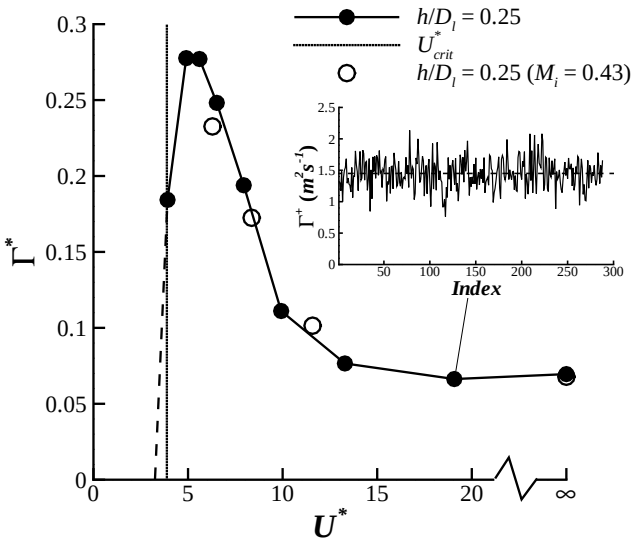

Figure 5.9: Total average non-dimensional vortex strength, Γ^*, against velocity ratio, U^* for an $h/D_l = 0.25$, $M_i = 0.58$ and $\delta^*/D_l = 0.11$)

The influence of headwind velocity (U_∞) on the average non-dimensional vortex strength (Γ^*) is presented in Fig. 5.9. The no-wind results are also presented, denoted by the $U^* = \infty$ data point. Overall the change from quiescent ($U_i/U_\infty = \infty$) to a modest headwind configuration ($U_\infty = 10ms^{-1}$, $U_i/U_\infty = 19.8$) results in no notable change in the total circulation (Fig. 5.9). In terms of the vortex strength trend with reducing velocity ratio, the variation is clear. High velocity ratios (U^*) are associated with a weak vortex and as the headwind speed increases the vortex strength increases monotonically up to a local maximum, before reducing thereafter. The observed variation in vortex strength with the velocity ratio, (U^*) is the result of a balance between two aspects;

the size of the sucked streamtube intersection with the ground plane and the level of ingested vorticity. At low wind speeds, the capture streamtube size is large but the approaching boundary layer vorticity levels are low. As U_∞ increases vorticity within the ground boundary layer increases resulting in a stronger vortex. However, with further increases in U_∞ the capture streamtube size will also decrease at a rate proportional to the inverse of the free-stream speed. The total vorticity within the sucked streamtube therefore peaks, at a specific velocity ratio U^*_{max} and reduces thereafter with decreasing velocity ratio. Eventually the blow-away condition is reached when the sucked streamtube lifts off the ground plane. This point is shown in Fig. 5.9 denoted by U^*_{crit}, and calculated from continuity considerations using Eq. 5.2.1[†]. The critical velocity was not examined for the datum height ($h/D_l = 0.25$) due to tunnel limitations. In addition to measurements being taken at the datum intake Mach number of 0.58, a limited set was taken at an M_i of 0.43. These results are also included in Fig. 5.9. As is the case under quiescent conditions, by non-dimensionalizing the vortex circulation by the intake velocity, U_i, no notable change is observed between the two Mach numbers.

$$U^*_{crit} = \left(\frac{U_i}{\bar{U}_\infty}\right)_{crit} = 4\rho^* \left(\frac{D_l}{D_i}\frac{h}{D_l} + \frac{D_l}{2D_i}\right)^2 \tag{5.2.1}$$

As can be seen in Fig. 5.9 at approximately the predicted critical velocity ratio the experiments give a non-zero vortex strength. This discrepancy is due to the definition of U^*. The velocity ratio, U^*, in Fig. 5.9 is defined as using the free-stream velocity, U_∞. However, to be consistent with different approaching boundary layers the velocity ratio definition should strictly use the area weighted average velocity within the sucked streamtube, $\bar{U}_\infty$. This is what is inherently assumed when estimating the critical velocity ratio using Eq. 5.2.1. Therefore since in the experiments there was a relatively large approaching boundary layer ($\delta^*/D_l = 0.11$) the critical velocity ratio appears to be too high. It will be shown below that with a thinner approaching boundary layer, in which the velocity profile is near uniform in the sucked streamtube, the predicted critical velocity ratio matches the measured blowaway velocity ratio.

As introduced above, an extensive total pressure survey was conducted at the nominal aerodynamic interface plane in conjunction with the PIV dataset. The corresponding total pressure contour plots for the majority of PIV configurations (see Appendix D) at an $h/D_l = 0.25$ and $\delta^*/D_l = 0.11$ is shown in Fig. 5.6 and 5.10. For all configurations illustrated in Fig. 5.10 a single region of relatively high local loss is observed immediately adjacent to the duct surface at the 180° location indicating that induced separation occurs for all cases. As discussed in §4.2, the DC_{60} parameter is used to quantify the level of in-duct flow non-uniformity. The DC_{60} trend with velocity ratio, U^*, is shown in Fig. 5.11 for the datum height of 0.25 (h/D_l). The same characteristic trend is captured with velocity ratio in comparison to the vortex strength variation; high velocity ratios are associated with a relatively low distortion value and as the

[†]Eq. 5.2.1 was derived assuming a uniform velocity profile with a circular, axi-symmetric sucked streamtube at far-field upstream of the intake. ρ^* is the density ratio equal to ρ_∞/ρ_i and can be calculated from the isentropic flow relationship for a given intake Mach number, M_i

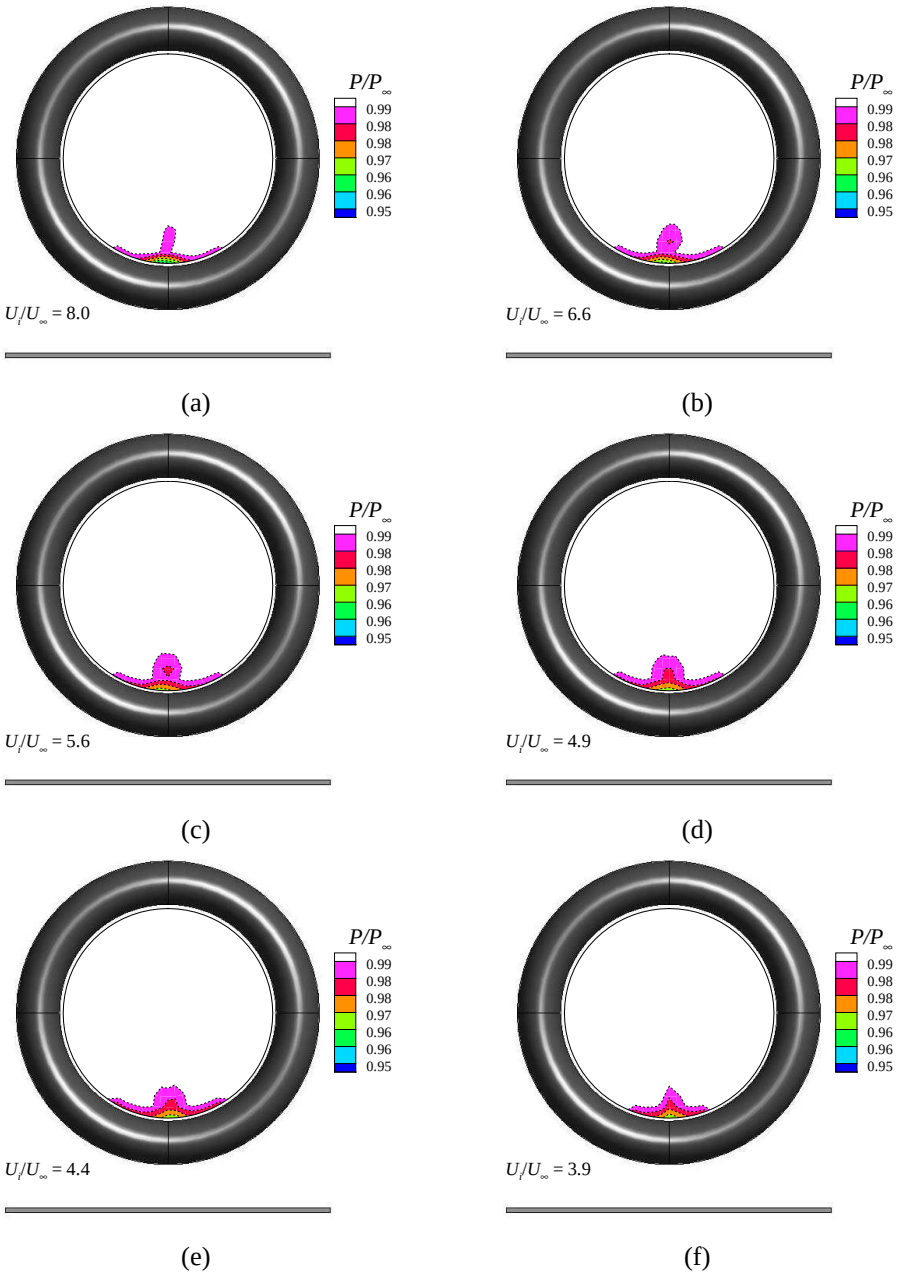

Figure 5.10: Effect of increasing headwind speed in the total pressure contours at the fan face for an $h/D_l = 0.25$, $M_i = 0.58$ and $\delta^*/D_l = 0.11$)

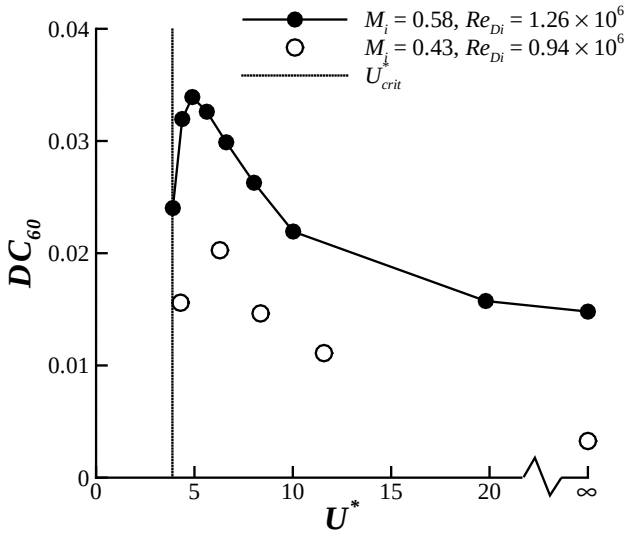

Figure 5.11: Fan face distortion, DC_{60}, against velocity ratio, U^*, for two intake Mach/Reynolds number combinations (δ^*/D_l = 0.11).

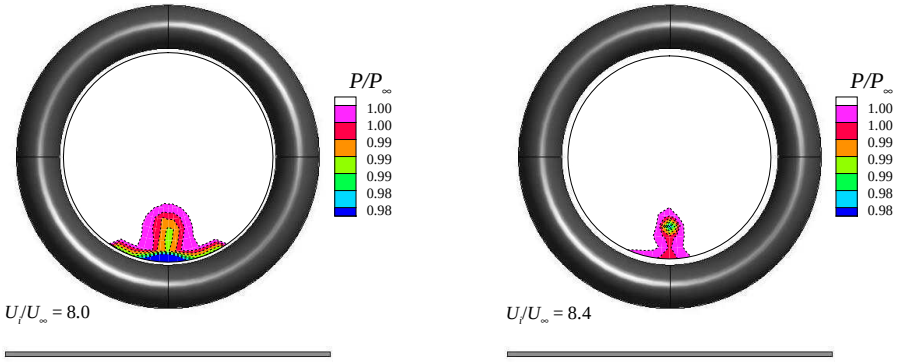

(a) M_i = 0.58, Re_{D_i} = 1.26 × 10^6 (b) M_i = 0.43, Re_{D_i} = 0.94 × 10^6

Figure 5.12: Effect of intake velocity on the in duct total pressure patterns (h/D_l = 0.25, δ^*/D_l = 0.11). NOTE: The scale has changed relative to the plots presented in Fig. 5.10.

velocity ratio reduces the DC_{60} monotonically increases to a local maximum before reducing. The velocity ratio at which the maximum distortion occurs, U^*_{max} is approximately the same as for the PIV vortex circulation measurements and is equal to 4.9 (U^*). This clearly demonstrates that the same characteristic features are observed at the PIV plane in comparison to that inside the intake duct.

However as was seen under quiescent conditions there is a sensitivity in both the ingestion location and the DC_{60} with intake velocity, U_i. Fig. 5.11 shows that when the intake Mach number and Reynolds number is reduced from 0.58 to 0.43 and from 1.26 to 0.94×10^6 respectively, there is approximately a 40% reduction in the DC_{60} across all investigated velocity ratios. As explained in §4.2.2, this reduction is coupled with the ingestion location moving away from the intake surface, towards the duct centreline (Fig. 5.12). As a consequence no vortex induced separation is experienced and therefore the DC_{60} is lower. As will be discussed in §8 Zantopp[71] has demonstrated, via CFD simulations, that this vortex induced separation is a Reynolds number dependant feature and does not occur for a full-scale simulation. It is expected that the distortion present at the lower Reynolds number of 0.94×10^6 is directly related to the loss associated with the vortex core. In contrast, at the higher Reynolds number of 1.26 $\times 10^6$, the loss is associated with the vortex and the consequent induced separation.

5.2.2 Ground Clearance

The influence of non-dimensional height on the vortex strength and fan face distortion is shown in Fig. 5.13. Although the basic vortex strength and DC_{60} trend with velocity ratio remains the same for different non-dimensional heights, there is some sensitivity to h/D_l. For a higher ground clearance of 0.4, the peak vortex strength has decreased and there is an increase in the associated U^*_{max}. For intermediate values of U_i/U_∞ the vortex strength is greater when the intake is further from the ground until under quiescent conditions ($U_i/U_\infty = \infty$) when it again reaches a relatively lower value. Similar trends are also observed for DC_{60} as a function of U_i/U_∞ and h/D_l (Fig. 5.13b).

The increase in peak vortex strength and the reduction in the corresponding velocity ratio for the lower h/D_l are expected trends. Due to the lower ground clearance there will be a greater interaction of the sucked streamtube with the ground plane, enabling a vortex to form at lower velocity ratios (i.e. higher headwind velocities). With vortex formation being possible at higher headwind speeds, the greater levels of approaching boundary layer vorticity inherent at these larger wind speeds leads to a higher peak vortex strength as the velocity ratio further reduces. However, for intermediate velocity ratios the underlying mechanism for the observed sensitivity with ground clearance is unclear. The flowfield will be affected by a number of factors such as the ground induced intake flow, the primary sources of vorticity and the interaction between the ground plane and the sucked streamtube shape. Within this transitionary region, the topology changes from being dominated by flow from underneath and behind the intake to a flowfield principally controlled by the approaching upstream flow. The overall balance between these aspects results in a stronger vortex system for a larger ground

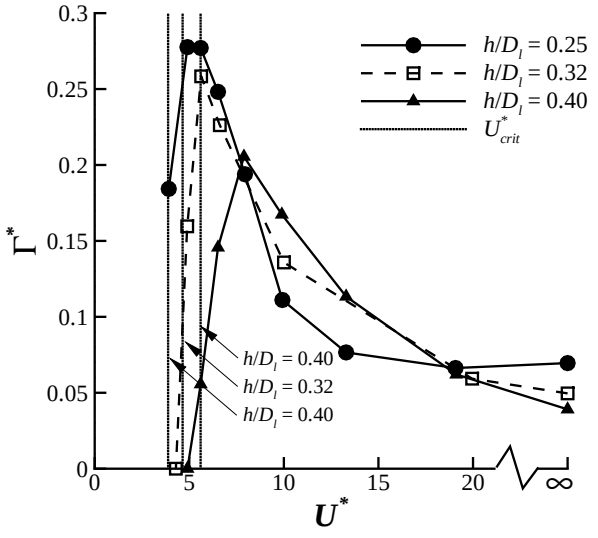

(a)

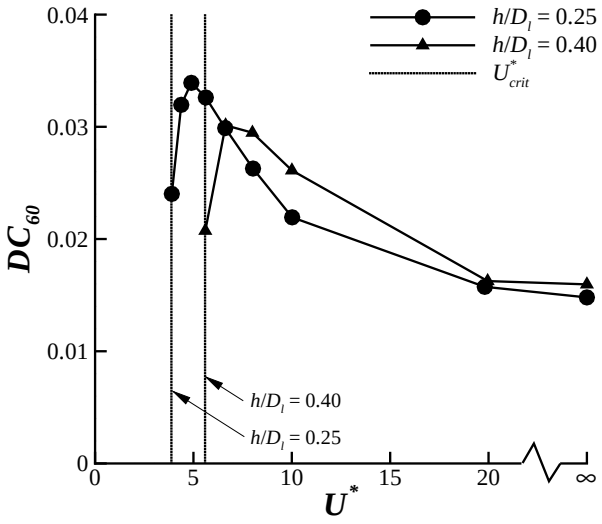

(b)

Figure 5.13: Effect of ground clearance on (a) the average non-dimensional vortex strength, Γ^*, and (b) the distortion coefficient, DC_{60} for $M_i = 0.58$, $\delta^*/D_l = 0.11$

clearance at these intermediate velocity ratios. This particular aspect will be discussed in further detail in §6.

As can be seen in Fig. 5.13a the vortex blowaway condition (U^*_{crit}) is reached for the intermediate ($h/D_l = 0.32$) and largest ground clearance ($h/D_l = 0.40$) investigated. For an approaching boundary layer of $\delta^*/D_l = 0.11$, the critical velocity ratio, U^*_{crit}, was found to be 4.29 and 4.90 respectively. This compares to 4.65 and 5.59 using Eq. 5.2.1. Hence the blowaway condition has been over predicted for both height-to-diameter ratios, and as explained above, this is a direct result of the freestream velocity being used in the velocity ratio definition, rather than the area weighted average velocity in the sucked streamtube, $\bar{U}_\infty$. This will be discussed further in the following section.

5.2.3 Approaching Boundary Layer

Another important aspect is the effect of the approaching boundary layer on vortex characteristics and formation mechanism. In practice, the full-scale intake is immersed in the near wall region of a thick atmospheric boundary layer, which is at least an order of magnitude larger than the intake dimension. It is anticipated that the vortex formation is affected by both the total ingested vorticity and vorticity distribution within the sucked streamtube. For the current wind tunnel experiments a scaled atmospheric boundary layer could not be replicated, so three different boundary layer thicknesses ($\delta^*/D_l = 0.11$, 0.07 and 0.03) were used to establish the sensitivity of the flow-field to this parameter. The boundary layer profiles and characteristics, for all investigated approaching boundary layer configurations across all tunnel speeds, are documented in Appendix C.1.

The effect of the approaching boundary layer thickness on the vortex strength is illustrated in Fig. 5.14 for both height-to-diameter ratios (h/D_l) of 0.25 and 0.4. In general, a reduction in δ^*/D_l from 0.11 to 0.07 has no notable effect on the vortex strength for both non-dimensional heights (Fig. 5.14). However, with a further reduction in the approaching boundary layer thickness to 0.03 (δ^*/D_l) reveals some sensitivity. Although there is no notable change in the peak vortex strength for $h/D_l = 0.25$, there is an alteration in the velocity ratio at which the peak occurs, U^*_{max}, which has increased from 4.9 to 5.7 (Fig. 5.14a). This subtle change is much clearer at the higher non-dimensional height of 0.4 where there is a notable change in the shape of the trend with velocity ratio in which U^*_{max} has increased from 8 to 10.1 and with a modest reduction in the corresponding peak vortex strength.

The increase in U^*_{max} is due to an alteration in the capture streamtube area for a given velocity ratio between the two boundary layer profiles. Since the velocity ratio, U^*, in Fig. 5.14 is defined using the free-stream velocity, a change in the boundary layer thickness results in no change in U^*. However, as explained above, the velocity ratio strictly should use the area weighted average velocity ratio within the sucked streamtube, since U^* is a measure of the contraction of the capture streamtube. With a thinner

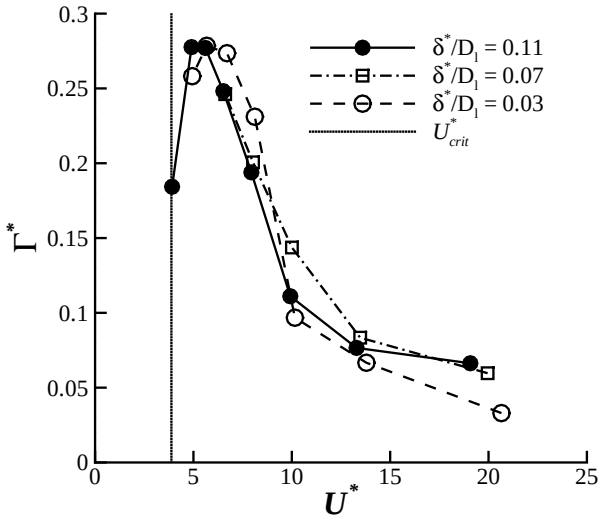

(a) $h/D_l = 0.25$

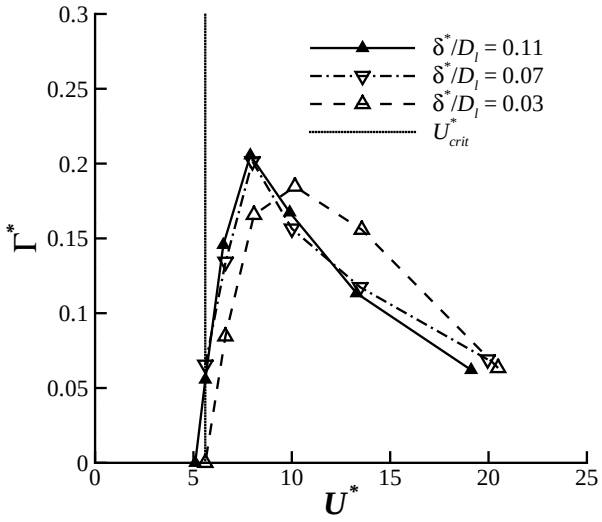

(b) $h/D_l = 0.40$

Figure 5.14: Effect of approaching boundary layer thickness on the average non-dimensional vortex strength, ($M_i = 0.58$)

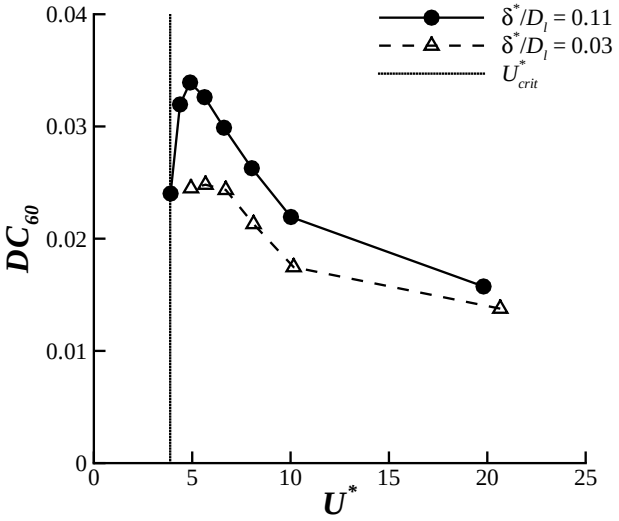

(a) $h/D_l = 0.25$

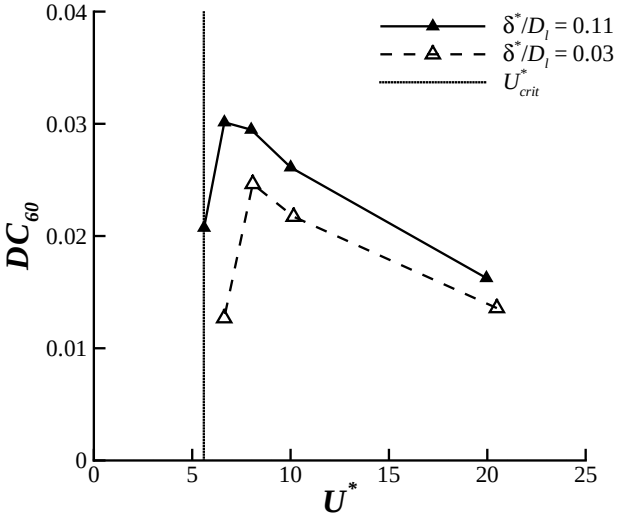

(b) $h/D_l = 0.40$

Figure 5.15: Effect of approaching boundary layer thickness on the in-duct distortion, DC_{60} ($M_i = 0.58$)

approaching boundary layer, the average velocity of the ingested air will be higher in comparison to a higher δ^*/D_l configuration. Hence the velocity ratio based on the average velocity in the sucked streamtube will therefore be larger. This is therefore why the data for $\delta^*/D_l = 0.03$ is shifted to higher velocity ratios in Fig. 5.14a and b. This will be further clarified in §8.2.4.

However most significantly, with a more uniform velocity profile in the sucked streamtube for the $\delta^*/D_l = 0.03$ case the velocity ratio at which the vortex is blown away now matches the predicted velocity ratio given by Eq. 5.2.1. As explained above, Eq. 5.2.1 assumes a uniform velocity profile within a circular axi-symmetric sucked streamtube, this is therefore the reason why both the experiment and predicted values are now in agreement. This is a significant finding and shows that the vortex blowaway condition matches when the capture streamtube lifts off the ground plane. This is very useful from a modelling point of view and will provide the basis for the theoretical model presented in §8.2.

In terms of the comparative insensitivity of the vortex strength to the approaching boundary layer, the relative magnitude is dominated by the source of vorticity for the vortex. For the head-wind formation mechanism this source of vorticity primarily comes from the approaching ground boundary layer. Within a turbulent boundary layer most of the vorticity lies close to the surface. The approaching boundary layers were measured using pitot rakes and, for all the boundary layer profiles tested, at least 90% of the integrated vorticity[‡] was positioned between the PIV measurement plane and the ground (see Appendix C.1). Furthermore it was found that, for a given tunnel velocity, the total vorticity within the different approaching boundary layers were largely the same. Consequently the boundary layer thickness is found to have no significant influence on the vortex strength measured at the PIV plane.

The corresponding plots for the DC_{60} are shown in Fig. 5.15. The DC_{60} trend is observed to be considerably more sensitive to changes in the approaching boundary. At a ground clearance of 0.25 (h/D_l) the peak distortion coefficient, $DC_{60,max}$, has reduced by 26% from 0.034 to 0.025, with the velocity ratio at maximum distortion, U^*_{max}, increasing from 4.9 to 5.7 (Fig. 5.15a). Similar observations are also seen for the higher ground clearance of $h/D_l = 0.4$ (Fig. 5.15b). The change in the velocity ratio of peak distortion is the same as that for the vortex strength and is due to a change in the sucked streamtube size for a given U^*. As explained above, this is because the average velocity within the capture streamtube will increase for the thinner approaching boundary layer. The decrease in peak DC_{60} for the thinner approaching boundary layer ($\delta^*/D_l = 0.03$) is associated with the lower integrated total pressure loss within this boundary layer for a given freestream velocity and intake streamtube. A further discussion on the effect of the approaching ground boundary layer on the vortex strength and fan face distortion will be given in §8.2.4.3, where the theoretical model is used to illustrate the aforementioned points discussed above.

[‡]This is calculated by assuming that the only contributor to the vorticity within the boundary layer is the wall normal velocity gradient term, $\partial v/\partial z$

5.3 Vortex Formation Regions

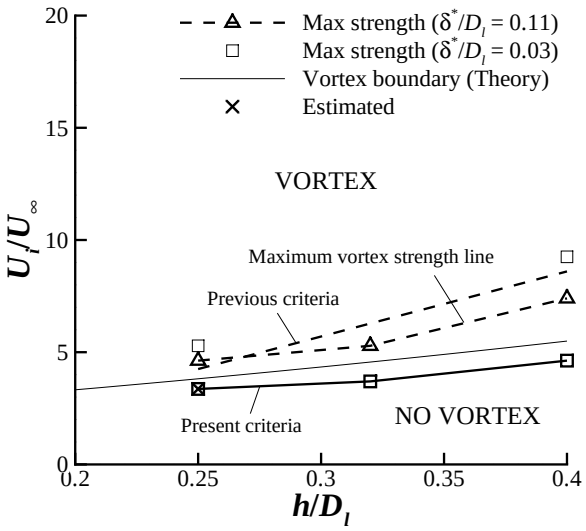

(a)

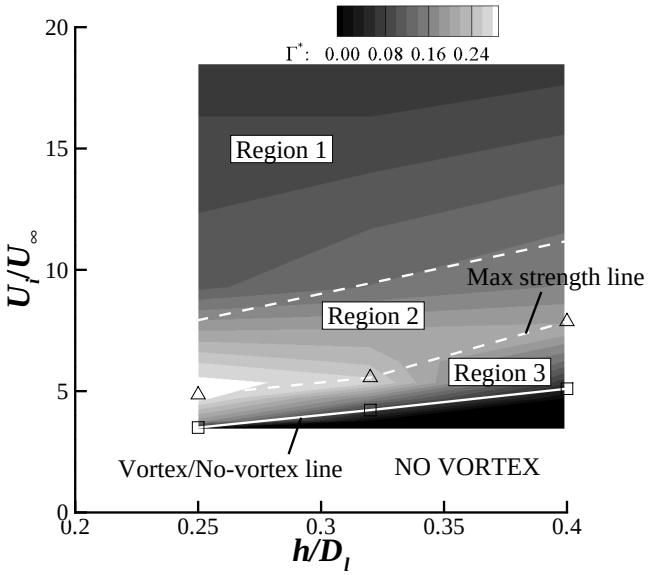

(b)

Figure 5.16: Headwind vortex formation/strength map (δ^*/D_l = 0.11, M_i = 0.58)

Based on the quantitative experimental observations a new vortex/no-vortex map can be constructed, as shown in Fig. 5.16a. This map applies for the δ^*/D_l = 0.11 approaching boundary layer and three data points are used to determine the vortex/no-vortex line. The data point at the lowest non-dimensional height of 0.25 (h/D_l) is extrapolated using the trend in Fig. 5.9 since the critical velocity ratio could not be established due to tunnel limitations. In contrast to previous maps, this dataset con-

centrates in a non-dimensional height range that is of most interest to conventional wing mounted engine installations. Relative to earlier research[10,37], it has been found that a vortex can form at lower than previously reported velocity ratios and a new criterion had been established. The revised boundary (Fig. 5.16) is also in agreement with the limited experimental data of Nakayama and Jones[37]. In addition to the vortex formation boundary, a locus of maximum vortex strength has been established which indicates for a given non-dimensional height what velocity ratio produces the strongest vortex and hence distortion at the fan face. Interestingly, the previous vortex formation criterion[10,37] is in a similar position to the currently measured maximum vortex strength line (Fig. 5.16a). This could be explained by the majority of previous work being based on visualizations which would tend to identify the cessation of a maximum strength vortex rather than a formation boundary.

In addition to the boundary determined from experiments and previous research, the predicted boundary at which the sucked streamtube lifts off the ground plane using Eq. 5.2.1 is also included. As stated above Eq. 5.2.1 gives the critical velocity ratio based on the area weighted average velocity within the sucked streamtube. Since the velocity ratio used in Fig. 5.16a is based on the free-stream velocity (U_∞), the theoretical boundary plotted in Fig. 5.16 is therefore applicable for a boundary layer that is infinitely small (i.e. $\delta^*/D_l = 0$). If one knows the state of the approaching boundary layer and the sucked streamtube characteristics at far-field upstream of the intake, then Eq. 5.2.1 can be used to determine the free-stream velocity, U_∞, required to blowaway the vortex, for any approaching boundary layer configuration.

Using the vortex characteristics averaged over 300 snapshots, contours of average non-dimensional vortex strength have been added to Fig. 5.16a as shown in Fig. 5.16b. This is a significant development relative to previous criteria which simply proposed a vortex formation criterion without any measure of the vortex strength[10,37]. The map applies for the $\delta^*/D_l = 0.11$ approaching boundary layer, although the general trend is expected to be the same for any approaching boundary layer configuration. Within this contour map there are three important vortex formation regions. The first, indicated by *Region 1* (Fig. 5.16b), shows that for a given U^* an increase in h/D_l results in a stronger vortex, although the gradient is mild. This can be explained by the lines of constant vortex strength in this region being approximately parallel to the formation boundary. This suggests that the strength of the vortex is set by its relative distance from U^*_{crit} at a given non-dimensional height. Stated in another way, the vortex strength depends on the level of interaction the sucked streamtube has with the ground plane. Hence if one was to compare two intakes at two different non-dimensional heights, the vortex strength will be the same for both configurations if the relative interaction of the capture streamtube with the ground is the same (i.e. if the ratio U^*/U^*_{crit} is the same for both cases). The second region, *Region 2*, is a transitional region which is just above the maximum distortion line and below the dashed line (Fig. 5.16b). In this region, for a given U^*, the higher ground clearance may no longer result in a stronger vortex, as the rate of increase in vortex strength with U^* reduces. *Region 3* is defined as being the region below the locus of maximum strength vortices and above the vortex/no-vortex

boundary. In this region the vortex can still be relatively strong in comparison to high velocity ratios, but its strength rapidly decreases with further reductions in velocity ratio.

5.4 Aerodynamic Self-Similarity

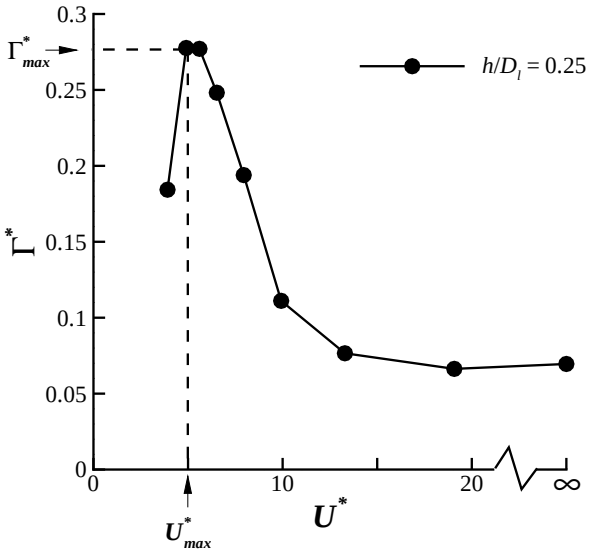

Figure 5.17: Example non-dimensionalization of the characteristics vortex strength curves to obtain the self-similarity property

When all the distributions of non-dimensional vortex strength (Γ^*) and fan face distortion (DC_{60}) against velocity ratio (Fig. 5.13a and 5.14 for the circulation and Fig. 5.13b and 5.15 for the DC_{60}) are normalised by the appropriate local maximum values and the corresponding velocity ratio, U^*_{max}, (Fig. 5.17) the profiles exhibit a self-similar trend (Fig. 5.18). This data reduction is based on a broad range of configurations including three non-dimensional heights and three boundary layer thicknesses. Both the distortion and non-dimensional vortex strength exhibit a power law distribution with reducing velocity ratio until the local peak is reached. Further reductions in velocity ratio, where the vortex strength reduces, can be represented using a linear approximation. The intersection of this linear line with the *x*-axis then gives the percentage reduction from the maximum velocity ratio, required to blow-away the vortex. Both the fan face distortion and PIV vortex strength measurements give the same blow-away velocity ratio which is approximately 65% of the velocity ratio at which the maximum occurs (Eq. 5.4.1). This finding will be used in the empirical model presented in §8.1.

$$\frac{U^*_{crit}}{U^*_{max}} = 0.65 \tag{5.4.1}$$

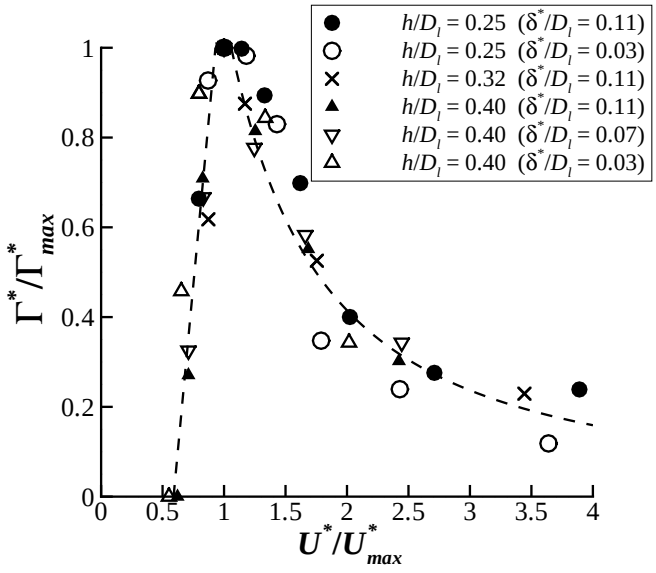

(a)

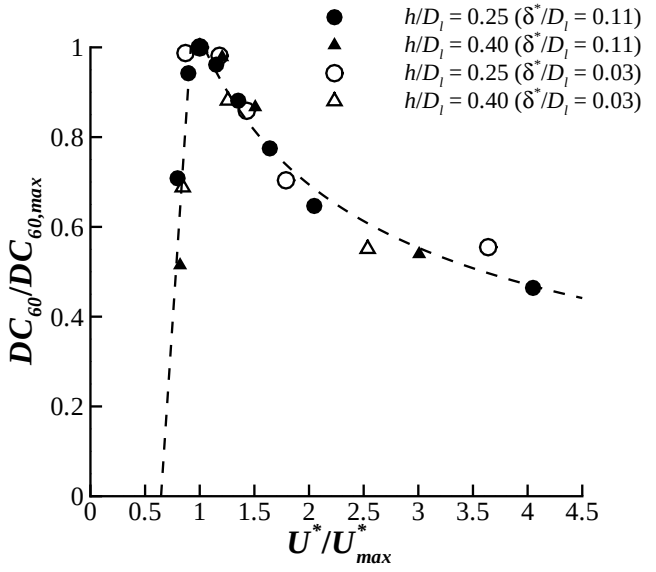

(b)

Figure 5.18: Self-similar profiles of (a) non-dimensional vortex strength, Γ^* and (b) in-duct distortion, DC_{60}

The self-similarity property associated with characteristic vortex strength and distortion trends with velocity ratio is useful from a modelling point of view. With knowledge of normalization parameters (Γ^*_{max}, $DC_{60,max}$ and U^*_{max}), for a given intake ground clearance (h/D_l), the vortex strength and distortion can be determined for any velocity ratio in question. As will be shown in §8.1 an empirical vortex strength prediction tool is developed which is centred around the aerodynamic self-similarity property demonstrated above. U^*_{max} is determined using Eq. 5.4.1 and 5.2.1 and an additional correlation is used to establish the corresponding peak vortex strength, Γ^*_{max}. Since it has been demonstrated above that the ground vortex agrees with known vortex models and that the vortex core size, r_c, is reasonably constant across all investigated configurations, the vortex only velocity field can therefore be determined. As will be discussed in §8.1 this tool could be used as part of a boundary condition code for CFD analysis of vortex induced fan vibration analysis.

5.5 Summary

A quantitative investigation of the headwind ground vortex mechanism has been conducted using a generic $1/30^{th}$ scale intake model at a representative intake Mach number of 0.58. Stereoscopic PIV measurements have been taken external to the intake along with fan face total pressure measurements for supporting analysis. The influence of velocity ratio (at constant intake velocity), height-to-diameter ratio, intake Mach number and approaching boundary layer thickness have been investigated. The experiments have enabled a more sophisticated understanding of the ground vortex characteristics and provide an improvement on current design rules. The effects of the important non-dimensional parameters investigated are summarized below.

1. A range of flow modes have been captured using the PIV technique that fundamentally depend on the velocity ratio and vorticity source.

2. At high velocity ratios the vortex strength and corresponding DC_{60} is low, as the velocity ratio is reduced the vortex strength and distortion increase and eventually reach a local maximum before reducing to zero at the vortex blow-away condition. This characteristic behaviour was observed for all non-dimensional heights and approaching boundary layer configurations and is primarily due to the variation of the integrated approaching vorticity within the sucked streamtube. This fundamentally is set by the balance between the increase in the approaching boundary layer vorticity as the headwind increases and the corresponding reduction in the sucked streamtube size as the velocity ratio reduces.

3. The velocity ratio at which the vortex no longer forms matches the predicted velocity ratio at which the sucked streamtube no longer has ground plane contact.

4. All characteristic vortex strength curves were found exhibit a self-similar trend when non-dimensionalised by the local peak vortex strength and corresponding

velocity ratio. This property is also demonstrated for the intake total pressure flow distortion parameter.

5. The vortex circulation scales with the intake velocity, U_i, for a given velocity ratio, non-dimensional height, and approaching boundary layer.

6. Reducing ground clearance was found to increase the peak vortex strength and to reduce the velocity ratio at which the maximum occurred.

7. For intermediate velocity ratios ($7 > U^* > 20$) the vortex strength is greater when the intake is further from the ground.

8. A reduction in the approaching boundary layer thickness from $\delta_*/D_l = 0.11$ to 0.03 leads to a 26% reduction in peak DC_{60}. This decrease is due to a reduction in integrated loss within the sucked streamtube. The peak vortex strength was largely uneffected as the integrated vorticity within the approaching boundary layer is dominated by the headwind velocity.

9. A new ground vortex map has been constructed which quantifies non-dimensional vortex strength as a function of ground clearance and velocity ratio. The minimum velocity ratio required for vortex formation is lower than previously reported and the map highlights regions of strong ground vortex magnitude.

CHAPTER 6

Take-off Simulations

An investigation into the effect of a moving ground plane on the formation of ground vortices with and without ambient wind has been completed. The experiments are aimed at further understanding the fundamental mechanisms in headwind conditions, whilst also understanding the formation characteristics during aircraft take-off. The experiments were conducted in the Cranfield University 8' $\times$ 6' low speed wind tunnel, which is equipped with a rolling ground plane to simulate the effect of a forward moving aircraft over a stationary surface. Quantitative measurements have been taken of the vortex strength using Stereoscopic Particle Image Velocimetry and fan face distortion from total pressure measurements inside the intake duct. This is the first known study to quantify the effect of a moving ground plane on the vortex formation and characteristics.

Due to the implementation of the rolling road, a different optical set-up was required for this series of experiments. This chapter therefore begins by giving a short description of the tunnel configuration, measurement set-up and methods. Following this a detailed description of the flow field is given using the PIV results. Subsequently, detailed analysis of the vortex strength and distortion measurements is presented.

6.1 Experiment Method

The tunnel configuration for the rolling road experiments is shown in Fig. 6.1. The moving ground plane is 2.75 *m* long and 1.2 *m* wide. The intake is located in the centre of the tunnel, approximately 1 *m* from the leading edge of the moving belt rig. Due to the implementation of the rolling road, the cameras have to be placed inside of the working section for this dataset (Fig. 6.1). This differs from all other experiments where the cameras were located underneath the tunnel floor (Fig. 3.2). However, the camera orientation relative to the laser light sheet, the laser position and height above the ground plane all remained the same as for the headwind (§5) and crosswind (§7) configurations. The measurement area is also approximately the same at 110×80 *mm* size leading to a 0.84 *mm* spatial resolution.

With regards to placing the camera inside the tunnel there are two major consequences.

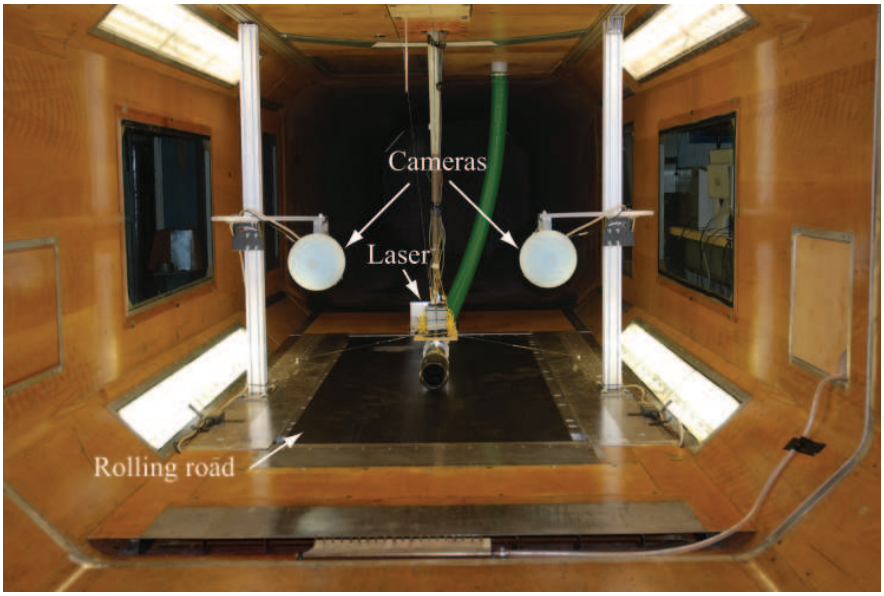

Figure 6.1: Tunnel layout for rolling road experiments

The first is the blockage within the tunnel that it introduces due to the support structure and camera mounts. This increases from approximately 0.003% without to 9.1% with the cameras. However this was principally accounted for by measuring the tunnel velocity in the working section using a pitot static tube, as was done for all experiments. The second limitation is that the camera field of view to the measurement plane is obstructed by the intake. This therefore limits the area with which velocity measurements can be taken. Consequently, the number of configurations that can be tested is restricted, as at high headwind speeds the vortex foot moves directly underneath the intake highlight plane and therefore out of the measurement domain.

6.1.1 Test Configurations

Measurements were predominately taken at the datum height of $h/D_l = 0.25$. With the intake placed at this ground clearance enables a greater range of headwind speeds that can be investigated. Limited measurements were also taken at a h/D_l of 0.4. All experiments were performed at an intake Mach number,M_i, of 0.58. The velocity of the rolling road is denoted by U_g and can be varied from 5 to 40 ms^{-1}. The difference between the free-stream velocity, U_∞, and the ground speed, U_g, is given by ΔU (Eq. 6.1.1). The velocity ratio, U^*, is defined as usual and is equal to the ratio of the intake velocity, U_i, to U_∞.

$$\Delta U = U_\infty - U_g \tag{6.1.1}$$

Two types of experiments have been performed for the rolling ground plane tests which relate to different ΔU velocities. For the first experiment the tunnel and the ground ve-

locities were synchronized (i.e. $\Delta U = 0\ ms^{-1}$)(Fig. 6.2a). To simulate a take-off the ground and tunnel speeds are increased together from zero in steps of 5 ms^{-1} whilst keeping ΔU constant and equal to approximately zero (Table 6.1). This experiment is of particular interest because it removes the approaching vorticity source, which has been known to feed ground vortices[10]. This experiment is akin to an aircraft take-off in quiescent conditions. It should be noted that during an actual take-off the aircraft is accelerating from a static position at the start of the runway. In the experiments it was impossible to simulate aircraft acceleration. Measurements were therefore taken at a number of discrete points during the acceleration phase. During data acquisition the ground and tunnel speeds are kept constant. Since the aim of this experiment was to simulate an aircraft taking off under no ambient wind conditions there should be no boundary layer growth on the rolling ground plane. Any boundary layer growth upstream of the moving belt was removed by utilizing the primary and secondary suction methods (Fig. 6.1). A discussion of the expected boundary layer state for the rolling road case is given in the subsequent section.

Config.	U_∞ (ms^{-1})	U_g (ms^{-1})	U^*
I	0	0	∞
II	9.9	10	19.5
III	15.2	15	12.7
IV	20.3	20	9.5
V	25.7	25	7.5
VI	30.9	30	6.2

Table 6.1: Summary of configurations investigated for the synchronized road and tunnel velocity experiments ($\Delta U \approx 0\ ms^{-1}$)

The second type of experiment performed was where the tunnel (U_∞) and ground (U_g) speeds were unsynchronized (i.e. $\Delta U \neq 0$) (Fig. 6.2b). This configuration simulates an aircraft take-off with an ambient headwind present. Two unsynchronized configurations were investigated with ΔU equal to approximately 10 and 20 ms^{-1} respectively. This configuration differs from the synchronized experiments as there is an approaching boundary layer developing on the ground upstream of the intake (Fig. 6.2b). But it also differs from the static ground experiments (Fig. 6.2c, Chapter 5) as the wall shear stress and hence approaching boundary layer vorticity is smaller. During experiments, the ground velocity is increased from zero and measurements were taken at selected rolling road velocities. The configurations for the unsynchronized experiments are summarized in Table 6.2. For this case the aim is for the approaching boundary layer to be most representative of in-service engines, therefore no boundary layer suction was implemented upstream of the intake. The thickness of the boundary layer in these conditions is expected to be similar to that for the same suction configuration as for the static ground case (i.e. $\delta^*/D_l = 0.11$). However no measurements of the boundary layer have been taken for this type of experiment.

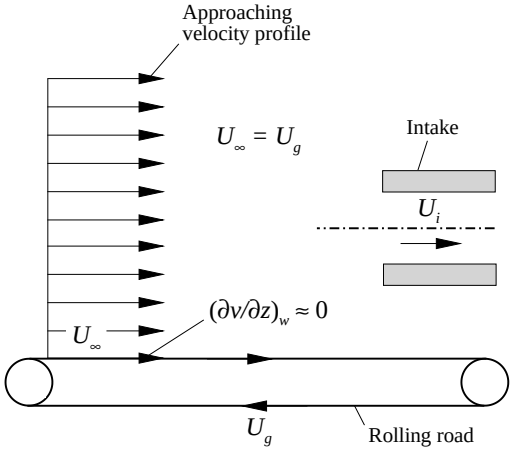

(a) Moving ground plane: Synchronized (Configs. I-VI)

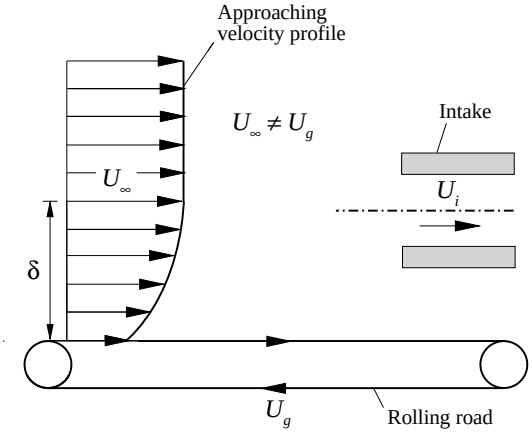

(b) Moving ground plane: Unsynchronized (Configs. VIII-XII & XIV-XVII)

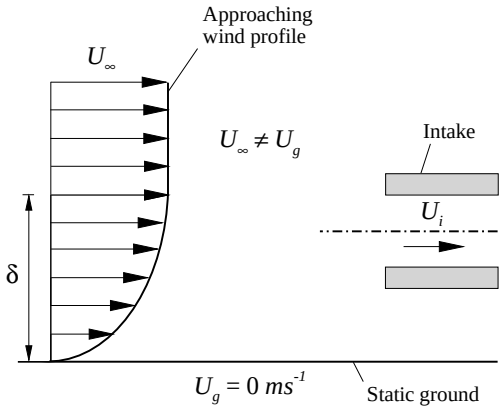

(c) Static ground plane (Configs. VII & XIII)

Figure 6.2: Schematic of static ground and rolling road synchronized (no ambient wind) and unsynchronized (ambient wind) experiments

Config.	U_∞ (ms^{-1})	U_g (ms^{-1})	U^*
	$\Delta U \approx 10\ ms^{-1}$		
VII	9.8	0	19.8
VIII	15.6	5	12.4
IX	20.8	10	9.3
X	26.1	15	7.4
XI	31.3	20	6.2
XII	36.6	25	5.3
	$\Delta U \approx 20\ ms^{-1}$		
XIII	19.1	0	10.0
XIV	26.1	5	7.4
XV	31.2	10	6.2
XVI	36.6	15	5.3
XVII	41.9	20	4.6

Table 6.2: Summary of configurations investigated for the rolling road experiments under headwind conditions

6.1.2 Experiment Uncertainties

The uncertainty analysis discussed in Chapter 3.7 and presented in detail in Appendix G still applies for this experiment dataset, however due to the different nature of the current tests, additional uncertainties apply. The rolling road velocity was measured using a optical sensor on the roller of the rolling road. The sensor measures the roller RPM and is converted to a velocity. The RPM is set by varying the voltage supplied to the motor and velocity was set to within 0.05 ms^{-1}. Belt suction was implemented throughout testing to ensure that the road did not lift or move laterally during tests. For the synchronized wind and road configurations although ideally there should be no boundary layer growth on the rolling ground plane there is expected to be a thin boundary layer present. Dimitriou[12] measured the boundary layer over the moving belt rig in the Cranfield University 8' $\times$ 6' wind tunnel with the tunnel and ground speeds synchronized at 35 ms^{-1} (i.e. $\Delta U = 0\ ms^{-1}$). The measurements revealed that the boundary layer thickness, δ, was approximately 2 mm within the central portion of the road at the approximate intake highlight plane location. Although inevitably there was some boundary layer growth on the rolling road, the wall normal velocity gradient is expected to be very low. This is the most important factor with regards to the strength of the vortex under headwind conditions.

6.2 Synchronized Wind and Road Velocity Experiments

In this section the results are presented for the synchronized wind and ground velocity experiments. As a reference, measurements are first compared with the results presented in Chapters 4 and 5 on the ground vortex aerodynamics under quiescent and headwind cases for a static aircraft. First the PIV measurements are discussed, with a description of the flowfield topology. The vortex characteristics at the PIV plane are then discussed which is then followed by analysis of the total pressure survey conducted at the fan face.

6.2.1 PIV Velocity Flowfield Quantification

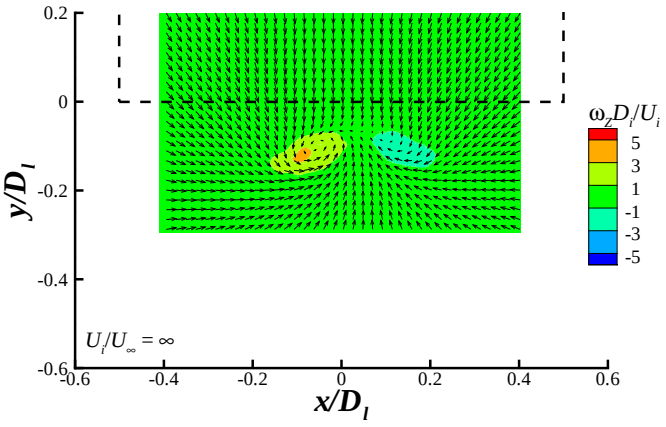

(a) $U_g = 0\ ms^{-1}$, $U_\infty = 0\ ms^{-1}$ (Config. I)

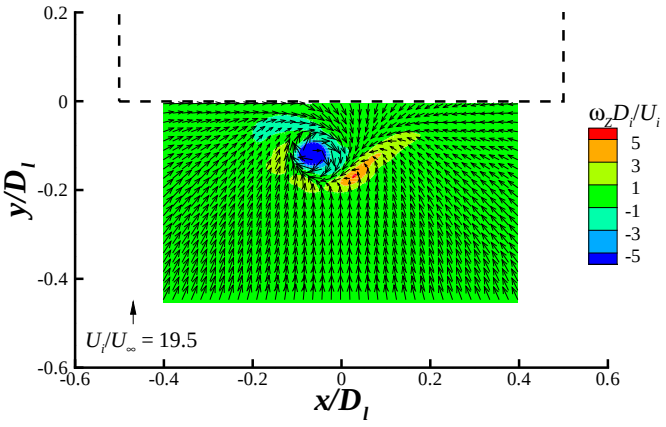

(b) $U_g = 10\ ms^{-1}$, $U_\infty = 9.9\ ms^{-1}$ (Config. II)

Figure 6.3: Time average flowfields of $x - y$ in-plane velocity vectors (only every 3^{rd} vector shown) and vorticity field for (a) static ground ($U_g = 0\ ms^{-1}$) under quiescent conditions ($U_\infty = 0\ ms^{-1}$) (Config. I, Table 6.1) and (b) for a $10\ ms^{-1}$ synchronised wind and ground velocity case (Config. II) ($h/D_l = 0.25$, $M_i = 0.58$)

As a reference, the time average in-plane vector and vorticity field for quiescent conditions (with no moving ground) is shown in Fig. 6.3a and the general features are summarized. Under such conditions two regions of opposite sign vorticity is observed (Fig. 6.3a). This is due to the formation of two counter rotating vortices, with the left vortex rotating anticlockwise. As discussed in §4 the vortices rotate in this sense due to the dominance of the vorticity bound in the flow between the intake and ground which travels in the negative y direction (Fig. 6.3a). For this configuration a dominant vortex exists which has positive vorticity (Fig. 6.3a), although two vortices are often observed.

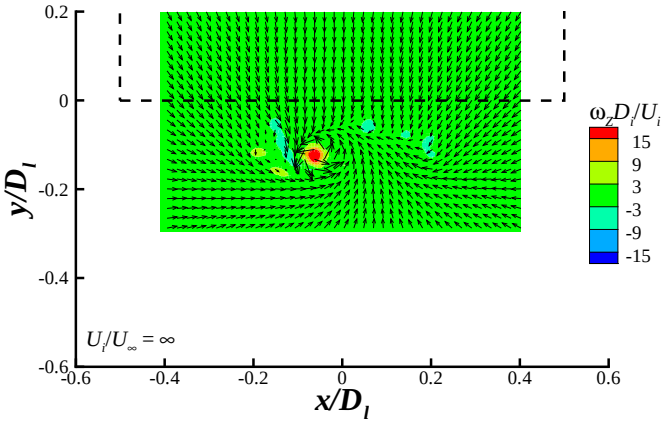

(a) $U_g = 0\ ms^{-1}$, $U_\infty = 0\ ms^{-1}$ (Config. I))

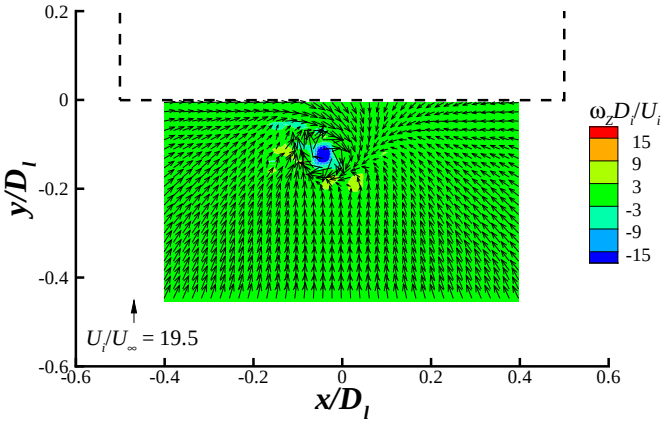

(b) $U_g = 10\ ms^{-1}$, $U_\infty = 9.9\ ms^{-1}$ (Config. II)

Figure 6.4: Example snapshots of vorticity and $x-y$ in-plane velocity vectors (only every 3^{rd} vector shown) with and without a rolling ground plane (Configs. I & II, Table 6.1) ($h/D_l = 0.25$, $M_i = 0.58$)

To simulate forward aircraft speed under no ambient wind conditions the ground and tunnel speeds are increased with the magnitudes the same (Fig. 6.2a). In this situation, there should be little or no boundary layer growth on the moving belt. The time average flowfield for a ground (U_g) and wind speed (U_∞) of 10 ms^{-1} is shown in Fig. 6.3b and is considerably different to quiescent conditions. A single dominant vortex is

observed, which is in a comparable position to the dominant vortex seen in quiescent conditions, but with the rotation in the opposite in direction (Fig. 6.3). This is due to the flowfield now being dominated by the relative headwind approaching flow due to the moving aircraft. For this configuration (U_g = 10 ms^{-1}) only a single vortex is seen for all flowfield snapshots, which is in contrast to quiescent conditions where two counter-rotating vortices were often observed. Given the observations seen in §5.1 a single dominant vortex was anticipated and is expected to be a result of small asymmetries inherent in the tunnel flowfield at low wind speeds (see §C.2). Inspection of the moving ground case average flowfield shows that the vorticity levels are also considerably higher (Fig. 6.3b). This is due to the single dominant vortex for this configuration being steadier in space and magnitude in comparison to the two vortices observed in quiescent conditions where in contrast the vortices were highly unsteady in time and to a lesser extent in space. Example instantaneous images (Fig. 6.4) reveal that when a vortex is present in both cases the vorticity levels are in general the same, which indicates that the strength as not altered significantly.

The time average flowfield for the moving ground case also shows a region of weaker opposite sign vorticity (Fig. 6.3b). This is not due to a second vortex, but rather it is vestigial vorticity associated with the opposite leg of the vortex line. As the advancing flow gets stronger, the contraction ratio of the sucked streamtube gets smaller. In turn the streamline curvature radius ahead of the intake at the PIV plane gets larger (i.e. the streamlines straighten). Consequently the flow has to turn more sharply into the dominant vortex and at a 15 ms^{-1} wind and ground configuration (Config. III) the formation of a second vortex appears sporadically however a presiding vortex still exists (Fig. 6.5a). An increase of just 5 ms^{-1} to 20 ms^{-1} reveals two equal strength contra-rotating vortices (Fig. 6.5b). The two vortices that form for this configuration are considerably steadier in time in comparison to quiescent conditions. This is because the flowfield is dominated by the induced vorticity approaching the intake (see Fig. 4.4). With a further increase in the ground and free-stream speed to 25 ms^{-1} reveals a symmetric flowfield (Fig. 6.5c).

The observations described above is generally what occurs for the static ground configurations with an increasing approaching headwind (as described in §5), however there are a number differing features. Firstly the occurrence of two equal strength contra-rotating vortices does not occur until the headwind is at approximately 40 ms^{-1}. This compares to 20 ms^{-1} for the moving ground plane configurations. Furthermore the vortices are considerably steadier in space in comparison to the static ground experiments for all investigated approaching headwind speeds. The smaller amplitude of vortex wandering ahead of the highlight plane is expected to be due to the following reasons. Since there is little or no approaching boundary layer the level of turbulent fluctuations present will be very small which will contribute to a steadier vortex being observed. In addition the sucked streamtube size will be smaller due to the higher average velocity in the capture streamtube. This will result in the streamlines being compressed together which restricts the movement of the vortex. This is clearly evident in the spatial average flowfield for a ground speed of 25 ms^{-1} (Fig. 6.5c).

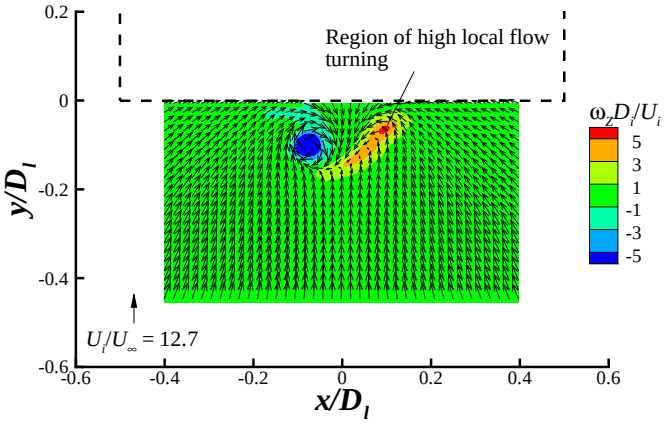

(a) $U_g = 15\ ms^{-1}$, $U_\infty = 15.2\ ms^{-1}$ (Config. III)

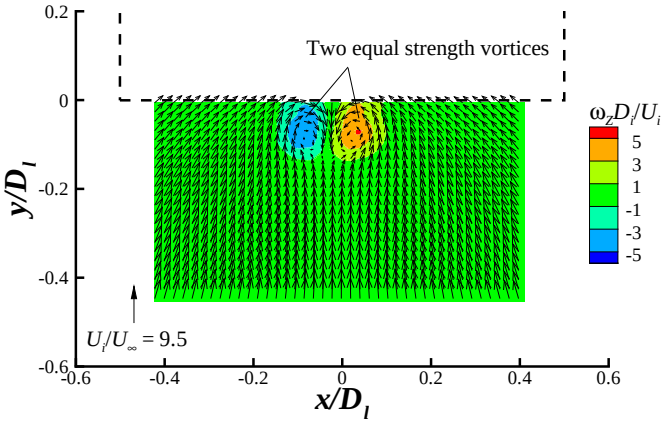

(b) $U_g = 20\ ms^{-1}$, $U_\infty = 20.3\ ms^{-1}$ (Config. IV)

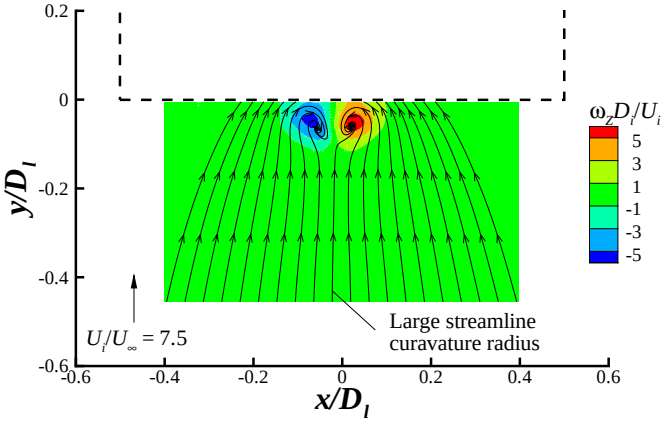

(c) $U_g = 25\ ms^{-1}$, $U_\infty = 25.7\ ms^{-1}$ (Config. V)

Figure 6.5: Time average flow-field for the synchronised wind and road cases ($\Delta U = 0\ ms^{-1}$) with an increasing ground velocity ($h/D_l = 0.25$, $M_i = 0.58$)

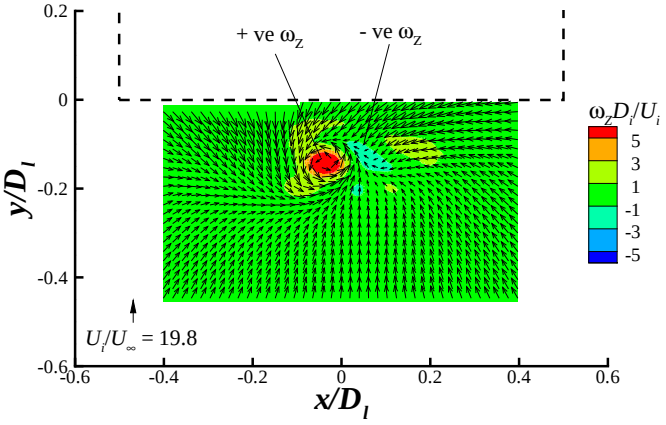

(a) $U_g = 0\ ms^{-1}$, $U_\infty = 9.8\ ms^{-1}$, $U^* = 19.8$ (Config. VII)

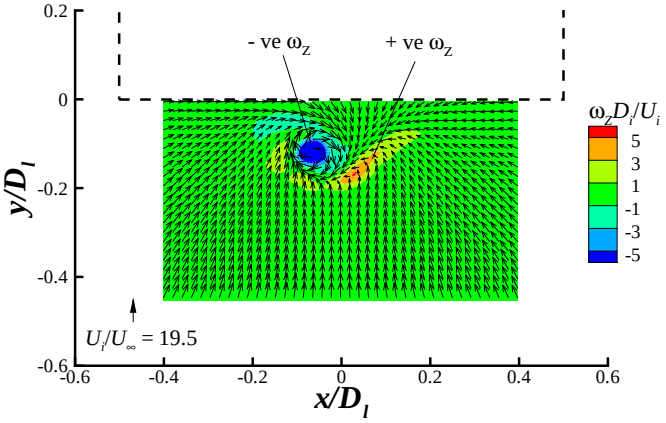

(b) $U_g = 10\ ms^{-1}$, $U_\infty = 9.9\ ms^{-1}$, $U^* = 19.5$ (Config. II)

Figure 6.6: Comparison of the time average flowfields for static ground (Config. VII) and moving ground cases (Config. II) with the same approaching headwind ($h/D_l = 0.25$, $M_i = 0.58$)

It is also of interest to compare the 10 ms^{-1} moving ground, no ambient wind, configuration (Config. II) to the static ground case with the same approaching headwind (Config. VIII). With little or no approaching vorticity this should reveal more on the dominant vorticity source at these low wind speeds. As discussed in Chapter 5.1, for a non-dimensional height of 0.25 (h/D_l) with the velocity ratio, U^*, equal to 19 the dominant vorticity source appears to still be related to the vorticity associated with the flow between the intake and the ground travelling in the negative y-direction. This is evident in Fig. 6.6a where there is a region of negative vorticity to the left of the dominant vortex. With the introduction of a moving ground plane (Fig. 6.6b), the sense of rotation of the primary vortex has changed and now has negative vorticity. The presence of a rolling road affectively increases the average velocity in the sucked streamtube, as the approaching boundary layer is removed, hence the area weighted average velocity ratio for this configuration will be lower. As was discussed in §5, this clearly demonstrates that the rotation switch between nowind and headwind modes is at a velocity ratio of approximately 20. Knowledge of this mode alteration is important, as a change in the flow topology such as this may result in different flow incidences being seen at the fan face, which is important with regards to fan vibration. Furthermore, in this velocity ratio region ($U_i/U_\infty \approx 19$) the flowfield is clearly in a transitional state, and is perhaps why only a single vortex is observed. In terms of the vorticity levels between the two cases no significant difference can be seen (Fig. 6.6) which suggests that the vortex strength has not altered significantly. This is discussed further in the following section.

6.2.1.1 Effect of Synchronized Rolling Road on Vortex Strength

To quantify the effect of the moving ground further the average vortex strength was calculated by individually analyzing the circulation of all identified vortices, over all flowfield snapshots, as described in §3.6 and in more detail in Appendix E. The results are plotted against the velocity ratio, U^*, for all synchronised wind and road cases and are compared to the static ground configurations in Fig. 6.7. The roman numerals in the figure represent the configurations as labelled in Table 6.1.

For low ground speeds (U_g = 0-15 ms^{-1}), with the approaching boundary layer vorticity removed, the vortex strength is almost identical to the corresponding static ground configurations (Fig. 6.7). Since there is almost no approaching boundary layer, this indicates that the dominant vorticity source, for a static ground at intermediate to high velocity ratios, is the induced vorticity. This is vorticity that has been generated by the flowfield induced by the intake suction along the ground. However since the vortex rotation has changed from a zero to a 10 ms^{-1} ground velocity (Fig. 6.6), it is not the vorticity bound in the induced flow travelling in the negative y-direction (as is the case for quiescent conditions), it is the vorticity associated with the flow in the positive y-direction (see Fig. 4.4). As the ground speed increases further, at this non-dimensional height (h/D_l = 0.25), a deviation in the strength from the static road configurations is not seen until the ground speed reaches 20 ms^{-1} (U_i/U_∞ = 9.5). At this headwind speed it is expected that the approaching boundary layer vorticity becomes

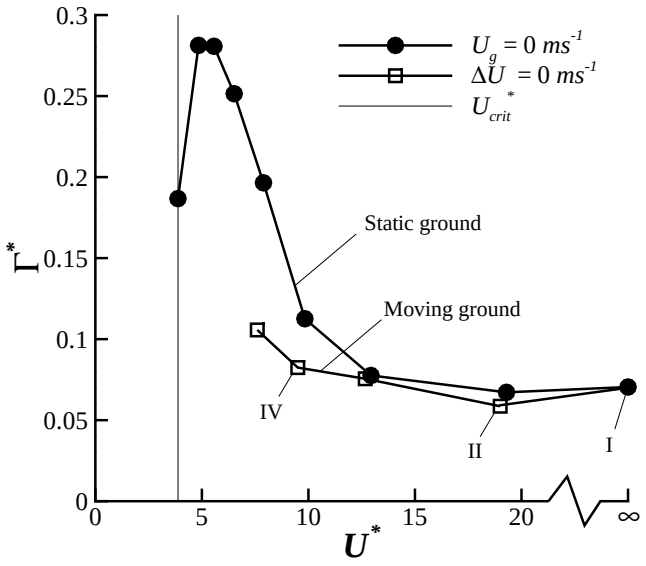

Figure 6.7: Average non-dimensional vortex strength, Γ^* against velocity ratio, U^* for a moving ground with comparison to a static ground (h/D_l = 0.25, M_i = 0.58). Note the roman numerals represent the test configurations in Table 6.1

dominant. With a further increase to 25 ms^{-1} there is approximately a 50% reduction in the strength in comparison to the static ground case at the same approaching wind speed (Fig. 6.7). With U_g = 30 ms^{-1} and the free-stream speed, U_∞, also equal to approximately 30 ms^{-1} (Config. VI) no vortex was present in the PIV measurement area, however the vector orientation at the edge of the domain suggests that a vortex is still forming and is directly underneath the intake highlight plane. However, unexpectedly Fig. 6.7 shows that the vortex strength is still increasing with ground speed, although the increase is moderate.

As explained above, although every effort was made to remove the boundary layer upstream of the intake by synchronizing the wind and road velocity and by implementing the primary and secondary boundary layer suction methods upstream of the moving belt, there is expected to be some boundary layer growth. In particular since the moving ground is of a finite width (equal to 1.2 *m*) the boundary layer thickness is expected to be relatively large at the edge of the rolling ground plane. One potential source of vorticity at high velocity ratios is that the sucked streamtube is larger than the width of the moving ground and therefore includes vorticity from the boundary layer growth at the sides of the belt. However for highest rolling road velocity ratio tested of 20 (U^*) the sucked streamtube width upstream of the intake is estimated to be approximately 0.9 *m* which is smaller than the width of the moving ground*.

*This is estimated from continuity considerations but ignores the interaction of the sucked streamtube with the ground plane. This interaction is expected to increase the sucked streamtube width by approximately 0.1 *m* at this velocity ratio. This was calculated using the assumptions described in §8.2

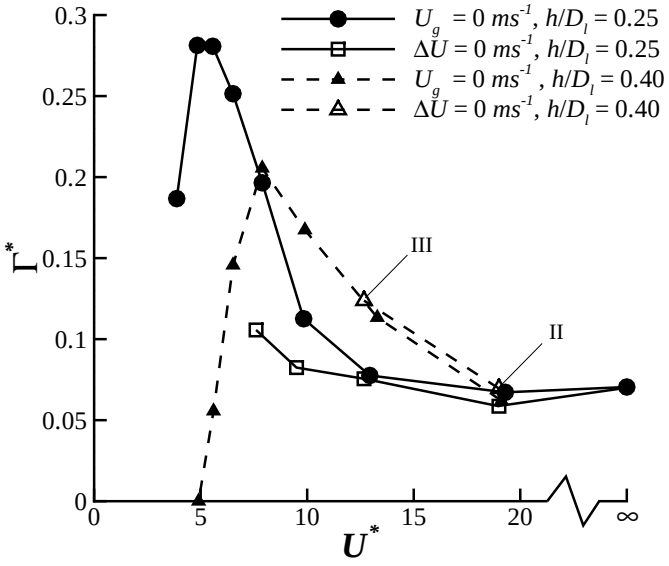

Figure 6.8: Average non-dimensional vortex strength, Γ^* against velocity ratio, U^* for moving and static ground cases with no ambient wind at two non-dimensional heights. Note the roman numerals represent the test configurations in Table 6.1 (M_i = 0.58)

A limited set of PIV measurements were also taken to quantify the effect of ground clearance for the synchronized wind and road velocity configurations. Ground speeds of 10 and 15 ms^{-1} were examined (Configs. II & III) at a non-dimensional height, h/D_l of 0.4. The vortex strength at this higher height-to-diameter ratio is plotted in Fig. 6.8 and compared with the static ground cases at the same h/D_l along with the measurements at the datum height of 0.25 (h/D_l). Surprisingly, the two velocity ratios investigated show no variation in the vortex strength in comparison to the static ground case at the same respective velocity ratios. Since the vortex strength is higher for the larger ground clearance, this suggests that the induced vorticity is stronger at the higher h/D_l. This finding is somewhat surprising for the following reason. For the no ambient wind configurations, it has been assumed that the induced vorticity is the governing vorticity source. This is generated due to the induced intake velocity field external to the intake interacting with the ground generating vorticity. Hence for low ground clearances and high intake velocities, the induced vorticity should be highest. This is believed to be why the vortex strength is stronger for low h/D_l in quiescent conditions, where there is no additional vorticity source (see §4). It is expected that synchronised wind and road configurations are akin to quiescent conditions. However, the above result contradicts this argument and suggests that there is perhaps an additional mechanism at play.

6.2.2 In-duct Total Pressure Survey

To accompany the vortex strength measurements and to reveal additional features of the flowfield inside the intake duct, total pressure measurements were also taken at the fan face. The resolution and number data points taken per configuration was the same as the headwind dataset in §5. The probes were also positioned 1.5 *mm* closer to the wall, in the same fashion as the headwind measurements, in anticipation of the vortex ingestion location being close to the intake wall (see Fig. 3.5a for the data point locations).

Fig. 6.9 displays the total pressure contours at the fan face for increasing ground speed with the wind and road velocities synchronised at a fixed ground clearance of 0.25 (h/D_l). As mentioned in §4.1, under quiescent conditions, the total pressure contours at the fan face is characterized by two regions of relatively high total pressure loss immediately adjacent to the duct surface (Fig. 6.9a). The introduction of a 10 ms^{-1} ground and approaching wind speed (Config. II) reveal only a single region of relatively high total pressure loss adjacent to the wall at the 180 degree position (Fig. 6.9b). This change is conjectured to be a consequence of the change in the rotation of the vortices as mentioned in Chapter 5. Nonetheless, is it clear that the moving ground plane has no significant influence on the average vortex ingestion location.

The distortion coefficient, DC_{60}, is plotted against velocity ratio, U_i/U_∞, for all investigated ground speeds under no ambient wind conditions (synchronised wind and road conditions), in Fig. 6.10. The trend is comparatively different to the circulation measurements at the PIV plane. With the exception of the data point at a velocity ratio of approximately 10 the DC_{60} monotonically decreases with increasing ground speed (reducing velocity ratio). With no approaching boundary layer the associated air within the sucked streamtube will have high momentum. In comparison, for the static ground case, the intake will be ingesting flow associated with the approaching boundary which inherently has a loss penalty. Therefore the loss within the vortex, for the static ground case, will be greater due to its association with the low momentum air associated with the ground boundary layer. This interpretation explains the relative difference between the static and moving ground cases, however it does not explain the reduction in DC_{60} with ground speed (Fig. 6.10). Inspection of the total pressure contours at the fan face (Fig. 6.9) reveal that the single loss core observed at a ground speed of 10 ms^{-1} reduces as the ground speed is further increased with the loss footprint also diminishing. As mentioned in Chapter 5, this single loss region is expected to be a result of vortex induced separation. However with the vortex strength moderately increasing with ground speed one would expect the induced separation to intensify. The spatial time average flowfield, however, shows that as the ground speed increases the two vortices that form get progressively closer to each other. Since the induced separation occurs in between the two vortices this mechanism is expected to inhibit local separation in this region. Therefore although the vortex strength increases modestly with reducing velocity ratio ($U_i/U_{\infty)}$ the induced separation decreases due to the separation of the vortex cores getting smaller. Since the loss associated with the induced separation is

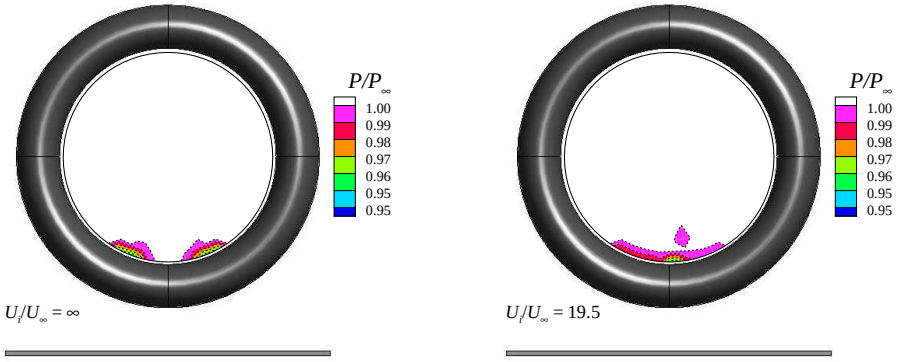

(a) $U_g = 0\ ms^{-1}$, $U_\infty = 0\ ms^{-1}$

(b) $U_g = 10\ ms^{-1}$, $U_\infty = 9.9\ ms^{-1}$

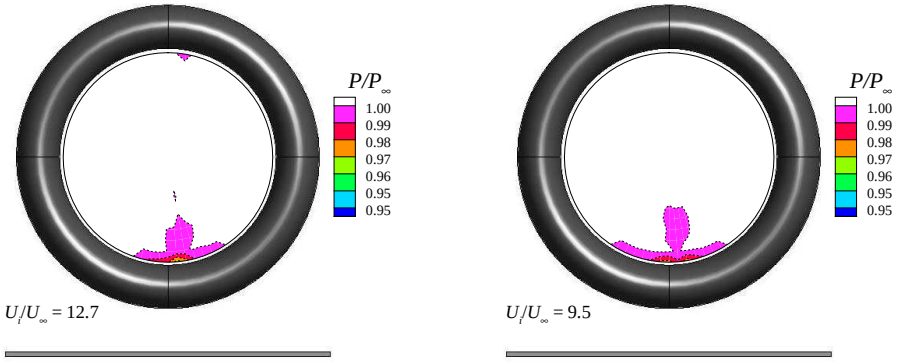

(c) $U_g = 15\ ms^{-1}$, $U_\infty = 15.2\ ms^{-1}$

(d) $U_g = 20\ ms^{-1}$, $U_\infty = 20.3\ ms^{-1}$

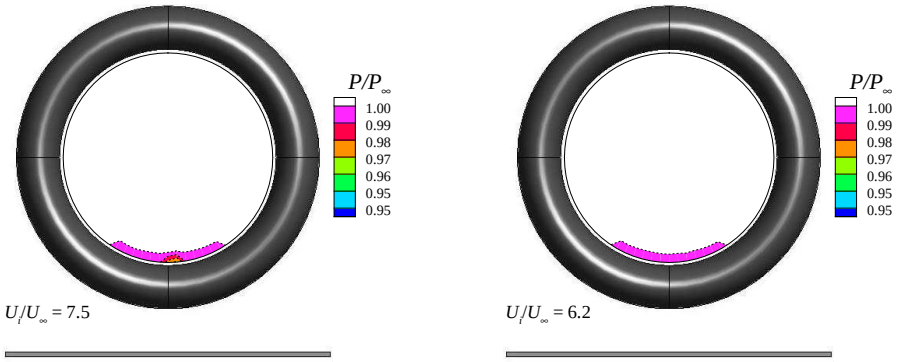

(e) $U_g = 25\ ms^{-1}$, $U_\infty = 25.7\ ms^{-1}$

(f) $U_g = 30\ ms^{-1}$, $U_\infty = 30.9\ ms^{-1}$

Figure 6.9: Contours of total pressure normalized by the working section total pressure for increasing ground speed from zero under no ambient wind conditions ($h/D_l = 0.25$, $M_i = 0.58$)

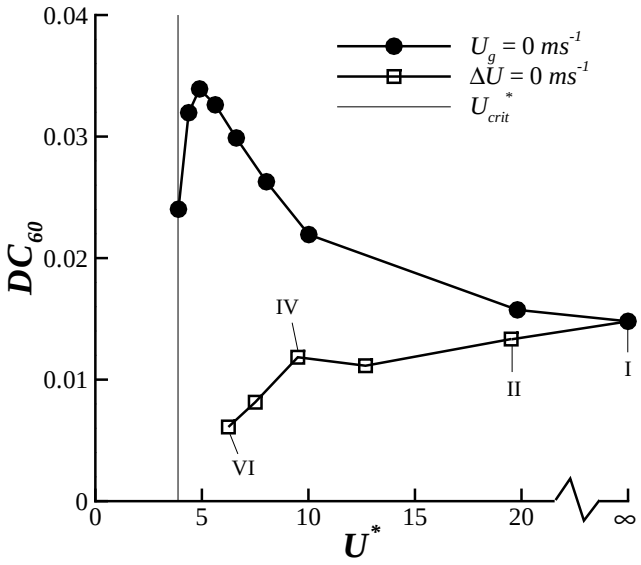

Figure 6.10: Fan face distortion for increasing ground speed in no ambient wind conditions ($\Delta U = 0\ ms^{-1}$) with comparison to a static aircraft in an increasing headwind ($h/D_l = 0.25$, $M_i = 0.58$)

dominant, the distortion at the fan face decreases with increasing ground speed.

6.3 Unsynchronized Wind and Road Experiments

In this section the results of the rolling ground plane experiments are presented in which the wind and road velocities are not equal in magnitude (i.e. $\Delta U \neq 0\ ms^{-1}$). This particular rolling road experiment is schematically shown in Fig. 6.2c and simulates an aircraft take-off in ambient headwind conditions. For this configuration an additional source of vorticity associated with the approaching boundary is present which differs from the no ambient wind case where there is no approaching vorticity. It also differs from the static ground case as the wall shear stress and hence vorticity generation at the wall is smaller, with the relative change between the two depending on the respective difference between the ground and approaching wind speeds. Two ambient headwind speeds, ΔU, of 10 and 20 ms^{-1} were investigated and the results are presented together below.

6.3.1 PIV Velocity Flowfield Quantification

Fig. 6.11b illustrates the time average flow field for a wind velocity, U_∞, equal to 20 ms^{-1} and a road velocity, U_g, of 10 ms^{-1} (i.e. $\Delta U = 10\ ms^{-1}$, Config. IX, Table 6.2). Also included in the figure is the time average flow field for a 10 ms^{-1} headwind with

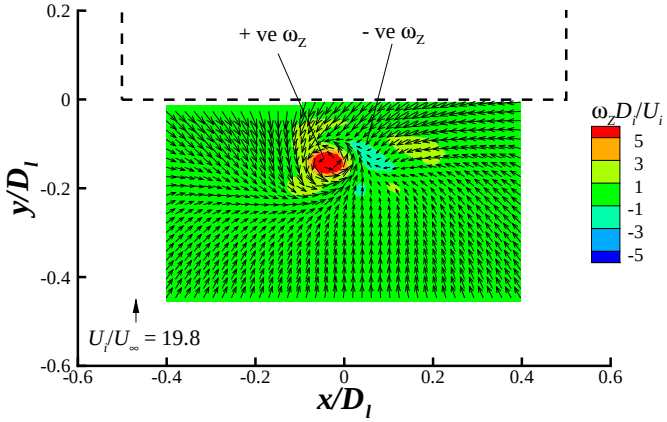

(a) $U_g = 0\ ms^{-1}$, $U_\infty = 9.8\ ms^{-1}$ (Config. VII)

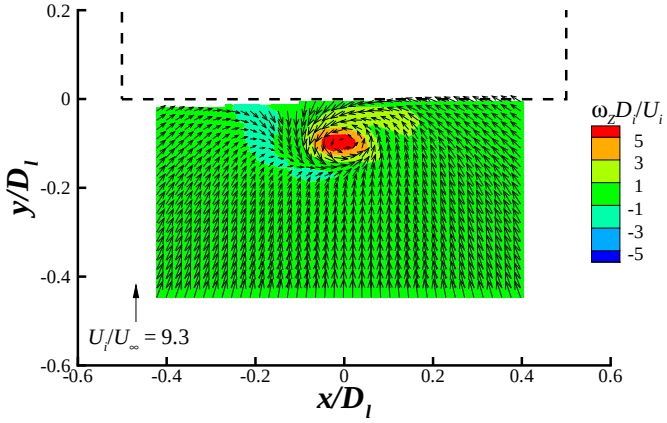

(b) $U_g = 10\ ms^{-1}$, $U_\infty = 20.8\ ms^{-1}$ (Config. IX)

Figure 6.11: Spatial average flow-field for increasing ground speed with $\Delta U = 10\ ms^{-1}$ ($h/D_l = 0.25$, $M_i = 0.58$)

a static ground for comparison (Fig. 6.11a, Config. VII). As already discussed, the flowfield for Config. VII still appears to be dominated by the gap flow between the intake and ground (as is the case under quiescent conditions). With the introduction of a 10 ms^{-1} ground speed and a corresponding increase in the freestream speed, U_∞, to 20 ms^{-1} (Config IX), Fig. 6.11b shows, as expected, the region of negative vorticity changes its position relative to the dominant vortex and is now on the left side. However Fig. 6.11 clearly shows that the dominant vortex has not changed its sense of rotation, only its position relative to the opposite source of vorticity has changed. This differs from the synchronised case (Fig. 6.6), where the dominant vortex rotational sense changes. This is expected to be due to the approaching vorticity source having a surplus amount of positive vorticity.

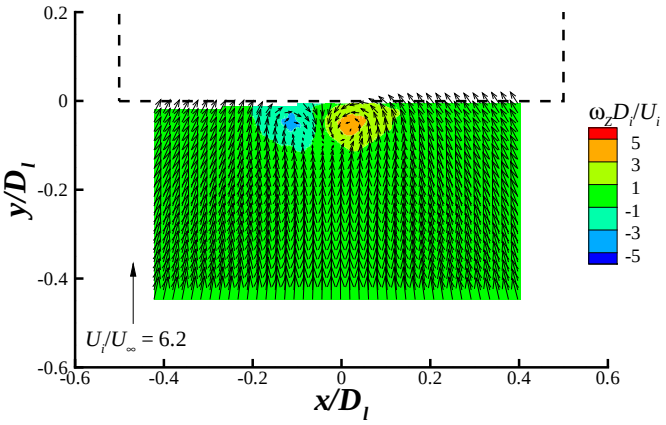

(a) $U_g = 20\ ms^{-1}$, $U_\infty = 31.3\ ms^{-1}$ (Config. XI)

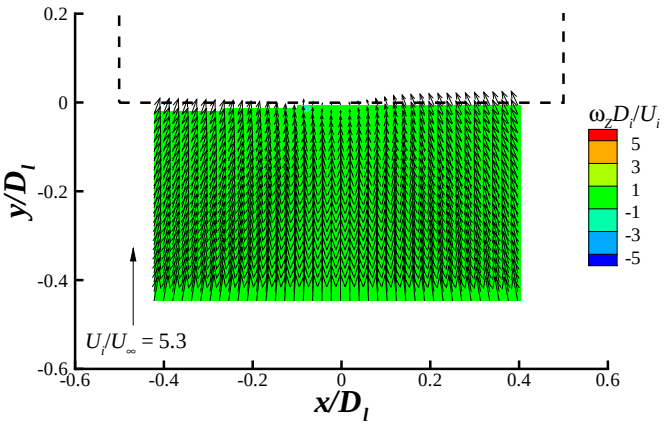

(b) $U_g = 25\ ms^{-1}$, $U_\infty = 36.6\ ms^{-1}$ (Config. XII)

Figure 6.12: Time average flow-field for (a) ground speed, U_g, equal to 20 ms^{-1} with a 31.3 ms^{-1} approaching wind speed (U_∞) and (b) ground speed of 25 ms^{-1} with a 36.6 ms^{-1} freestream speed ($h/D_l = 0.25$, $M_i = 0.58$)

As the ground speed increases the trends are largely the same as the no ambient wind (synchronised wind and road) configurations in terms of the flow topology. Two equal strength contra-rotating vortices were observed at a velocity ratio, U^*, of 6.3 (Fig.

6.12a), which compares to 9.5 for the no ambient wind case (Fig. 6.5b). The spatial unsteadiness of the vortex at the PIV plane increases with the introduction of an approaching boundary layer. As the ground speed increases, and the velocity ratio reduces the the average vortex position at the PIV plane moves closer to the highlight plane. With a velocity ratio, (U_i/U_∞), of 5.3, the vortex has moved outside of the measurement domain (Fig. 6.12b) and could be detected directly underneath the intake highlight plane from the vector orientations at the edge of the interrogation region. With the ambient wind at 20 ms^{-1} (i.e. $\Delta U = 20\ ms^{-1}$) a vortex was present in the PIV plane at a velocity ratio as low as 5.3 (U_i/U_∞). Further reductions in the velocity ratio to 4.6, however, saw the vortex move outside the domain once again. These observations are expected as the relative difference between the ground and wind speeds increase (i.e. as the ambient headwind increases) the boundary layer thickness will increase which results in lower average velocity in the sucked streamtube. As a consequence the capture streamtube size will increase.

6.3.2 Effect of Asynchronous Rolling Road on Vortex Strength

Fig. 6.13 plots the vortex strength against the velocity ratio for both 10 and 20 ms^{-1} ambient headwind cases. The results are again compared to the baseline static ground configurations which were presented in §5. For the moving ground experiments under a 10 ms^{-1} ambient wind the reference condition is indicated by the letter *a* in Fig. 6.13. This is for a static ground in a 10 ms^{-1} headwind. With the addition of a small ground speed of just 5 ms^{-1} and with the approaching wind increasing by the same amount, the vortex strength is largely unchanged and most significantly no deviation from the static ground configuration is seen. Clearly in this velocity ratio region ($U_i/U_\infty > 12$), the approaching vorticity has no influence on the vortex strength which is undoubtedly seen in the no ambient wind measurements (Fig. 6.7). A further increase in the ground speed sees the constant headwind line ($\Delta U = 10\ ms^{-1}$) deviating away from the static ground configuration characteristic curve ($U_g = 0\ ms^{-1}$). In this velocity ratio region the approaching vorticity has a dominating affect. Therefore with the rolling road in operation, the vortex strength reduces as the approaching vorticity decreases due to the lower shear stress at the ground plane. With the ground speed, U_g, increasing to 15 ms^{-1} a sharp increase in the vortex strength occurs (Fig. 6.7), however the strength is still significantly lower than the static ground case. At this velocity ratio, U_i/U_∞ of 7.4, the vortex strength has reached a maximum. This is due to the integrated vorticity within the sucked streamtube reaching a maximum. A further reduction in the velocity ratio leads to a small decrease in the vortex strength. At a $U_i/U_\infty = 5.3$ the vortex moved outside the measurement domain and therefore no further data could be taken.

At an ambient headwind of 20 ms^{-1} the characteristic trends are the same. However with the relative difference between the ground and tunnel speed being larger, the vortex strength is higher. For this ambient wind configuration, the reference position is indicated by the letter *b* in Fig. 6.7 and is the point associated with a static ground with the intake under a 20 ms^{-1} headwind. As the starting point is in the most sensitive

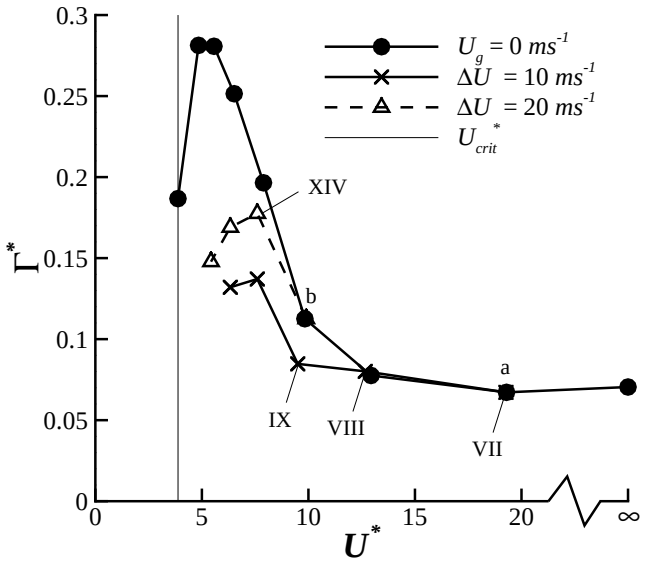

Figure 6.13: Non dimensional vortex circulation, Γ^* against velocity ratio, U^*, for increasing aircraft speed, U_g, in a 10 and 20 ms^{-1} ambient wind with comparison to a static aircraft increasing headwind speed. The roman numerals represent the configurations summarized in Table 6.2 ($h/D_l = 0.25$, $M_i = 0.58$)

velocity ratio region in terms of vortex strength, a small ground speed of 5 ms^{-1} and a corresponding increase in the approaching wind leads to a sharp increase in the vortex strength (Fig. 6.7). As expected the increase is not as significant as the static ground case, since the vorticity levels are lower. With further increases in ground speed, the vortex strength reduces until the vortex could not be seen.

6.3.3 Fan face Total Pressure Survey

A comparison of the total pressure contours at the fan face for a static ground in a 10 ms^{-1} headwind (Config. VII) and a 20 ms^{-1} moving ground with a 30 ms^{-1} approaching wind (Config. XI) is shown in Fig. 6.14. A clear difference can be seen between the two contour plots. With a greater approaching wind velocity the vortex strength increases and it is expected that there is also an increase in the unsteadiness at the fan face which ultimately leads to a larger loss footprint within the intake duct. A small region of relatively high local loss immediately adjacent to the intake wall is still evident at the 180 degree position, which is expected to be a result of a vortex induced separation. The loss in this region is not as high as the static ground configuration due to the expected increase in the vortex unsteadiness at this higher approaching wind speed. In general the total pressure pattern is very similar to the static ground configuration at the same approaching headwind speed of 30 ms^{-1} as shown in §5. These observations agree with the PIV vortex strength measurements.

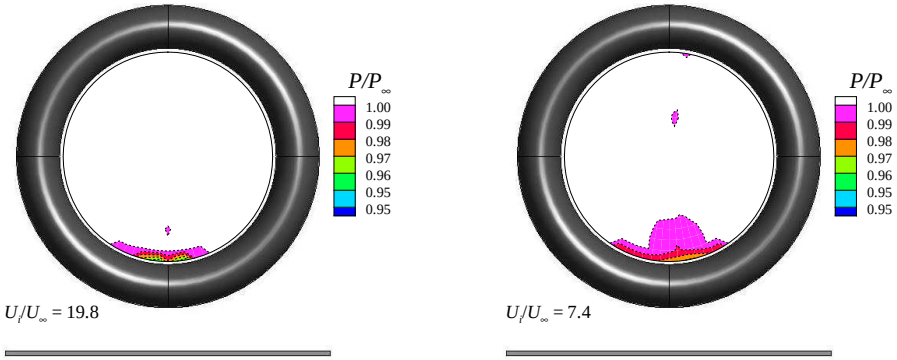

(a) $U_g = 0\ ms^{-1}$, $U_\infty = 10\ ms^{-1}$ (b) $U_g = 20\ ms^{-1}$, $U_\infty = 30\ ms^{-1}$

Figure 6.14: Comparison between fan face total pressure contours for static and moving ground cases in a $U_\infty = 10\ ms^{-1}$ headwind ($h/D_l = 0.25$, $M_i = 0.58$)

The distortion coefficient, DC_{60} is plotted against the velocity ratio for both ambient wind conditions in Fig. 6.15. The variation in DC_{60} is again the same as for the vortex strength measurements; at an ambient headwind of 10 ms^{-1}, the introduction of a small ground speed and corresponding increase in the approaching wind velocity (Config. VIII) sees no departure from the static ground configuration at the same effective velocity ratio (Fig. 6.15). For the DC_{60} the line of constant ΔU does not depart from the constant $U_g = 0$ line until the velocity ratio reduces below approximately 10. This is slightly different to the circulation where the value was roughly 12. The peak distortion for both ambient headwind cases also occurs at a slightly lower velocity ratio (Fig. 6.15).

6.4 Further Discussion

Given the trends observed, particularly for the no ambient wind configurations, some significant conclusions can be made with regards to the dominant vorticity source as a function of velocity ratio. Previously it was thought that the velocity ratio at which the vortex or vortices change rotation from the nowind to headwind modes was indicative of a change in the dominant vorticity source from the induced vorticity to the approaching boundary layer vorticity. It is clear from the results that even with the vortices rotating in accordance with the headwind mode, the induced vorticity still dominates. However, it is the induced vorticity associated with the streamwise flow (positive y-direction) rather than vorticity bound in the flow induced between the intake and the ground travelling in the opposite direction (negative y-direction). This was clearly evident with the removal of approaching vorticity which lead to no change in the vortex strength from the corresponding static ground configuration. Both the circulation and the distortion measurements suggest that the approaching vorticity only becomes influential on the strength of the vortex for velocity ratios roughly lower than

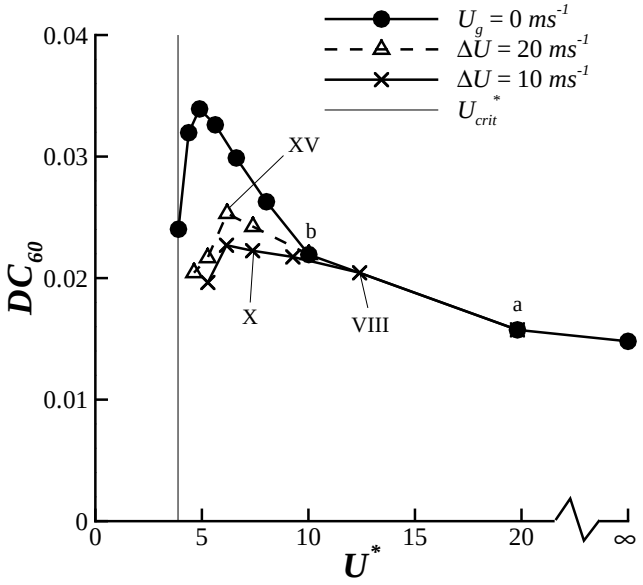

Figure 6.15: Fan face distortion, DC_{60}, against velocity ratio for increasing ground speed, U_g, in a 10 and 20 ms^{-1} ambient wind with comparison to a static aircraft increasing headwind speed (h/D_l = 0.25, M_i = 0.58)

12 (Fig. 6.16, Region B). However, what is unclear is why the approaching vorticity has no influence on the vortex strength at the investigated high velocity ratios.

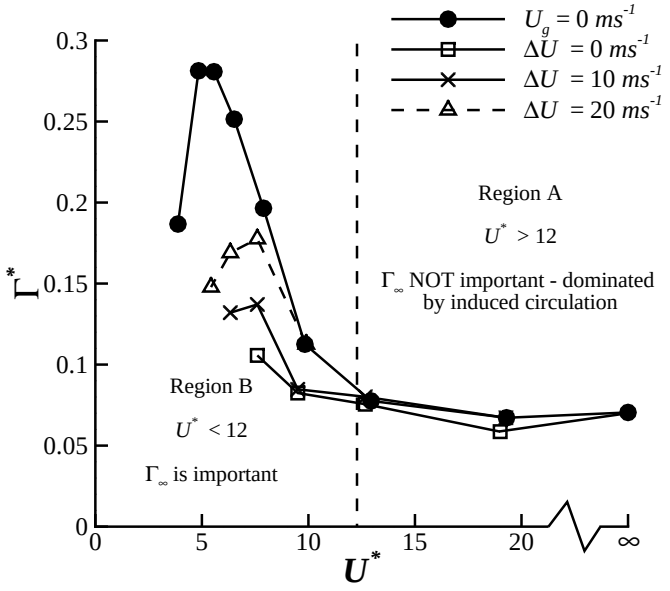

Figure 6.16: Vortex strength against velocity ratio revealing two regions of differing dominant vorticity sources for the datum height of 0.25 (h/D_l)

The limited results at the higher non-dimensional height are somewhat counter intuitive, suggesting that the induced vorticity is stronger at higher ground clearances. However, at this height the transition between the nowind and headwind modes was not observed; the headwind mode was always dominant. This therefore suggests that the interaction between the gap (negative y direction) and approaching (positive y direction) flows is smaller and therefore the vortex reaches a higher level of strength, as the approaching induced vorticity appears to be stronger.

6.4.1 Implications to Aircraft Operations

As well as aiding in understanding the fundamental mechanisms which determine the vortex strength in headwind conditions, the rolling ground plane experiments have implications on aircraft operations. The circulation against velocity ratio is again shown in Fig. 6.17, but also included in the figure is the approximate start and end of runway conditions with no ambient wind (Fig. 6.17a) and with a 20 ms^{-1} ambient wind (Fig. 6.17b). The results have demonstrated that a vortex is still expected to form with the aircraft moving. However it will not only form, but also intensify before the blowaway condition is reached (U^*_{crit}). The larger the ambient headwind, the stronger the vortex will be. But with a larger ambient headwind the vortex will blowaway faster as the aircraft moves down the runway (Fig. 6.17b). Although an intake at a higher height-to-diameter ratio may experience a stronger vortex when formed, its blowaway condition will be reached at a much lower aircraft speed.

6.5 Summary

In this chapter experiments investigating the vortex formation and characteristics with a rolling ground plane have been conducted. The results have significance on both the formation mechanisms and aircraft operations. Experiments have been performed to simulate an aircraft take-off in no ambient wind and headwind conditions. For the former it is believed that the only source of vorticity is the induced vorticity whereas in the latter there is also a contribution from the approaching boundary layer. The following conclusions can be made:

1. The results suggest that the ground vortex will increase in strength before reducing during take-off.
2. The synchronised wind and road experiments, which simulates an aircraft take-off under no ambient wind conditions, have shown that for a $h/D_l = 0.25$ the approaching vorticity source has no impact on the vortex strength for velocity ratios greater than 12 (U^*).
3. This result implies that for a $h/D_l = 0.25$ and $U^* > 12$, it is not important to simulate aircraft take-off.

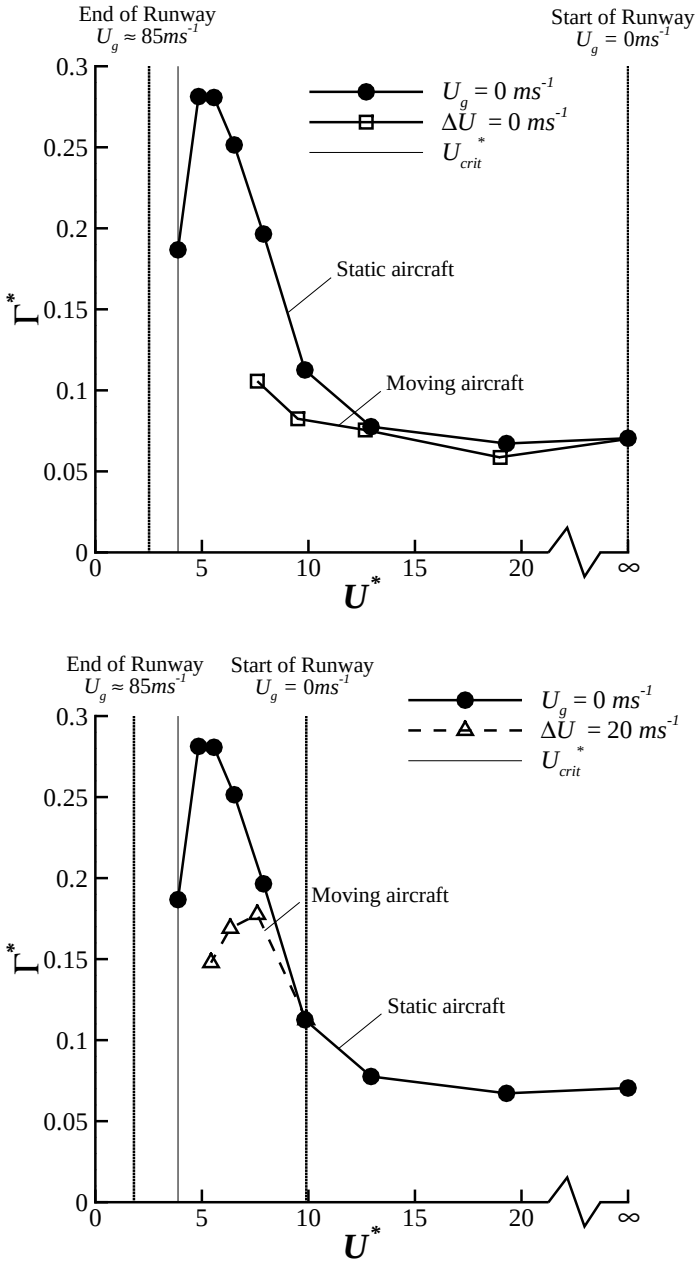

Figure 6.17: Vortex Strength against velocity ratio revealing the approximate start and end of runway velocity ratios for take-off under (a) quiescent conditions and (b) 20 ms^{-1} headwind

4. As the velocity ratio reduces below 12, the approaching vorticity becomes the dominant source for ground vortex formation and a 50% reduction in the vortex strength is observed between the static and moving ground cases.

5. For a $h/D_l = 0.25$ and $U^* < 12$, it is therefore important to simulate aircraft take-off to capture the correct trends.

6. The asynchronous experiments, which simulates an aircraft take-off under headwind conditions, reveal that as the difference between the ground and the tunnel speeds increase the vortex circulation reaches a higher level. Hence the stronger the headwind during take-off, the higher the level of strength reached by the vortex as the aircraft speed increases. However the faster the vortex will blowaway.

CHAPTER 7

Crosswind Conditions

An intake operating statically in crosswind conditions close to the ground represents one of the severest conditions that an aircraft engine intake will encounter in practice. Not only is the intake susceptible to lip separation but it can also ingest a strong ground vortex. It is therefore important to understand the characteristics of vortex formation under such conditions and also to understand the interactions between the vortex and the separation behaviour. This chapter presents an extensive study of the crosswind ground vortex. In the same fashion as for the headwind mechanism, the important aerodynamic and geometric parameters are discussed in turn.

In the first section of this chapter, the salient features of the crosswind ground vortex flowfield are discussed. Both PIV and in-duct total pressure measurements are presented which represent typical configurations and the main features of the flowfield are highlighted. This is then followed by a quantitative examination of the parameters of fundamental interest, from both an industrial and fluid dynamic perspective. First the effect of contraction ratio is discussed with the primary focus on vortex strength and distortion variation. This is followed by a sensitivity study to changes in ground clearance and also to alterations in the approaching boundary layer thickness. Finally, the effect of reducing the yaw angle from ninety degrees to a pure headwind configuration is quantified. The chapter concludes with a discussion of the comparative difference between the crosswind and headwind formation mechanisms.

7.1 Flow Topology

At the lowest crosswind velocity ($U_i/U_\infty = 18.3$), a single ground vortex forms ahead of the highlight plane approximately in line with the intake centreline. Fig. 7.1a shows an example single snapshot of the out-of-plane non-dimensional vorticity contours, $\omega_z D_l/U_i$, and the in-plane $u - v$ velocity vectors. As expected, the rotational sense of the vortex is clockwise, due to the direction from which the wind approaches the intake. This is due to the vortex being associated with the lower of the two trailing vortices that form on the leeward edge of the intake when the sucked streamtube has no interaction with the ground[10] (Fig. 2.10a). The corresponding total pressure con-

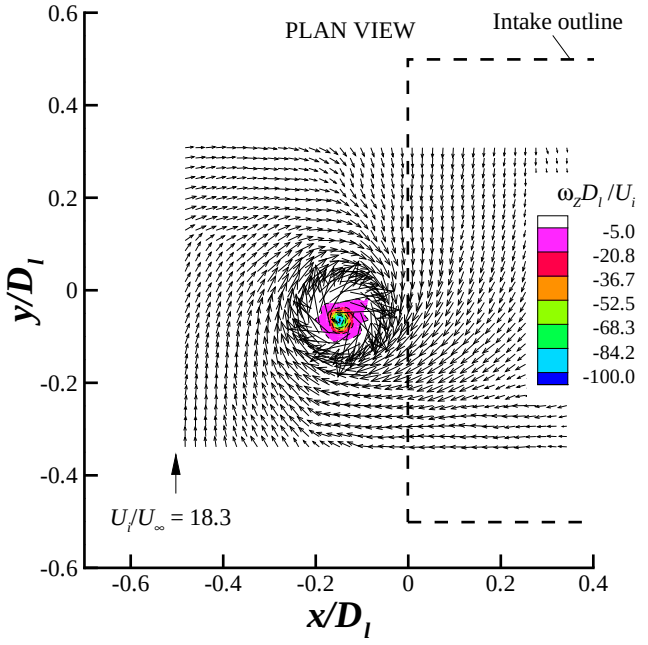

(a)

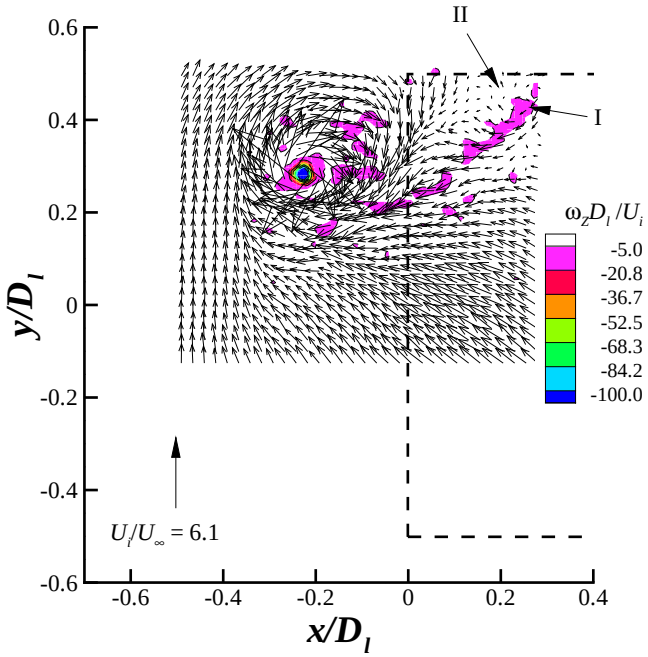

(b)

Figure 7.1: Typical flowfield snapshots of the crosswind ground vortex at two different velocity ratios (U^*) of 18.3 and 6.1 for an $h/D_l = 0.25$, $M_i = 0.55$, and $\delta^*/D_l = 0.11$

tour plot at the nominal fan face location (Fig. 7.2) illustrates that the vortex location relative to the engine centreline is at a more upwind position relative to its position external to the intake. This observation has been reported in previous studies and is due to the interaction with the intake surface.

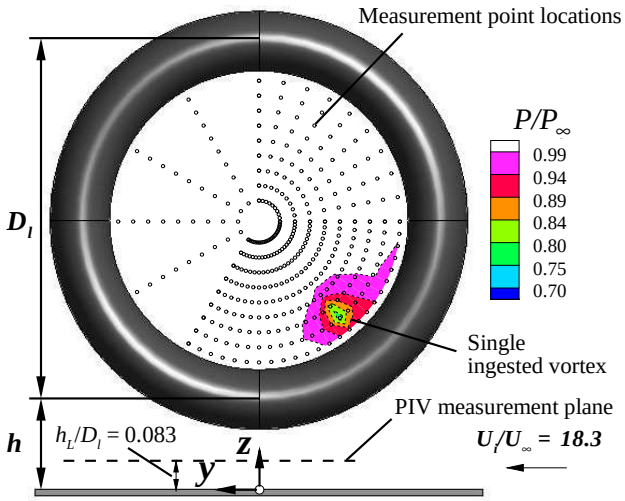

Figure 7.2: Example total pressure contour plot at the fan face at an $h/D_l = 0.25$ and a velocity ratio, $U^* = 18.3$. Also included in the figure are the measurement point locations for the induct total pressure measurements, the intake height definition and the PIV measurement plane location relative to the intake.

As the velocity ratio (U_i/U_∞) reduces to 6.1, the vortex position changes considerably in the positive *y*-direction (i.e. in the windward direction) and moderately in the negative *x*-direction (Fig. 7.1b). Inspection of the peak vorticity levels shows an increased level and there is also a considerable change in the overall vorticity field. A feature at intermediate to low velocity ratios is a region of high, positive and negative, vorticity emanating from underneath and behind the intake which is drawn into the vortex (Region I, Fig. 7.1b). This trail of vorticity, which is travelling towards the vortex, is due to a strong interaction between the approaching flow and the vortex induced velocity field. As a result a dividing streamline forms which divides the two different flows apart. This dividing streamline emanates from a region of low velocity magnitude (Region II, Fig. 7.1b) and is expected to be related with the closely positioned saddle point which is associated with the edge of the sucked streamtube. As the velocity ratio reduces the vortex approaching vorticity will strengthen. At the same time the sucked streamtube will get smaller and the approaching flow emanating from the underneath the intake will have to turn more sharply into to the vortex due to the smaller capture streamtube size. Hence the levels of vorticity along the dividing streamline will increase which may act as a source of vorticity for the vortex. This will be discussed in further detail at the end of this section.

Fig. 7.3 illustrates the effect of reducing velocity ratio on the average vortex core position at the PIV plane. The horizontal and vertical bars represent the standard deviation

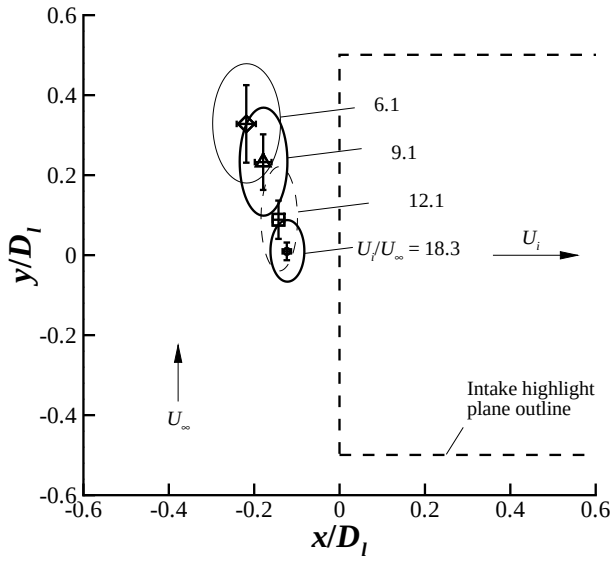

Figure 7.3: Average vortex core locations for selected velocity ratios ($h/D_l = 0.25, M_i = 0.55$). Bars indicate the standard deviation in the x, y core position and the shapes indicate the full extent of movement over all 300 snap-shots

of the core locus relative to the time averaged location. The full extent of the vortex movement is approximated by the enclosed shapes centred on the average vortex core locations. As the crosswind velocity increases and the velocity ratio (U_i/U_∞) reduces the vortex position at the PIV plane moves across the intake highlight plane in the positive y-direction. A reduction in velocity ratio from 18.3 to 6.1 corresponds to a movement in the average core location from y/D_l = 0.01 to 0.33 (U_i/U_∞ = 6.1) with the standoff distance from the highlight plane also increasing from x/D_l = -0.12 to -0.22. The error bars indicate that the unsteady vortex movement increases significantly with reducing velocity ratio and that the spatial unsteadiness is predominately confined to the y-direction.

For each configuration 300 flow-field snapshots were acquired and as with quiescent (§4), headwind (§5) and rolling road experiments (§6) each vortex snapshot has been assessed to determine the vortex characteristics as described in Appendix E. Fig. 7.4 shows example variations in vortex strength, vortex core size and Vatistas shape factor across all snapshots for a single configuration. At this velocity ratio (U_i/U_∞ = 18.6), non-dimensional height (h/D_l = 0.4) and approaching boundary layer (δ^*/D_l = 0.11) the average vortex strength, Γ, was calculated to be 3.6 m^2s^{-1} with a standard deviation of 0.5 m^2s^{-1} (12% of the mean). As the crosswind velocity increased and the corresponding velocity ratio reduces, the standard deviation was to found to increase moderately. The increase in the standard deviation at lower velocity ratios is expected to be a result of an increased level of velocity perturbations due to an increase in vorticity within the approaching boundary layer. Further evidence of this hypothesis is seen when there is a thinner approaching boundary layer (δ^*/D_l = 0.03); with all other conditions the same, the vortex strength increased to 4.3 m^2s^{-1}, but with the

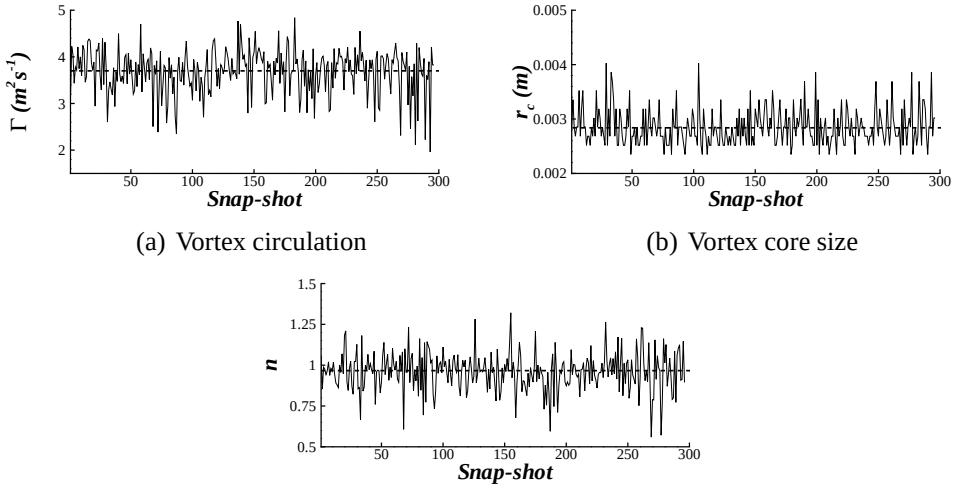

(a) Vortex circulation

(b) Vortex core size

(c) Vatistas shape factor

Figure 7.4: Typical variations in vortex circulation, core size and Vatistas shape factor (h/D_l = 0.4, U_i/U_∞ = 18.6 and δ^*/D_l = 0.11)

standard deviation reducing to 0.3 m^2s^{-1} (7% of the mean). This reduction in the variation of vortex strength is due to the measurement plane being closer to the edge of the boundary layer which is associated with lower levels of turbulence intensity, and hence velocity perturbations (see Appendix C).

The average circumferential swirl velocity distribution was determined for all vortex snapshots (as described in §3.6) and was used to determine the vortex core radius, r_c, for each vortex realization. Fig. 7.4b shows the variation of vortex core size for a typical configuration across all PIV flow-field snapshots. The average r_c value was found to be 2.8 mm (= $0.056r_i$) and is generally typical of all investigated configurations. The average core radius over all configurations was approximately 3 mm (= $0.06r_i$). The tangential velocity distribution for each vortex was also used to determine Vatistas shape factor, n, across all PIV snapshots (Fig. 7.4c). The average n value for this particular example is 0.96 and across all configurations is on average a value of approximately 1.

With each individual vortex core being identified for all flowfield snapshots, a vortex alignment average of the flowfield was performed for a range of velocity ratios at a fixed height, h/D_l, of 0.25. This averaging technique, sometimes referred to as the conditional average in the literature[61], is used to evaluate the flowfield topology in further detail with particular focus on the effect of velocity ratio, U^*. The vortex alignment average is advantageous because it removes the ambiguity of vortex wander associated with the simple time average method[18].

The average vector field (after alignment of all vortex centres), for four different velocity ratios, is shown in Fig. 7.5a-d. Also included in the figure are contours of non-dimensional out-of-plane vorticity ($\omega_Z D_l/U_i$) with Fig. 7.5e-h showing the corresponding profiles of non-dimensional out-of-plane velocity (w/U_i). For the highest

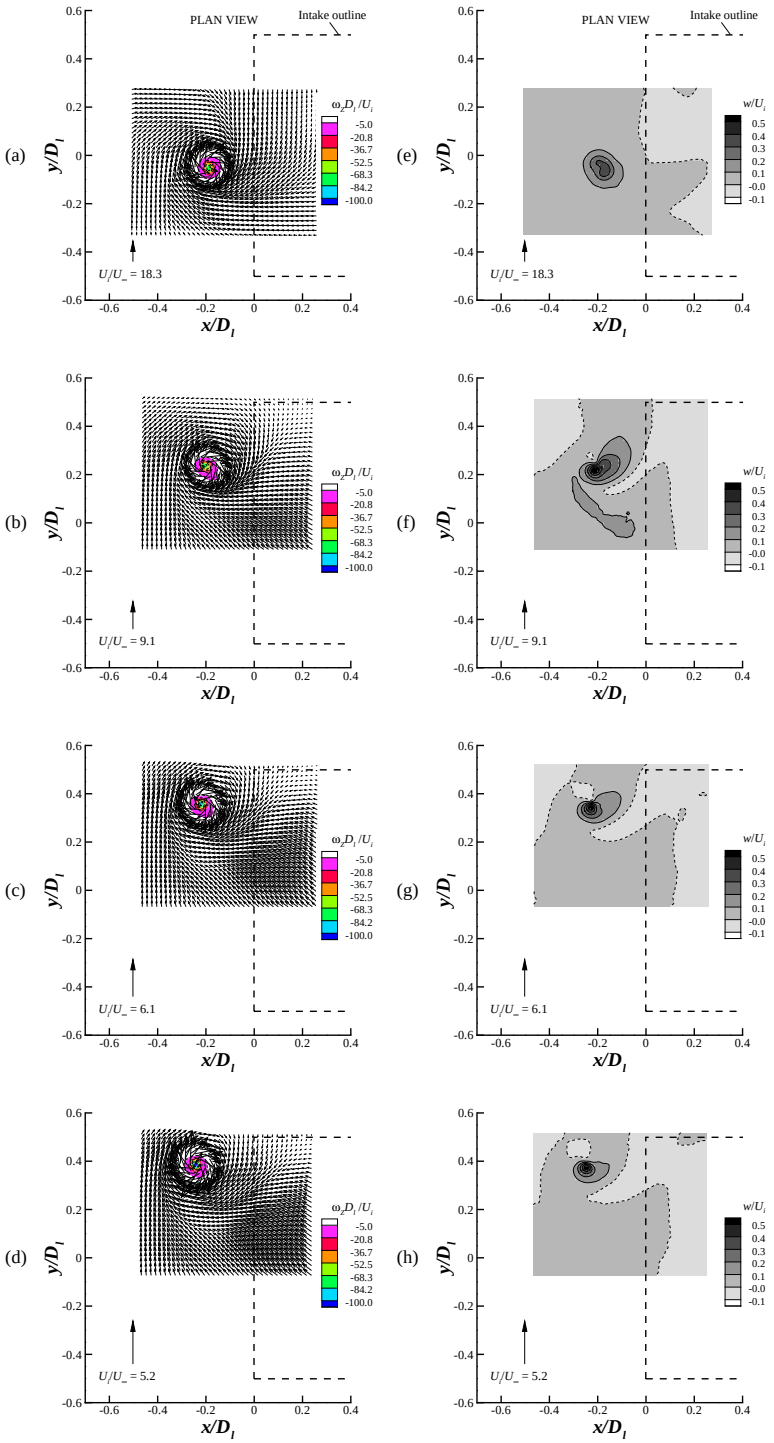

Figure 7.5: Conditional average vector and vorticity field (only every 3^{rd} vector shown) and out of plane velocity (w) field for an $h/D_l = 0.25$ and $M_i = 0.55$

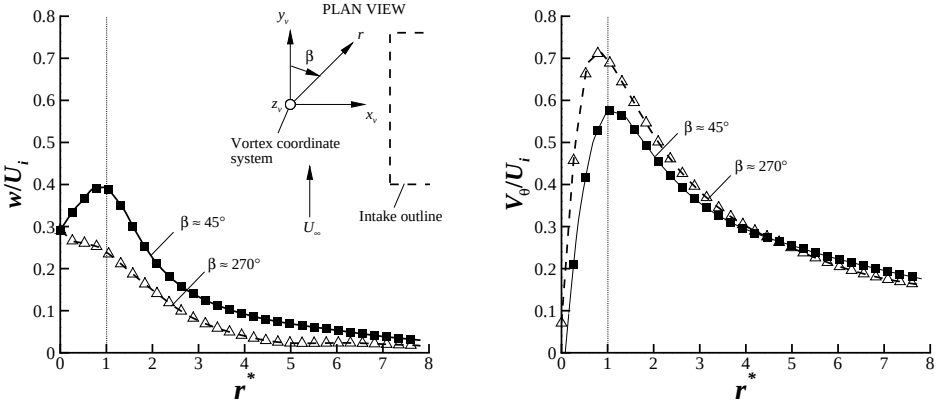

Figure 7.6: Typical distributions of (a) non-dimensional out-of-plane velocity, w/U_i, and (b) non-dimensional tangential velocity, V_θ/U_i, with radial distance from the centre of the vortex for the conditional average field ($h/D_l = 0.25$, $M_i = 0.55$ and $U_i/U_\infty = 18.3$)

velocity ratio ($U_i/U_\infty = 18.3$) a predominately axi-symmetric vector and vorticity flow-field is observed (Fig. 7.5a). The highest out-of-plane velocities are observed in the region of the core of the vortex (Fig. 7.5b) with the maximum velocity occurring at a radial position equal to the core radius and at a circumferential position, β, equal to 45° (Fig. 7.6a). Not surprisingly, the tangential velocity is a maximum at a circumferential position where the crosswind and local vortex vector have the same directions (i.e $\beta = 270°$) (Fig. 7.6b).

As the velocity ratio reduces, the sucked streamtube size decreases and the average in-plane velocity vectors become more asymmetric due to an increasing influence from the crosswind velocity and the flow between the intake and the ground plane (Fig. 7.5). As a consequence, a dividing streamline forms that separates the approaching flow, which is between the intake highlight plane and the vortex (travelling in the positive y-direction), and the clockwise rotating fluid associated with the vortex (Fig. 7.7). This dividing streamline forms part of the expected saddle point at the edge of the capture streamtube. The presence of the dividing streamline has an impact on the out-of-plane velocity contours, which show that for reducing velocity ratio an increasingly large region of downward velocity (negative z direction) is drawn in towards the outer region of the vortex (Fig. 7.5e-h). This is accompanied by a smaller peak region, of upward (i.e. away from the ground), out-of-plane velocity.

An explanation for these observations relates to the convection of ambient vortex lines associated with the approaching (positive y direction) flow. At low crosswind velocities (high contraction ratios) the flow-field is dominated by a strong clockwise vortex (Fig. 7.5a). As explained above this vortex is associated with the lower trailing vortex that forms when the capture streamtube has no interaction with the ground (see Fig. 2.10a)(i.e. the vortex is associated with the viscous flow over the intake). However there is an additional vorticity source proceeding towards the intake associated with

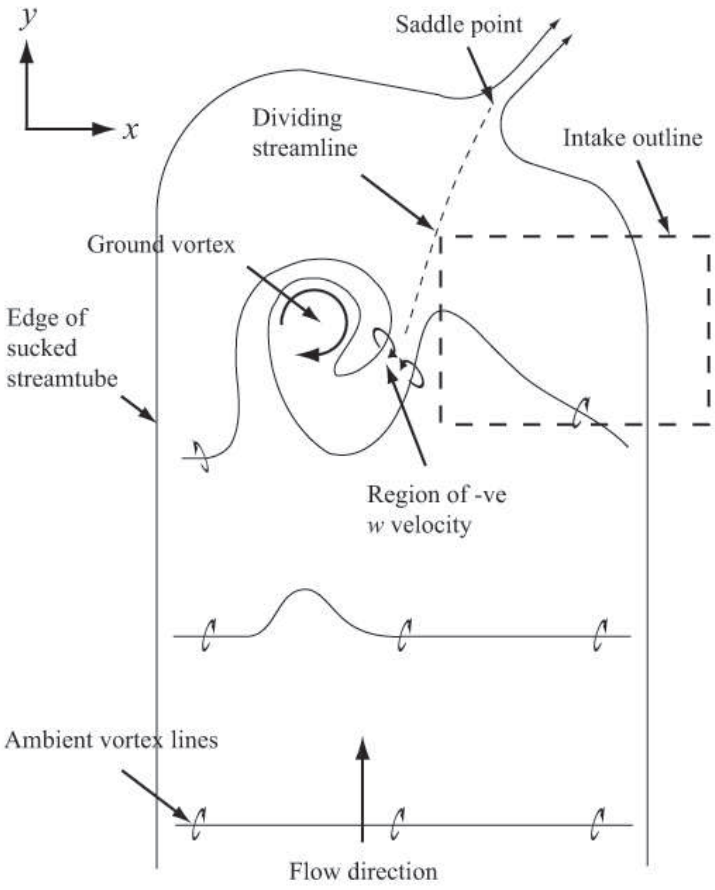

Figure 7.7: Convection of ambient vortex lines around the dominant vorticity source in 90 degree crosswind conditions

the approaching boundary layer. It is believed that it is the interaction between the two primary vorticity sources that causes an increasingly large region of downward w velocity to form (Fig. 7.5e-h). The expected situation is sketched in Fig. 7.7 which shows the deformation of the vortex lines associated with the crosswind velocity. Far upstream of the intake the vortex lines are perpendicular to the flow and parallel to the ground. As the vortex lines approach the intake they will be deformed by the strong velocity gradients associated with the vortex and intake induced flowfields as sketched in Fig. 7.7. The ambient vortex lines wrap around the dominant vorticity source and as a consequence the leg of each side of the deformed line interacts will each other to result in a region of downward velocity as indicated in Fig. 7.7. As the crosswind velocity increases the approaching vorticity will increase. This therefore results in a larger interaction of the ambient vortex lines with themselves as they wrap around the dominant vorticity source.

7.1.1 Vortex Start-Up Transient

A limited set of measurements were taken to examine the start-up transient of the crosswind ground vortex. PIV measurements were taken at a h/D_l of 0.25 at a velocity ratio, U_i/U_∞, of 18.4 with the intake angle to the wind direction, ψ, equal to 50°. The PIV flowfield snapshots were acquired at 7.5 Hz. For this experiment data acquisition commenced and the intake suction was initiated approximately between the first and second flowfield snapshots. The quasi-steady state suction velocity is reached approximately 1 s after the shutter valve is released (see §3.2.1 for further details). Fig. 7.8 and 7.9 shows the vorticity field and in-plane streamline patterns for the first 12 flow-field realizations acquired (i.e. the first 1.47 s of data acquisition). Fig. 7.8a represents the flowfield just before the suction started and is therefore at time, $t \approx 0s$. Each subsequent snap-shot is acquired at times equi-spaced by 1/7.5 s.

At $t \approx 0s$ the streamline lines are approximately straight and equally spaced across the whole measurement domain (Fig. 7.8a). There is no presence of a vortex inside or outside the region of interest. The angle in the streamlines relative to the wind direction is expected to be due to the presence of the intake. With the intake suction being triggered between $t = 0$ and $0.13s$, an immediate but subtle change in the streamline pattern is observed at $t = 0.13s$ (Fig. 7.8b). Within the central proportion of the measurement domain, the streamlines appear to be converging towards each other as they travel in the positive y direction. This can clearly be seen at a coordinate position of (-0.2,0.3) (Fig. 7.8b), where the streamlines are much closer together in comparison to an upwind position of say (-0.2,-0.3). This is an indication that there is a contraction in the streamlines in the near field wake region of the intake. At $t = 0.27s$, the streamlines have further converged together at (-0.2,0.3) and there is a clear indication of a vortex just outside the interrogation region at a coordinate position of approximately (-0.2,0.4). This is apparent as there is a small local region of reverse flow at (-0.2,0.3). With a further advance in time to $t = 0.4s$ a weak vortex materializes in the measurement domain (Fig. 7.8d) which appears to have emerged from the intake wake region.

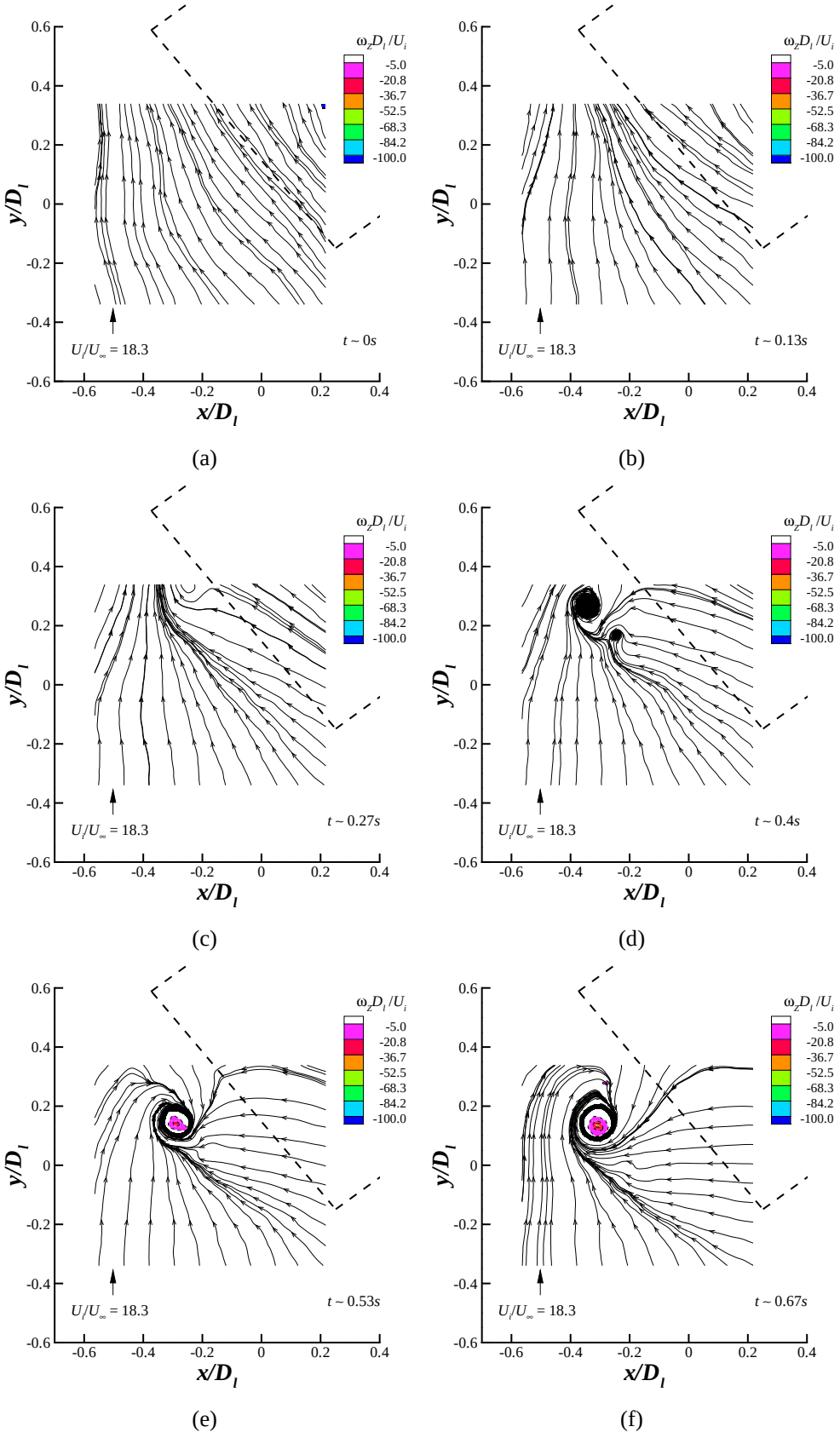

Figure 7.8: Vortex start-up transient in 50 degree crosswind conditions ($\psi = 50°$) for an $h/D_l = 0.25$ and $U^* = 18.3$

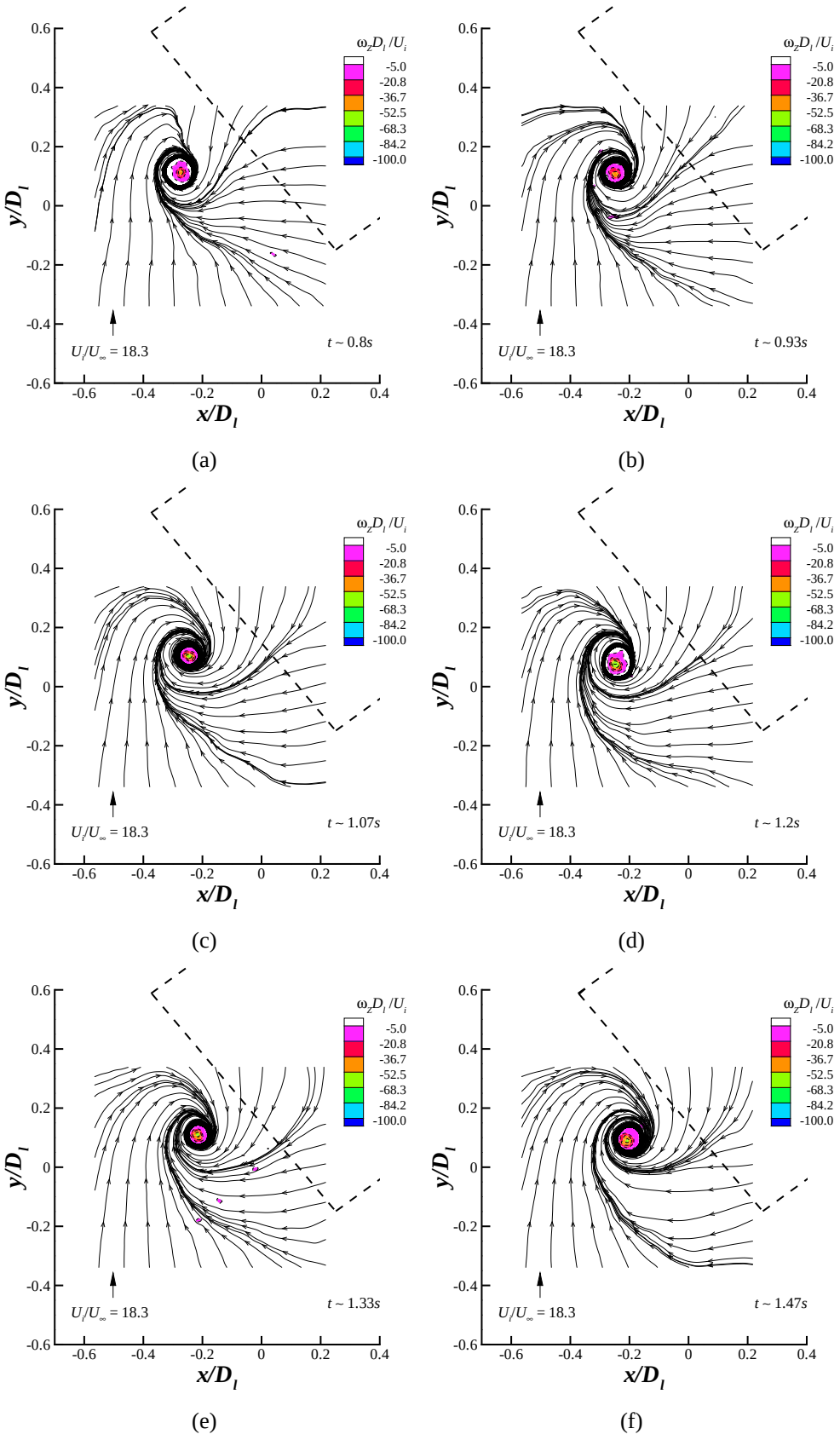

Figure 7.9: Vortex start-up transient in 50 degree crosswind conditions, continued

As time progresses further the vortex grows in strength and travels upwind (i.e. negative y direction) until a quasi-steady state is achieved. The vortex position appears to have reached a quasi-steady state position at the PIV plane after approximately $1.07s$.

The vortex strength, Γ, core size, r_c, and Vatistas shape factor, n, have been computed for each time step, as shown in Fig. 7.10. Only the first 10 s of the total 40 s run time is shown for clarity. The dotted line represents the time average value for each respective parameter over all 300 snap-shots. As expected when the vortex first appears in the measurement domain the vortex is weak (Fig. 7.10a). The vortex continuously grows in strength for approximately 1.5 s before a reduction is seen (Fig. 7.10a). Interestingly the core size and the Vatistas shape factor show no noticeable variation between the transient and quasi-steady state regions (Fig. 7.10b-c). In order to obtain an approximate transient formation time, the average, $\bar{\Gamma}$, and standard deviation, σ_Γ, of the vortex strength was calculated over all snapshots excluding the transient. The formation time, t_v, was defined as being the time taken for the circulation to be within two standard deviations of the mean (Eq. 7.1.1). Using this criterion gave a transient formation time, t_v, of 0.93 s.

$$\Gamma(t) > \bar{\Gamma} - 2\sigma_\Gamma \tag{7.1.1}$$

The only other known study to examine the transient start-up of the ground vortex was conducted by de Siervi et al[10]. In this particular work the transient start-up mechanism was investigated with a twin inlet configuration (i.e. with no approaching boundary layer vorticity) and was also under 90 degree crosswind conditions. This differs from the current experiments which uses a single intake close to a ground plane partially immersed in the approaching boundary layer which is at 50 degrees orientation to the wind direction. As explained above, the qualitative flow visualization studies by de Siervi et al were instrumental in understanding the formation mechanism of the crosswind ground vortex. In their work it was concluded that the source of vorticity for the vortex was associated with the vorticity emanating off the intake surface. This vorticity is convected back upstream during the start-up transient by the induced intake velocity field to form a vortex. The findings from this current study clearly agree with these observations. It is quite evident that a weak vortex forms downstream of the intake, which can be inferred from the streamline curvature and pattern in Figs. 7.8b-d. Once formed the vortex grows in strength and moves upstream into a quasi-steady state (Fig. 7.9). De Siervi et al[10] also provided a time scale for the transient formation time, which was quoted to be in the order of $10H/U_\infty$. For the current study the formation time scale is approximately $100H/U_\infty$. It is expected, however, that the velocity ratio will have an effect on the formation time since this should dictate how rapidly vorticity from the intake surface is shed into the near wake of the intake and then convected back upstream to form a vortex. Perhaps a better time scale for vortex formation, t_v, which gives more realistic values for both experiments is given by Eq. 7.1.1.

$$t_v \approx \frac{4D}{U_\infty}\frac{U_i}{U_\infty} \tag{7.1.2}$$

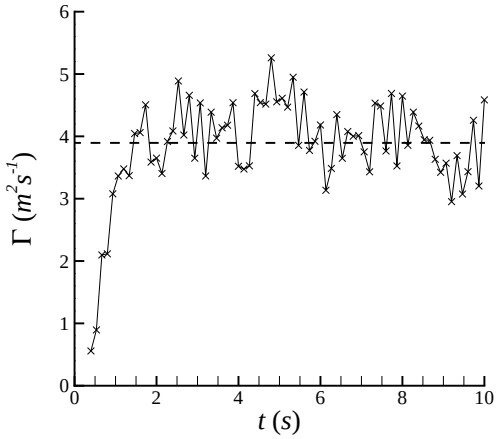

(a) Vortex circulation

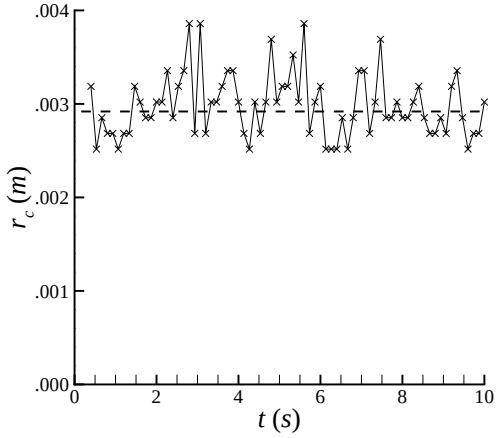

(b) Vortex core size

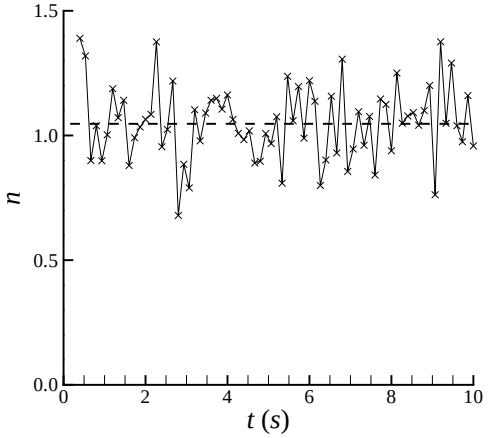

(c) Vatistas shape factor

Figure 7.10: Variation in (a) vortex circulation, Γ, (b) vortex core size, r_c, and (c) Vatistas shape factor, n, with time for the transient start-up experiment ($h/D_l = 0.25$, $M_i = 0.55$, $U_i/U_\infty = 18.3$ and $\psi = 50°$)

7.2 Effect of Principle Parameters

In this section the effect of the important aerodynamic and geometric parameters are discussed. First the effect of contraction ratio (U_i/U_∞) is dealt with and is split into two subsections; vortex strength quantification and in-duct total pressure measurements. Following this the effect of non-dimensional height will be discussed as well as the approaching boundary layer thickness. Finally the effect of yaw angle is presented, in which the crosswind and headwind formation mechanisms will be compared.

7.2.1 Effect of Contraction Ratio

Although the effect of contraction ratio has already been discussed above on the flow topology, this section primarily concentrates on the quantification of the vortex circulation and in-duct flow distortion and how both vary with velocity ratio.

7.2.1.1 Vortex Strength Quantification

PIV and total pressure measurements were taken for a range of crosswind velocities varying from 10 to 40ms^{-1} (19 -78Kts). For each configuration the average vortex strength has been determined by averaging the circulation values over all flow-field snapshots (see Appendix E for full details). Fig. 7.11 shows the effect of reducing the velocity ratio (U^*) on the average non-dimensional vortex strength, Γ^*. For a low ground clearance, $h/D_l = 0.25$, the vortex strength monotonically increases with decreasing velocity ratio. By non-dimensionalising the vortex strength by the intake highlight diameter, D_l, and the intake velocity, U_i, shows that there is very little difference when the intake Mach number is reduced from 0.55 to 0.43. At this ground clearance ($h/D_l = 0.25$) the critical point at which the sucked streamtube clears the ground plane is expected to be at $U^*_{crit} = 3.88$, as indicated in Fig. 7.11. This assumes a circular, axi-symmetric, sucked streamtube and has been predicted from continuity considerations. The critical velocity ratio, under crosswind conditions, could not be investigated due to tunnel limitations at the time of testing. At the higher ground clearance of $h/D_l = 0.4$, the vortex strength initially increases and reaches a local maximum at $U^* = 9.1$. A further reduction in the velocity ratio results in a decrease in the vortex strength. This attributed to the 'cross-wind' ground vortex intermittently detaching from the ground to form a second trailing vortex due to a reduced level of interaction between the sucked streamtube and the intake outer surface. This point will be discussed in further detail below. The critical velocity ratio, for this height-to-diameter ratio is expected to occur at $U^*_{crit} = 5.6$.

Within previously published literature the effect of velocity ratio on the crosswind vortex strength has been the subject of conflicting reports. Some workers postulated that a higher velocity ratio would result in a stronger ground vortex[6,50] - perhaps due to larger footprint of the sucked streamtube with the ground. Brix et al[6] reported

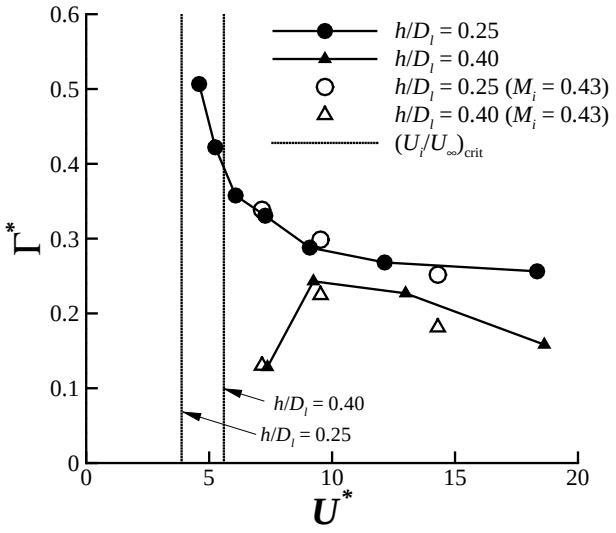

Figure 7.11: Effect of velocity ratio on the vortex circulation for two height-to-diameter ratios and intake Mach numbers at a fixed approaching boundary layer of $\delta^*/D_l = 0.11$

quantitative results for crosswind configurations which showed that the vortex strength increased with reducing velocity ratio, within the intake duct. This is in agreement with the current observations (Fig. 7.11). De Sievri et al[10] showed that the formation of the ground vortex requires no upstream ambient vorticity. Transient start-up studies of the formation mechanism in crosswind showed that the ground vortex forms in the near wake region of the intake and is associated with the vorticity of the separated shear layer on the outer surface of the intake, as discussed above. On this basis it is expected that the increased vorticity levels within the boundary layer on the intake surface, with reducing velocity ratio, would result in the formation of a stronger ground vortex.

7.2.1.2 In-duct Flow Distortion

Total pressure measurements have been taken at a nominal fan face location within the duct for a range of streamtube contraction ratios. The effect of velocity ratio on the total pressure contours at the fan face is shown in Fig. 7.12. Similar to the observations in the PIV plane, the average vortex location moves further downwind (or clockwise), as the velocity ratio reduces. A reduction in velocity ratio from 18.3 to 6.1 results in the average vortex position moving circumferentially around the intake from 140° to 162.5° with the corresponding radial position moving slightly towards the intake centre line (r_v/r_i = 0.84 to 0.74) (Fig. 7.2 and Figs. 7.12a-d). As the contraction ratio reduces below 7.3, crosswind lip separation occurs ($\theta \approx 30°$ to 140°) which increases in strength and size as the velocity ratio reduces further (Fig. 7.12d-f). At the lowest velocity ratio ($U^* = 4.6$) the separation has extended radially away from the wall considerably (Fig. 7.12f).

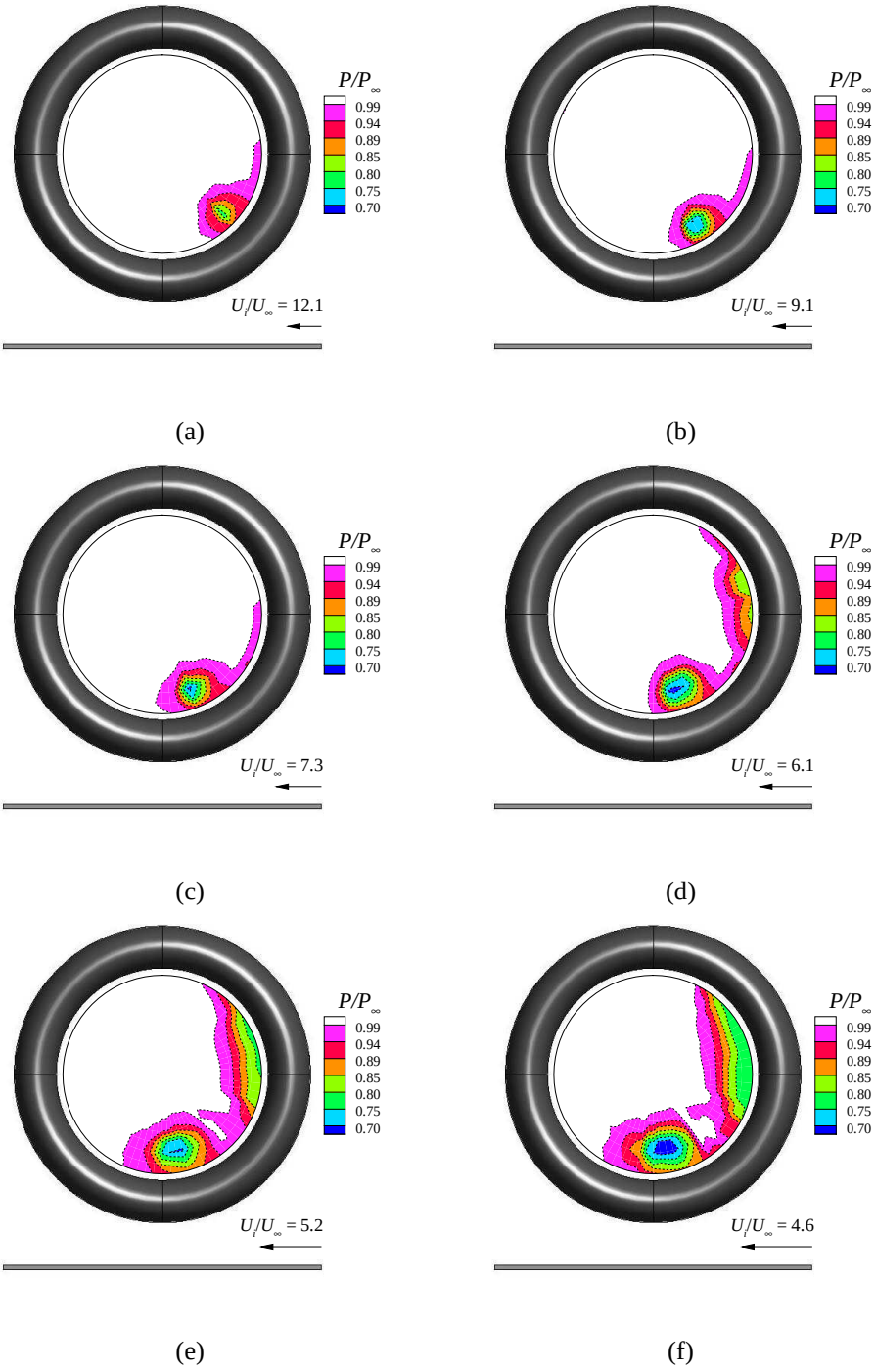

Figure 7.12: Total pressure contours at the fan face for increasing crosswind speed

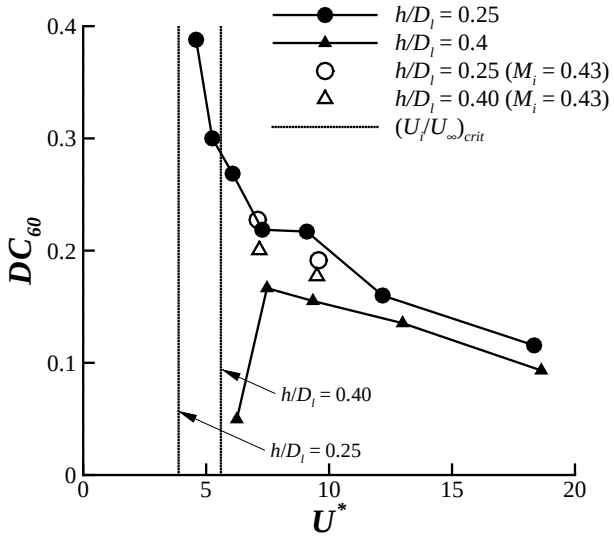

(a)

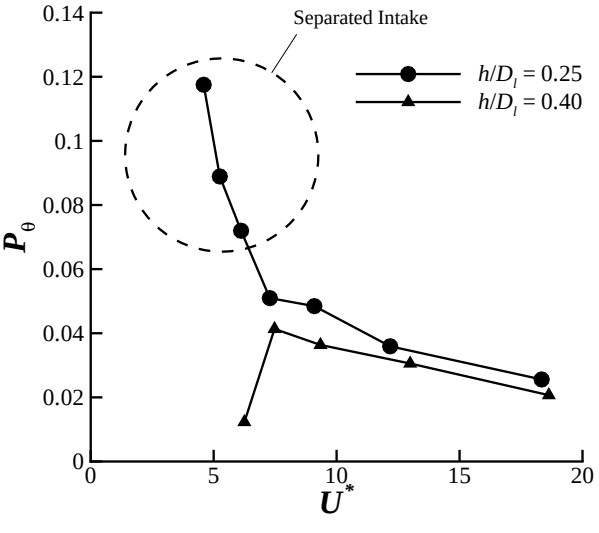

(b)

Figure 7.13: Effect of velocity ratio on the (a) DC_{60} and (b) P_θ for two height-to-diameter ratios and intake Mach numbers for a fixed approaching boundary layer of $\delta^*/D_l = 0.16$

From the total pressure measurements the distortion at the fan face has been characterized using the DC_{60} parameter, as with the quiescent and headwind measurements. The DC_{60} trend with velocity ratio is displayed in Fig. 7.13a for two height-to-diameter ratios. As expected, the general trend with velocity ratio is similar to the vortex strength measurements (Fig. 7.13). At the datum height ($h/D_l = 0.25$) a reduction in the velocity ratio leads to a monotonic increase in the distortion. Initially the increase in DC_{60} is small with velocity ratio, owing to the small increase in vortex strength. At a velocity ratio of 6.1 lip separation occurs on the windward side of the intake (Fig. 11d) and grows with further reductions in velocity ratio (Fig. 7.12d-f). The onset of separation leads to a sharp increase in the distortion (Fig. 7.13a). For all cases with lip separation the peak loss within the vortex is higher in comparison to the loss associated with the separation, therefore P_{60} is always associated with the vortex.

$$P_\theta = \frac{P_\infty - \bar{P}_{60}}{P_\infty} \tag{7.2.1}$$

To clarify the impact of the separation on the vortex induced distortion an additional distortion descriptor, P_θ, has been examined which is based on free-stream total conditions, P_∞, rather than the fan face average pressure, P_f (Eq. 7.2.1). This distortion parameter isolates the loss due to the vortex only since the free-stream conditions (i.e. P_∞) does not include the effects of separation and $\bar{P}_{60}$ is always associated with the loss within the vortex. This revised distortion parameter is plotted Fig. 7.13b for both investigated height-to-diameter ratios. It is quite evident from this plot that the onset of separation significantly effects the distortion within the vortex. As separation is initiated a step increase in the distortion is observed within the vortex. As the velocity ratio reduces further the separation grows radially away from the wall (Fig. 7.12e-f) and the rate of increase in distortion with reducing velocity ratio is now significantly larger (Fig. 7.13b).

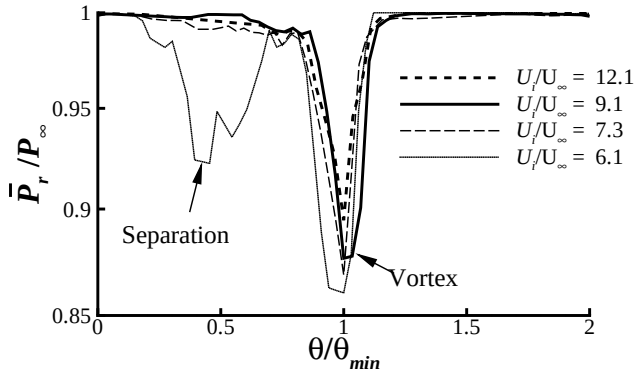

Figure 7.14: Radially averaged circumferential pressure plots for various velocity ratios at a $h/D_l = 0.25$

To further examine the effect of separation on the vortex, the radially averaged circumferential pressure distribution has also been plotted for a various velocity ratios with

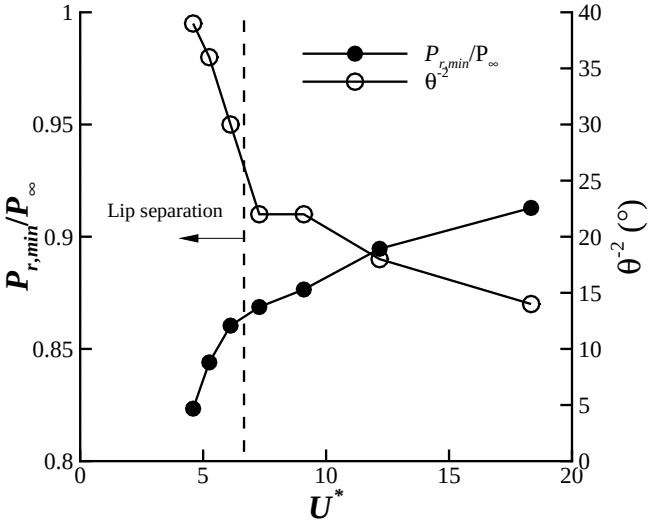

(a)

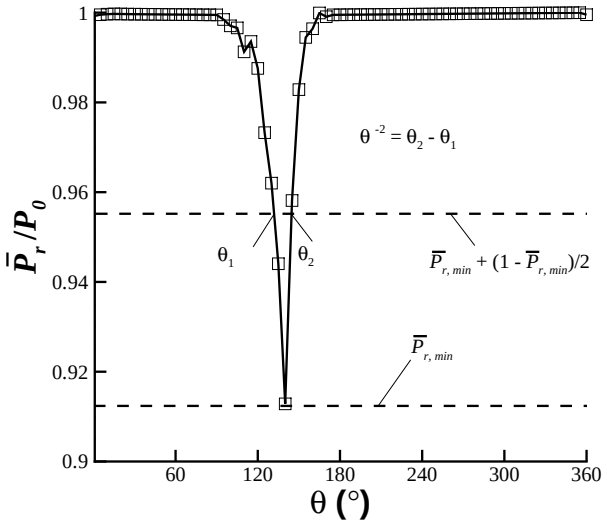

(b)

Figure 7.15: Effect of velocity ratio on the minimum average radial pressure ratio and the extent at 50% of the minimum pressure

and without separation (Fig. 7.14). At a velocity ratio of 6.1, when separation first occurs, a broadening of the vortex loss signature is observed along with a greater pressure loss (Fig. 7.14). This can clearly be seen in Fig. 7.15a which plots the loss extent, θ^{-2}, at 50% of the minimum pressure loss, $\overline{P}_{r,min}$, (Fig. 7.15b for definition) against velocity ratio. Also included in the figure is the minimum radial average pressure, $\overline{P}_{r,min}$, loss against velocity ratio. At the onset of separation, between $U^* = 7.3$ and 6.1, a step increase in the loss extent of the vortex is observed. The increase in the extent, θ^{-2}, is considerably larger than the increase in the minimum radial average pressure. It is therefore the increase in pressure loss foot print at the fan face which largely accounts for the step increase in distortion as separation occurs.

The reason for the increase in the total pressure loss and also the vortex circulation, as separation occurs, is expected to be related to a change in the sucked streamtube characteristics. A significant flow blockage is introduced on the windward side of the intake and as a consequence it is possible that a larger proportion of mass flow is therefore drawn in from behind the intake on the leeward side. Since the source of vorticity for the ground vortex under crosswind conditions is associated with that shed off the intake surface, the ingested vorticity will therefore increase.

At the higher ground clearance of $h/D_l = 0.4$ the distortion initially increases and reaches a local maximum at $U^* = 7.4$, this is slightly different to the vortex strength measurements where a local peak occurred at $U^* = 9.1$. This discrepancy is attributed to the intermittent attachment of the lower trailing vortex to the ground at a $U^* = 7.4$. At this velocity ratio the lower trailing vortex was only very occasionally seen to attach to the ground and it is expected that when no vortex can be detected at the PIV plane, the ground vortex instead forms a trailing vortex off the leeward edge of the intake. Full scale engine visualizations in crosswind (§A.3) show that, during this intermittent attachment phase, when the vortex is not attached to the ground and trails in the crosswind direction (positive y-direction), the vortex is still ingested into the intake at approximately the same location as when the vortex is in contact with the ground. Only when the velocity ratio is further reduced no clear vortex can be seen at the fan face.

7.2.2 Effect of Ground Clearance

Two height-to-diameter ratios (h/D_l) of 0.25 and 0.4 have been studied and Fig. 7.11 shows the effect of this height variation on the PIV vortex strength and Fig. 7.13 on the fan face distortion parameter. Both the PIV vortex strength (Fig. 7.11) and fan face distortion (Fig. 7.13) show that the lower non-dimensional height ($h/D_l = 0.25$) results in a stronger vortex and consequently larger fan face distortion. At the larger velocity ratios the differences are modest and both the vortex circulation (Fig. 7.11) and the intake distortion (Fig. 7.13) show that the ground vortex reduces with increasing velocity ratio for both ground clearances investigated. For the highest velocity ratios ($U_i/U_\infty > 7$), when a vortex is ingested at both non-dimensional heights, it is evident that a 60% increase in the ground clearance (i.e. from an $h/D_l = 0.25$ to 0.4) only

results in a modest decrease in the vortex strength and distortion. This is particularly evident in the distortion measurements (Fig. 7.13a).

However, there are some notable differences due to the ground clearance at the lower velocity ratios ($U_i/U_\infty < 7$) where the results diverge depending on the non-dimensional height (h/D_l) (Figs. 7.11 and 7.13). For the larger ground clearance ($h/D_l = 0.4$), as mentioned above, the vortex circulation reaches a maximum at a velocity ratio of 9.1, below which the vortex diminishes. A similar effect is seen DC_{60} measurements, although the local maximum occurs at a slightly different velocity ratio ($U_i/U_\infty = 7.4$). This is in contrast with the lower height configuration ($h/D_l = 0.25$) where the vortex strength and duct distortion monotonically increase as the velocity ratio reduces. The reason for these differences is due to the different interaction of the sucked streamtube with the ground plane. As discussed above, a necessary condition for the ground vortex formation is that the sucked streamtube is sufficiently large to intersect with the ground plane. The approaching sucked streamtube reduces in tandem with the velocity ratio and, for this reason, at each intake height there is a specific velocity ratio at which the approaching sucked streamtube lifts clear of the ground. This is the expected point at which the ground vortex will cease to occur and is indicated as U^*_{crit} in Figs. 7.11 and 7.13. As already mentioned these limits are never reached for the individual height configurations due to wind tunnel limitations.

For the larger height of $h/D_l = 0.4$, some interesting behaviour is observed for velocity ratios below 9.1 (i.e. as the vortex strength is diminishing with reducing U^*). As already explained the discrepancy in the velocity ratio of maximum strength and maximum distortion is attributed to the intermittent attachment of the ground vortex to the ground plane. As can be seen from the full scale engine test visualizations in Appendix A.3, the vortex can be ingested into the intake, but is not always attached to the ground. This is clearly evident in Figs. A.5a and A.6e-f in Appendix A.3. This is believed to be what is occurring at a velocity ratio, (U_i/U_∞) of 7.4 at the highest ground clearance of 0.4 (h/D_l). The PIV measurements for this configuration show that only occasionally, a strong clockwise vortex is observed at the PIV plane (Fig. 7.16a). Due to the strength and rotation of the vortex, this is clearly the 'cross-wind' vortex which is associated with the lower trailing vortex that would form if the intake was far from the ground. When this strong vortex is not observed inside the measurement domain, sometimes it can be detected just outside from the vector orientations and magnitude. However, often no strong vortex can be detached inside or outside the interrogation region. When this is the case, weaker clockwise, counter-clockwise and sometimes contra-rotating vortices were observed at the PIV plane (Fig. 7.16b-c). These flow features under crosswind conditions has never been reported previously and contradicts the 'rotation bias' reported by de Siervi et al[10]. It is clear that since the 'crosswind' ground vortex is expected to have formed a trailing vortex, a switch in the dominant vorticity source has occurred and is now associated with the approaching boundary layer vorticity. This can be seen in Fig. 7.16b which shows two contra-rotating vortices rotating in accordance with the headwind formation mechanism. This behaviour has also been seen in full scale engine tests, as shown in Fig. A.8.

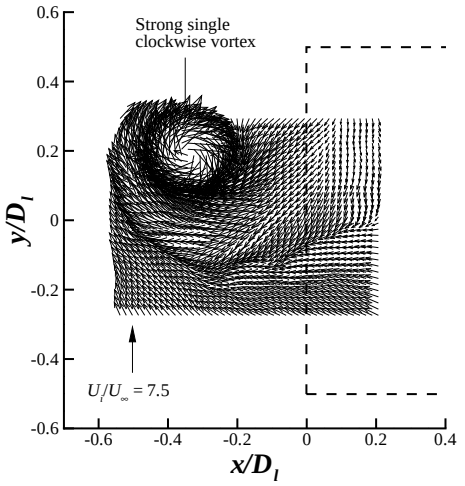

(a) Strong clockwise vortex

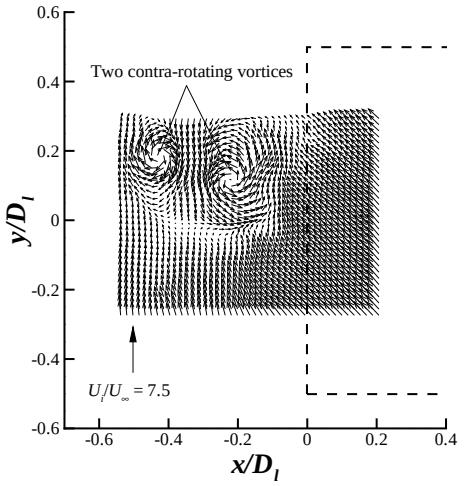

(b) Two contra-rotating vortices

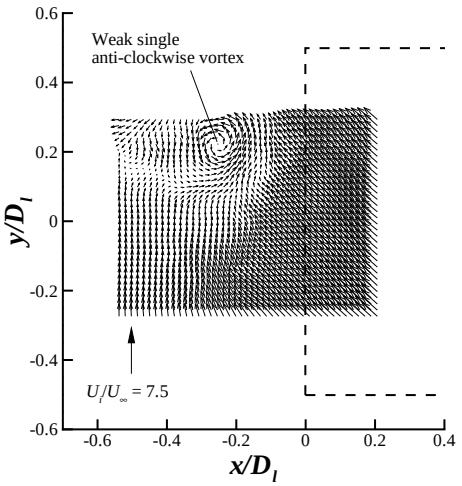

(c) Weak anti-clockwise vortex

Figure 7.16: Example snapshots under crosswind conditions, revealing different flow modes at a velocity ratio close to the critical ($h/D_l = 0.4$, $\delta^*/D_l = 0.11$ and $M_i = 0.55$)

The above observations suggest that the disappearance of a strong vortex does not necessarily coincide with the sucked streamtube lifting off the ground plane, but rather there is insufficient interaction of the capture streamtube with the near wake region of the intake to cause the lower trailing vortex to attach to the ground. In this case the approaching boundary layer vorticity dominates and it is this that causes weaker vortices to form. This will be discussed further when comparing the headwind and crosswind formation mechanisms in the discussion section at the end of this chapter.

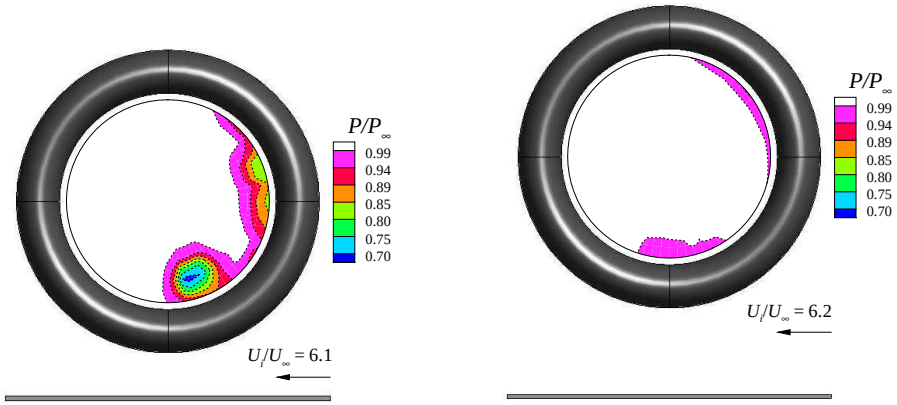

(a) (b)

Figure 7.17: Contours of total pressure at the fan face for (a) an $h/D_l = 0.25$ and (b) an $h/D_l = 0.40$ at a comparable velocity ratio of $U_i/U_\infty \approx 6.2$ and at constant $\delta^*/D_l = 0.93$.

Also of significant importance is the sensitivity of ground clearance to the separation behaviour. It has already been mentioned above that lip separation effects the vortex characteristics; however it is also clear from the total pressure survey, that the vortex affects the onset of separation. One of the major consequences of ground vortex ingestion is the mass flow distortion that it introduces to the fan face. This distortion is most significant when in crosswind due to the large size of the total pressure loss region at the fan face (in comparison to headwind) (Fig. 7.12). Since the ingested mass flow is held constant, the non-uniformity introduced by the ingested vortex forms an effecting flow blockage and additional mass flow must be ingested elsewhere in the intake to account. This places additional local lip loading on other areas within the intake resulting in a premature lip separation on the windward side. This has clearly been demonstrated in Fig. 7.17 which shows the effect of ground clearance on the fan face total pressure contours. For the low ground clearance ($h/D_l = 0.25$), due to the interaction of the sucked streamtube with the ground, a large single ground vortex is ingested (Fig. 7.17a) which is also accompanied by lip separation on the windward side of the intake, at this velocity ratio. In contrast, at the same velocity ratio but at a higher ground clearance of $h/D_l = 0.4$ (Fig. 7.17b), no clear vortex is ingested and no significant lip separation occurs. This is clear evidence of premature lip separation induced by ground vortex ingestion and is very significant not only to the performance of the engine but also to fan vibration. In addition, this clearly demonstrates that the ground plane must be incorporated to assess intake lip performance during the design

process.

In terms of the vortex strength sensitivity to ground clearance (Figs. 7.11 and 7.13), although the differences at high velocity ratios are small it is expected that the lower ground clearance generates a stronger vortex due to the increased interactional effect of the suck stream-tube with the ground. It is known in the literature that an intake in proximity with the ground redistributes the pressure field around the intake circumference, increasing lip loading towards the top. This results in a larger proportion of mass flow being ingested from above the intake[17]. As a consequence, the local sucked streamtube size over the intake increases which leads to an increased level of interaction with the intake surface. As a consequence the level of ingested vorticity shed from the outer intake will increase leading to a stronger vortex.

7.2.3 Approaching Boundary Layer Thickness

As mentioned in §5.2.3 an atmospheric boundary layer, which is applicable to a full scale intake in practice, could not be replicated in the wind tunnel. Hence, in order to establish the sensitivity of the approaching boundary layer thickness on ground vortex formation and characteristics a number of boundary layer thicknesses were studied by utilizing the boundary layer suction methods upstream of the intake (see Fig. 3.2). The effect of the orientation of vorticity within the approaching boundary layer has previously been studied qualitatively on the crosswind formation mechanism[10]. However, this study concentrated on its effect on the vortex rotation, rather than the vortex strength and distortion characteristics. From this previous research, it was found that the upstream vorticity orientation had no influence on the vortex sense of rotation. The conclusion was that the dominant source of vorticity for the vortex was associated with the lower trailing vortex that would form when the sucked streamtube has no ground plane contact (see Fig. 2.10). It is therefore the rotation of the vorticity associated with this trailing vortex that determines the sense of rotation for the ground vortex. As far as the author is aware no sensitivity study has been conducted on the effect of boundary layer thickness, δ, under 90° crosswind conditions. Within this research (for $\psi = 90°$) two boundary layer thicknesses of $\delta^*/D_l = 0.11$ and 0.03 were investigated and Fig. 7.18 shows the effect of this variation on both the non-dimensional vortex strength and in-duct distortion parameter.

Both the vortex strength at the PIV measurement plane (Fig. 7.18a) and the distortion at the fan face (Fig. 7.18b) show that a reduction in the approaching boundary layer thickness from $\delta^*/D_l = 0.11$ to 0.03 has no notable effect. In terms of the vortex strength this is not surprising given the results under headwind conditions* (§5.2.3) where the peak vortex strength was largely unaffected by the same change in the approaching boundary layer thickness (i.e. $\delta^*/D_l = 0.11$ to 0.03). In addition, as mentioned in §5.2.3, the integrated vorticity within the approaching boundary layer, per unit width, is approximately the same between the two boundary layer configurations

*Particularly since under headwind conditions the primary vorticity source is the approaching boundary layer

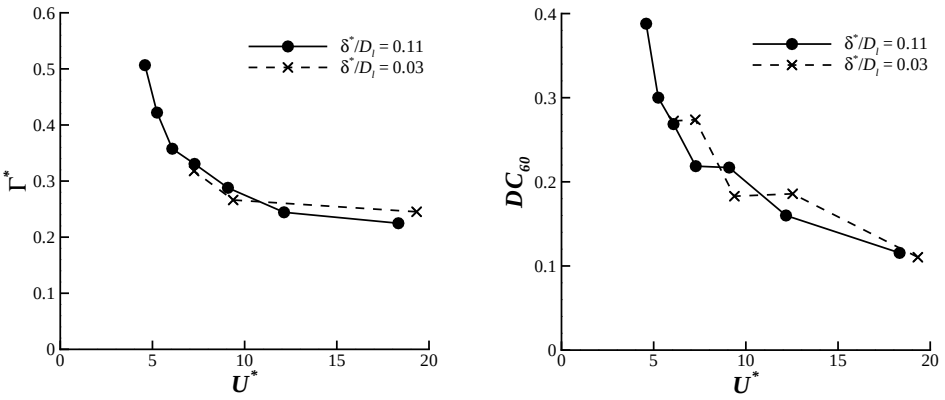

Figure 7.18: Effect of approaching boundary layer thickness on (a) the PIV vortex strength and (b) fan face distortion, DC_{60}, for an $h/D_l = 0.25$

(see Appendix C.1). One would expect that if the vortex is effected by the approaching flow, a smaller distortion, DC_{60}, would be observed at the fan face for the $\delta^*/D_l = 0.03$ boundary layer. This is because the ingested air within the sucked streamtube will contain higher momentum flow in comparison to the $\delta^*/D_l = 0.11$ configuration (as with the headwind mechanism). The negligible difference observed between the boundary layer thicknesses implies that the source of flow for the vortex is not associated with the approaching flow. This finding agrees with the observations put forward by de Sievri et al[10] that the vortex is associated with the near wake region of the intake.

7.2.4 Effect of Yaw Angle

A study has also been conducted to examine the sensitivity of the vortex characteristics to the mean wind direction (ψ) relative to the intake. Within previously published literature the ground vortex formed in pure crosswind conditions (i.e. $\psi = 90°$) has always been regarded as the strongest vortex[6] (relative to smaller yaw angles), however this has not been quantitatively proven, and no data is available to quantify the relative difference between the headwind and crosswind mechanisms. In addition, since crosswind conditions generally represent the design limit of intakes (due to separation), it is of interest to understand how sensitive the vortex strength and distortion is to moderate reductions in the crosswind direction. Within this work a range of yaw angles (ψ) have been investigated between 0 and 90 degrees primarily at a velocity ratio, $U^* = 19$ ($U_\infty = 10ms^{-1}$). Due to slight differences in the intake velocity as the yaw angles changes, the velocity ratio ranged from 18.3 to 19.4. Measurements were predominately taken at the fan face distortion with a smaller dataset being taken to quantify the effect on the vortex strength at the PIV measurement plane.

The vortex aligned average has been used to demonstrate the effect of reducing yaw angle from a 90 degree crosswind ($\psi = 90°$) to a pure headwind configuration ($\psi = 0°$)

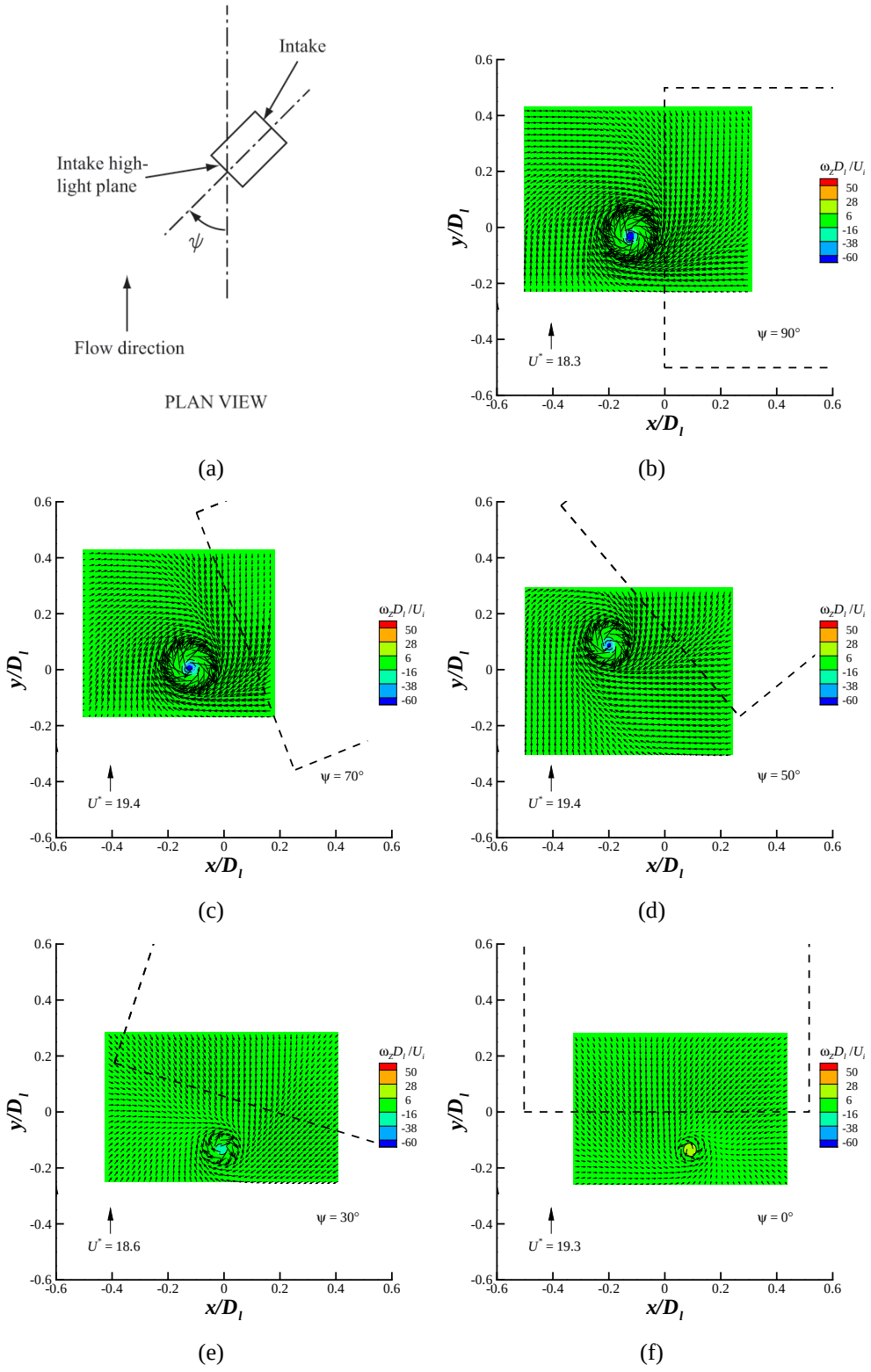

Figure 7.19: Effect of yaw angle, ψ, on the conditional average flowfield at a fixed height of $h/D_l = 0.25$ and approaching boundary layer thickness, $\delta^*/D_l = 0.11$ and velocity ratio of $U^* = 19$

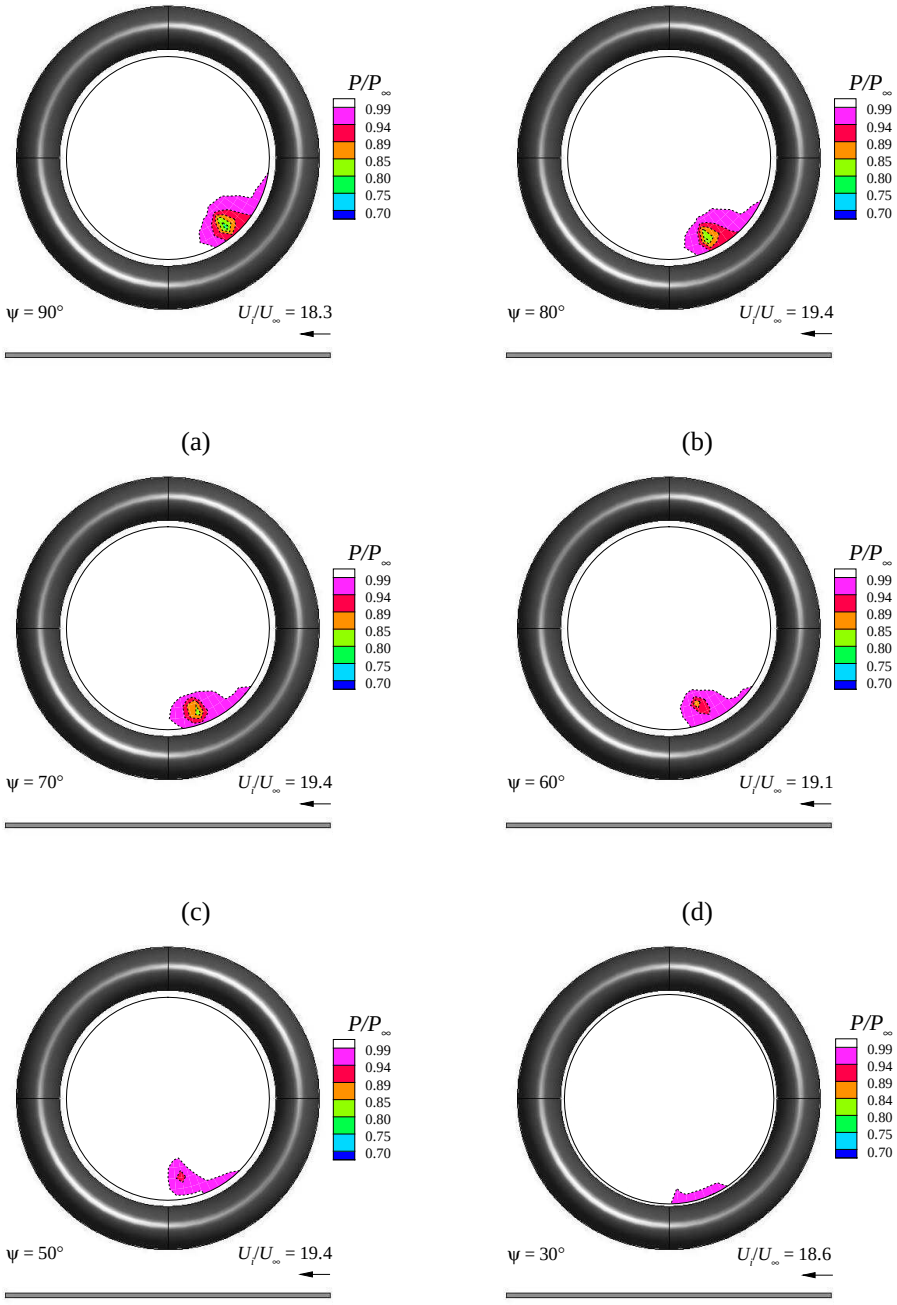

Figure 7.20: Total pressure contours at the fan face for reducing yaw angle, ψ, at a fixed height of $h/D_l = 0.25$ and approaching boundary layer thickness, $\delta^*/D_l = 0.11$ and velocity ratio of $U^* = 19$

on the vortex flow-field at the PIV measurement plane (Fig. 7.19). A reduction from $\psi = 90°$ to $\psi = 70°$ shows no notable difference in the velocity vector magnitudes however there is a difference in the peak vorticity level which has reduced from approximately -80 to -70 ($\omega_Z D_l/U_i$). The largest difference in the vector field is observed between yaw angles of 50 and 30°, where there is a significant reduction in the velocity vector magnitude (Fig. 7.19c-d). For all investigated non zero crosswind angles, with the velocity ratio U^* at 19, only a single vortex is observed which has negative vorticity. However a change from a 30° to a 0° headwind configuration leads to a change in the rotation of the dominant vortex (Fig. 7.19e) which now has positive vorticity. The change in rotation is expected to be due to a change in the dominant vorticity source or possibly due to an increasing influence from the induced vorticity for a pure headwind configuration. As discussed in § 5 it is expected that only a single vortex is observed under headwind conditions ($\psi = 0°$), for a velocity ratio of 19 (U^*), due to very small asymmetries present in the tunnel flowfield.

The effect of reducing the yaw angle, ψ, from 90 degrees on the total pressure contour patterns at the fan face is shown in Fig. 7.20. As mentioned above, at 90 degrees crosswind the vortex is ingested at the 140° position and at a radial position equal to $0.84 r_v/r_i$. The contour plot for this configuration is again shown in Fig. 7.20a. As the crosswind angle (ψ) reduces the vortex moves clockwise around the intake and slightly inboard; at 50° yaw the vortex is at a circumferential position of 170 degrees and a radial position of $0.74 r_v/r_i$ (Fig. 7.20e). The most notable difference in the fan face total pressure contours occurs between the yaw angles of 50 and 30° (Figs. 7.20e-f), as with the vector plots (Figs. 7.19c-d), where no loss core can be identified at a yaw angle of 30°.The contour plot at this yaw angle looks largely the same as the $\psi = 0°$ configuration. This change in the radial location of the vortex and loss footprint perhaps indicates a cessation in the formation of a trailing vortex off the leeward edge of the intake between the yaw angles of 50 and 30°.

In terms of the vortex strength a reduction in the yaw angle was found to have a $\sin^3$ variation on the vortex strength. This is shown in Fig. 7.21a where the vortex circulation data with yaw angle has been non-dimensionalized by the corresponding values at 0 and 90 degrees yaw ($\psi = 0$ and 90°) in the form given by Eq. 7.2.2. Similar observations were also seen for the distortion, DC_{60}, however this parameter followed a $\sin^6$ variation (Eq. 7.2.3) (Fig. 7.21b). This is expected to be due to the fact that the pressure scales with the velocity squared.

$$\eta = \frac{\Gamma^*_\psi - \Gamma^*_{\psi=0}}{\Gamma^*_{\psi=90} - \Gamma^*_{\psi=0}} = \sin^3\psi \tag{7.2.2}$$

$$\zeta = \frac{DC_{60}^{\psi} - DC_{60}^{\psi=0}}{DC_{60}^{\psi=90} - DC_{60}^{\psi=0}} = \sin^6\psi \tag{7.2.3}$$

The variation in the vortex strength can be partly explained by considering the expected mechanism that sets the vortex strength under crosswind conditions. As explained

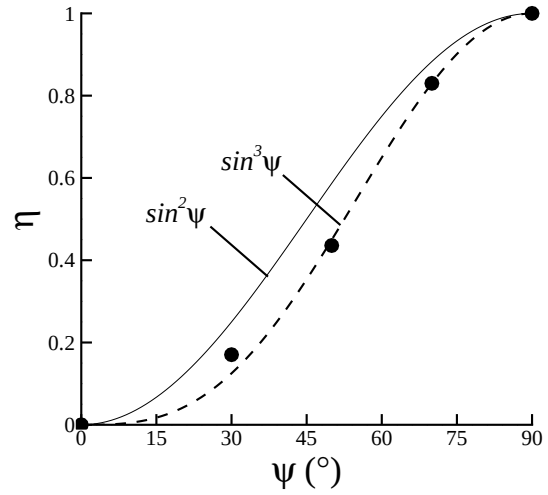

(a)

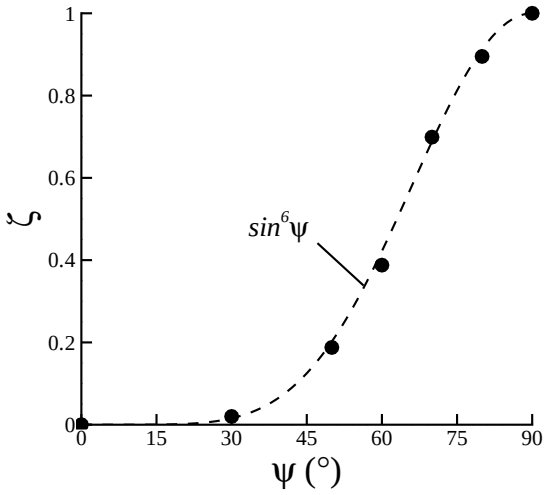

(b)

Figure 7.21: Normalized (a) non-dimensional circulation, Γ^*, and (b) fan face distortion, DC_{60}, against yaw angle for an $h/D_l = 0.25$ and approaching boundary layer thickness, $\delta^*/D_l = 0.11$ and velocity ratio of $U^* = 19$

above the vorticity source, at least under significant crosswind angles, is related to the vorticity created over the intake surface. This fundamentally depends on the crosswind component of velocity (*v* velocity); the stronger the *v* velocity, the higher the levels of vorticity that will be generated over the intake surface and therefore into the near wake of the intake. The crosswind component varies as the sine of the crosswind angle (ψ). However what also matters is the total area of the intake encompassed by the sucked streamtube. The larger the crosswind angle the larger the amount of vorticity ingested from the intake outer surface. This will fundamentally depend on the orientation of the capture streamtube relative to the intake axis and will also vary with the sine of the crosswind direction (ψ). Equating the two factors gives a sine squared variation, which has also been plotted in Fig. 7.21a and does not show a significant difference from a sine function to the power of three. The extra $\sin\psi$ term, required to give a $\sin^3$ relationship, could be related to the change in the sucked streamtube shape as the yaw angle and hence interaction of the capture streamtube with the intake increases.

7.3 Further Discussion

A comparison between the crosswind and headwind formation mechanisms in terms of vortex strength and distortion is shown in Fig. 7.22. The trend with velocity ratio is largely the same for both mechanisms; high velocity ratios are associated with a weak vortex and as the velocity ratio reduces the vortex strength and distortion progressively increase to a local maximum. In terms of vortex strength, the largest differences between the headwind and crosswind mechanisms are seen at the largest velocity ratios and at the lowest non-dimensional heights. One of the most notable differences between the two formation mechanisms, however, is the opposing trend with ground clearance for intermediate velocity ratios (7 ¡ U^* ¡ 19). For crosswind, low ground clearances result in a strong vortex whereas for headwind, in this velocity ratio region, the opposite is true. In crosswind it is the ingested vorticity from the intake surface that matters. This will increase at lower non-dimensional heights, due to the larger interaction with the ground plane which ultimately results in a larger interaction of the sucked streamtube with the intake surface. In contrast, under headwind conditions, it is the approaching and induced vorticity sources that dominate, and it is the balance between both which is expected to result in a stronger vortex being observed at higher ground clearances (for intermediate velocity ratios). However, as was seen in the foregoing chapter, at high velocity ratios with the removal of the approaching vorticity source, a stronger vortex was still seen at higher ground clearances. This implies that the induced vorticity is the cause for a stronger vortex at higher ground clearances; however the exact mechanism is unknown.

The most significant conclusion must be taken from the in-duct distortion measurements where the difference between headwind and crosswind conditions is very significant. The reason for the greater difference being observed in the DC_{60} trend in comparison to the circulation measurements is twofold. Firstly in headwind condi-

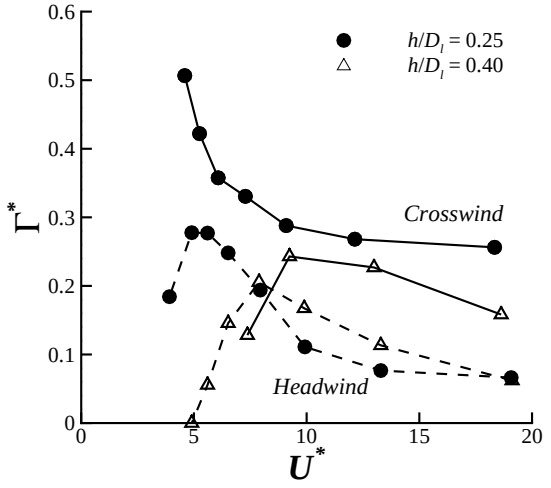

(a)

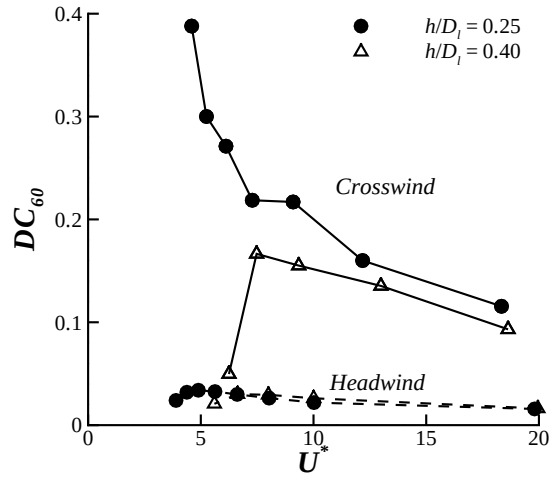

(b)

Figure 7.22: Comparison of the trends with velocity ratio and non-dimensional height between the crosswind and headwind formation modes

tions, two vortices were observed and the vortex strength results plotted in Fig. 7.22a is a sum of the absolute magnitudes of both average vortex strengths. In contrast, under crosswind conditions predominately a single vortex was observed for all configurations. This single vortex is in general three times the strength of any single vortex generated under headwind conditions with all other conditions the same. Since the pressure is proportional to the velocity squared, a crosswind vortex that has a strength of say $6m^2s^{-1}$ will generate a distortion in the order of 9 times larger than a single headwind vortex with a strength of $2m^2s^{-1}$. For two headwind vortices of $2m^2s^{-1}$ the distortion will be approximately 4.5 times larger. Secondly the differing distortion levels is related to the differing vorticity sources between the two mechanisms, which is the reason for a stronger vortex being observed under crosswind conditions. However an important distinction between the headwind and crosswind cases is that approximately 40% of the distortion for the former is a result of vortex induced boundary layer separation within the intake duct. Therefore potentially, the difference between the two mechanisms in terms of DC_{60} is even larger than portrayed in Fig. 7.22b. On the other hand, as will be discussed in the following chapter, Zantopp[71] has shown that the vortex induced separation is a Reynolds number effect. Hence, although there is no evidence, a similar feature could be present in the crosswind results, but because the loss under such conditions is significantly larger, such features are not as easily identifiable.

7.4 Summary

Ground vortex formation under 90 degree crosswind conditions has been comprehensively characterized. Both external velocity flowfield measurements and in-duct total pressure measurements have been used to establish the underlying features of the flowfield. The important non-dimensional parameters have been investigated, including the velocity ratio (U_i/U_∞), ground clearance (h/D_l), approaching boundary layer thickness (δ^*/D_l) and intake Mach number (M_i). In addition the effect of yaw angle has been quantitatively established and the relative difference between the crosswind and headwind mechanisms has been identified and discussed. This is the first known study of its kind to provide both vortex strength and in-duct distortion measurements for such a vast array of configurations. The most important conclusions are summarized below:

1. Ground vortex formation under crosswind conditions leads to premature lip separation.

2. The crosswind ground vortex generates at least a three times stronger vortex in comparison to any single vortex produced in headwind conditions. However the distortion, DC_{60}, is at best 20 times greater and at worst 40 times larger in comparison to headwind conditions.

3. At the datum height of 0.25 (h/D_l) the vortex strength and distortion monotonically increase with reducing velocity ratio.

4. The increase in vortex strength with reducing velocity ratio is believed to be related to the greater level of vorticity being generated over the intake surface as the crosswind velocity increases.

5. The vortex strength scales with the intake Mach number.

6. Lower ground clearances generate a more intense vortex and is conjectured to be a result of a greater interaction of the sucked streamtube with the intake outer surface leading to higher level of ingested vorticity off the intake surface.

7. At a h/D_l of 0.4 the vortex strength reaches a maximum and reduces thereafter at a velocity ratio approximately 1.5 times the expected critical

8. The reduction in strength is associated with a change in the dominant vorticity source, from that associated with the near wake of the intake, to the approaching boundary layer vorticity. This change was signified by the occurrence of a range flow modes in which clockwise, counter-clockwise and a pair contra-rotating vortices were observed.

9. The approaching boundary layer thickness was found to have no notable difference in the vortex strength and in-duct distortion.

10. The variation in yaw angle from a ninety to a zero degree configuration was found to have a $\sin^3$ variation on the vortex strength and $\sin^6$ variation on the fan face distortion, DC_{60}.

CHAPTER 8

Discussion and Synthesis

In the preceding chapters a wealth of quantitative experimental data on the ground vortex, under a number of operating conditions, has been presented. This dataset has provided a significant insight into the formation characteristics and understanding of the ground vortex behaviour. In particular trends have been established on the vortex strength at the PIV plane and distortion at the fan face by varying important geometric and aerodynamic parameters, such as ground clearance (h/D_l),velocity ratio (U_i/U_∞), and approaching boundary layer thickness (δ^*/D_l). In this chapter a number of methods are proposed for modelling the ground vortex characteristics which capture the trends observed. One approach is to develop an empirical based method and the second approach is a purely analytical model.

The motivation for this section is driven by two aspects. From an industrial perspective it is advantageous to have accurate knowledge of the vortex characteristics (i.e. the vortex strength, size and distortion) to determine its impact on the downstream turbomachinery. For example current vortex induced fan vibration analysis relies on CFD predictions of ground vortex ingestion. The solution at the fan face, which includes the ingested vortex, is imposed as a boundary condition upstream of a modelled fan assembly[16]. However this method has drawbacks as there is no control of the boundary conditions and it is difficult to interpret the results without knowing the characteristics of the vortex which has been imposed. This therefore presents a difficultly in ascertaining whether any change in the modal forces between fan blade designs is a result of a change in the vortex characteristics or due to a change in the blade design itself. For this reason it would be advantageous to have a boundary condition code which can prescribe a 'standard' or user defined vortex upstream of the fan blades. Experimental results have shown that the ground vortex agrees with known vortex models (§4-7). Such models can be used to predict the vortex only velocity field, which is vital in being able to determine the boundary conditions; however knowledge of the vortex strength and size is required. Although generating boundary conditions is beyond the remit of this project, a method of determining the vortex strength for a given configuration is possible and this is one aim of this chapter.

In addition to the industrial viewpoint, from an academic perspective it is desirable to seek an analytic solution that can predict the vortex strength. If such an *a priori*

prediction exists it would demonstrate that the underlying mechanisms involved are fully understood. Even if such a tool cannot completely capture the physics, it should be instructive in understanding the fundamental mechanisms.

This chapter presents two prediction methods, both of which can be used to determine the vortex strength. The first is an empirically based model, centred on the self-similar property of the characteristic non-dimensional vortex strength against velocity ratio profiles. The second is a theoretically based model, which primarily takes into account the vorticity source within the approaching boundary layer to predict the vortex strength. This theoretical model first is compared to the experimental results and then is used to examine additional configurations that have not been experimentally investigated. Finally a discussion is given which summarizes the results from the model and includes a discussion of results from supporting work which addresses important issues such as Reynolds and Mach number influences.

8.1 Empirical Model

In this section an empirical vortex strength prediction tool is presented. The model is based around a function which is used to model the aerodynamic self-similarity property presented in §5.4, along with additional correlations to determine the vortex strength for a variety of configurations. This model can predict the vortex strength, Γ, and distortion, DC_{60}, at the fan face for any height-to-diameter ratio, h/D_l, U_i/U_∞ and approaching boundary layer, δ^*/D_l, under headwind conditions. An extension to this model is also presented with enables the vortex characteristics to be determined for any yaw angle between 0 and 90°. The following section describes the methodology behind the model which is then followed by an example application.

8.1.1 Headwind Vortex Strength Empirical Model

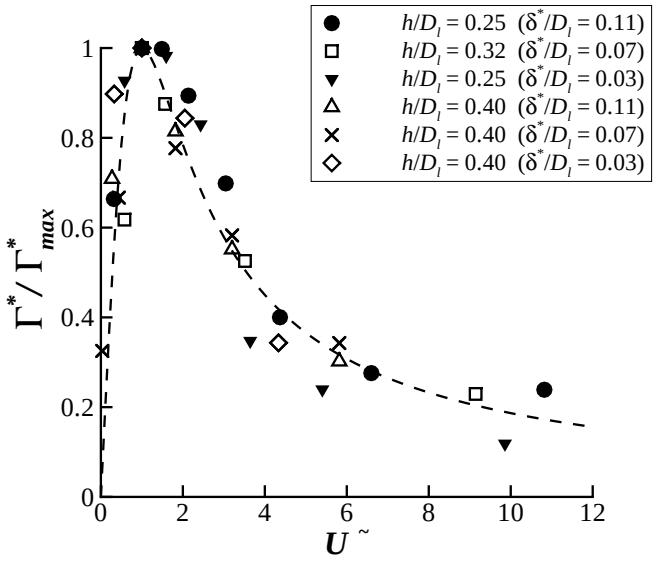

Figure 8.1: Self-similar profiles of (a) non-dimensional vortex strength, Γ^* and (b) distortion coefficient, DC_{60} in headwind conditions

$$U^{\sim} = \frac{\dfrac{U^*}{U^*_{max}} - U^*_R}{1 - U^*_R} \tag{8.1.1}$$

$$U^*_{crit} = \left(\frac{U_i}{U_\infty}\right)_{crit} = 4\rho^* \left(\frac{D_l}{D_i}\frac{h}{D_l} + \frac{D_l}{2D_i}\right)^2 \tag{8.1.2}$$

$$\frac{\Gamma^*}{\Gamma^*_{max}} = \frac{2^{1/k} U^{\sim}}{\left[1 + U^{\sim 2k}\right]^{1/k}} \tag{8.1.3}$$

The self-similar vortex strength against velocity ratio plot, originally shown in §5.4, is again shown in Fig. 8.1a, but in a slightly altered form to aid the curve fitting process. Here the abscissa has been transformed using Eq. 8.1.1 so that the data goes through the origin and enables the results to be modelled using Eq. 8.1.3. The parameter, U^*_R, in Eq. 8.1.3, is the ratio U^*_{crit}/U^*_{max}. This is the ratio of the vortex blow-away (or critical) velocity ratio to the velocity ratio at which the maximum strength vortex occurs, for a given non-dimensional height. This ratio is determined from the intersection of the self-similar vortex strength curve with the *x*-axis and is a constant equal to 0.65 (§5.4). This value represents the average for all configurations tested. The critical velocity ratio, U^*_{crit}, is the velocity ratio at which the sucked streamtube lifts of the ground plane. This is calculated using Eq. 8.1.2 and is derived from continuity considerations assuming a circular axi-symmetric capture streamtube at far field upstream of the intake. The ratio $\rho^* = \rho_\infty/\rho_i$ in Eq. 8.1.2 is ratio of the density of the approaching flow at far-field, ρ_∞, divided by the density of the flow at the intake throat, ρ_i.

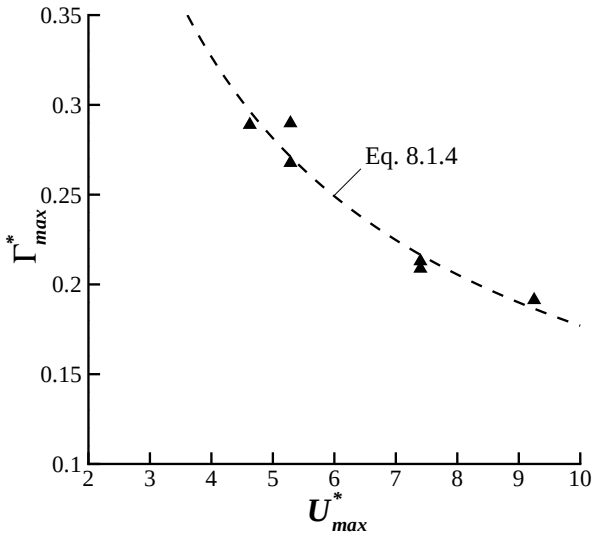

Figure 8.2: Correlation of maximum strength vortices against the corresponding velocity ratio ($\psi = 0°$)

With the vortex strength self-similar profile in the form shown in Fig. 8.1 a least squares curve fit of the data has been performed to determine the factor *k* in Eq. 8.1.3. For the vortex strength the *k* factor equals approximately 1.1. In order to determine the vortex strength for any velocity ratio and height-to-diameter ratio (h/D_l) knowledge of Γ^*_{max} and U^*_{crit} is required. From experiments it has been shown that the vortex blow-away condition, U^*_{crit}, approximately matches the velocity ratio when the sucked streamtube has no ground plane contact (§5.3). This criterion is given by Eq. 8.1.2 and is crucial to the model, as it accounts for the effect of ground clearance (h/D_l). In terms of Γ^*_{max}, by correlating all maximum strength vortices, for all configurations, against the corresponding velocity ratio, U^*_{max} (Fig. 8.2) a relationship is found in the form of Eq. 8.1.4. The constants, *b* and *c* are equal to 0.83 and -0.7 respectively. At

this point it should be emphasized that use of Eq. 8.1.3 is limited to the velocity ratios below approximately 19. This is because as the velocity ratio goes to infinity, Γ^*/Γ^*_{max} would tend to zero (i.e. the vortex strength would be zero). This of course is not the case as under quiescent conditions the vortex strength is non-zero (see §4). However results indicate that there is no notable difference in the strength between $U^* = 19$ and ∞. Hence it would be reasonable to assume that for velocity ratios greater than 19 the vortex strength is approximately equal to the no-wind vortex strength.

$$\Gamma^*_{max} = b \cdot (U^*_{max})^c \tag{8.1.4}$$

From experiments under headwind, crosswind and rolling road configurations, the vortex core size is on average 3*mm* or 6% of the intake inner diameter, D_i. It has also been found that the Vatistas shape factor, n, is also generally constant across all configurations and on average is equal to 1. This is a significant finding as with knowledge of the vortex circulation, using the above method, the in-plane, vortex only, velocity field can be calculated for any configuration under headwind conditions using the Vatistas vortex model. This model gives the tangential and radial velocity components given by Eqs. 8.1.5 and 8.1.6 respectively[64] where $r^* = r/r_c$.

$$V_\theta = \frac{\Gamma}{2\pi r_c}\left[\frac{r^*}{(1+r^{*2n})^{1/n}}\right] \tag{8.1.5}$$

$$V_r = \left[\frac{2(1+n)\,r^{*(2n-1)}}{1+r^{*2n}}\right]\frac{\nu}{r_c} \tag{8.1.6}$$

Using the above vortex model the tangential, V_θ, and radial, V_r, velocity components can be calculated. The velocities can then be converted to the Cartesian velocity components using Eqs. 8.1.7 and 8.1.8.

$$u = -V_\theta \sin\theta + V_r \cos\theta \tag{8.1.7}$$

$$v = V_\theta \cos\theta + V_r \sin\theta \tag{8.1.8}$$

8.1.2 Headwind Vortex Distortion Empirical Model

It is also useful, particularly from a CFD validation perspective, to have knowledge of the corresponding distortion, DC_{60}, at the fan face. The simplest method, to predict DC_{60} for any configuration under headwind conditions, is to relate circulation (Γ^*) to DC_{60}. A straight correlation between the circulation and distortion for each configuration is given in Fig. 8.3. Two trends are shown; the first is for an intake Mach number, M_i, of 0.58 and the second for $M_i = 0.43$. The correlations given by Eqs. 8.1.9 and 8.1.10 are different due to the lower distortion magnitude being seen for the latter case as it does not suffer from a vortex induced local separation at the duct surface. This is due to the ingestion location being away from the intake wall (see §5.2.1) for the $M_i = 0.43$ configuration. As will be discussed in §8.3, the vortex induced separation is a Reynolds number effect, therefore although the trend at an $M_i = 0.58$ is at a more representative Mach number, the $M_i = 0.43$ correlation is also given as this does not include the vortex induced separation.

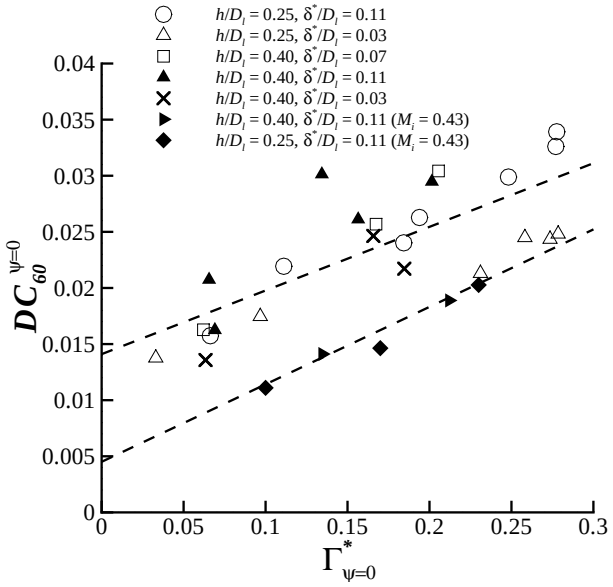

Figure 8.3: Correlation between the headwind fan face distortion, $DC_{60}^{\psi=0}$ and non-dimensional circulation, $\Gamma^*_{\psi=0}$ at two intake Mach numbers

In addition, Fig. 8.3 shows that the regression fit of the data does not go through zero, for both correlations. This is surprising as one would expect zero vortex strength to correlate to zero fan face distortion. It is believed that this condition is not satisfied because of the differences in the shapes of the self-similar curves between the two parameters (see §5.4). Ideally this correlation would go through the origin; however since no data is available close to zero, the correlations shown in Fig. 8.3, given by Eq. 8.1.9 for $M_i = 0.58$ and Eq. 8.1.10 for $M_i = 0.43$, are used to determine the fan face distortion assuming that the corresponding vortex strength is known.

$$DC_{60}^{\psi=0} = 0.0567\Gamma^{*} + 0.0141 \tag{8.1.9}$$

$$DC_{60,2}^{\psi=0} = 0.069\Gamma^{*} + 0.00451 \tag{8.1.10}$$

8.1.3 Extension to Crosswind

Although the formation mechanisms in headwind and crosswind conditions are considerably different, it is possible to use the headwind empirical model to determine the characteristics at other yaw angles by making use of additional experimental correlations and assumptions. This would then enable the vortex only velocity field to be determined for any yaw angle between zero and ninety degrees, with use of Vatistas vortex model (as shown above).

$$\eta = \frac{\Gamma^*_{\psi} - \Gamma^*_{\psi=0}}{\Gamma^*_{\psi=90} - \Gamma^*_{\psi=0}} = \sin^3 \psi \tag{8.1.11}$$

$$\zeta = \frac{DC_{60}^{\psi} - DC_{60}^{\psi=0}}{DC_{60}^{\psi=90} - DC_{60}^{\psi=0}} = \sin^6 \psi \tag{8.1.12}$$

In §7.2.4 the trends of vortex circulation and DC_{60} were presented as a function of yaw angle. It was shown that by non-dimensionalising the circulation trend with crosswind angle by the respective values at zero, $\Gamma^*_{\psi=0}$ and ninety degrees yaw, $\Gamma^*_{\phi=90}$, in form given by Eq. 8.1.11 the data can be modelled by a $\sin^3$ function (Fig. 8.4a). The fan face distortion also follows a similar trend (Fig. 8.4b) however for this parameter the data follows a $\sin^6$ function (Eq. 8.1.12). Since the vortex characteristics can be calculated under headwind conditions ($\psi = 0$) using the above method, a means of determining the characteristics under ninety degree crosswind conditions is required. This will enable the properties at intermediate yaw angles to also be computed. In the following, a crude method of determining the characteristics under ninety degree crosswind conditions is proposed. This will then enable the correlations given by Eqs. 8.1.11 and 8.1.12 for intermediate yaw angles to be implemented.

$$DC_{60}^{\psi=90} = \phi \cdot DC_{60}^{\psi=0} \tag{8.1.13}$$

where

$$\phi = f\,(h/D_l)$$

In general the variation in the vortex strength, Γ^*, and distortion, DC_{60}, with velocity ratio, between the two mechanisms is the same; high velocity ratios are associated with a weak vortex and as the velocity ratio reduces the strength monotonically increases to a local maximum before reducing to zero at the critical velocity ratio. In contrast the effect of ground clearance is different between the headwind and crosswind mechanisms; at intermediate velocity ratios low ground clearances generate a strong vortex for the latter and a weaker vortex for the former. One approach of capturing these trends is to correlate the distortion under headwind conditions, $DC_{60}^{\psi=0}$, with the distortion under crosswind, $DC_{60}^{\psi=90}$, for all investigated velocity ratios, U^*, at each respective non-dimensional height (h/D_l), as shown in Fig. 8.5. Here the DC_{60} parameter

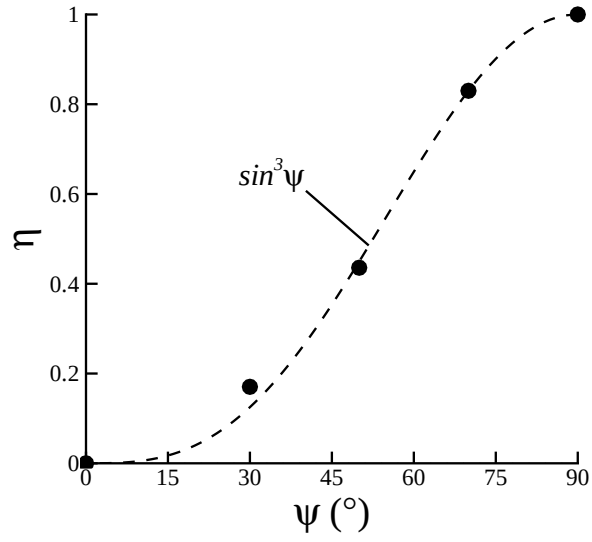

(a)

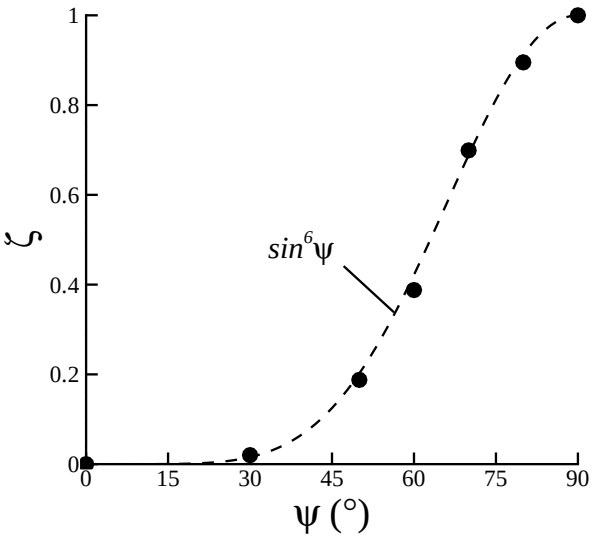

(b)

Figure 8.4: Normalised (a) non-dimensional circulation, Γ^*, and (b) fan face distortion, DC_{60}, against yaw angle

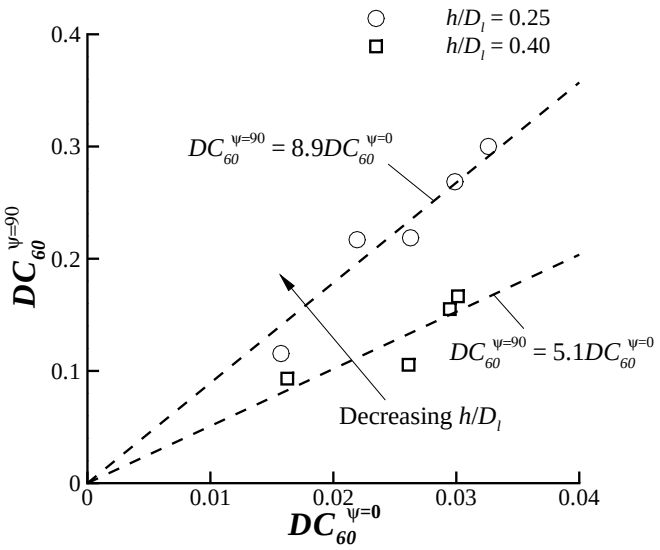

Figure 8.5: Correlation between the distortion under headwind ($\psi = 0°$) and crosswind ($\psi = 90°$) conditions for varying velocity ratio at two non-dimensional heights

is used, rather than the vortex circulation, as it provides a better correlation. In addition the $M_i = 0.58$ distortion data has been implemented, as there is a larger dataset available (Fig. 8.3b). Since the variation with velocity ratio for both mechanisms is largely the same, the correlation results in a linear relationship through the origin, for both non-dimensional heights. The gradient of the line, denoted by ϕ, is then assumed to be purely a function of h/D_l (Eq. 8.1.13). Therefore in order to determine the characteristics for a given height-to-diameter ratio, a relationship is needed between ϕ and the ground clearance, h/D_l. Due to only two common non-dimensional heights being investigated for both mechanisms, a linear dependency is assumed between ϕ and h/D_l as shown in Fig 8.6. Therefore for a given non-dimensional height, ϕ can be calculated using the linear relationship in Fig. 8.6 given by Eq. 8.1.14. Hence with the fan face distortion under headwind conditions, $DC_{60}^{\psi=0}$, being given by the method described in §8.1.2, the distortion under ninety degree crosswind conditions, $DC_{60}^{\psi=90}$, can be calculated using Eq. 8.1.13.

$$\phi = -25.3 \cdot \left(\frac{h}{D_l}\right) + 15.3 \tag{8.1.14}$$

$$\Gamma^*_{\psi=90} = 1.11 \cdot DC_{60}^{\psi=90} + 0.0075 \tag{8.1.15}$$

To determine the vortex circulation under ninety degree crosswind conditions, denoted by $\Gamma^*_{\psi=90}$ the distortion and vortex strength for $\psi = 90$ are again correlated to establish a relationship, as shown in Fig. 8.7. A good correlation is found, however as for the headwind mechanism, the regression fit does not pass through zero. Again this is not ideal and one would expect the data to go through the origin. However since there is

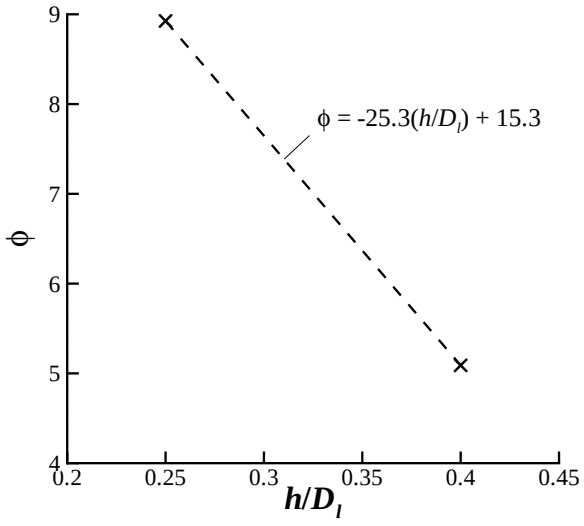

Figure 8.6: Correlation between ϕ and h/D_l

no additional data available at low distortion values this cannot be confirmed and the equation of the line given by Eq. 8.1.15 is used to determine the circulation, $\Gamma^*_{\psi=90}$.

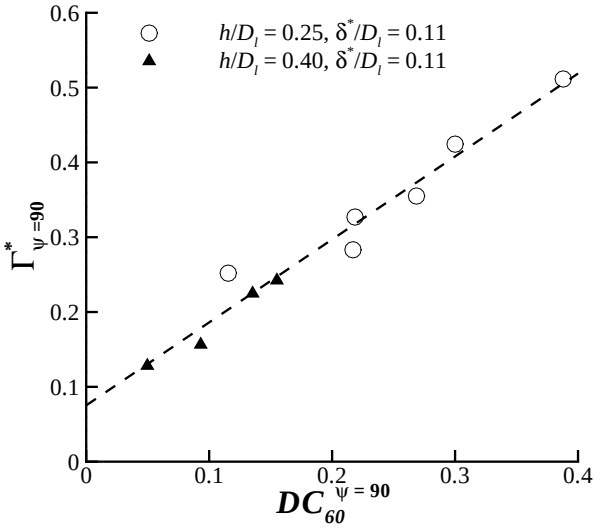

(a)

Figure 8.7: Correlation between non-dimensional circulation, Γ^* and distortion coefficient, DC_{60} for $\psi = 90°$

8.1.4 Example Application

In this section an example application of how to determine the vortex strength and distortion using the empirical model is given. The input values used in this example are summarized in Table 8.1. The procedure to determine the vortex strength under headwind conditions from the initial input parameters is outlined in flow diagram schematic in Fig. 8.8a. The method is also outlined mathematically below. As explained above the vortex core size and Vatistas shape factor are approximately constant across all configurations in headwind and crosswind. The core size is roughly 6% of the intake inner diameter, D_i and the Vatistas shape factor, n, is on average 1. These findings are significant as, along with the empirical prediction tool, that will be outlined below, the vortex only velocity field can be calculated using the Vatistas vortex model (as shown above). This is very useful in developing a boundary condition code for vortex induced fan vibration analysis.

Parameter	Value
U_i	190 ms^{-1}
U_∞	18 ms^{-1}
h/D_l	0.315
D_l	0.12 m
D_l/D_i	1.2
ψ	70°
M_i	0.58

Table 8.1: Input values for example application of empirical model prediction tool

First the equivalent vortex characteristics under headwind conditions must be calculated using the input parameters given in Table 8.1. From the given intake velocity, U_i and headwind speed U_∞, the velocity ratio, U^*, is as follows:

$$U^* = \frac{U_i}{U_\infty} = \frac{190}{18} = 10.556$$

Since the vortex blow-away velocity ratio, U^*_{crit}, is function of the non-dimensional height, h/D_l, this can be calculated using Eq. 8.1.2. However first the density ratio, ρ^*, must be calculated. This is the ratio of the density at far-field, ρ_∞, to the density at the intake throat, ρ_i, and can be calculated using isentropic relations for a given intake Mach number assuming $\gamma = 1.4$[1].

$$\rho^* = \frac{\rho_\infty}{\rho_i} = \left(1 + \frac{\gamma - 1}{2} M_i^2\right)^{1/(\gamma-1)}$$
$$\frac{\rho_\infty}{\rho_i} = \left(1 + 0.2 \times (0.58)^2\right)^{2.5}$$
$$\frac{\rho_\infty}{\rho_i} = 1.178$$

Hence the critical velocity ratio, U^*_{crit}, can be determined given that the non-dimensional height, h/D_l, is equal to 0.315, the diameter ratio, D_l/D_i, is equal to 1.2, and D_i equal to 0.1 via Eq. 8.1.2:

$$U^*_{crit} = \left(\frac{U_i}{U_\infty}\right)_{crit} = 4\rho^* \left(\frac{D_l}{D_i}\frac{h}{D_l} + \frac{D_l}{2D_i}\right)^2$$
$$= 4 \times 1.178 \left(1.2 \times 0.315 + \frac{0.12}{0.2}\right)^2$$
$$= 4.507$$

From experiments the ratio of the critical velocity ratio to the velocity ratio at which the maximum strength vortex, U^*_{max}, occurs is 0.65. This is displayed mathematically below.

$$U^*_R = \frac{U^*_{crit}}{U^*_{max}} = 0.65$$

Hence U^*_{max} is given by:

$$U^*_{max} = \frac{U^*_{crit}}{0.65} = \frac{4.507}{0.65} = 6.934$$

The maximum vortex strength, Γ^*_{max}, for a $h/D_l = 0.315$ can then calculated using the empirical relationship given by Eq. 8.1.4:

$$\Gamma^*_{max} = 0.83 \cdot (U^*_{max})^{-0.7}$$
$$= 0.83 \times (6.934)^{-0.7}$$
$$= 0.214$$

Now in order to calculate the vortex strength for the velocity ratio in question $U^{\sim}$ needs to be computed via Eq. 8.1.1 as follows:

$$
\begin{aligned}
U^{\sim} &= \frac{\dfrac{U^*}{U^*_{max}} - U^*_R}{1 - U^*_R} \\
&= \frac{\dfrac{10.556}{6.934} - 0.65}{1 - 0.65} \\
&= 2.492
\end{aligned}
$$

The ratio Γ^*/Γ^*_{max} can then be calculated using Eq. 8.1.3 given that k is equal to 1.1.

$$
\begin{aligned}
\frac{\Gamma^*}{\Gamma^*_{max}} &= \frac{2^{1/k} U^{\sim}}{\left[1 + U^{\sim 2k}\right]^{1/k}} \\
&= \frac{2^{0.909} 2.492}{\left[1 + 2.492^{2.2}\right]^{0.909}} \\
&= 0.672
\end{aligned}
$$

Therefore the non-dimensional vortex strength under headwind conditions is:

$$
\begin{aligned}
\Gamma^*_{\psi=0} &= \Gamma^*_{max} \times \frac{\Gamma^*}{\Gamma^*_{max}} \\
&= 0.214 \times 0.672 \\
&= 0.144
\end{aligned}
$$

With the intake highlight diameter, $D_{l,}$ equal to $0.12m$ and the intake velocity, U_i, is $190ms^{-1}$, the average vortex strength, $\overline{\Gamma}$, is therefore equal to $3.28m^2s^{-1}$.

The distortion under pure headwind conditions, $\psi = 0$ can then estimated using Eq. 8.1.9:

$$
\begin{aligned}
DC_{60}^{\psi=0} &= 0.0567\Gamma^* + 0.0141 \\
&= 0.022
\end{aligned}
\tag{8.1.16}
$$

Note that if this prediction method is to be applied to a full scale intake, Eq. 8.1.10 may give a more representative DC_{60} value as this correlation does not includes the effects of vortex induced separation within the intake duct at the lower Reynolds number. This will be discussed further in §8.3. However the DC_{60} value given by Eq. 8.1.9 still must be calculated, as it is this value that is correlated with the corresponding distortion under 90 degree crosswind conditions.

Now the characteristics need to be estimated for the ninety degree crosswind case. First ϕ must be evaluated for the non-dimensional height of interest. This given via Eq. 8.1.14.

$$\begin{aligned}\phi &= -25.3 \cdot \left(\frac{h}{D_l}\right) + 15.3 \\ &= 7.331\end{aligned}$$

Therefore the relationship between the distortion under pure headwind and crosswind conditions is given by:

$$\begin{aligned}DC_{60}^{\psi=90} &= 7.331 \cdot DC_{60}^{\psi=0} \\ &= 7.331 \times 0.0223 \\ &= 0.163\end{aligned} \tag{8.1.17}$$

The corresponding circulation value under 90 degree crosswind conditions can then be estimated by Eq. 8.7:

$$\begin{aligned}\Gamma^*_{\psi=90} &= 1.11 \cdot DC_{60}^{\psi=90} + 0.0075 \\ &= 0.189\end{aligned}$$

Since the circulation is desired at $\psi = 70°$ this is now possible using Eqs. 8.1.11. Rearranging this relationship yields:

$$\begin{aligned}\Gamma^*_{\psi=70} &= \left[\Gamma^*_{\psi=90} - \Gamma^*_{\psi=0}\right] \sin^3 \psi + \Gamma^*_{\psi=0} \\ &= [0.045] \sin^3 70 + 0.144 \\ &= \underline{\mathbf{0.181}}\end{aligned}$$

The distortion at the conditions of interest can also be calculated using Eq. 8.1.12.

$$\begin{aligned}DC_{60}^{\psi=70} &= \left[DC_{60}^{\psi=90} - DC_{60}^{\psi=0}\right] \sin^6 \psi + DC_{60}^{\psi=0} \\ &= [0.141] \sin^6 70 + 0.0223 \\ &= \underline{\mathbf{0.119}}\end{aligned} \tag{8.1.18}$$

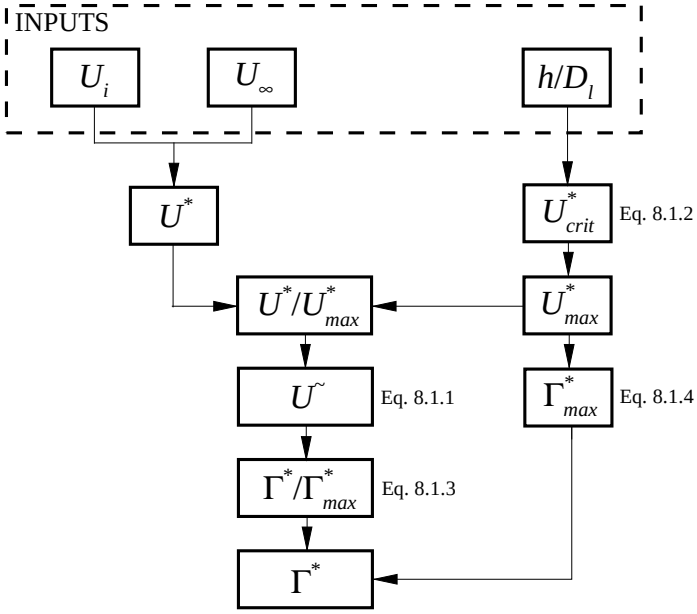

Figure 8.8: Flow chart illustrating the procedure to determine the vortex strength in headwind conditions using the empirical prediction tool

Parameter	Value	Eq.
U^*	10.556	-
U^*_{crit}	4.507	8.1.2
U^*_{max}	6.934	$U^*_{crit}/U^*_{max} = 0.65$
U^*/U^*_{max}	1.522	-
Γ^*_{max}	0.214	8.1.4
$U^{\sim}$	2.492	8.1.1
Γ^*/Γ^*_{max}	0.672	8.1.3
$\Gamma^*_{\psi=0}$	0.144	8.1.4
$DC_{60}^{\psi=0}$	0.022	8.1.9
$DC_{60}^{\psi=90}$	0.163	8.1.17
$\Gamma^*_{\psi=90}$	0.189	8.7
$DC_{60}^{\psi=70}$	0.181	8.1.18
$\Gamma^*_{\psi=70}$	0.119	8.7

Table 8.2: Summary of results from example application of empirical model prediction tool

8.2 Theoretical Model

In this section, a theoretical based model is presented which can predict the vortex strength under headwind conditions ($\psi = 0$). In Chapter 5 the vortex strength trend with velocity ratio was established. It was found that for different intake non-dimensional heights and approaching boundary layer configurations the general trend with velocity ratio was the same; high velocity ratios are associated with a weak vortex and as the velocity ratio reduced the vortex strength increased to a local maximum and then reduced thereafter until the critical velocity ratio, U^*_{crit}, was reached. It was postulated in §5 that this trend is a result of two opposing mechanisms. The first, which acts to increase the vortex strength, is related to the increase in vorticity within the approaching ground boundary layer as the headwind speed increases. The second, which acts to reduce the total vorticity within the capture streamtube, is the reducing sucked streamtube size with decreasing velocity ratio. However, most surprisingly, in Chapter 6.2, it was found that at high velocity ratios ($U^* > 12$) the approaching vorticity had no impact on the total vortex strength. This indicates that at high velocity ratios it is the induced vorticity that dominates the flowfield.

One of the primary aims of the model is therefore to predict the total approaching circulation within the sucked streamtube and to see how this varies with velocity ratio. The results will then be compared with experiments and should reveal, firstly, how large the approaching circulation is and how this compares to the experiments. Secondly, it should reveal whether the trend observed with velocity ratio is as expected and is due to the variation in the integrated vorticity within the sucked streamtube. In addition given the rolling ground plane results, extensions to the model will also be presented which attempts to account for the induced circulation source.

This section first begins by discussing the vorticity sources involved in the headwind mechanism to calibrate the reader. Following this the different levels of the model that will be presented are briefly discussed. The methodology used to calculate the total approaching circulation within the sucked streamtube is presented and subsequently the results for each level of the model is presented and discussed.

8.2.1 Vorticity Sources

In Chapter 4 quantitative results of the vortex strength under quiescent conditions were presented. Under such conditions in general two vortices were observed and it was found that the rotation of the vortices was such that the left vortex had positive vorticity and the right negative vorticity. Taking into account the rotation of the vortices this suggests that it is the vorticity associated with suction induced boundary layer, on the ground, beneath the intake that dominates (see Fig. 2.6). This circulation is positive and is denoted by Γ^+_{id} (Fig 8.9). It is also envisaged that there will be a near equal source of circulation approaching the intake. This is also associated with the suction induced velocities and will have negative sign, Γ^-_{id} (Fig. 8.9). Ignoring vorticity sources from

the intake surface it can therefore be assumed that the total induced circulation is given by Eq. 8.2.1.

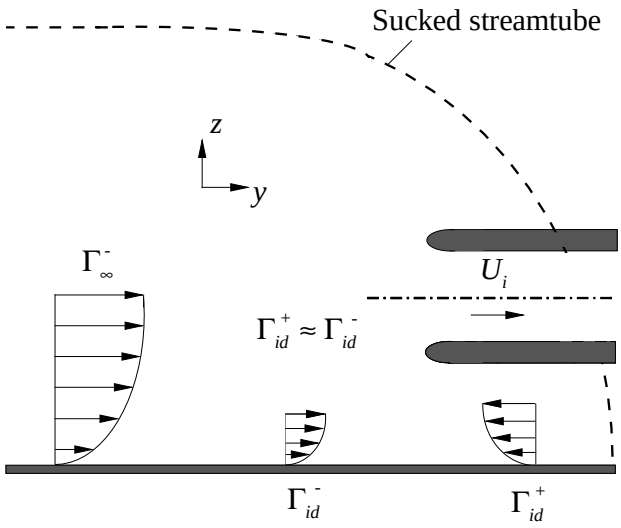

Figure 8.9: Primary vorticity sources under headwind conditions

$$\Gamma_{id} = \Gamma_{id}^{+} + \Gamma_{id}^{-} \tag{8.2.1}$$

Experiments in quiescent conditions revealed that as the ground clearance, h/D_l, increases the strength of the vortex decreases (Fig. 8.10) (see §4). This is a result of lower local induced velocities immediately adjacent to the ground at higher non-dimensional heights. It is therefore expected that the level of induced circulation is a function of the intake Mach number, M_i, the Reynolds number based on the intake diameter, Re_{D_l} and most importantly the degree of interaction between the sucked streamtube and the ground plane (Eq. 8.2.2). This fundamentally depends on h/D_l and U_i/U_∞. The induced circulation will be highest for the largest intake diameter, D_l and intake Mach number, M_i, and the lowest non-dimensional height, h/D_l.

$$\Gamma_{id}^{*} = \frac{\Gamma_{id}}{U_i D_l} = f\left[\frac{h}{D_l}, \frac{U_i}{U_\infty}, M_i, Re_D\right] \tag{8.2.2}$$

Since Γ_{id} is a function of the contraction ratio, in headwind conditions there will be a contribution to the total vortex strength from the induced circulation. Experiments with a rolling plane with no ambient wind (i.e. with the ground and tunnel speeds the same) demonstrated that the induced circulation accounts for all of the circulation at intermediate to high velocity ratios (i.e. $U_i/U_\infty > 12$). Furthermore at the lowest investigated non-dimensional height (h/D_l) of 0.25 the induced circulation is roughly constant for all velocity ratios tested with a moderate increase being seen at the lowest U_i/U_∞.

For the case of an intake in headwind conditions an additional source of circulation is introduced into the flow-field which is associated with the headwind approaching boundary layer. This circulation source has negative sign, Γ_∞^- (Fig. 8.9). As the approaching headwind speed increases the vorticity, ω_∞^-, within the boundary layer will increase, leading to an increase in circulation. Dimensional analysis shows that the approaching boundary layer circulation, Γ_∞, is a function of the following variables:

$$\Gamma_\infty^* = \frac{\Gamma_\infty}{U_i D_l} = f\left[\frac{h}{D_l}, \frac{U_i}{U_\infty}, M_i, Re_D, \frac{\delta}{D_l}\right] \tag{8.2.3}$$

Experiments revealed that the change from quiescent to a modest headwind configuration ($U_i/U_\infty = 19$) revealed no notable change in the vortex strength (see §5.2.2). It can therefore be assumed that at high velocity ratios (say $U_i/U_\infty > 19$) the vortex strength has reached an asymptotic limit where no further reduction in the vortex strength is seen as the velocity ratio is increased. Hence at these high velocity ratios the vortex strength is equal to the no-wind vortex strength.

8.2.2 Estimatation of Γ_{id}

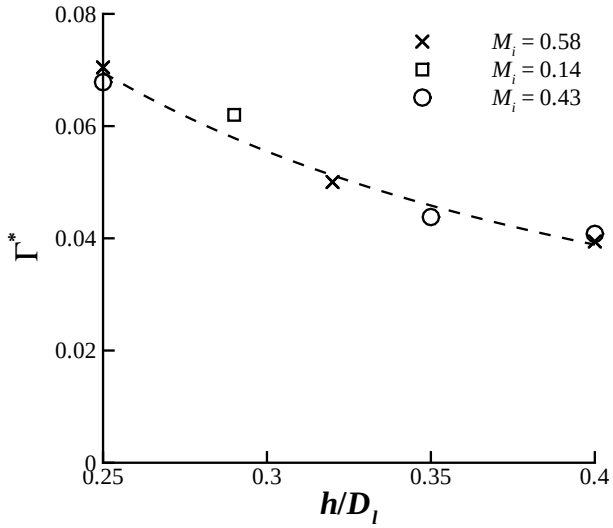

Figure 8.10: Effect of ground clearance on the vortex strength under no-wind conditions ($U^* = \infty$)

An estimation of the induced circulation, Γ_{id}, can be taken from the quiescent conditions experiments. Since under such conditions, by definition, no approaching circulation is present, the total vortex strength for this configuration must be due to the induced circulation alone. The circulation generated is a result of the induced intake flow field interaction with the ground plane, generating vorticity. Hence the strength

will reduce as the ground clearance increases, as the induced velocities immediately adjacent to the wall will reduce. Three height-to-diameter ratios were tested under quiescent conditions at the same intake Mach number, M_i,of 0.58 and the vortex strength results as a function of ground clearance, originally shown in §4, are again plotted in Fig. 8.10. The vortex strength trend with h/D_l shows approximately a power law dependency and can therefore be modelled using Eq. 8.2.4. The constants, d and e in Eq. 8.2.4 are are equal to 0.0125 and -1.2 respectively.

$$\Gamma^*_{id,max} = d\left(\frac{h}{D_l}\right)^e \tag{8.2.4}$$

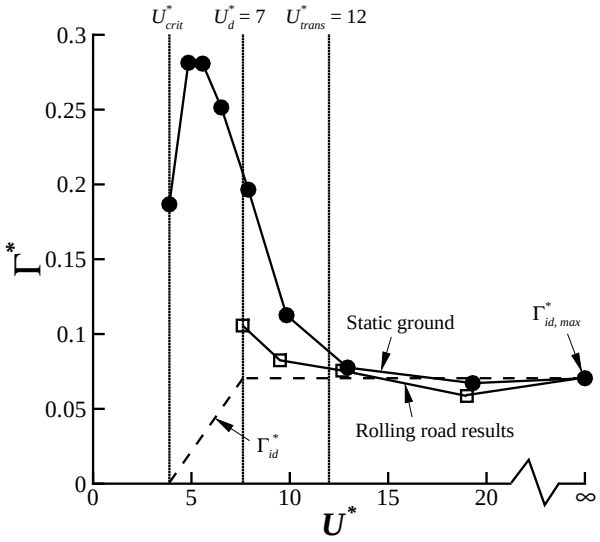

Figure 8.11: Non-dimensional vortex strength variation with velocity ratio for the static and moving ground configurations with the predicted variation of the induced circulation, Γ^*_{id}, also included for an $h/D_l = 0.25$ and $M_i = 0.58$

To estimate how the induced circulation will vary with reducing velocity ratio the synchronised rolling road plane results can be used (§6.2). For these experiments no approaching boundary layer was present, therefore it can assumed that the primary source of circulation is that associated with the induced circulation, Γ_{id}. Under such conditions, at the datum height of 0.25 (h/D_l), the vortex strength was found to be approximately constant for all investigated velocity ratios (i.e. from $U^* = \infty$ to 7) (Fig. 8.11). Most significantly, however, it was found that for velocity ratios greater than 12 the vortex strength was the same as for the static ground configurations (i.e. with an approaching boundary layer present) (Fig. 8.11). As explained above this indicates that for a ground clearance of $h/D_l = 0.25$ the approaching circulation has no impact on the vortex strength for velocity ratios greater than 12. As measurements were only taken to a velocity ratio of approximately 7, for the take-off simulations, an assumption must be made as to how the induced circulation, Γ_{id}, varies from $U^* = 7$ to the critical

velocity ratio (U^*_{crit}). By definition a necessary boundary condition is that Γ_{id} must go zero as the sucked streamtube lifts off the ground plane. With no additional information available, it is therefore assumed that the induced circulation reduces linearly from a velocity ratio of 7 (for $h/D_l = 0.25$) where the induced circulation is approximately equal to $\Gamma_{id,max}$ to the critical velocity ratio, U^*_{crit}, where Γ_{id} must be zero (Fig. 8.11). This can be expressed mathematically below for a non-dimensional height of 0.25 (h/D_l):

$$\Gamma^*_{id} = \begin{cases} \dfrac{\left(U^* - U^*_{crit}\right)}{\left(7 - U^*_{crit}\right)}\Gamma^*_{id,max} & U^* < 12 \\ \Gamma^*_{id,max} & U^* > 12 \end{cases}$$

Since very little data was taken at other ground clearances for the synchronised rolling ground plane experiments, some additional assumptions are used to enable the induced circulation model to be implemented at other height-to-diameter ratios. The fundamental affect of increasing the non-dimensional height of the intake is a reduction in the interaction between the ground plane and sucked streamtube. By definition the induced circulation is strongly influenced by this interaction. It is therefore expected that the velocity ratio at which the approaching circulation becomes dominant over the induced circulation, denoted by U^*_{trans}, is also a function of the capture streamtube interaction with the ground. Hence it is therefore expected that the transition velocity ratio will scale with the critical velocity ratio, U^*_{crit}. For the datum height of 0.25, U^*_{trans}, is 12 which normalised by the critical velocity ratio gives 3.1* and is denoted by Π_1 (Eq. 8.2.5). This empirically based constant can be used to determine the transition velocity ratio for a given non-dimensional height given that the critical velocity ratio can be calculated using Eq. 8.1.2.

$$\Pi_1 = \frac{U^*_{trans}}{U^*_{crit}} = 3.1 \tag{8.2.5}$$

In the same manner it is also expected that the velocity ratio at which the induced circulation starts to diminish, symbolized by U^*_d, is also a function of ground clearance. As mentioned above, for a non-dimensional height of 0.25 (h/D_l), this is assumed to occur at a velocity ratio of 7 which non-dimensionalised by the critical velocity ratio gives 1.8. This empirical constant is designated by Π_2, as shown in Eq. 8.2.6.

$$\Pi_2 = \frac{U^*_d}{U^*_{crit}} = 1.8 \tag{8.2.6}$$

Therefore the variation in the induced circulation, for any given non-dimensional height, can be predicted by:

*For a non-dimensional height of 0.25 the critical velocity ratio, U^*_{crit}, is equal to 3.88 and can be calculated using Eq. 8.1.2

$$\Gamma^*_{id} = \begin{cases} \dfrac{\left(U^* - U^*_{crit}\right)}{\left(U^*_d - U^*_{crit}\right)}\Gamma^*_{id,max} & U^* < U^*_d \\ \Gamma^*_{id,max} & U^* > U^*_d \end{cases}$$

where U^*_d is determined from Eq. 8.2.6 with U^*_{crit} being determined by Eq. 8.1.2.

The induced circulation trend with velocity ratio for the three non-dimensional heights investigated under headwind conditions is shown in Fig. 8.12. Note that the assumptions used in the above ignore the single data point taken at the higher height-to-diameter ratio of 0.4, for the synchronised rolling ground plane experiments.

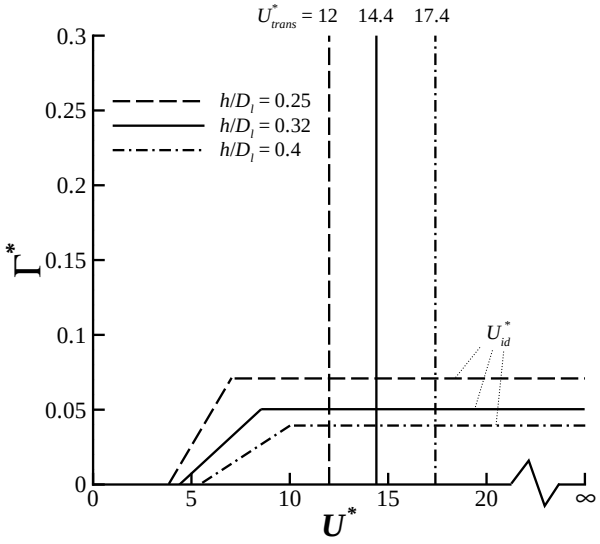

Figure 8.12: Predicted variation in the induced circulation for the three non-dimensional heights investigated in the headwind experiments. Also included in the figure is the predicted velocity ratio at which the approaching circulation starts to have an effect, U^*_{trans}

Since the induced circulation under quiescent conditions is of opposite sign to the approaching boundary layer circulation, it is assumed that the total circulation of the vortex system is a linear difference between the circulation sources (Eq. 8.2.7).

$$\Gamma = \Gamma_\infty - \Gamma_{id} \tag{8.2.7}$$

8.2.3 Calculation of Γ_∞

The approaching boundary layer circulation, Γ_∞, is determined by integrating vorticity over the whole cross-section of the sucked streamtube, at far-field, upstream of the intake. The total amount of vorticity within the boundary layer is given by Eq. 8.2.8.

$$\begin{aligned}\omega &= \nabla \times V \\ &= \left(\omega_x, \omega_y, \omega_z\right) \\ &= \left(\frac{\partial w}{\partial y} - \frac{\partial v}{\partial z}, \frac{\partial u}{\partial z} - \frac{\partial w}{\partial x}, \frac{\partial v}{\partial x} - \frac{\partial u}{\partial y}\right)\end{aligned} \tag{8.2.8}$$

At far-field, upstream of the intake, it is assumed that the flow is uniform in the x and y directions. Hence the only source of vorticity is due to the variation in streamwise (positive y direction) velocity, v, normal to the wall. Therefore Eq. 8.2.8 reduces to:

$$\omega \approx -\frac{\partial v}{\partial z} \tag{8.2.9}$$

Boundary layer measurements in the wind tunnel show that the velocity profile follows a power law approximation, of the form given in Eq. 8.2.10, with $n_{bl} \approx 7$ (see Appendix C.1 for the profiles).

$$\frac{v(z)}{U_\infty} = \left(\frac{z}{\delta}\right)^{\frac{1}{n}} \tag{8.2.10}$$

The vorticity can therefore be determined by taking the derivative of Eq. 8.2.10. This has been evaluated using a second order central difference scheme with a forward difference being implemented at the wall (where $N = L_q/dz$ with dz being the resolution and L_q is the height of the sucked streamtube (Fig. 8.13):

$$\frac{\partial v}{\partial z} = \begin{cases} \dfrac{v_{i+1} - v_i}{dz} & i = 1 \\ \dfrac{v_{i+1} - v_{i-1}}{dz} & i = 2 : N \end{cases}$$

In order to integrate this vorticity distribution an estimation of the length scale of the sucked streamtube size, L_q, is needed (Fig. 8.13). For a given mass flow, $\dot{m}$, and average approaching headwind speed within the sucked streamtube, $\bar{U}_\infty$ (Eq. 8.2.11), the capture streamtube area, A_∞ and radius, r_∞, at far field upstream of the intake can be estimated from the continuity equation, and are given in Eq.8.2.12 and 8.2.13 respectively (Note $L_q = 2r_\infty + H$). As mentioned above, a vortex can only form if $r_\infty > H$ (Fig. 8.14).

$$\bar{U}_\infty = \frac{1}{A_\infty} \int_{A_\infty} v(z)\, dA_\infty \tag{8.2.11}$$

$$A_\infty = \frac{\dot{m}}{\rho_\infty \bar{U}_\infty} \tag{8.2.12}$$

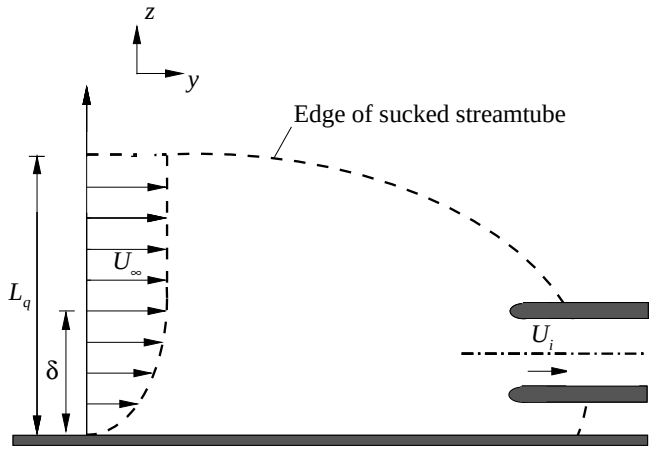

Figure 8.13: Side view of model topology

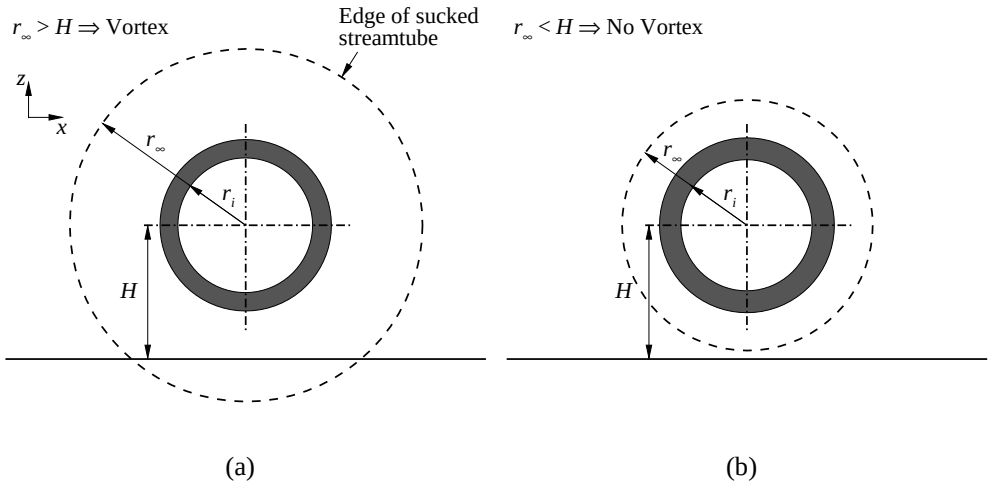

Figure 8.14: Criteria for vortex formation

$$r_\infty = \sqrt{\frac{1}{\pi}\left(\frac{\dot{m}}{\bar{U}_\infty \rho_\infty}\right)} \tag{8.2.13}$$

Since $\bar{U}_\infty$ depends on A_∞ and vice versa, an initial estimate must be made of $\bar{U}_\infty$ to determine A_∞. An obvious choice is to use the free-stream velocity, U_∞ to provide an initial guess for A_∞. Using this value an estimate for the average velocity within the sucked streamtube can be determined using Eq. 8.2.11.

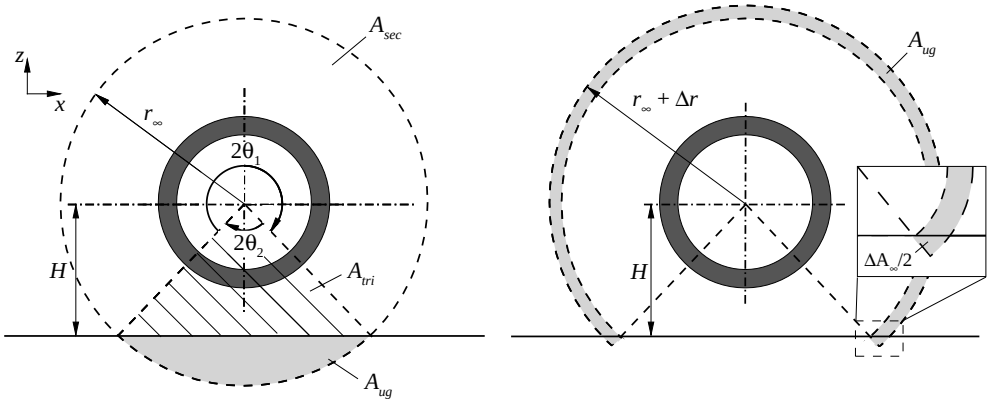

(a) (b)

Figure 8.15: Model assumption for the effect of the capture streamtube shape on the interaction with the ground plane, also including the definition of the parameters used

An issue is the interaction of the capture streamtube shape with the ground. Since the sucked streamtube is assumed to be circular there will be a proportion of total area, A_{ug}, that will be below the ground plane (Fig. 8.15). This, of course, is not physically possible and conservation of mass states that this area must be accounted for elsewhere. Here it is assumed that the sucked streamtube remains circular with its radius increasing by an amount, Δr, such that $A_{og} = A_\infty$ (Fig. 8.15), where A_{og} is the area above the ground. In order to calculate the increase in radius required to meet the necessary condition that $A_{og} = A_\infty$ the area above the ground is first split into two sub-regions; A_{sec} and A_{tri} (Fig. 8.15a) with the equations and relationships between the areas given in Eqs. 8.2.15-8.2.16).

$$A_\infty = A_{og} + A_{ug} \tag{8.2.14}$$

$$= (A_{sec} + A_{tri}) + A_{ug} \tag{8.2.15}$$

where

$$A_{sec} = r_{\infty}^2 \theta_1 \tag{8.2.16}$$

$$A_{tri} = r_{\infty} H \tag{8.2.17}$$

$$\theta_1 = \pi - \cos^{-1}\left(\frac{H}{r_{\infty}}\right) \tag{8.2.18}$$

It is then assumed that the area, A_{sec}, increases by Δr such that it equals the original, A_{sec} area plus the area underneath the ground, A_{ug} (Eq. 8.2.19).

$$\frac{1}{2}\left(r_{\infty} + \Delta r\right)^2 \theta_1 \approx A_{sec} + A_{ug} \tag{8.2.19}$$

Rearranging yields:

$$\Delta r^2 + 2 r_{\infty} \Delta r + \left[r_{\infty}^2 - \frac{2\left(A_{sec} + A_{ug}\right)}{\theta_1} \right] = 0 \tag{8.2.20}$$

Eq. 8.2.20 is a quadratic equation in Δr of the form $a\Delta r^2 + b\Delta r + c$ and is solved using Eq. 8.2.21 where only the positive solution is needed.

$$\Delta r = \frac{-b + \sqrt{b^2 + 4ac}}{2a} \tag{8.2.21}$$

Hence the new sucked streamtube size is then:

$$r_{\infty,new} = r_{\infty} + \Delta r \tag{8.2.22}$$

Since θ_1 in Eq. 8.2.19 is also dependent on r_{∞} this method has an error, in Δr. This is due to θ_1 not accounting for the change in r_{∞}. This therefore results in a small fraction of the increased area being added below the ground plane (Fig 8.15b).

Now that an estimate of the sucked streamtube size has been obtained, the mass flow rate is computed (using Eq. 8.2.23) and compared with the target mass flow, $\dot{m}_{target}$. This gives $\Delta\dot{m}$ (Eq. 8.2.24) which is converted to an area, ΔA_{∞} (via Eq. 8.2.25). This area represents the error due to the initial estimate of L_q and due to the error associated with Eq. 8.2.19. The whole process is then repeated by setting $\Delta A_{\infty} = A_{ug}$ in Eq. 8.2.15 and by calculating a new A_{sec}, A_{tri} and θ_1 based on the corrected r_{∞} in Eqs. 8.2.16 - 8.2.18. By iterating a number of times, the solution converges to the required mass flow. In general 5 iterations were required and Fig. 8.16 shows an example of the convergence.

$$\dot{m} = \rho_{\infty} \int_0^{L_q} v(z) dA_{\infty} \tag{8.2.23}$$

$$\Delta\dot{m} = \dot{m}_{target} - \dot{m}_{actual} \tag{8.2.24}$$

$$\Delta A_{\infty} = \frac{\Delta\dot{m}}{\rho_{\infty} U_{\infty}} \tag{8.2.25}$$

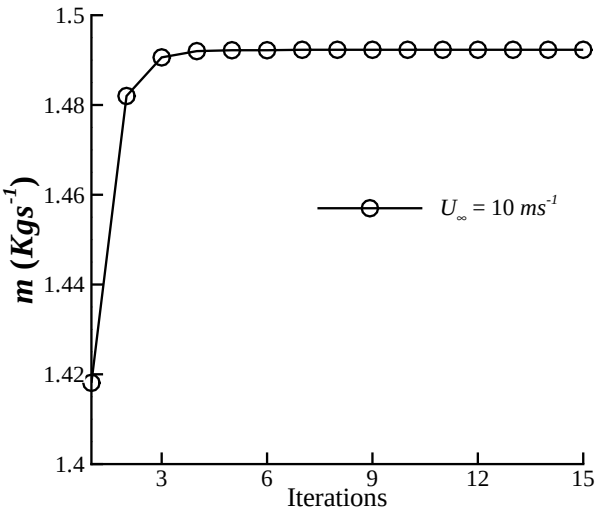

Figure 8.16: Example convergence of intake mass flow using the model

Now that an estimate of the sucked streamtube size and shape has been obtained the total circulation within the capture streamtube, Γ_{∞}, can be calculated. The integration was performed using a numerical trapezoidal scheme (Eq. 8.2.26), with the area parameters being defined in Fig. 8.17.

$$\Gamma_{\infty} = \int_{A_{\infty}} \omega_{\infty} dA_{\infty} \approx \sum_{i=1}^{N} \omega_i dA_i \tag{8.2.26}$$

where

$$dA_i = \begin{cases} \dfrac{dz}{2}\left(x_j + x_{j+1}\right) & j = 1 \\ dz\left(x_j + x_{j+1}\right) & j = 2 : N \end{cases}$$

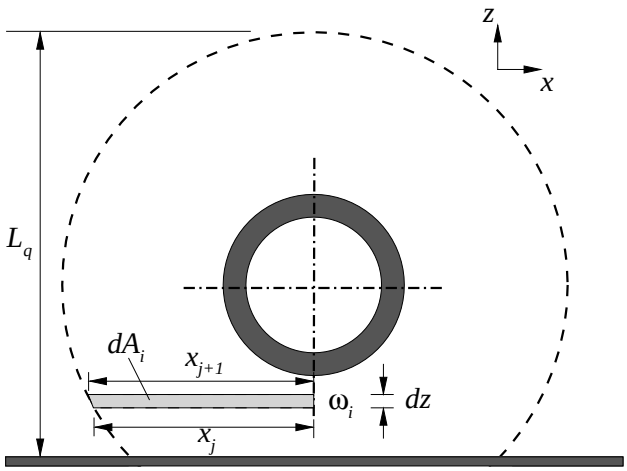

Figure 8.17: Schematic of a typical sucked streamtube cross-section describing the suction envelope parameters

8.2.4 Model Results

In this section the model results are presented. Given that the induced circulation appears to have a significant influence at high velocity ratios three different levels of the model are presented and discussed separately. A description of each model is given under each sub heading.

8.2.4.1 Model A

For this model (Model A) only the approaching circulation source is considered. The total vorticity within the sucked streamtube at far-field is integrated for the full range of investigated velocity ratios. The results for the model at a non-dimensional height, h/D_l, of 0.25 with an intake diameter, D_l and velocity, U_i, equal to model scale (i.e. $0.12m$ and $190ms^{-1}$ respectively) within an δ^*/D_l approaching boundary layer equal to 0.11 is shown in Fig. 8.18. The results are in line with expectations; high velocity ratios are associated with a weak vortex and as the velocity ratio reduces the vortex strength increases to a local maximum before reducing to zero at the critical velocity ratio. This result confirms the hypothesis stated above that the circulation trend with velocity ratio observed in the experiments is largely a function of the integrated approaching boundary layer vorticity within the sucked streamtube.

Comparing with the experiments, the agreement is encouraging for such a simple prediction tool. The peak vortex strength is within 8% of the experiments. The corresponding velocity ratio is predicted to be 6.33 which compares to 4.9 for the experiments, although the model results show little deviation in strength from the maximum as the velocity ratio is reduced further to 4.9. However the agreement at high veloc-

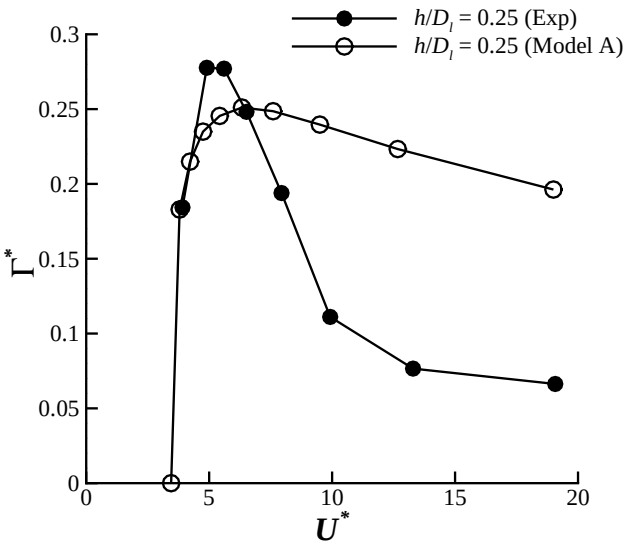

Figure 8.18: Predicted total non-dimensional total circulation of the vortex, Γ^*, with comparison to experiments for $h/D_l = 0.25$ and $\delta^*/D_l = 0.11$

ity ratios is not good; at a U^*, of 19 the vortex strength has been considerably over predicted, with circulation three times larger than the experiments. Given the findings from the synchronised rolling ground plane experiments (§6.2), where the vortex strength did not deviate from the static ground configuration even with the approaching circulation being largely removed, this result is perhaps not surprising.

Predictions have also been computed for height-to-diameter ratios of 0.32 and 0.4 for direct comparison with the experimental results (Fig. 8.19). In general as the ground clearance increases the prediction improves, particularly in terms of the peak vortex strength, where at $h/D_l = 0.4$, the value is within 0.8% of the experiments. Again the corresponding velocity ratio has been slightly over predicted at 9.52 (U^*_{max}) in comparison to 7.88 for the experiments, but as for the lower height-to-diameter ratio there is little change in the predicted strength between these two velocity ratios. The relative difference between the model and experimental results at high contraction ratios is roughly the same for all investigated non dimensional heights and has been over predicted by three times approximately. This perhaps demonstrates that the discrepancy at high velocity ratios is not a function of ground clearance, but rather there is an additional mechanism that is not being captured by the model.

8.2.4.2 Model B Results

The second level of the model (Model B) not only accounts for the approaching circulation but also the induced circulation, Γ_{id}. Since Γ_{id} cannot be determined analytically, empirical correlations are used along with some additional assumptions, as discussed in §8.2.2, to provide an estimate for the induced circulation source. In this model the

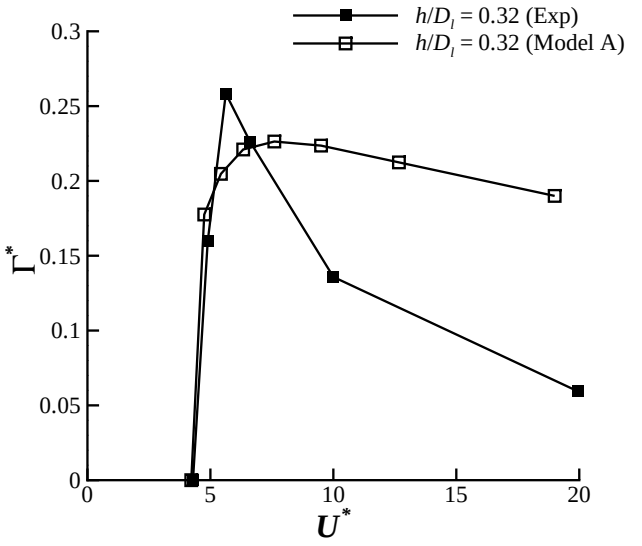

(a)

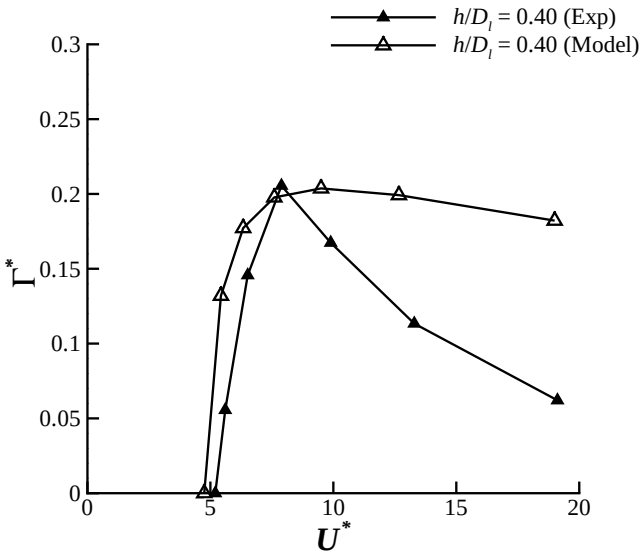

(b)

Figure 8.19: Predicted total non-dimensional circulation of the vortex, Γ^*, for Model A with comparison to experiments for (a) $h/D_l = 0.32$ and (b) $h/D_l = 0.40$ with $\delta^*/D_l = 0.11$ and $M_i = 0.58$

total circulation is assumed to be a linear difference between the approaching and circulation sources (Eq. 8.2.7). The results for Model B are shown in Fig. 8.20 and compared with the experiments at the datum height of 0.25 (h/D_l).

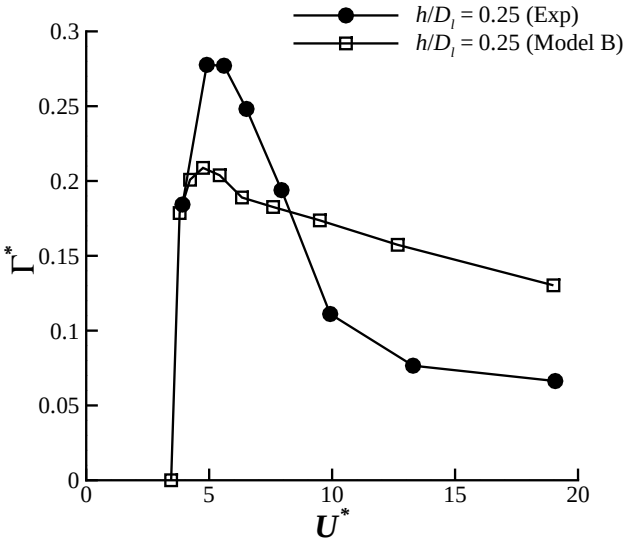

Figure 8.20: Predicted non-dimensional total circulation of the vortex, Γ^*, for Model B with comparison to the experiments for a $h/D_l = 0.25$ and $\delta^*/D_l = 0.11$, $M_i = 0.58$

The inclusion of the induced circulation now gives the correct velocity ratio at which the peak vortex strength occurs (Fig. 8.20). The shape of the trend is also improved with a higher relative strength being observed at lower velocity ratios in comparison to higher contraction ratios. However the model is still not correct as the circulation is again over predicted at high velocity ratios. In addition with the assumptions used for the induced circulation the vortex strength at low velocity ratios is now under predicted.

8.2.4.3 Model C Results

The third and final model (Model C) also takes into consideration both the approaching and induced circulation sources. However this model also considers the results from the synchronised rolling ground plane experiments (§6.2) where the it was found that for velocity ratios greater than 12 at a non-dimensional height of 0.25 (h/D_l), the approaching circulation had no impact on the vortex strength. As explained above, it is expected that this transition point scales with the critical velocity ratio as given by Eq. 8.2.5. Model C therefore only accounts for the approaching circulation source when the velocity ratio reduces below a certain threshold given by U^*_{trans} (Eq. 8.2.5). The total circulation is therefore given by the following:

$$\Gamma^* = \begin{cases} \Gamma^*_{id} & \text{for } U^* > U^*_{trans} \\ \Gamma^*_{\infty} - \Gamma^*_{id} & \text{for } U^* < U^*_{trans} \end{cases}$$

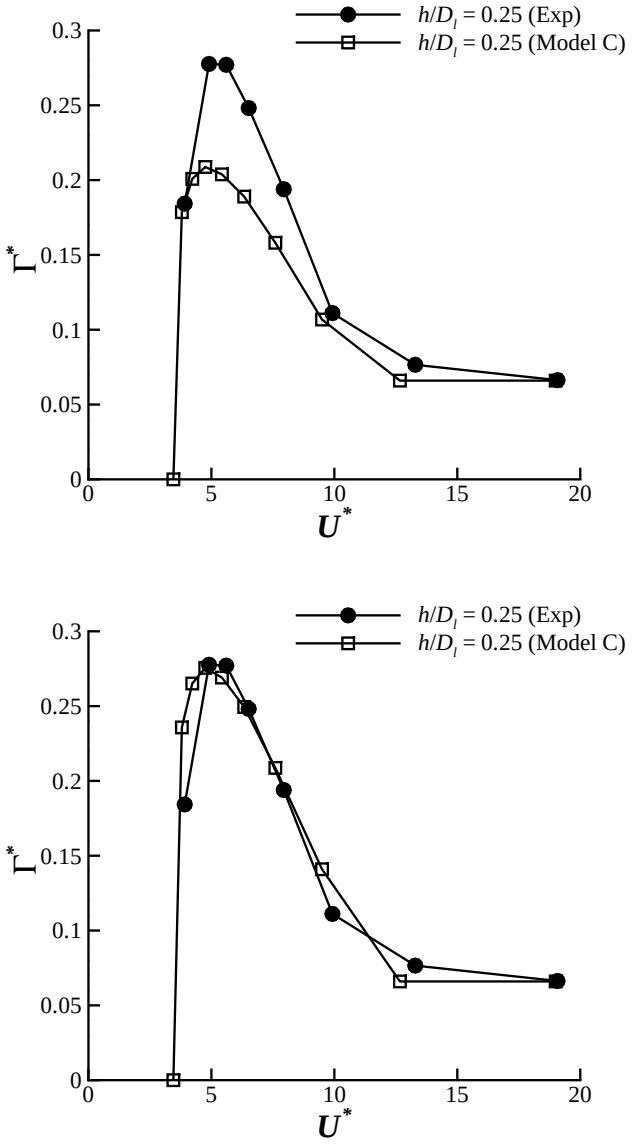

Figure 8.21: Predicted non-dimensional total circulation of the vortex, Γ^*, for Model C with comparison to experiments at a $h/D_l = 0.25$ and $\delta^*/D_l = 0.11$ and $M_i = 0.58$

where $U^*_{trans} = \Pi_1 U^*_{crit}$

The results for Model C are shown in Fig. 8.21 for the datum configuration (h/D_l = 0.25, δ^*/D_l = 0.11). The shape of the trend with velocity ratio now almost exactly matches the experimental results. As required the predicted vortex strength at high velocity ratios (i.e. $U^* > 12$) is almost exactly that of the experiments. However the vortex strength at lower velocity ratios ($U^* < 12$), where both the induced and approaching circulation sources contribute, is still under predicted. By multiplying the circulation prediction by an empirical constant for velocity ratios less than 12 ($U^* < 12$), such that the predicted peak vortex strength matches the measured peak vortex strength, the prediction gives very good agreement against the experimental data (Fig. 8.21b). The empirical constant, ϕ_2, is equal to 1.32, and is expected to represent the inaccuracies in the prediction of the induced circulation, the interaction between the two primary vorticity sources (i.e. the approaching and induced) and also the assumptions relating the sucked streamtube size, shape and interaction with the ground plane.

Model C has also been applied to other height-to-diameter ratios to validate the assumptions relating to the induced circulation and also to test the empirical constant, ϕ_2. The results for the model at a non-dimensional height (h/D_l) of 0.32, using the same empirical constant as for h/D_l = 0.25, shows excellent agreement. Although the model has been manufactured from the experimental results, this perhaps demonstrates that the assumptions used relating to the induced circulation and velocity ratio at which the approaching circulation becomes influential are valid. However, at the higher height-to-diameter ratio (h/D_l) of 0.4 the vortex strength is over predicted using the same constant. By reducing ϕ_2, for this non-dimensional height, so that the predicted peak vortex strength matches the experiments, good agreement is again found. The empirical constant in this case is equal to 1.16. The reduction in ϕ_2 is not surprising since the constant is expected to represent the interactions between vorticity sources and the assumptions relating to the sucked streamtube characteristics, all of which will be a function of ground clearance.

In addition to the affect of non-dimensional height, alternative approaching boundary layer configurations have been investigated to further validate the model and also to support the comments made in §5.2.3 relating to the influence of δ on the vortex characteristics. Fig. 8.23a illustrates the affect of changing the boundary layer thickness, δ^*/D_l from 0.11 to 0.03 which is directly comparable to the change investigated in the experiments (§5.2.3). A reduction in the approaching boundary layer thickness leads to a 22% reduction in the peak circulation with the corresponding velocity ratio (U^*_{max}) increasing from 4.75 to 5.46. Although the reduction in strength was not observed in the experiments, at this particular ground clearance (h/D_l = 0.25), a corresponding reduction in the velocity ratio was encountered. The experiments also revealed, at a higher ground clearance of h/D_l = 0.4 that the critical velocity ratio moderately increases, as δ^*/D_l decreases from 0.11 to 0.03. This is also captured in the model where at a lower ground clearance of h/D_l = 0.25 the critical velocity ratio increases from 3.4 to 3.8. As stated numerous times, the changes in the critical and peak vortex strength velocity ratios is due to the incorrect definition being used. The correct

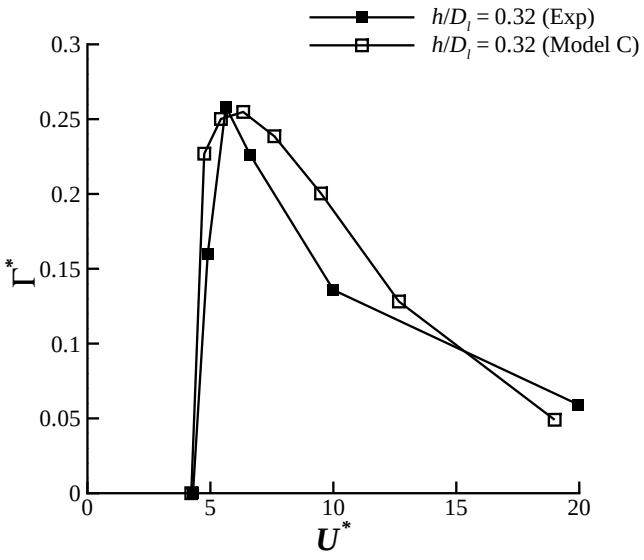

(a)

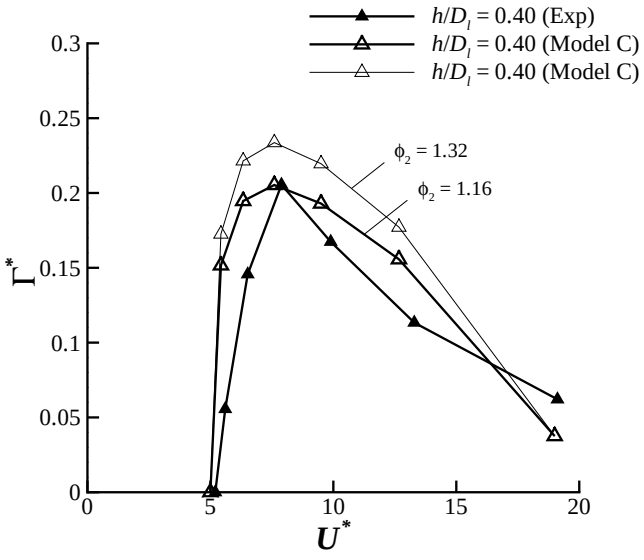

(b)

Figure 8.22: Predicted non-dimensional total circulation of the vortex, Γ^*, for Model C with comparison to experiments for (a) $h/D_l = 0.32$ and (b) $h/D_l = 0.40$ for a $\delta^*/D_l = 0.11$ approaching boundary layer and $M_i = 0.58$

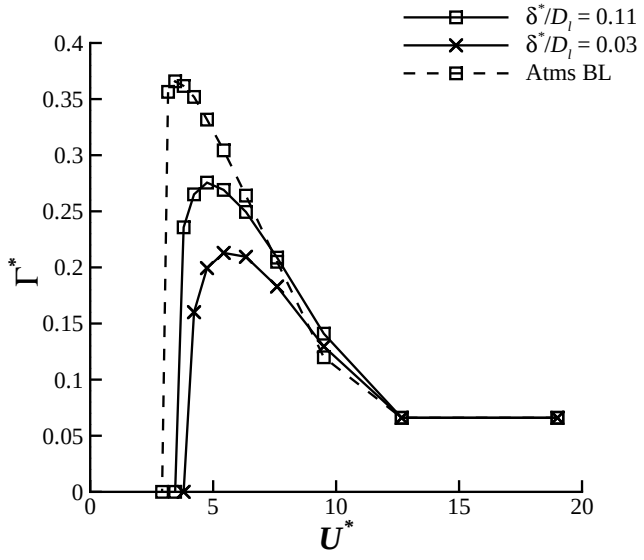

(a)

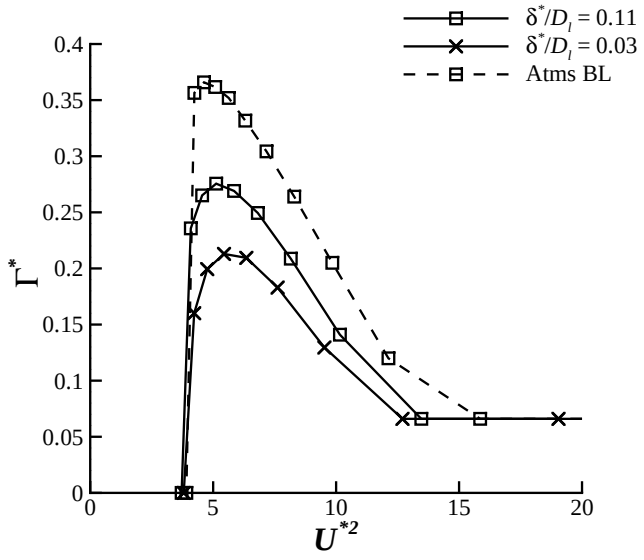

(b)

Figure 8.23: Effect of approaching boundary layer thickness on the predicted vortex strength against (a) conventional velocity ratio, U^* and (b) area weighted average velocity ratio, $\overline{U^*}$ (h/D_l = 0.25 and M_i = 0.58)

definition of velocity ratio, denoted by U^{*2}, uses the area weighted average velocity within the sucked streamtube. Fig. 8.23b illustrates that by using this definition the same critical velocity ratio is seen across all boundary layer thicknesses. Since in the literature U^* is commonly used this is believed to be one of the reasons why there are discrepancies in the vortex formation criterion as discussed in §2.1.

$$\frac{v}{v_{ref}} = \frac{\log(z/z_0)}{\log\left(z_{ref}/z_0\right)} \tag{8.2.27}$$

With the prediction tool being validated against the experiments and showing reasonably good agreement the model has been used to explore the affect of an atmospheric approaching boundary layer, which is representative of in service engine operating conditions. The velocity profile prescribed for this simulation was taken from Hoxey and Richards[19] where a logarithmic profile is presented for heights below $25m$ (Eq. 8.2.27). This profile is normalised by the velocity at a reference height,z_{ref} and is given by v_{ref}. At full scale, z_{ref} is typically $10m$ with the height being non-dimensionalised by the roughness height, z_0, of the site in question. For airport runaways the recommended value of z_0 is equal to $0.03m$[13]. Since this is a model scale simulation the reference heights have been scaled by the full to model scale ratio (i.e. $1/30^{th}$). The velocity ratio, U^*, has been calculated using the reference velocity, which at model scale is at a height of $0.333m$. Results for the simulation are illustrated alongside the boundary layer configurations investigated in the experiments (Fig. 8.23a). Since there is a contribution to the vortex strength across the complete height of the sucked streamtube the vortex strength is predicted to be considerably stronger at all velocity ratios, particularly in terms of the peak vortex strength (Fig. 8.23a).

8.2.4.4 Extension of Model to Total Pressure Observations

The theoretical model can also be used to illustrate the relatively greater sensitivity of the total pressure measurements to changes in boundary layer thickness, in comparison to the vortex strength. As observed in §5.2.3, it was shown that a change in the approaching boundary layer thickness, δ^*/D_l, from 0.11 to 0.03 leads to a 26% reduction in the peak distortion coefficient, $DC_{60,max}$, whereas no such decrease was observed for the vortex circulation. It was hypothesized that the reduction is DC_{60} is associated with the lower integrated loss within the sucked streamtube. In contrast the circulation, which is dominated by the vorticity levels, does not alter significantly because the vorticity is largely influenced by the magnitude of the free-stream velocity, which does not change. Although the distortion coefficient cannot be predicted, the model can be used to integrate the loss within the approaching boundary layer inside the sucked streamtube between the two boundary layer configurations. The relative difference can then be compared with the change in the predicted vortex circulation between the two δ^*/D_l configurations, as shown in Fig. 8.23.

Using the known boundary layer profile given by Eq. 8.2.10 the loss in dynamic head

from free-stream, at each *ith* station within the boundary layer, can be calculated by first computing the change in the local velocity from that in free-stream conditions using Eq. 8.2.28. The change in dynamic pressure can then be calculated via Eq. 8.2.29.

$$\Delta v_i = U_\infty - v_i \tag{8.2.28}$$

$$\Delta q_i = 1/2 \rho_\infty \Delta v_i^2 \tag{8.2.29}$$

In the same way as the approaching vorticity, the loss is then integrated across the whole of the sucked streamtube using a numerical trapezoidal scheme (Eq. 8.2.30). The parameters used in the integration are shown in Fig. 8.17 as before.

$$\Delta Q_\infty = \frac{1}{A_\infty} \int_{A_\infty} \Delta q dA_\infty \approx \frac{1}{A_\infty} \sum_{i=1}^{N} \Delta q_i dA_i \tag{8.2.30}$$

where

$$dA_i = \begin{cases} \dfrac{dz}{2}\left(x_j + x_{j+1}\right) & j = 1 \\ dz\left(x_j + x_{j+1}\right) & j = 2 : N \end{cases}$$

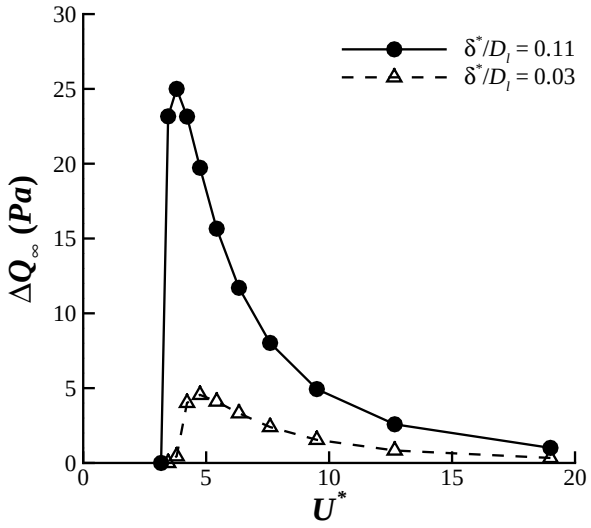

Figure 8.24: Intergrated loss within the sucked streamtube for two different approaching boundary layer thicknesses ($h/D_l = 0.25$ and $M_i = 0.58$)

The results from the two boundary layer configurations are plotted in Fig. 8.24 and the difference is quite evident. Increasing δ^*/D_l from 0.03 to 0.11 leads to approximately a five times larger peak loss within the sucked streamtube. This provides good

evidence that the change in the DC_{60} between the two approaching boundary layer configurations is associated with the difference in the integrated loss between the two.

8.3 Further Discussion

The prediction tools presented above enable the vortex strength to be estimated for any height-to-diameter ratio over a wide range of velocity ratios. In both methods an intrinsic assumption is that the strength scales with the intake diameter, D_l, and velocity, U_i. This is vitally important as it enables the predictions to be applied to any Reynolds and intake Mach number. Experiments indicate that in terms of the intake velocity this is a valid assumption. However it is unknown how the strength will scale with Reynolds number by increasing the intake diameter, D_l, and there is no data in the open literature. As well as vortex strength it is important to understand how the important aerodynamic parameters effect the fan face distortion, DC_{60}. In contrast to the vortex strength, some sensitivity was observed with intake velocity which is believed to be related to the vortex proximity with the wall and its consequent interaction with the intake boundary layer (§5.2.1). In the following section these issues are discussed in further detail.

8.3.1 CFD Studies

In conjunction with this research two MSc. projects[42,71] were conducted to provide supporting CFD studies. The simulations were designed to exactly replicate the experiments in terms of model design and size and in terms of the experiment configurations tested. In the most recent study[71] significant advances were made and a range of configurations were investigated not only to compare with experiments but also to investigate other important aspects which were impossible using the current test rig. Comparison between the experiments, CFD simulations and the model are displayed in Fig. 8.25. The agreement between the three datasets is remarkable. This demonstrates the quality of the CFD simulations and the experiments, but also shows that a simple prediction model which takes a matter of seconds to compute, gives largely the same predictions as the CFD, which in contrast takes weeks to perform.

In addition to the configurations examined in the experiments, full-scale simulations were conducted by Zantopp[71] to investigate the Reynolds number dependency in both headwind and crosswind configurations. In this study the full scale intake has an inside diameter, D_i, of 3 m which is thirty times larger than the model scale simulations. This corresponds to a Reynolds number based on the intake inner diameter, Re_{D_i}, of 3.91×10^7 which compares to 1.26×10^6 for the scaled simulations. Fig. 8.26a compares the CFD results for the experiment and full scale simulations under headwind conditions. Also included in the figure is the model prediction at full scale. By non-dimensionalising the vortex strength by the intake diameter and velocity good agreement is found between the two Reynolds numbers with even better agreement

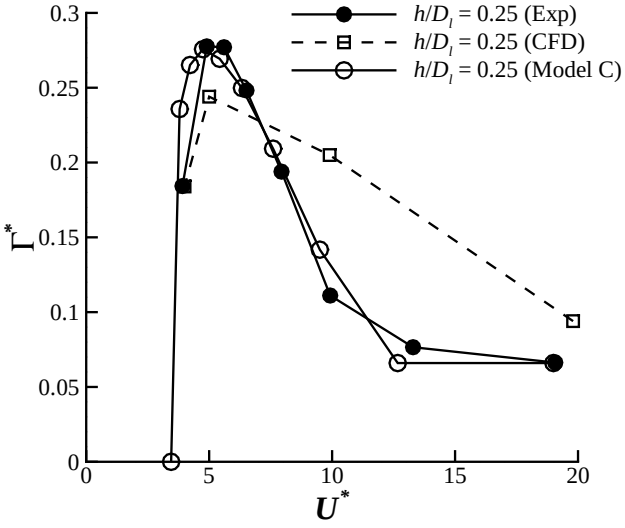

(a) $h/D_l = 0.25$

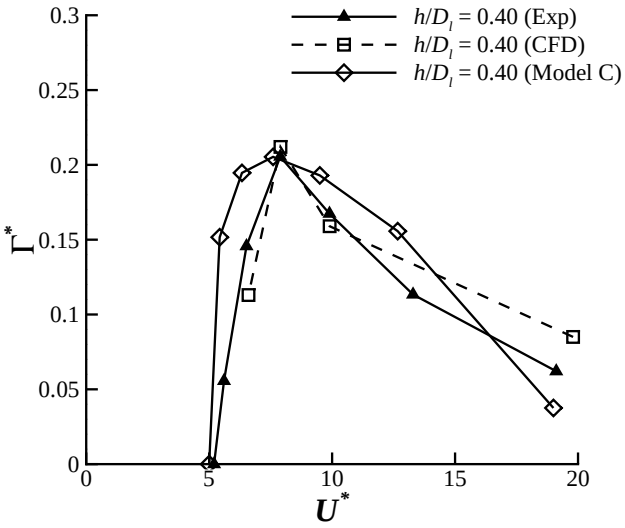

(b) $h/D_l = 0.40$

Figure 8.25: Comparison between experiments, CFD and theoritical model ($M_i = 0.58$ and $\delta^*/D_l = 0.11$)

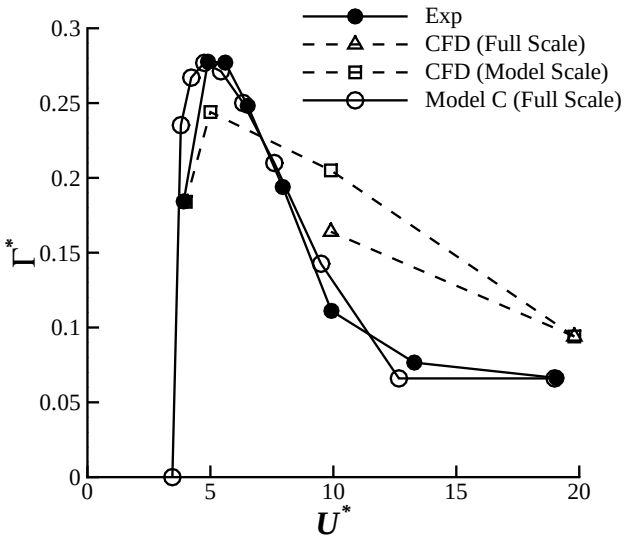

(a) Headwind

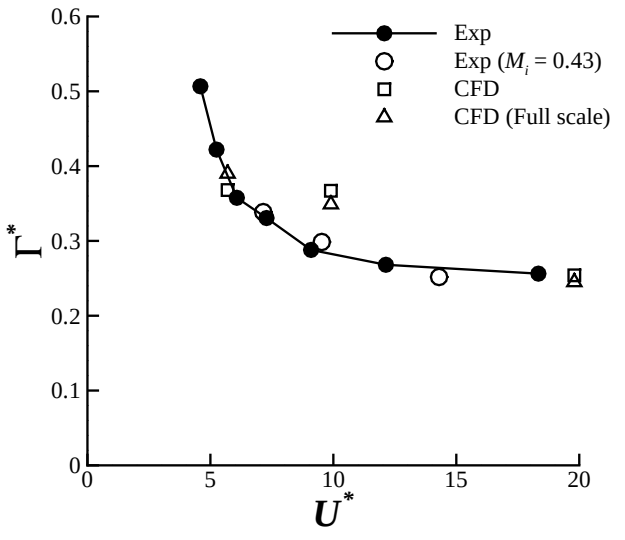

(b) Crosswind

Figure 8.26: Non-dimensional vortex strength against velocity ratio comparing the experiments and CFD predictions at model and full scale (h/D_l = 0.25, M_i = 0.58 and δ^*/D_l = 0.11)

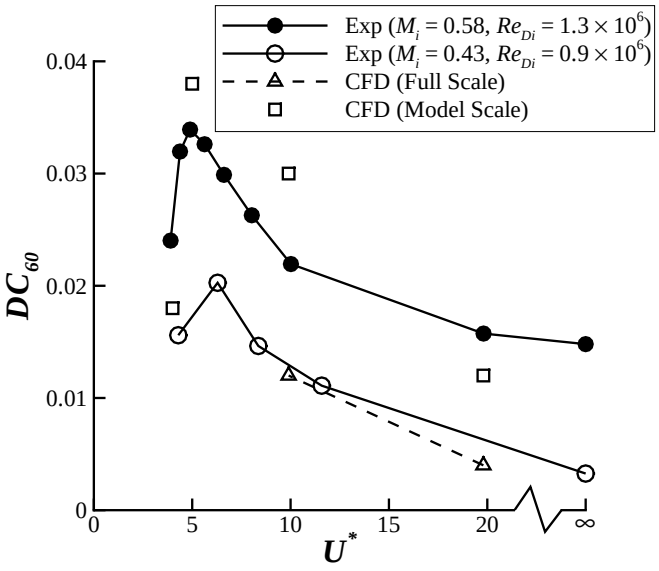

Figure 8.27: Comparison between experiment results at two different intake Mach numbers and the CFD results for model and full scale simulations under headwind conditions both at $h/D_l = 0.25$ and $\delta^*/D_l = 0.11$

being found under crosswind conditions (Fig. 8.26b). The results therefore justify the rationale behind the choice of non-dimensionalization and warrants the utilization of the empirical and theoretical vortex strength models to higher Reynolds numbers applications.

For the distortion, however, a different story is seen in terms of Mach and Reynolds number dependency. Fig. 8.27 compares the DC_{60} values between the CFD scaled and full scale simulations with the experiment data at two different intake velocities corresponding to intake Mach numbers of 0.43 and 0.58 and intake Reynolds numbers of 1.3 and 0.94×10^6. As illustrated in §5.2.1 the relatively modest increase in the Mach number and Reynolds number alters the average fan face radial ingestion location (r_v/r_i) from 0.64 to 0.94. This coincides with a two fold increase in the distortion at the fan face (Fig. 8.27). With limited additional knowledge it is difficult to ascertain whether this increase in the distortion relates to the increase in Mach number and/or the Reynolds number or to the vortex proximity with the intake wall. CFD analysis by Zantopp[71] clarifies this issue with Fig. 8.28a contrasting the fan face total pressure contours between the experiments and the model scale and full scale simulations. The plots shows there is a marked resemblance between the experiment and CFD plots, which both show a region of low total pressure adjacent to the wall at the 180 degree position. Zantopp points out that this low pressure region is in fact a result of vortex induced separation; locally between the two vortex core positions and that the loss within the vortex core is considerably smaller. This observation agrees with the experiments and illustrates that the increase in DC_{60} seen as the Mach number and Reynolds number increases is in fact driven by the change in vortex position to one in proximity with the wall which has additional consequences of vortex induced separation. Further

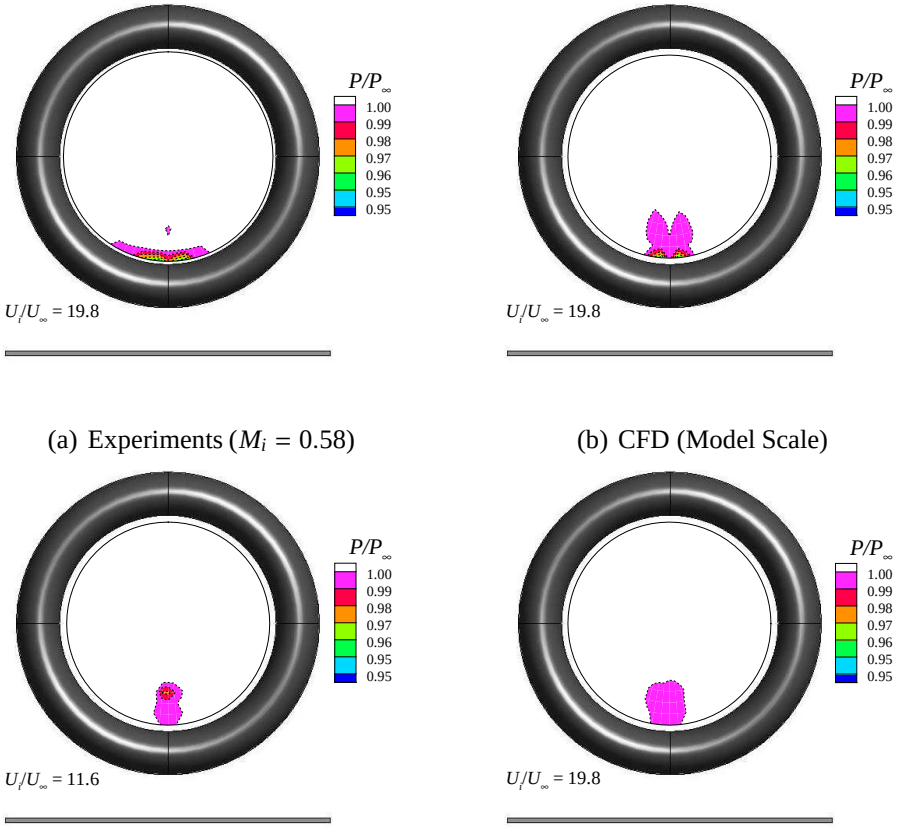

(a) Experiments ($M_i = 0.58$) (b) CFD (Model Scale)

(c) Experiments ($M_i = 0.43$) (d) CFD (Full Scale)

Figure 8.28: Comparison of the fan face total pressure contours between CFD scaled and full scale simulations and the experiment data at two intake Mach number/Reynolds number combinations for a $h/D_l = 0.25$ and $\delta^*/D_l = 0.11$ (CFD Data after Zantopp) (a)-(b) $Re_{D_i} = 1.26 \times 10^6$ and $M_i = 0.58$, (c) $Re_{D_i} = 0.94 \times 10^6$ and $M_i = 0.43$ (d) $Re_{D_i} = 3.91 \times 10^7$, $M_i = 0.58$

analysis by Zantopp shows that for the high Reynolds number simulation no such separation region is observed. This indeed indicates that the separation region between the two vortices is a Reynolds number dependent feature. Perhaps more significantly, with the complication of the vortex induced separation removed, the predicted DC_{60} at full scale agrees very well with the experiments at the lower intake Mach number (Fig. 8.27). This result suggests that the distortion induced within the vortex alone is Reynolds number independent, but due to the global sensitivity of the intake aerodynamics at low Reynolds number additional features may mask the results, which may suggest otherwise.

8.4 Summary

Two model prediction methods have been developed, one empirical and one theoretical. The former method gives a more accurate prediction whereas the latter has been developed to aid in further understanding the mechanism that sets the vortex strength under headwind conditions.

The empirical model is centred on the aerodynamic self-similarity property and implements additional experimental correlations to determine the normalization parameters. The model is applicable to velocity ratios between 20 and the critical (i.e. the blow away velocity ratio) and can be used to estimate the vortex strength and distortion for any height-to-diameter ratio, approaching boundary layer thickness, and any yaw angle between zero and ninety degrees.

The theoretical model has been developed based on the primary vorticity sources under headwind conditions. This model considers both the approaching and induced circulation sources as being the major contributors to the vortex strength and is only applicable to the headwind mechanism. The approaching circulation has been determined by integrating the vorticity within the sucked streamtube whereas the induced circulation source is empirically determined from the rolling ground plane experiments. Due to the nature of the findings in for the aforementioned experiments, different levels of model development were presented and are summarized below:

- **Model A**: The first model only considers the approaching source and was found to give good predictions at low velocity ratios, but over predicted the strength at high velocity ratios.
- **Model B**: Considers the approaching and induced circulation sources and assumes that the total strength is a linear difference between the two. This model predicts the peak velocity ratio correctly and also gives better prediction at higher velocity ratios, but is still over predicted. In addition it also now under predicts the strength at low velocity ratios.
- **Model C**: Given the results of the rolling ground plane experiments, only the induced circulation is considered for velocity ratios greater than a specified frac-

tion of the critical velocity ratio. For when both the approaching and induced circulation sources are applicable, the total strength is again given by a linear difference of the two and an empirical constant is applied to match the peak vortex strength with the experiments. This represents the interactions associated with the circulations source and also the inaccuracies in the assumptions relating to the sucked streamtube size, shape and interaction with the ground plane. Model C was found to give good predictions and captures the correct trends at all investigated ground clearances.

With the aid of supporting CFD studies by Zantopp[71] some important conclusions can be drawn:

- The vortex strength scales with the intake diameter,D_l, and velocity, U_i.
- At model scale, for $M_i = 0.58$, 40% of the distortion under headwind conditions is due to vortex induced local separation within the intake, which is not present under higher Reynolds number conditions according to CFD simulations.

CHAPTER 9

Conclusions

An extensive quantitative study of the characteristics of vortices forming between the ground and a generic $1/30^{th}$ scale model intake has been conducted at a representative intake Mach number. Both external velocity flowfield measurements using the Stereoscopic Particle Image Velocimetry (SPIV) technique and in-duct total pressure measurements have been used to quantify the underlying features of the flowfield. The important non-dimensional parameters have been independently assessed including the velocity ratio (U_i/U_∞), the intake non-dimensional height (h/D_l), approaching boundary layer thickness (δ^*/D_l), intake Mach number (M_i) and yaw angle (ψ). In addition to the non-dimensional parameters of fundamental interest, the effect of moving ground plane has been studied which effectively removes the approaching vorticity source to reveal a greater understanding of the mechanism under headwind conditions as well as giving greater insight into the formation of vortices during take-off. The key findings from each dataset is summarised in the following sections. The implications of the conclusions on engine design and testing is then stated.

9.1 Quiescent Conditions

Under quiescent conditions the flowfield is dominated by the flow emanating from underneath and behind the intake. This results in the formation and ingestion of two contra-rotating vortices.

- The two vortices that form are considerably unsteady and often only a single vortex prevails. This vortex can switch from side to side with a corresponding change in the rotation of the vortex. An alteration in the rotational sense of the vortex is likely to lead to a corresponding change in the local fan blade incidences and therefore fan stress behaviour.
- After an initial phase featuring two unsteady contra-rotating vortices, the flowfield ultimately locks into a single vortex flow mode which is considerably more stable, with the rotation of the vortex remaining unchanged.

- The primary vorticity source under quiescent conditions is associated with the intake induced flowfield which interacts with the ground plane. Consequently as the non-dimensional height increases, the interaction of the induced flowfield with the ground decreases. This therefore reduces vorticity production and hence the overall vortex strength.

9.2 Headwind Conditions

- A completely new vortex formation map has been established, which not only indicates when a vortex will be present for a given configuration, but also quantifies its strength. This is a significant improvement from previous correlations established in the literature[37,50] and provides advanced design rules for engine installations and operations.

- A characteristic trend has been established between vortex strength and velocity ratio. At high contraction ratios the vortex circulation is initially low and as the velocity ratio reduces the vortex intensifies, reaches a local maximum and then rapidly reduces to zero thereafter. This characteristic trend is a result of the integrated vorticity within the sucked streamtube and was found for all non-dimensional heights and approaching boundary layer configurations.

- When the trends are non-dimensionalised by the local peak vortex strength (Γ^*_{max}) and corresponding velocity ratio (U^*_{max}) all curves exhibit a self-similar property. The distortion coefficient also demonstrates the same characteristic. This verifies that the relative level of vortex strength, for a given non-dimensional height, is fundamentally determined by the corresponding level of interaction between the sucked streamtube and the ground plane. For a certain velocity ratio range, this can lead to a larger vortex strength being encountered at higher ground clearances.

- The vortex was found to blow-away when the sucked streamtube is predicted to lift off the ground plane.

- The aerodynamic self-similarity property has been used to develop an empirical vortex strength prediction method. This tool can predict the vortex strength for any configuration under headwind conditions and most significantly enables the operating conditions of the worst case vortex to be established for any non-dimensional height and approaching boundary layer.

9.3 Take-off Simulations

Experiments were performed to investigate the formation of ground vortices during aircraft take-off using a rolling ground plane in the wind tunnel. Two types of tests

were conducted. The first was to simulate an aircraft acceleration in no ambient wind conditions. This was achieved by synchronising the tunnel and ground speeds and increased both from zero with measurements being taken at selected velocities. The second test was where the speeds were unsynchronised to simulate a take-off in headwind conditions. The findings are summarized below:

- The synchronised experiments reveal that the approaching vorticity source has no impact on the vortex strength at high velocity ratios. As the velocity ratio is lowered below a specific threshold the approaching vorticity becomes influential and significant differences are observed between the moving and static ground configurations at the same respective velocity ratio. The result suggests that during the early stages of aircraft take-off, under no-ambient wind conditions, the strength of the vortex remains largely constant, before reducing thereafter.
- The asynchronous configuration, experiments imply that for an aircraft accelerating down the runway during take-off a vortex will not only form but will increase in strength, before being removed. The stronger the headwind, the higher the level of strength reached by the vortex, but the faster the vortex will blow-away down the runway.

9.4 Model Development

An additional model has been developed to predict the vortex strength under headwind conditions primarily from theoretical considerations. This model considers both the approaching and induced circulation sources. The former was predicted by integrating the vorticity within the approaching boundary layer within the sucked streamtube whereas the latter was estimated empirically from the synchronised rolling ground plane experiments.

The approaching circulation within the sucked streamtube was found to agree very well with experiments at low velocity ratios. However at high contraction ratios the predicted circulation was three times larger than experiments. This result concurs with the rolling ground plane experiments, that the approaching circulation source has no impact on the vortex strength at high velocity ratios. By including the effects of the induced circulation, in light of the rolling ground plane results, good agreement was found across all velocity ratios and all non-dimensional heights.

9.5 Crosswind Mechanism

The ground vortex aerodynamics in crosswind is considerably different to that under quiescent or headwind conditions. The vortex formed is primarily associated with the vorticity shed from the intake outer surface. For this reason the traits associated with this formation mechanism are considerably different.

- For the majority of configurations only a single vortex forms which is approximately three times stronger than any single headwind vortex. The distortion at the fan face is at best 20 times larger and at worst 40 times greater.

- In crosswind conditions the vortex strength trend with velocity ratio is similar to that in headwind conditions. As the velocity ratio is reduced the vortex is initially weak, grows in strength, reaches a local maximum and reduces thereafter. This increase in strength is expected to be primarily associated with the increase in vorticity over the intake outer surface, rather than the ground plane.

- For all velocity ratios in crosswind conditions, lower ground clearances produce a stronger ground vortex. In 90 degree crosswind conditions the associated ground vortex was found to initiate premature lip separation.

- The effect of yaw angle exhibits a $\sin^3\psi$ variation on the vortex strength for yaw angles, ψ, between 0 and 90 degrees. In contrast the distortion parameter demonstrates a $\sin^6\psi$ variation which is expected given that pressure inherently scales with the velocity squared. These findings along with other correlations have been used to extend the empirical model non zero yaw angle applications.

- When the operating velocity ratio is close to the blow-away the dominant vorticity source changes and is now associated with the approaching flow. This is signified by the occurrence of weaker clockwise, counter-clockwise and contra-rotating vortices which have never been reported previously. Engine test visualizations reveal a similar behaviour (see Fig. A.8).

9.6 Implications on Model Scale Tests

- Experiments have shown that for a given intake yaw angle, ground clearance and velocity ratio, the non-dimensional vortex strength is same for different intake Mach numbers. Therefore in order to determine the vortex strength for a given configuration, experiments do not have to be performed at a representative intake Mach number (M_i).

- However in headwind conditions, tests have revealed a sensitivity in the vortex ingestion location with M_i. Since the radial location of the vortex at the fan face significantly effects fan vibration, experiments focused on this aspect should be conducted at a representative intake Mach number.

- With the aid of supporting CFD studies by Zantopp[71], it has been concluded that the ingested vortex under certain circumstances at model scale, induces local separation within the intake, which leads to a higher distortion. CFD simulations have shown that this does not occur at higher Reynolds number. Therefore, in order to interpret model scale results to full scale, one must be aware of such Reynolds number effects.

- Take-off simulations imply that in order to model the effects of moving aircraft a rolling ground plane must be used. Experiments performed with a static ground will lead to pessimistic results.

9.7 Applicability of Research to Full Scale Engines

In the following the application of the model scale experiments to full-scale engine operations is discussed. Given the findings from this study this section concludes how the vortex characteristics (i.e. the vortex strength and DC_{60}) are expected to vary from the scaled model results when considering the effects of Reynolds number, intake Mach number and also the differing geometry associated with a full scale intake.

9.7.1 Reynolds Number Effects

As stated above for all headwind configurations the ingested vortex induced local separation within the intake. Supporting CFD studies by Zantopp[71] showed that for a full scale intake, this feature was not evident. It is therefore expected that the DC_{60} values presented in this thesis will be higher in comparison to the equivalent full scale situation. However, for the measurements at the lower intake Mach of 0.43 the vortex was ingested away from the intake wall and no induced separation was experienced. The DC_{60} for this configuration agreed very well with the full scale simulations conducted by Zantopp[71]. In terms of vortex strength, the full scale simulations by Zantopp showed that the vortex strength approximately scales with the intake diameter in both headwind and crosswind cases. This finding along with the fact that the circulation scales with the intake velocity for all experiment configurations investigated, warrants the utilization of the empirical and theoretical vortex strength models to higher Reynolds numbers applications.

9.7.2 Compressibility Effects

All experiments have been primarily performed at an intake Mach number of 0.58. This is representative of full scale intakes, hence compressibility effects are already accounted for in the experiment results. Nonetheless it has been shown that the vortex strength scales with the intake velocity over a wide range of Mach numbers varying from 0.14 to 0.58 which indicates that compressibility has no impact on the vortex characteristics. However it is expected that the operating Mach number will have a small impact on the sucked streamtube size, which therefore will have a minor influence on the velocity ratio at which the blow-away velocity ratio is reached (Eq. 5.2.1).

9.7.3 Geometric Effects

The model intake implemented in the experiments conducted in this thesis, is a generic, cylindrical, axi-symmetric intake. In comparison to a full scale intake the model has no droop, no scarfing, no hub or rotating fan and no diffuser and the intake lip is also considerably thicker to ensure that the intake does not separate under most conditions at the lower Reynolds number. The droop and scarfing of the intake are expected to have a small impact on the sucked streamtube characteristics. For this reason both effects may slightly reduce the velocity ratio at which the sucked streamtube lifts off the ground plane due to the engine axis being directed towards the surface. Consequently this potentially could increase the vortex strength as the relative interaction of the capture streamtube with the ground plane will be greater. In crosswind the vortex strength is primarily set by the vorticity generation over the intake surface, hence the exact geometry within the intake should not significantly alter the vortex characteristics.

9.8 Implications on Engine Testing and Design

The key conclusions stated above have the following implications on engine testing and design.

9.8.1 Test Bed Experiments

- The empirical model presented in §8.1 can be used to pinpoint the conditions which generate the strongest vortex under both headwind and crosswind conditions. With the aid of this prediction tool tests can be focused on such conditions to simulate the worst case scenario that an engine will experience.
- When determining the velocity ratio at which the engine is operating under, one must account for the boundary layer thickness.
- If it is desirable to conduct tests which generate the most detrimental vortices, reducing the non-dimensional height of the intake significantly increases the required capability of the blower to reproduce such conditions. For example reducing the ground clearance of the intake from 0.4 to 0.25 (h/D_l), at an intake Mach number of 0.58, doubles the headwind speed at which the strongest vortex occurs from 20 to $40ms^{-1}$.
- To assess intake lip performance in crosswind the ground plane must be included and must be at the correct ground clearance.
- For engine tests focused at high velocity ratios, the findings under quiescent conditions, imply that in order to capture the correct conditions during engine testing, the ground plane must be correctly positioned and must extend as far back behind the intake as possible.

- In addition since it is the suction induced flowfield between the intake and ground that matters, the nacelle shape may also influence this flowfield. It is therefore recommended that engine tests should include as much of the nacelle as possible underneath the engine, for high velocity ratio headwind tests. Exposing the appendages around the outside of the fan casing to the flow, as is customarily done during engine tests (see Fig. A.7), may introduce additional vorticity to the vortex which in the real situation would not be generated. Therefore the vortex strength and hence fan forcing behaviour maybe different between testing and the real situation. For low velocity ratio headwind cases this is not vital as a significant proportion the ingested flow emanates from in front of the engine.

- Similarly, under crosswind conditions, it is the flow over the intake nacelle that is important to the vortex strength. Hence under such conditions the complete nacelle should be installed on the engine.

9.8.2 Engine Installations

As mentioned in the introduction of this thesis, the general trend of turbofan configurations is to increase the by-pass ratio, in order to strive for greater propulsive efficiency. For wing mounted engine installations this has implications on ground operations because the intake is non-dimensionally closer to the ground plane. In this study, primarily two ground clearances have been investigated which represent potential future changes.

- Reducing the non-dimensional height of the intake increases the interaction of the sucked streamtube with the ground plane. As a consequence a higher wind velocity is required to lift the capture streamtube clear from the surface. Higher wind velocities are associated with greater levels of vorticity and therefore the vortex reaches a higher level of strength. This is the biggest disadvantage in reducing the ground clearance.

- With current engine installations being roughly at the highest ground clearance investigated in this thesis, the vortex would be quickly removed as the aircraft increases in speed down the runway. A rolling take-off procedure potentially could be used to ensure that a vortex never forms during the take-off envelope. However a reduction in the non-dimensional height means that a vortex will be sustained for longer periods of time and will also reach a higher level of strength during the take-off phase. The number of vortex events during the lifetime of the engine is therefore set to significantly increase.

- As explained above the model prediction methods developed enable the conditions of the strongest vortex to be predicted for any configuration under headwind conditions. This is a very useful tool to have during the design phase of

engine development, as with knowledge of the exact worst case operating conditions, CFD simulations or engine test bed experiments can be performed to determine its impact on engine performance.

- In crosswind the reduced ground clearance has addition consequences. The increased strength and sustainability of the vortex leads to premature intake lip separation. This would severely compromise the engine performance as well as significantly increasing vibrational stresses on the fan blades.

9.9 Recommendations for Future Work

This thesis provides an extensive quantitative study of ground vortex formation. The majority of areas have been covered, experimentally; however there are still a number of outstanding issues which are outlined under the following headings.

9.9.1 Further Experimental Investigations

1. Further examination of the effect of a rolling ground plane at different ground clearances to further understand the variation in the induced circulation source.

2. The velocity measurements presented in this thesis were all taken external to the intake. Therefore an obvious extension to this work would be to take PIV measurements inside the intake duct which is at a location of most interest to engine performance.

3. As already explained the experiment rig used in this project is limited to examining flow directions between zero and ninety degrees. Therefore a follow on project might look at the formation characteristics of ground vortices forming in flow angles greater than ninety degrees, as well as the formation of vortices during reverse thrust operation. Both of which have not been investigated in great depth in the literature.

4. Conduct full scale experiments to validate the scaling laws assumed in the model.

9.9.2 Further Model Development

The theoretical model developed in this thesis has been manufactured from the experimental results. However it is believed that with further research this model can be developed further without any reliance on experimental data. Some of the main tasks in achieving this are:

1. Develop a method of predicting the level of induced vorticity for a given configuration.

2. Understand the interaction between the induced and approaching circulation sources.

3. Understand how the sucked streamtube interacts with the ground plane.

Bibliography

[1] J. Anderson. *Modern Compressible Flow*. McGraw Hill, New York, 3^{rd} edition, 2003.

[2] G. K. Batchelor. *An Introduction to Fluid Dynamics*. Cambridge University Press, 1967.

[3] M. Bhagwat and G. Leishman. Correlation of helicopter rotor tip vortex measurements. *AIAA Journal*, 38:301–308, 2000.

[4] N. Bissenger and G. Braun. On the inlet vortex system. NASA CR-132536, National Aeronautics and Space Administration, 1974.

[5] S. Brix. *Untersuchungen zur Entstehung und Stärke von Triebwerkseinlaufwirbeln*. PhD thesis, RWTH Aachen, 2004.

[6] S. Brix, G. Neuwerth, and D. Jacob. The inlet-vortex system of jet engines operating near the ground. AIAA Paper 2000-3998, 14-17 August 2000.

[7] C. Burley, T. Brooks, B. van der Wall, H. Richard, M. Raffel, P. Beaumier, Y. Delrieux, J. Lim, Y. Yu, C. Tung, K. Pengel, and E. Mercker. Rotor wake vortex definition - initial evaluation of 3-c piv results of the hart-ii study. In *28^{th} European Rotorcraft Forum*, number 50, Bristol, England, 17-20 September 2002.

[8] J. F. Campbell and J. R. Chambers. Patterns in the sky: Natural visualizations of aircraft flow fields. Technical Report NASA SP-514, NASA Langley Research Centre, 1994.

[9] J. Colehour and B. Farquhar. Inlet vortex. *Journal of Aircraft*, 8(1):39–43, 1971.

[10] F. de Siervi, H. C. Viguier, E. M. Greitzer, and C. S. Tan. Mechanisms of inlet vortex formation. *Journal of Fluid Mechanics*, 124:173–207, 1982.

[11] L. Di Mare, G. Simpson, and A. Sayma. Fan forced response due to ground vortex ingestion. In *Proceedings of ASME Turbo Expo 2006: Power for Land, Sea and Air*, number GT2006-90685, Barcelona, Spain, 2006.

[12] I Dimitriou. Use of a narrow belt for moving ground simulation and its effects on the aerodynamic forces generated on a formula-1 car. Master's thesis, Cranfield University, 2001.

[13] ESDU. Data item 82026: Strong winds in the atmospheric boundary layer. part i: Hourly-mean wind speeds. Technical report, ESDU International Ltd., 2002.

[14] P. Funk, D. Parekh, D. Smith, and J. Dorris. Inlet vortex alleviation. volume AIAA 2001-2449, 2001.

[15] D. Glenny. Ingestion of debris into intakes by vortex action. Technical Report C.P. No. 1114, Ministry of Technology, Aeronautical Research Council, 1968.

[16] J. Green. Forced response of a large civil fan assembly. In *Proceedings of ASME Trubo Expo 2008: Power for Land, Sea and Air*, number GT2008-50319, Berlin, Germany, June 9-13 2008.

[17] C. Hall. *Fan Nacelle Interactions in Natural Wind*. PhD thesis, Cambridge University, 2001.

[18] J. Heineck, G. Yamauchi, A. Wadcock, L. Lourenco, and Abrego. A. Application of three component piv to a hovering rotor wake. In *56thAnnual Forum of the American Helicopter Society*, Virgina Beach, VA, USA, 2000.

[19] R. P. Hoxey and P. J. Richards. Structure of the atmospheric boundary layer below 25*m* and implications to wind loading on low rise buildings. *Journal of Wind Engineering and Industrial Aerodynamics*, 41-44:317–327, 1992.

[20] H. Huang, D. Dabiri, and M. Gharib. On the errors of digital particle image velocimetry. *Measurement Science and Technology*, 8:1427–1440, 1997.

[21] TSI Incorporated. Insight 3g - data acquision, analysis and display software - user's guide, 2005.

[22] SAE International. Gas turbine engine inlet flow disortion guidelines. Aerospace Recommended Practice ARP 1420, Febuary 2002.

[23] J. Jeong and F. Hussain. On the identification of a vortex. *Journal of Fluid Mechanics*, 285:69–94, 1995.

[24] M. Jermy and W. H. Ho. Location of the vortex formation threshold at sunction inlets near ground planes by computational fluid dynamics simulation. *Proceedings of the Institution of Mechanical Engineers*, 222 Part G: J. Aerospace Engineering:393–402, 2008.

[25] C. Johns. The aircraft engine inlet vortex problem. In *AIAA' s Aircraft Technology, Integration and Operation (ATIO) 2002 Technical*, volume AIAA 2002-5894. AIAA, 1-3 Oct 2002.

[26] A. Karlsson and L. Fuchs. Time evolution of the vortex between an air inlet and the ground. AIAA Paper 2000-0990, 10-13 Jan 2000.

[27] A. Karlsson and L. Fuchs. Vortex systems and the interaction between an air inlet and the ground. ICAS2000 Paper ICA0522, 2000.

[28] R. D. Keane and R. J. Adrian. Optimization of particle image velocimeters. part i: Double pulsed systems. *Measurement Science and Technology*, 1:1202–1215, 1990.

[29] H. J. Klein. Vortex inhibitor for aircraft jet engines. US Patent 2,915,262, December 1^{st} 1959.

[30] G. Leishman. *Principles of Helicopter Aerodynamics*, chapter Rotor Wakes and Blade Tip Vortices, pages 567–654. Cambridge Aerospace Series, New York, 2^{nd} edition edition, 2006.

[31] W. Liu, E. Greitzer, and C. Tan. Surface static pressures in an inlet vortex flow field. *Journal of Engineering for Gas Turbines and Power*, 107:387–393, 1985.

[32] D. MacManus. Personal communication.

[33] D. Motycka. Ground vortex - limit to engine/reverser operation. In *Transactions of the ASME Gas Turbine Conference*, number Paper No. 75-GT-3, March 2-6 1975.

[34] D. Motycka and W. Walter. Experimental investigation of inlet ground vortices during reverse thrust operation. In *AIAA/SAE 11^{th} Propulsion Conference*, volume AIAA Paper No. 75-1322, 29^{th} Sept - 1^{st} Oct 1975.

[35] D. Motycka, W. Walter, and G. Muller. An analytical and experimental study of inlet ground vortices. In *AIAA/SAE 9^{th} Propulsion Conference*, volume AIAA Paper No. 73-1313, Nov 5-7 1973.

[36] J. Murphy, D. MacManus, and M. Taylor. A quantitative study of intake ground vortices. ISABE Paper ISABE-2007-1209, Beijing, China, Sept. 2-7 2007.

[37] A. Nakayama and J. Jones. Correlation for formation of inlet vortex. *American Institute of Aeronautics and Astronautics*, 37(4):509–510, 1998.

[38] C. Petracci, C. van Doorne, J. Westerweel, and B. Lecordier. *Analysis of Stereoscopic PIV Measurements Using Synthetic PIV Images*, pages 199–210. Particle Image Velocimetry: Recent Improvements. Springer, Berlin, 2004.

[39] A. K. Prasad. Stereoscopic particle image velocimetry. *Experiments in Fluids*, 29(2):103–116, 2000. Review paper.

[40] M. Raffel, H. Richard, K. Ehrenfried, B. van der Wall, C. Burley, P. Beaumier, K. McAlister, and K. Pengel. Recording and evaluation methods of piv investigations on a helicopter rotor model. *Experiments in Fluids*, 36:146–156, 2004.

[41] M. Raffel, C. Willert, and J. Kompenhans. *Particle Image Velocimetry: A Pratical Guide*. Springer-Verlag, Berlin, 1998.

[42] L. Rehby. Jet engine ground vortex studies. Master's thesis, Cranfield University, 2007.

[43] L. Rodert and F. Garrett. Ingestion of foreign objects into turbine engines by vortices. Technical Report NACA TN 3330, National Advisory Committee for Aeronautics, 1953.

[44] F. Scarano. Iterative image deformation methods in piv. *Measurement Science and Technology*, 13:R1–R19, 2002.

[45] F. Scarano and M. L. Riethmuller. Iterative multigrid approach in piv image processing with discrete window offset. *Experiments in Fluids*, 26:513–523, 1999.

[46] A. Secareanu, D. Moroianu, A. Karlsson, and L. Fuchs. Experimental and numerical study of the ground vortex interaction in an air-intake. AIAA Paper 2005-1206, 10-13 Jan 2005.

[47] J. Seddon and E. L. Goldsmith. *Intake Aerodynamics*. Blackwell Science, Oxford, 1999.

[48] C. Sheaf. Personal communication, 2008.

[49] H. W. Shin, W. K. Cheng, E. M. Greitzer, and C. S. Tan. Inlet vortex formation due to ambient vorticity intensification. *American Institute of Aeronautics and Astronautics*, 24(4):687–689, 1986.

[50] H. W. Shin, E. M. Greitzer, W. K. Cheng, C. S. Tan, and C. L. Shippee. Circulation measurements and vortical structure in an inlet vortex flow field. *Journal of Fluid Mechanics*, 162:463–487, 1986.

[51] A. Shmilovich. Active system for wide area suppression of engine vortex. US Patent 6,763,651, July 10^{th} 2004.

[52] A. Shmilovich and Y. Yadlin. Engine vortex flows and methods of ground vortex alleviation. In *Proceedings of the 3^{rd} International Conference on Vortex Flows and Vortex Models*, Yokohama, Japan, 2005.

[53] A. Shmilovich and Y. Yadlin. Engine ground vortex control. AIAA Paper 2006-3006, San Francisco, California, 5-8 June 2006.

[54] D. M. Smith and J. Dorris. Aircraft engine apparatus with reduced inlet vortex. US Patent 6,129,309, 10^{th} Oct 2000.

[55] W. J. Smith. *Modern Optical Engineering*. McGraw-Hill, New York, 3^{rd} edition, 2000.

[56] M. J. C. Swainston. Vortex formation near the intakes to turbomachinery and duct systems. *Heat and Fluid Flow*, 4(2):92–100, 1974.

[57] J. R. Taylor. *An Introduction to Error Analysis: The Study of Uncertainties in Physical Measurements*. University Science Books, California, 1982.

[58] K. Thomas. Personal communication. 2007.

[59] M. Tobak and D. J. Peake. Topology of three-dimensional separated flows. *Annual Review of Fluid Mechanics*, 14:61–85, 1982.

[60] C. Tropea, A. Yarin, and J. Foss, editors. *Springer Handbook of Experimental Fluid Mechanics*. Springer Verlag, Berlin, 2007.

[61] B. van der Wall and H. Richard. Analysis methodology for 3-c piv data of rotary wing vortices. *Experiments in Fluids*, 40:798–812, 2006.

[62] C. R. Vanfleet and W. C. Ruehr. Method and apparatus for limiting ingestion of debris into the inlet of a gas turbine engine. US Patent 4,070,827, 31st Jan 1978.

[63] G. H. Vatistas and V. Kozel. A simpler model for concentrated vortices. *Experiments in Fluids*, 11:73–76, 1991.

[64] G. H. Vatistas, S. Lin, and P. M. Li. A similar profile for the tangential velocity in vortex chambers. *Experiments in Fluids*, 6:135–137, 1988.

[65] I. A. Waitz, E. M. Greitzer, and C. S. Tan. *Fluid Vortices*, volume 30 of *Fluid Mechanics and its Applications*, chapter Vortices in Aero-Propulsion Systems, pages 471–532. Kluwer Acedemic Publishers, 1995.

[66] S. Walker. Two-axes scheimpflug focusing for particle image velocimetry. *Measurement Science and Technology*, 13:1–12, 2002.

[67] F. White. *Viscous Fluid Flow*. McGraw Hill, New York, 3rd edition, 2006.

[68] D. D. Williams and L. E. Surber. *Practical Intake Aerodynamic Design*, chapter Intake /Engine Compatibility, pages 21–71. Blackwell Science, 1993.

[69] J. Wu, H. Ma, and M. Zhou. *Vorticity and Vortex Dynamics*. Springer-Verlag, Berlin, 2006.

[70] Y. Yadlin and A. Shmilovich. Simulation of vortex flows for airplanes in ground operations. AIAA Paper 2006-0056, Reno, Nevada, 9-12th Jan 2006.

[71] S. Zantopp. Jet engine ground vortex studies. Master's thesis, Cranfield University, 2008.

APPENDIX A

Full Scale Engine Visualizations

This appendix presents pictures from full scale engine visualizations. The pictures have been taken from both in service engines and during engine tests*. The visualizations have been referenced throughout this thesis to demonstrate the similarity between scaled wind tunnel model experiments and the full scale observations.

A.1 No Wind

(a) Clockwise vortex (b) Anti-clockwise vortex

Figure A.1: Visualization of different flow modes under no-wind conditions for a single run($h/D_l \approx 0.40$)[48].

Fig. A.1 shows example video snap-shots of ground vortex ingestion within a full scale engine during tests under near quiescent conditions. Both snap-shots were taken during the same run with the intake non-dimensional height at approximately 0.4 (h/D_l). Only a single vortex is observed which is found to switch from side to side. As the vortex switches sides its rotational sense within the intake changes. Fig. A.1a shows the

*Note some of the pictures are of poor quality as they have been extracted from low resolution videos.

vortex rotating clockwise within the intake, whereas in Fig. A.1b the vortex is to the right side and is rotating anti-clockwise within the intake duct. The experimental results presented in §4 are in accord with these observations.

A.2 Head Wind

Fig. A.2 shows two example snap-shots taken from the same engine test video under headwind conditions. In Fig. A.2a two contra-rotating vortices can just about be distinguished whereas in Fig. A.2b a single ground vortex is observed. These flow modes are in accordance with the experimental observations.

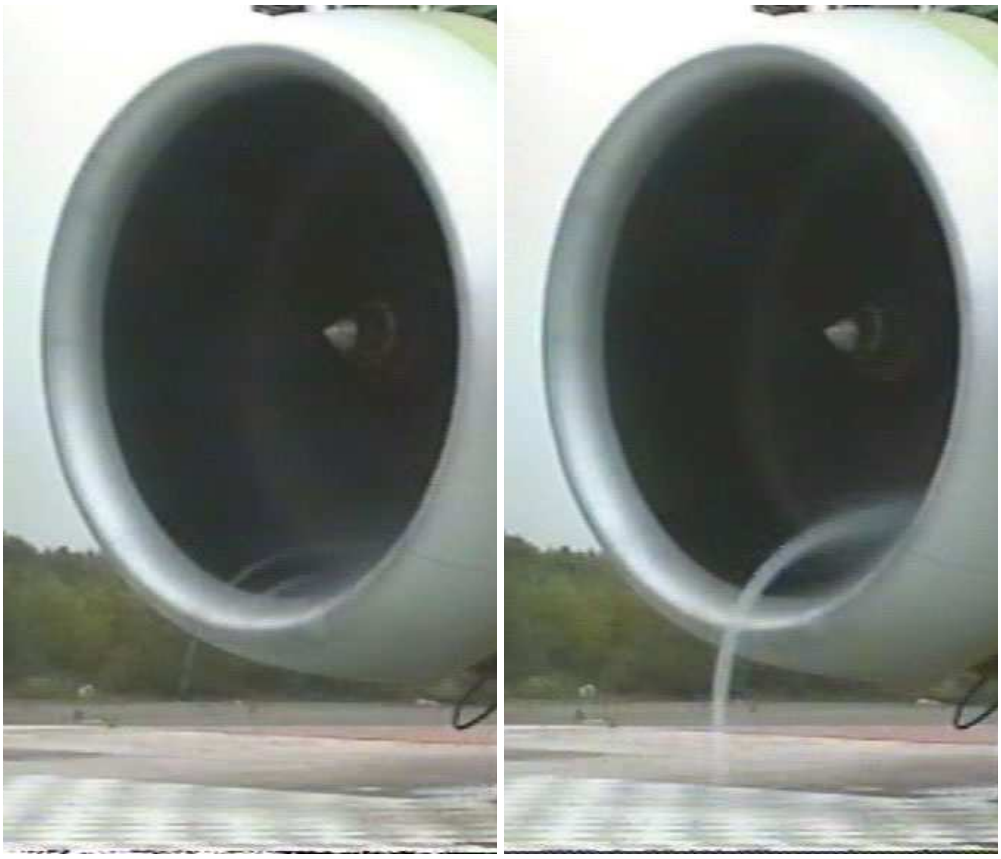

(a) Two vortices (b) Single vortex

Figure A.2: Full scale engine test visualizations of ground vortex ingestion under headwind conditions during a single run($h/D_l \approx 0.30$)[48].

A.3 Cross Wind

The effect of wind direction on the flowfield topology under crosswind conditions is shown in Fig. A.3. For a left to right cross flow (Fig. A.3a) the vortex rotates clockwise within the intake[†]. The rotation of the vortex can be inferred from the direction in which the vortex is travelling inside the intake duct due to the vortex-wall interaction. In Fig. A.3a the vortex moves anti-clockwise around the intake as it travels into the engine. In contrast in Fig. A.3b the flow is going from right to left generating an anticlockwise vortex within the intake, which therefore causes the vortex to travel clockwise as the vortex is ingested.

(a) Flow from right to left (b) Flow from left to right

Figure A.3: Effect of wind direction on the flowfield topology[48]

Fig. A.4 illustrates the unsteady movement of the crosswind ground vortex across the intake highlight plane for a ground clearance of approximately 0.3 (h/D_l). This sequence of video snap-shots were taken from consecutive frames over a time period of 0.4s. This vortex movement was captured in the scaled model experiments (see Fig. 7.3).

[†]when facing and looking into the engine

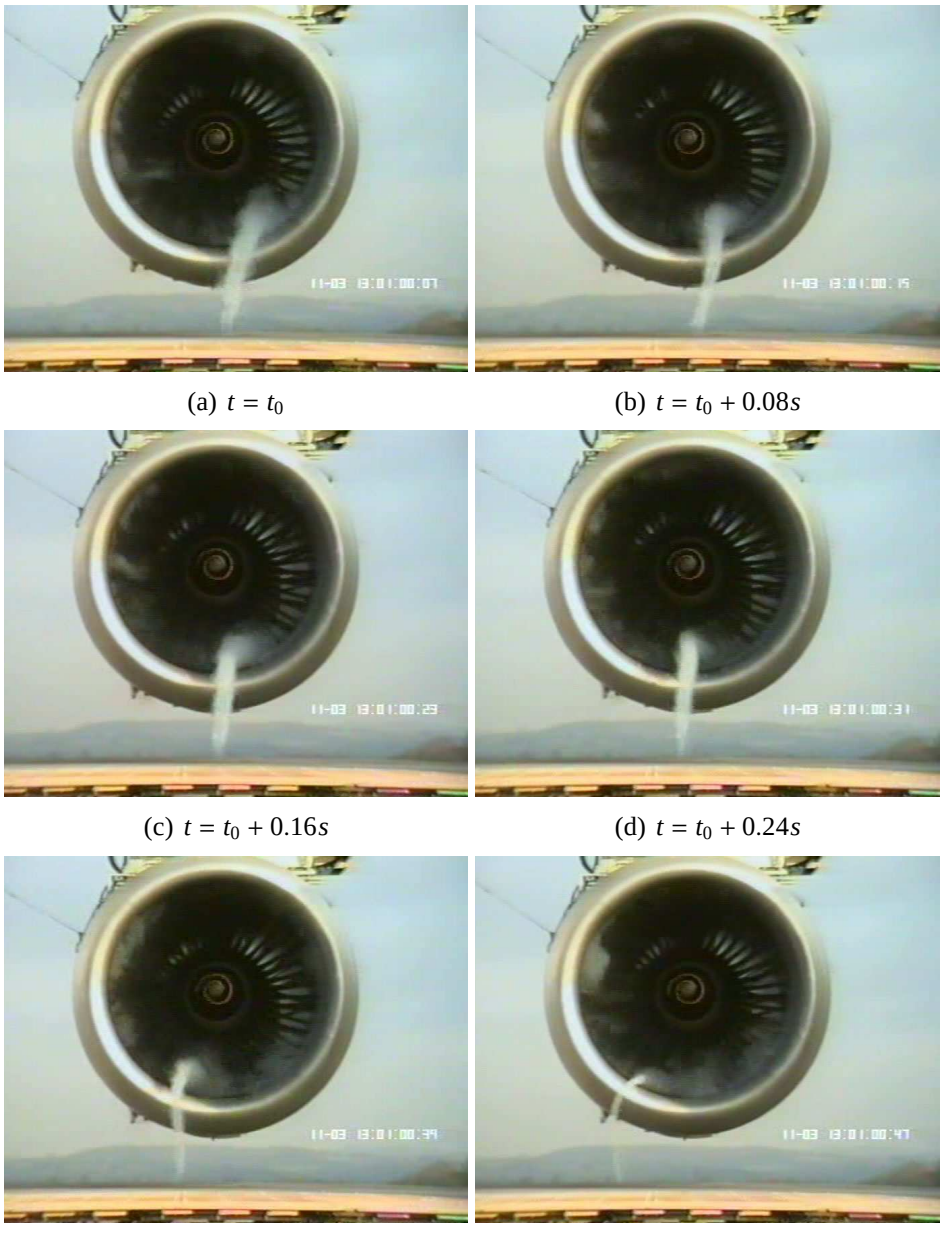

(a) $t = t_0$ (b) $t = t_0 + 0.08s$

(c) $t = t_0 + 0.16s$ (d) $t = t_0 + 0.24s$

(e) $t = t_0 + 0.32s$ (f) $t = t_0 + 0.40s$

Figure A.4: Movement of cross-wind ground vortex ahead of the highlight plane ($h/D_l \approx 0.30$)[48].

(a) $t = t_0$

(b) $t = t_0 + 0.04s$

(c) $t = t_0 + 0.08s$

(d) $t = t_0 + 0.12s$

(e) $t = t_0 + 0.16s$

(f) $t = t_0 + 0.20s$

Figure A.5: Reattachement of ground vortex ($h/D_l \approx 0.30$) and $U_i/U_\infty \approx 7$[48].

Fig. A.5 illustrates some of the features of the ground vortex behaviour, under cross-wind conditions when the vortex is close to the blow-away condition. For this image set, the velocity ratio is around 7 (U^*) and the height-to-diameter ratio is approximately 0.3 (h/D_l). Therefore using the vortex map presented in Fig. 2.3 it can be seen that the operating condition is close to the formation boundary. Under such conditions the vortex is observed to be very unsteady and often the vortex loses ground plane contact and then reattaches randomly at a later time. The series of snap-shots shown in Fig. A.5 illustrates the reattachment phase of the vortex to the surface.

In contrast, the series of video snap-shots shown in Fig. A.6 demonstrates the blow-away nature of the vortex under crosswind conditions. An interesting feature is that despite the vortex being downstream of the engine, there can still be ground plane contact (Fig. A.6). Eventually the vortex detaches from the surface to form a trailing vortex, however the vortex is still clearly ingested into the intake.

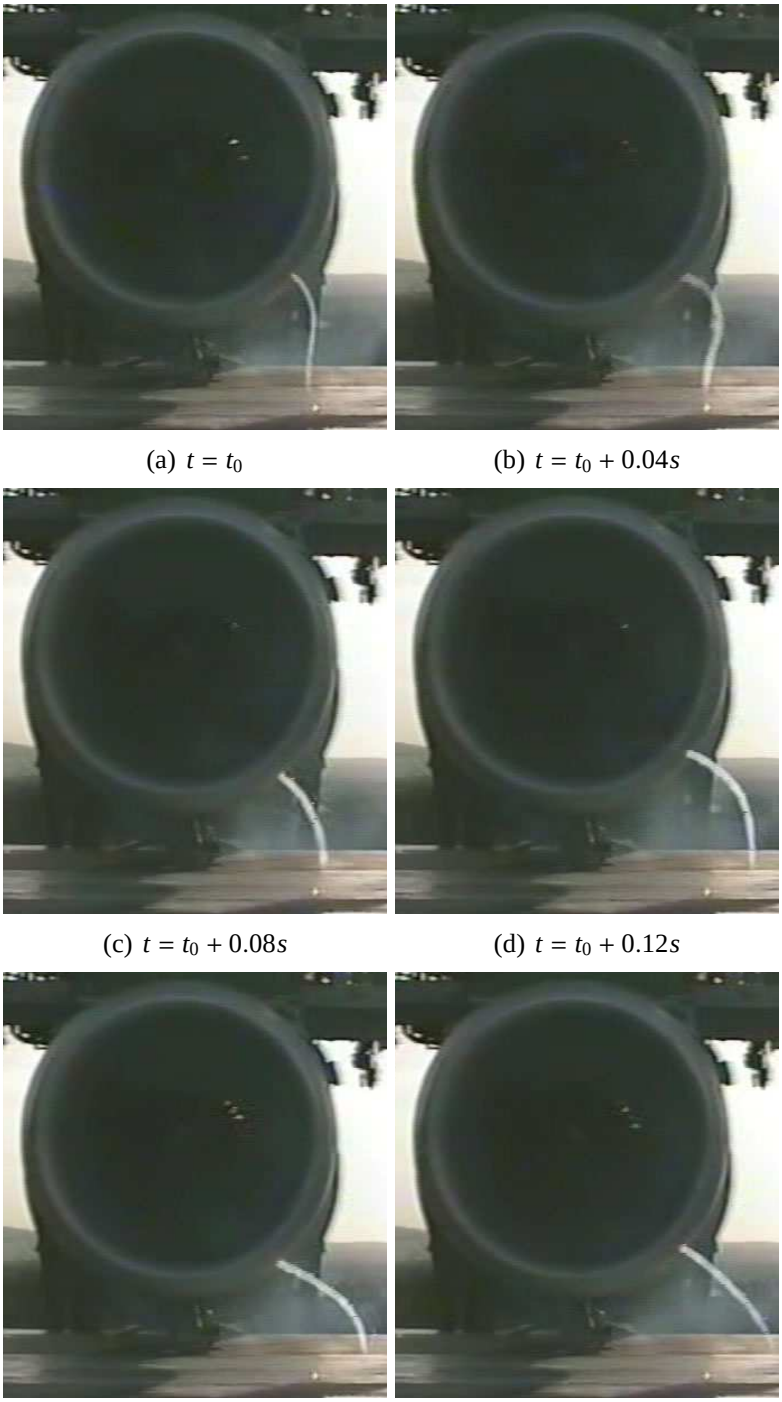

(a) $t = t_0$ (b) $t = t_0 + 0.04s$

(c) $t = t_0 + 0.08s$ (d) $t = t_0 + 0.12s$

(e) $t = t_0 + 0.16s$ (f) $t = t_0 + 0.20s$

Figure A.6: Blow-away of vortex at U_i/U_∞ close to the critical value[48].

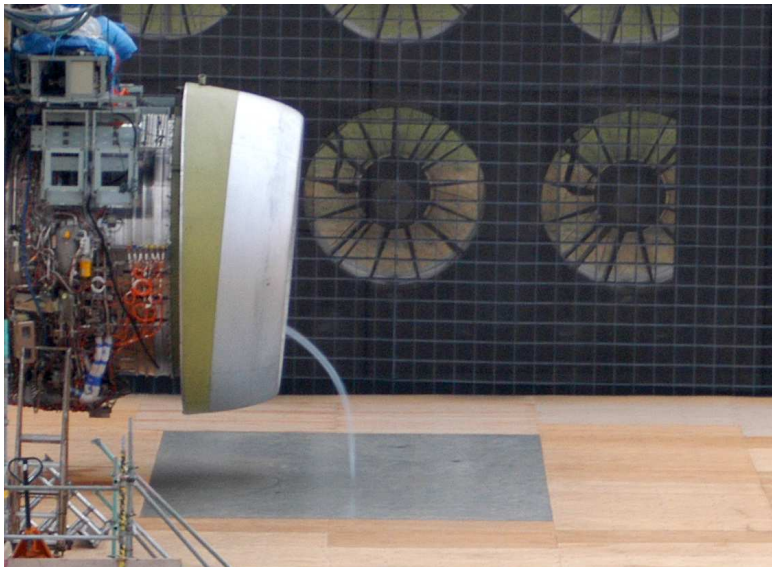

Figure A.7: Stand-off distance of crosswind ground vortex (conditions unknown)[48]

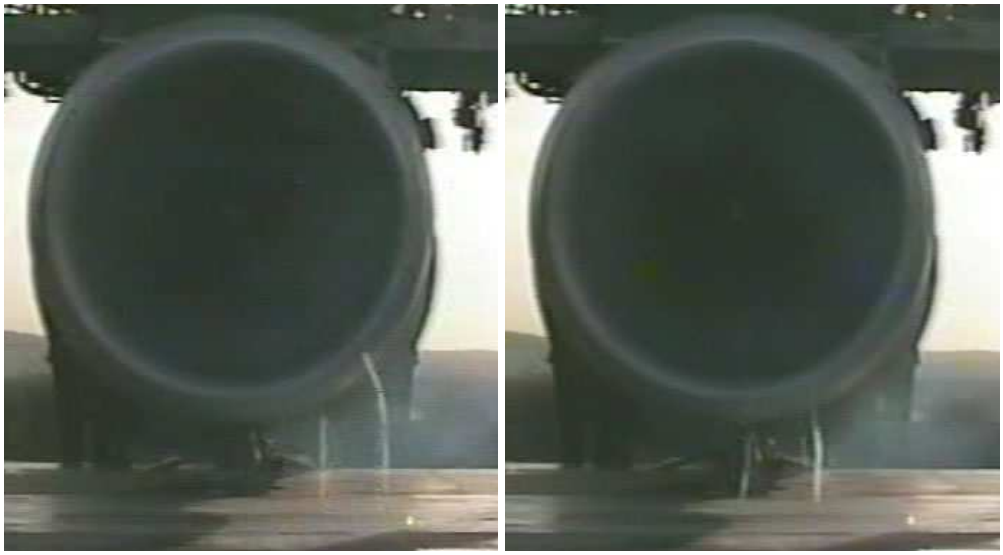

(a) (b)

Figure A.8: Crosswind flow modes at U_i/U_∞ close to the critical value illustrating the ingestion of two weak vortices[48].

A.4 Reverse Thrust

A series of video snap-shots shown in Fig. A.9 illustrates ground vortex ingestion in a C-17 aircraft moving backwards under the influence of reverse thrust operation. Vortex formation under such conditions has been known to initiate engine surge because the vortex often is ingested into the core of the engine[33]. Fig. A.9 illustrates that the vortex is often ingested into the core. The image set also demonstrates the highly unsteady nature of the vortex at this height-to-diameter ratio.

(a) $t = t_0$ (b) $t = t_0 + 1s$

(c) $t = t_0 + 2s$ (d) $t = t_0 + 3s$

(e) $t = t_0 + 4s$ (f) $t = t_0 + 5s$

Figure A.9: Ground vortex ingestion during reverse thrust operation with the aircraft moving backwards (h/D_l estimated to be approx 2.0) ©Keith Thomas[58].

APPENDIX **B**

Experiment Set-Up

This appendix gives further details of the experiment set-up including the suction system and the PIV configuration.

B.1 Suction System

The suction system consisted of a large vacuum tank situated outside the tunnel. The tank has a capacity of approximately 60 m^3 and was connected to the intake model via a network of ducting. The network consisted of a total length of approximately 40 *m* of 8 *inch* bore ducting (Fig. B.1a). Once the ducting is above the tunnel working section a 90 degree bend is used to direct the tubing directly towards the tunnel floor. A diffuser is then used which is situated immediately above the tunnel working section (Fig. B.2) to bring the diameter of the ducting down to approximately that of the intake (the start of the diffuser can be seen protruding the tunnel wall in Fig. B.1b). A small section of green flexible tubing (with an inside diameter of 4 *inchs*) is used between the start of the diffuser and the straight through duct section (Fig. B.1c). This straight through duct section can be replaced with a sonic throat designed for a specific Mach number (see §B.1.1), when a lower Mach number is required. A small section of rigid ducting approximately 1.5 *m* in length then connects the straight through duct to the back of the intake model (Fig. B.1c).

For the crosswind experiments, the ducting system within the tunnel working section was slightly different. The turntable above the tunnel was rotated through ninety degrees and the strut was attached to the second position from the centre of the mounting plate*. A ninety degree bend is attached to the 1.5 *m* length rigid ducting and a smaller length of rigid ducting, approximately 0.4 *m* in length, is then attached to the other end. The intake model was then attached to the end of the 0.4 *m* length ducting.

Above the tunnel, approximately 2 *m* before the 90 degree bend that turns the ducting in through the roof of the tunnel, a gate valve is located which was always fully open during these tests. A quick release shutter valve was also located approximately

*This differs from the headwind configuration where the mounting plate is aligned with the flow direction and attached to the most downstream location

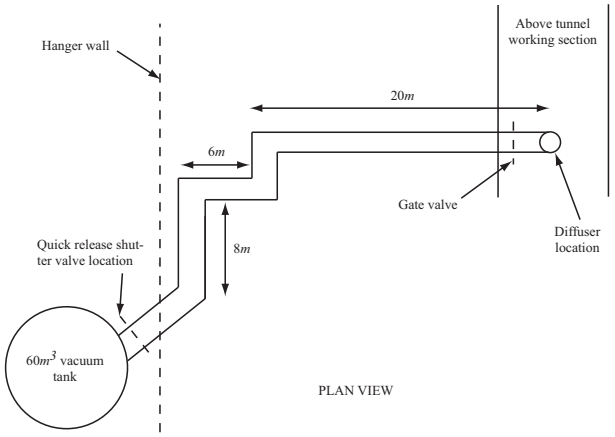

(a)

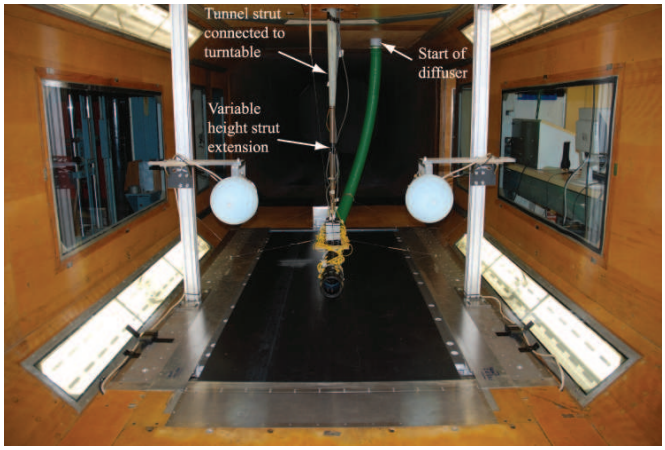

(b)

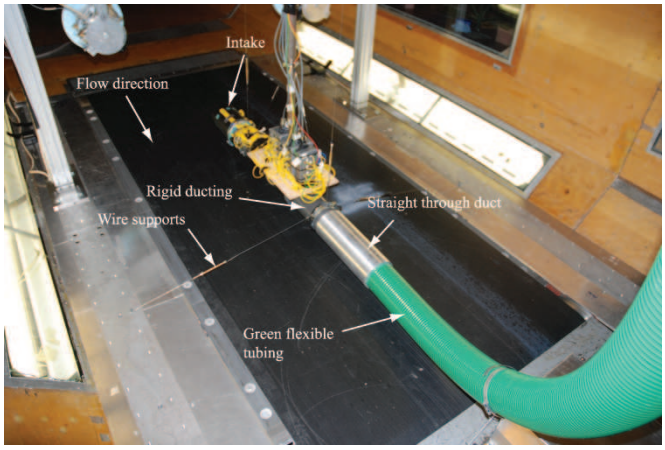

(c)

Figure B.1: Ducting set-up within the tunnel working section

2 *m* from the exit of the suction tank (Fig. B.1a). This was controlled by a power switch which was located inside the tunnel control room. When the suction was re-

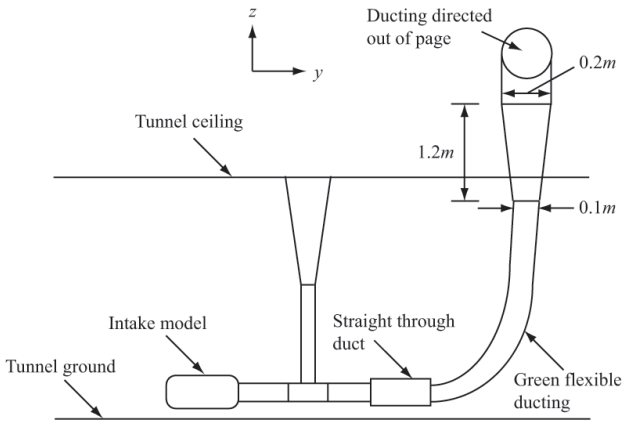

Figure B.2: Schematic side view of the tunnel working section illustrating the ducting set-up for the headwind configuration and the diffuser location and dimensions

quired, the shutter was opened within approximately 0.1 *s*. This therefore exposed the vacuum to the air within the tunnel creating suction through the model intake and the associated ducting system. The mass flow was monitored using 8 static pressure ports pneumatically averaged within the intake duct. A maximum mass flow was achieved of approximately 1.49 kgs^{-1}, 1 *s* after initiation. For a fully vacuumed tank, in which the pressure was at -990 *mbar* within the chamber, a constant maximum mass flow was achieved for approximately 22 *s*. Before each run it was ensured that the pressure in the chamber was at least -950 *mbar*, which guaranteed a run time of 20 *s*. Two vacuum pumps connected in series are used to draw all the air from the tank to create a vacuum again. The pumps were run continuously throughout testing and required roughly 10 minutes for a vacuum of -950 *mbar* to be achieved from atmospheric conditions.

B.1.1 Sonic Nozzle Design

A sonic nozzle and a straight through duct section were designed to be placed just behind the 1.5 *m* rigid ducting in the working suction of the tunnel (Fig. B.1c, labelled 'straight through duct' in picture). The sonic nozzle was designed so that the flow chokes at the throat of the duct insert. The area ratio between the sonic nozzle throat and the intake inner diameter corresponds to a Mach number of 0.43. A diagram of the sonic nozzle is shown in Fig. B.3a. To achieve the maximum mass flow in the system, a straight through duct was implemented instead of the sonic throat. With this in place the flow appeared to choke at the entrance to the diffuser which had an inside diameter of 4 *inchs* (Fig. B.1b). It was expected to have occurred here due to boundary layer growth in the ducting system. For this duct configuration the intake Mach number, M_i, reached a value of 0.58, under headwind conditions and 0.55 under crosswind conditions. This corresponds to a mass flow of 1.49 and 1.46 kgs^{-1} respectively. The geometry of the straight through duct section is shown in Fig. B.3b.

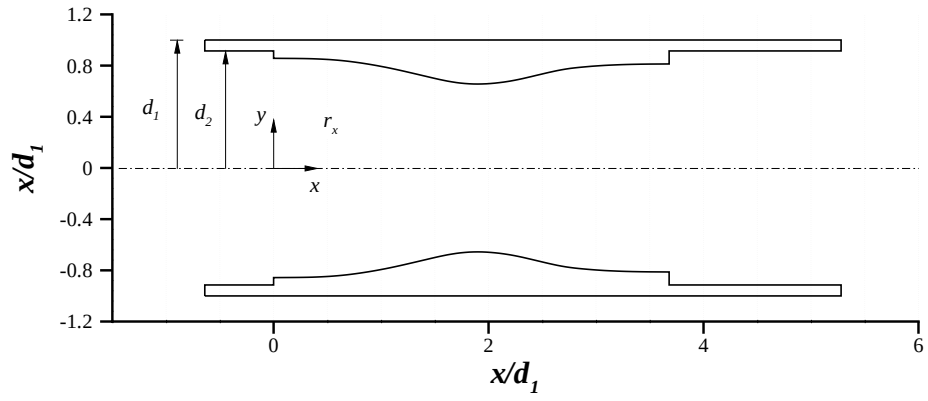

(a)

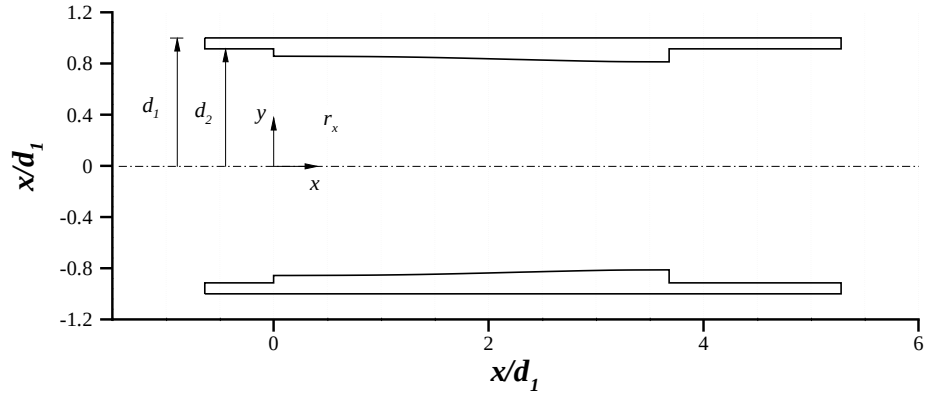

(b)

Figure B.3: (a) Sonic throat designed for an intake Mach number of $M_i = 0.43$ and (b) the straight through duct

B.2 SPIV Set-Up

Within in this section additional information on the PIV set-up is given. A picture of the camera location underneath the perspex insert for the static ground tests is shown in Fig. B.4. This picture illustrates the orientation of the cameras relative the flow direction. Both cameras were operated in partial scatter with respect to the light sheet direction. For all set-ups the cameras were at 45° inclination to the light sheet for optimum accuracy.

With the TSI system the calibration is performed using a black, square calibration grid of white dots displaced by 10mm. The dots are located on planes with alternating depths displaced by a distance of 0.5 *mm*. A mirror is situated at one end of the plate, perpendicular to the face and is located between the two planes of dots. The calibration plate is positioned in the area of interest, with the mirror facing the laser direction. The plate was orientated so that it was level with the ground plane and its height was 10mm from the surface. The laser position was adjusted so that the beam reflects back into

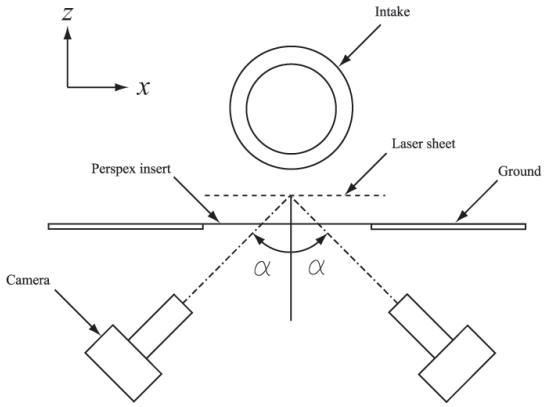

Figure B.4: Schematic of the camera location and orientation for the static ground headwind and crosswind configurations (flow is into the page)

itself from the mirror of the calibration plate. This ensures that the light sheet is parallel and in-line with the plate.

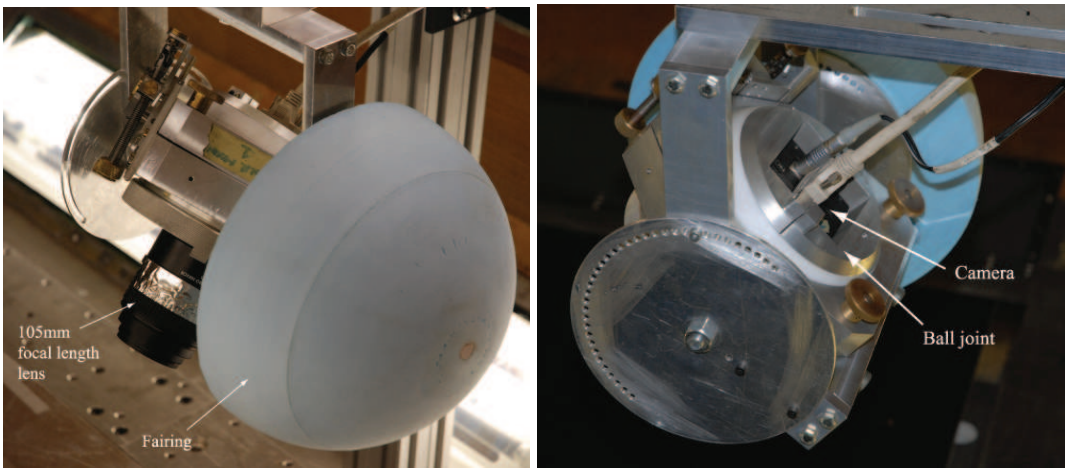

(a) (b)

Figure B.5: Picture of camera mounts used in the experiments to satisfy the Scheimpflug condition

The cameras are focused onto the calibration plate by satisfying the Scheimpflug condition, so that the dots on each plane are well focused. The Scheimpflug condition was achieved using custom made camera mounts in which the camera is located in a ball joint enabling two-axis Scheimpflug focusing. Since the cameras were always at one angle with respect to the object plane, focusing only needed to be performed on one axis. With the Scheimpflug condition satisfied, pictures of the calibration plate were taken.

Within Insight 3G the local magnification factor between the image and the object

plane is determined using a second order warping approach of the acquired calibration plate pictures. Each image is cross-correlated with the correlation peaks indicating the position of the white dots on the calibration grid. A three point Gaussian estimator is then used to determine the points to sub pixel accuracy. The coordinates of the points are constructed into a grid and a least squares fit of the positions is applied using a third order polynomial to each image-object point pairs. The least squares solution gives a total of six polynomial equations for each camera. A set of coefficients is then determined which enables the grid image to be reconstructed into a back projected image with a constant magnification factor.

B.2.1 Optics Configuration

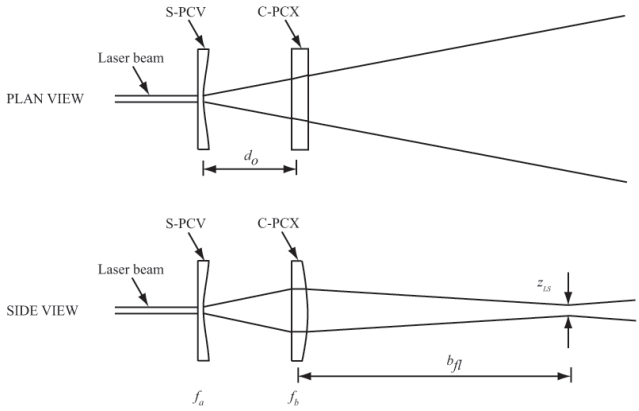

(a)

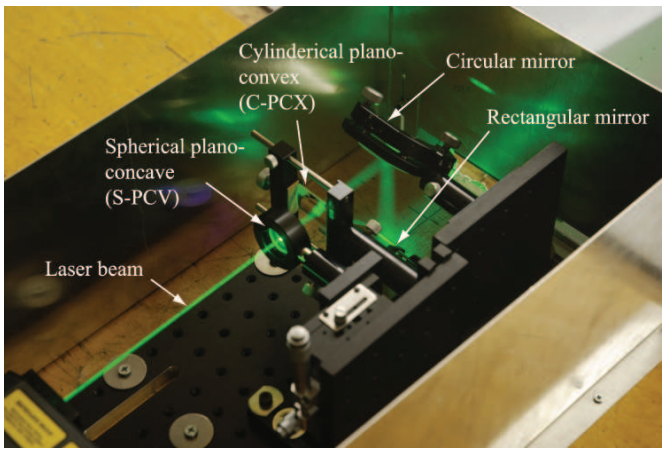

(b)

Figure B.6: Optics configuration

The optics configuration used for all PIV experiments was a combination of spherical plano-concave lens (S-PCV) and a cylindrical plano-convex lens (C-PCX). A

schematic of the arrangement and photograph of the set-up with the laser in operation is given in Fig. B.6. The S-PCV lens diverges the laser beam in all directions. The C-PCX lens is then used to restrict the divergence to one plane (Fig. B.6a), whilst focusing on a plane perpendicular to the divergent stratum. The distance over which the light sheet is focused is given by the back focal distance, b_{fl}. Given that the distance between the optics and measurement plane is fixed[†], the gap between the lens, d_o is adjusted to achieve optimal focus of the light sheet for a given b_{fl}. This distance can be determined from thin lens theory[55]:

First the combined focal length the two optics is determined given by Eq. B.2.1:

$$f_{ab} = \frac{f_a f_b}{f_a + f_b - d_o} \tag{B.2.1}$$

The back focus distance, b_{fl}, from the second principal point of optic f_b (Fig. B.6a) is then calculated using the combined focal length, f_{ab}, the distance between the two optics, d_o, and the focal length of the first optic, f_a, via Eq. B.2.2[55]:

$$b_{fl} = f_{ab}\frac{f_a - d_o}{f_a} \tag{B.2.2}$$

The optic configuration used in all experiments is given in Table B.1.

b_{fl}	f_a	Diameter	f_b	Size	d_o	Δz_{LS}
≈ 2000	-33	10	+63	100×40	≈ 32	1.5

Table B.1: Optics configuration used in the experiments (all dimensions are in *mm*)

[†]This distance is effectively the b_{fl}

APPENDIX C

Empty Wind Tunnel Measurements

In this appendix measurements of the Cranfield University 8′×6′ wind tunnel flow with no intake model or ducting installed is presented. This appendix includes boundary layer measurements on the tunnel ground plane at position approximately equal to the intake location for a completely empty tunnel. In addition PIV measurements of the tunnel flowfield are presented.

C.1 Boundary Layer Measurements

The location of the boundary layer measurements and its relative position from the different boundary layer suction methods is shown in Fig. C.1. For all measurements the PIV seeding rake was in place at the same location as that used in the PIV experiments (Fig. C.1). Boundary layer data was also taken without the seeding rake in position for the full range of configurations to quantify its influence on the boundary layer characteristics. Due to tunnel limitations at the time of testing data could only be taken up to a tunnel speed, U_∞, of 40 ms^{-1}. The profiles, for all three suction configurations, from the lowest investigated tunnel velocity of 10 ms^{-1} in steps of 5 ms^{-1}, is shown in Figs. C.2 and C.3.

For each profile the primary boundary layer characteristics have been determined. This includes the boundary layer thickness, δ, at 99% of the free-stream velocity, U_∞. The displacement thickness, δ^*, and momentum thickness, θ, both of which are defined in Eq. C.1.1 and C.1.2.

$$\delta^* = \int_0^{y\to\infty} \left(1 - \frac{u}{U_\infty}\right) dy \tag{C.1.1}$$

$$\theta = \int_0^{y\to\infty} \frac{u}{U_\infty}\left(1 - \frac{u}{U_\infty}\right) dy \tag{C.1.2}$$

The boundary layer shape factor, H_{bl}, which is the ratio of the displacement to the momentum thickness (Eq. C.1.3) and the Reynolds number based on the displacement thickness, Re_{δ^*} (Eq. C.1.4), have also been determined for each profile.

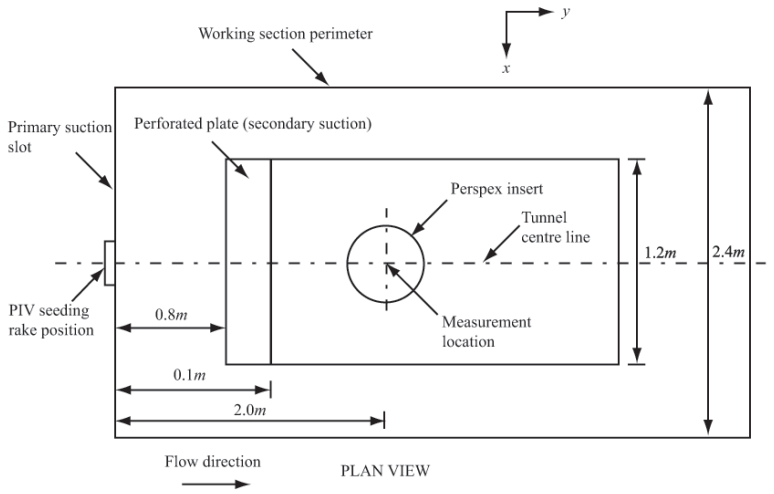

Figure C.1: Location of boundary layer measurements relative to the suction slots used to control the boundary layer thickness

$$H_{bl} = \frac{\delta^*}{\theta} \tag{C.1.3}$$

$$Re_{\delta^*} = \frac{\delta^* U_\infty}{\nu} \tag{C.1.4}$$

In addition the wall normal velocity gradient, $\partial v/\partial z$, has been integrated from the ground up to the PIV plane location ($z = h_L$) (Eq. C.1.5) and also across the whole boundary layer thickness, δ (Eq. C.1.6). Both parameters are an indication of the amount of circulation within the boundary layer per unit width and will aid in interpreting the vortex strength data for different boundary layer thicknesses presented in §5.2.3. All parameters for all configurations both with and without the seeding rake in position are summarized in Tables C.1-C.3.

$$\Gamma_{piv} = \int_0^{h_L} \frac{\partial v}{\partial z} \partial x \partial z \tag{C.1.5}$$

$$\Gamma_{tot} = \int_0^{\delta} \frac{\partial v}{\partial z} \partial x \partial z \tag{C.1.6}$$

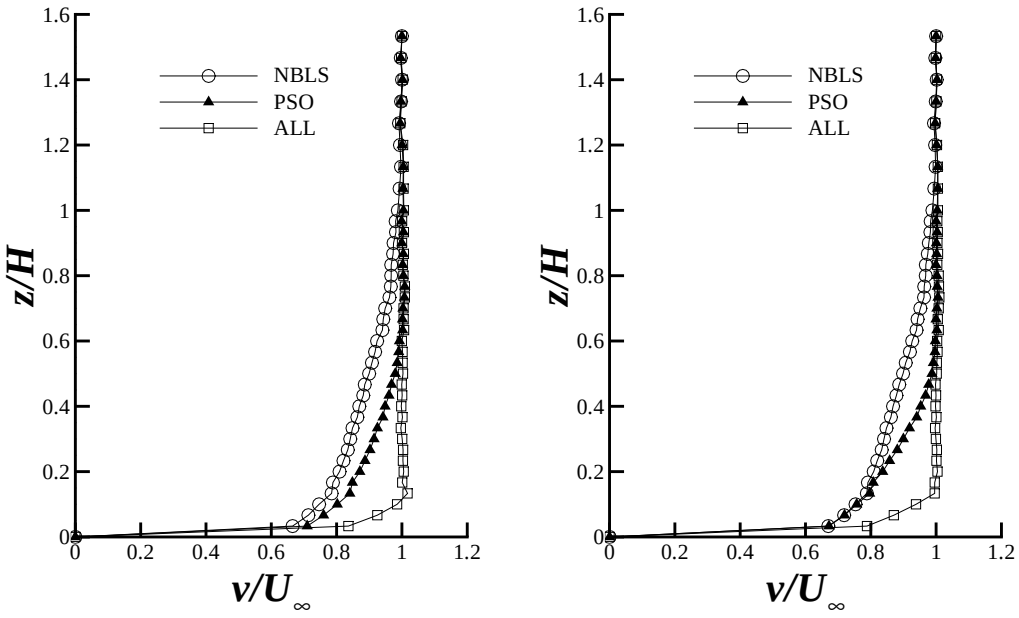

(a) $U_\infty = 10\ ms^{-1}$ (b) $U_\infty = 15\ ms^{-1}$

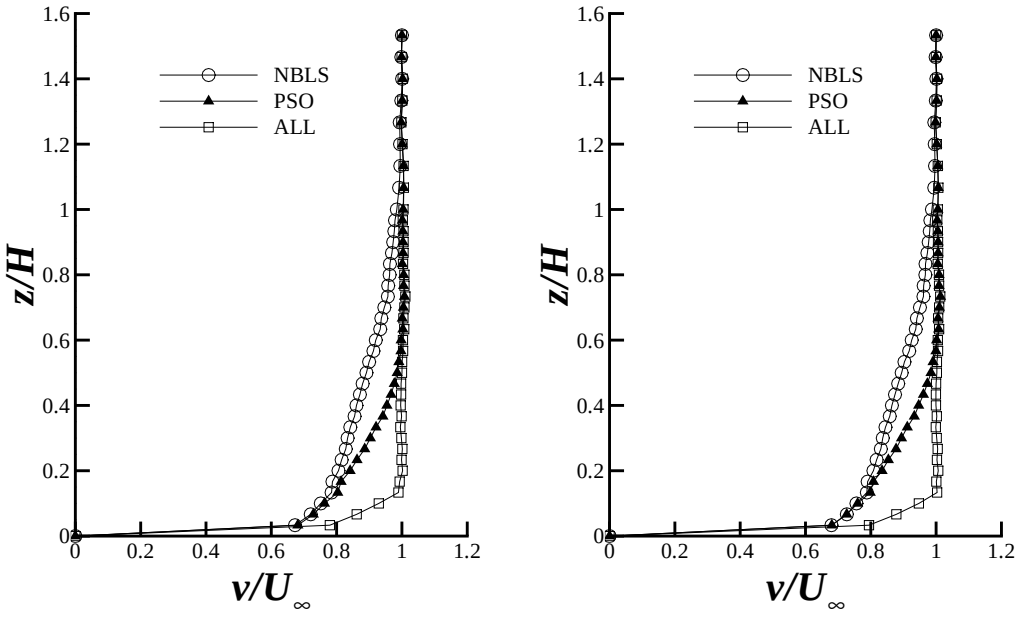

(c) $U_\infty = 20\ ms^{-1}$ (d) $U_\infty = 25\ ms^{-1}$

Figure C.2: Boundary layer profiles with the tunnel empty in the $8' \times 6'$ wind tunnel. Note H is the centreline height of the intake for the datum ground clearance of 0.25 (h/D_l)

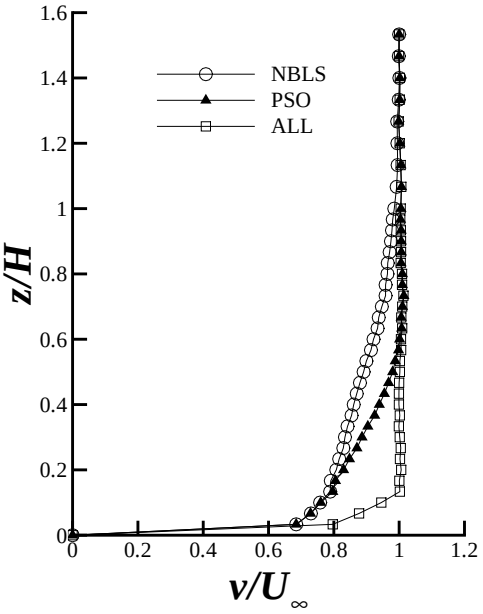

(a) $U_\infty = 30\ ms^{-1}$

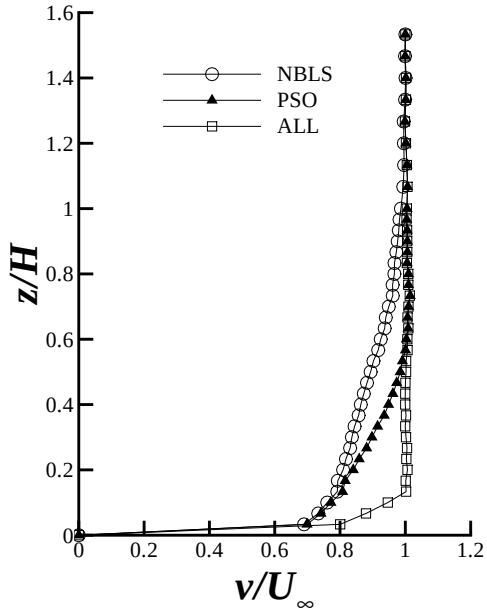

(b) $U_\infty = 35\ ms^{-1}$

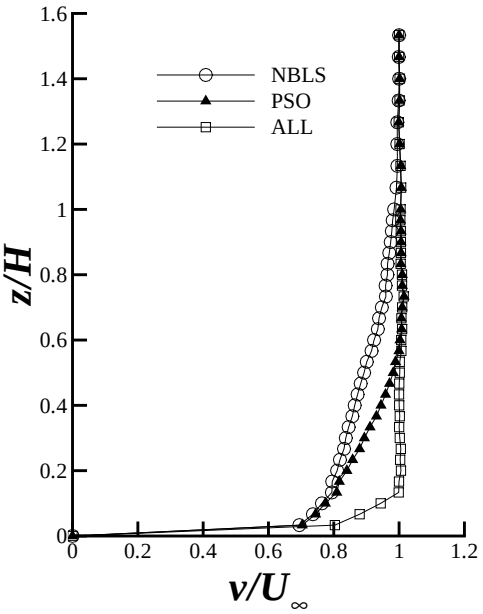

(c) $U_\infty = 40\ ms^{-1}$

Figure C.3: Boundary layer profiles with the tunnel empty in the $8' \times 6'$ wind tunnel, continued

U_∞ (ms^{-1})	δ/D_l	δ^*/D_1	θ/D_l	H_{bl}	$1/n_{bl}$	Re_{δ^*}	$\Gamma_{piv}/(U_\infty D_l)$	$\Gamma_{tot}/(U_\infty D_l)$
With Seeding Rake								
9.950	1.050	0.111	0.071	1.566	0.105	8700	11.983	14.018
14.434	1.050	0.110	0.070	1.612	0.104	12932	12.474	14.511
19.335	1.050	0.114	0.073	1.625	0.107	17880	12.419	14.465
24.152	1.000	0.111	0.071	1.635	0.108	21744	12.519	14.513
29.433	1.050	0.113	0.073	1.637	0.105	26478	12.384	14.335
34.235	1.000	0.111	0.071	1.640	0.106	30349	12.489	14.416
39.127	1.050	0.111	0.072	1.640	0.102	34800	12.553	14.456
Average	**1.036**	**0.111**	**0.072**	**1.622**	**0.105**	-	**12.403**	**14.388**
Without Seeding Rake								
9.950	0.375	0.064	0.030	2.133	0.156	5005	12.228	13.963
14.434	0.375	0.063	0.030	2.067	0.151	7413	12.790	14.566
19.335	0.375	0.063	0.030	2.075	0.148	9853	12.833	14.540
24.152	0.400	0.064	0.031	2.083	0.140	12510	12.918	14.620
29.433	0.400	0.062	0.030	2.102	0.133	14597	12.914	14.504
34.235	0.400	0.062	0.030	2.111	0.130	16888	13.047	14.614
39.127	0.400	0.060	0.029	2.121	0.124	18903	13.199	14.697
Average	**0.389**	**0.062**	**0.030**	**2.099**	**0.140**	-	**12.847**	**14.501**

Table C.1: Boundary layer characteristics for when no upstream suction is implemented (NBLS)

U_∞ (ms^{-1})	δ/D_l	δ^*/D_1	θ/D_l	H_{bl}	$1/n_{bl}$	Re_{δ^*}	$\Gamma_{piv}/(U_\infty D_l)$	$\Gamma_{tot}/(U_\infty D_l)$
With Seeding Rake								
9.633	0.475	0.068	0.036	1.634	0.118	5357	13.247	14.880
14.213	0.475	0.075	0.040	1.645	0.143	8849	12.739	14.741
19.168	0.475	0.073	0.039	1.646	0.138	11503	12.732	14.637
23.906	0.425	0.074	0.039	1.650	0.155	14537	12.720	14.653
28.874	0.450	0.076	0.040	1.649	0.150	17785	12.666	14.576
33.725	0.425	0.072	0.037	1.649	0.146	19657	12.875	14.679
38.602	0.425	0.072	0.038	1.648	0.145	22631	12.910	14.693
Average	**0.450**	**0.073**	**0.038**	**1.646**	**0.142**	**14331**	**12.841**	**14.694**
Without Seeding Rake								
9.633	0.450	0.064	0.032	2.071	0.121	5004	13.225	14.742
14.213	0.425	0.061	0.030	2.064	0.117	7168	13.668	15.142
19.168	0.425	0.059	0.028	2.078	0.113	9261	13.610	15.018
23.906	0.425	0.054	0.025	2.094	0.098	10608	14.028	15.241
28.874	0.425	0.056	0.027	2.104	0.101	13255	13.900	15.156
33.725	0.425	0.055	0.025	2.116	0.101	15136	13.861	15.140
38.602	0.425	0.055	0.025	2.124	0.101	17294	13.871	15.147
Average	**0.429**	**0.058**	**0.027**	**2.093**	**0.107**	-	**13.738**	**15.084**

Table C.2: Boundary layer characteristics for when only primary suction is applied (PSO)

U_∞ (ms^{-1})	δ/D_l	δ^*/D_1	θ/D_l	H_{bl}	$1/n_{bl}$	Re_{δ^*}	$\Gamma_{piv}/(U_\infty D_l)$	$\Gamma_{tot}/(U_\infty D_l)$
With Seeding Rake								
9.357	0.100	0.029	0.003	1.645	0.122	2261	16.363	16.430
14.015	0.150	0.033	0.006	1.656	0.120	3865	15.655	15.973
18.822	0.150	0.034	0.007	1.654	0.129	5380	15.394	15.767
23.646	0.100	0.031	0.005	1.655	0.172	6094	15.591	15.807
28.575	0.100	0.031	0.005	1.652	0.171	7343	15.488	15.708
33.451	0.100	0.031	0.004	1.652	0.168	8469	15.474	15.684
38.373	0.125	0.031	0.005	1.651	0.133	9711	15.415	15.648
Average	**0.118**	**0.031**	**0.005**	**1.652**	**0.145**	-	**15.626**	**15.860**
Without Seeding Rake								
9.357	0.100	0.024	0.002	2.039	0.115	1853	16.448	16.406
14.015	0.100	0.026	0.002	2.066	0.143	3095	16.145	16.200
18.822	0.100	0.028	0.002	2.086	0.148	4372	15.961	16.031
23.646	0.100	0.030	0.003	2.105	0.167	5821	15.661	15.836
28.575	0.100	0.030	0.004	2.114	0.168	7114	15.530	15.716
33.451	0.100	0.030	0.004	2.124	0.161	8216	15.568	15.722
38.373	0.100	0.030	0.003	2.131	0.152	9261	15.610	15.732
Average	**0.100**	**0.028**	**0.002**	**2.095**	**0.151**	-	**15.846**	**15.949**

Table C.3: Boundary layer characteristics for when both suctions methods are in operation

From the results summarized in Tables C.1-C.3 a number of points can be made:

- The boundary layer characteristics are roughly constant across all tunnel speeds both with and without the PIV seeding rake upstream.
- The PIV seeding rake has a large impact on the boundary layer thickness when no boundary layer suction is implemented upstream. δ/D_l increases from 0.389 without the seeding rake to 1.036 with. This difference can be seen in Fig. C.4a.
- For the cases with just the primary suction and with both suction methods implemented, the seeding rake has no obvious impact on the boundary characteristics (Fig. C.4b-c).
- The integrated vorticity within the approaching boundary layer, Γ_{tot}, is largely only a function of the free-stream velocity, U_∞. For the investigated boundary layer thicknesses Γ_{tot} increases slightly as δ reduces.
- In general at least 90% of the approaching boundary layer circulation is located below the PIV measurement plane.

C.2 PIV Measurements of Freestream

PIV measurements of the tunnel flow were taken subsequent to the rolling ground plane experiments. Data was taken at the ground vortex measurement location (i.e. at a plane parallel to the ground at a height $h_L/D_l = 0.083$), with no intake or ducting installed in the tunnel. For these tests the cameras were located inside the tunnel working section (see Fig. 6.1) with the rolling road installed and with the seeding rake in the usual position. Data was taken at two tunnel speeds of 10 and 20 ms^{-1} for two boundary layer configurations (with no suction and with all boundary layer suction). For each configuration 500 flowfield snap-shots were acquired to obtain a reasonable average of the flow. The resulting average flowfields for all four combinations are shown in Fig. C.5 which plots contours of v-velocity. It is clear from contour plots and the average streamlines that there is an asymmetry in the flow. For all cases there is a negative lateral velocity gradient (i.e. $\partial u/\partial x = -ve$). This could be due to asymmetries naturally present in the flowfield or it may be a result of the light sheet not being parallel to the ground plane.

The fluctuating velocities (u', v', w') have also be calculated for all four configurations over all 500 flowfield snapshots. From this the rms fluctuations (i.e. $\sqrt{u'^2}$, $\sqrt{v'^2}$, $\sqrt{w'^2}$) have been computed at each grid point and averaged over the whole measurement domain. The values for each configuration are summarized in Table C.4 and have been compared with the measurements of the fluctuating velocities for a flat-plate presented in White[67] (Fig. C.6). The comparison between both datasets is in good agreement.

$U_\infty\ (ms^{-1})$	BLS1	BLS2	y/δ	$\sqrt{u'^2}/U_\infty$	$\sqrt{v'^2}/U_\infty$	$\sqrt{w'^2}/U_\infty$
9.950	n	n	0.08	0.059	0.076	0.046
9.357	y	y	0.83	0.001	0.009	0.007
19.335	n	n	0.08	0.055	0.072	0.043
18.822	y	y	0.56	0.028	0.026	0.033

Table C.4: Turbulence characteristics at the PIV measurement plane for an empty tunnel

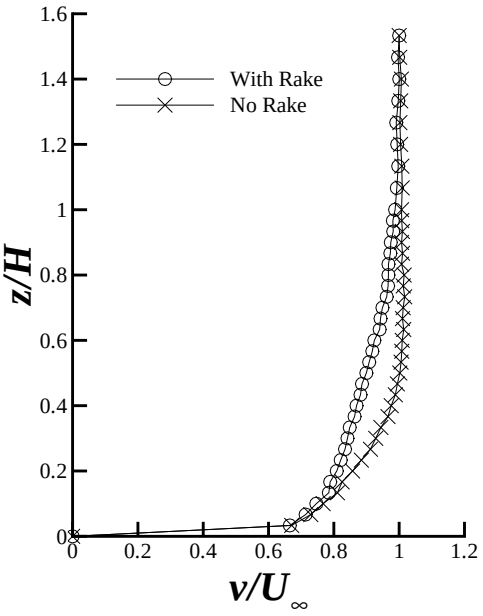

(a) No boundary layer suction (NBLS)

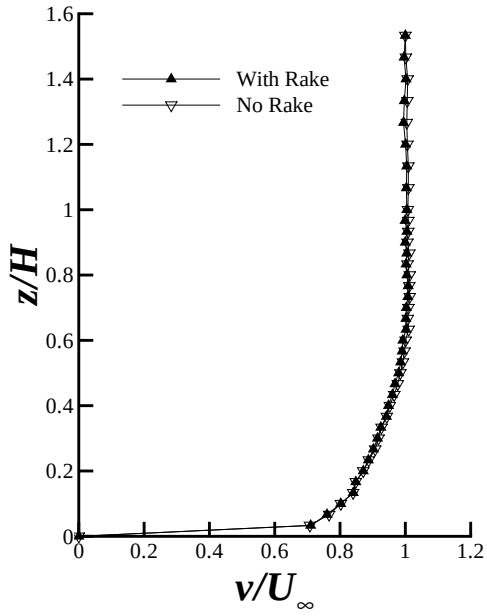

(b) Primary suction only (PSO)

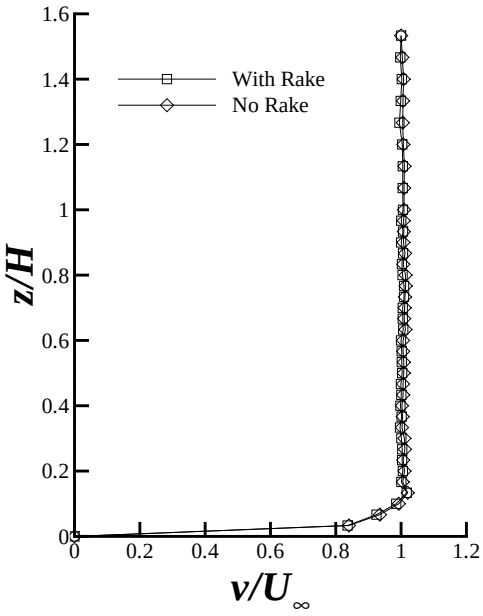

(c) All boundary layer suctions (ALL)

Figure C.4: Effect of rake presence on the boundary profile at the intake position for all three suction configurations

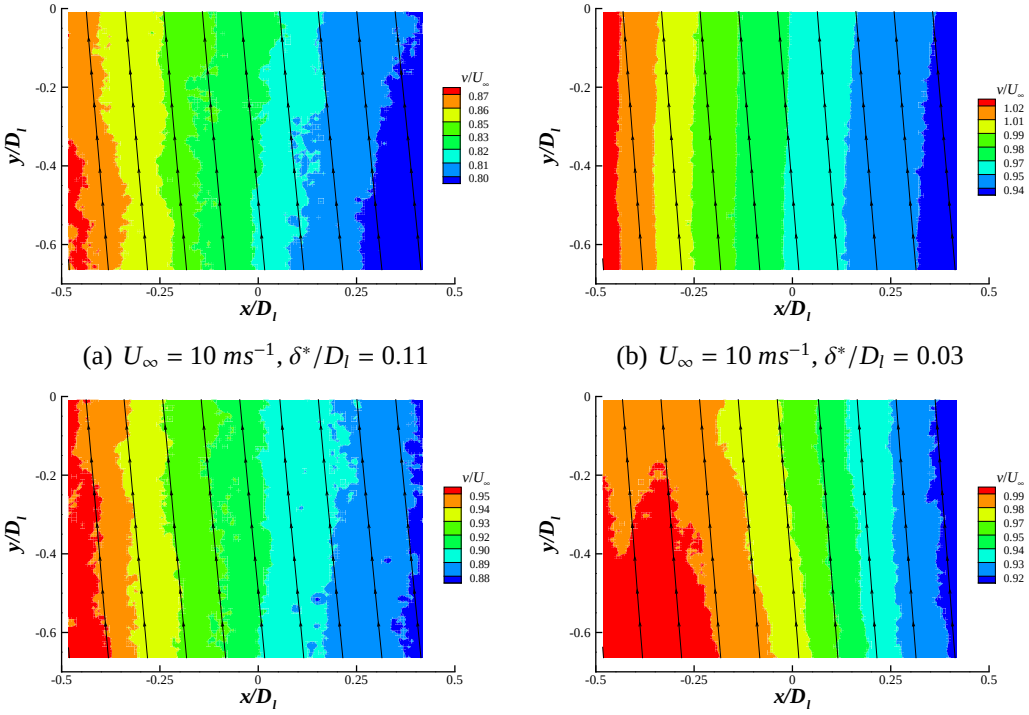

(a) $U_\infty = 10\ ms^{-1}$, $\delta^*/D_l = 0.11$ (b) $U_\infty = 10\ ms^{-1}$, $\delta^*/D_l = 0.03$

(c) $U_\infty = 20\ ms^{-1}$, $\delta^*/D_l = 0.11$ (d) $U_\infty = 20\ ms^{-1}$, $\delta^*/D_l = 0.03$

Figure C.5: Plots of streamwise (v-velocity) velocity

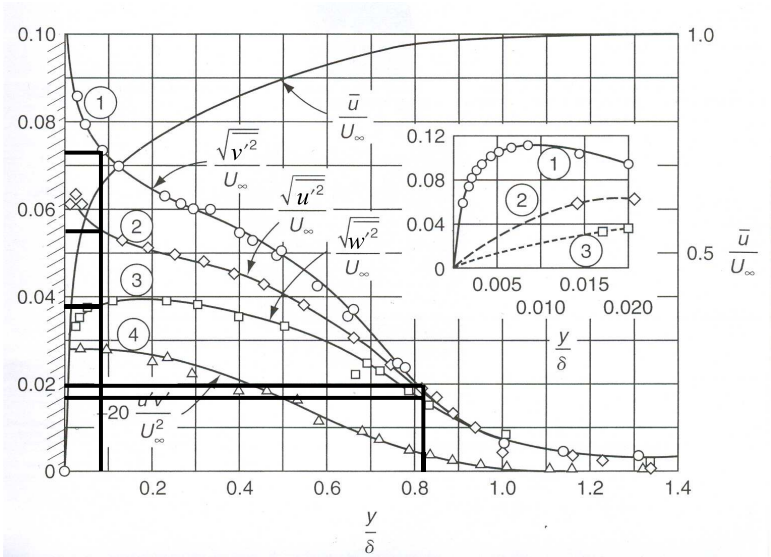

Figure C.6: Flat plate measurements of the fluctuating velocities, u', v' and w' [67]

APPENDIX **D**

Test Matrix

D.1 Headwind

Table D.1: Test matrix for the headwind experiments

h/D_l	U_∞ **(**ms^{-1}**)**	U^*	PIV	TP	Γ^*	DC_{60}
$\delta^*/D_l = 0.11$, $M_i = 0.58$						
0.250	0.000	∞	✓	✓	0.070	0.015
	9.580	19.808	✓	✓	0.066	0.016
	14.434	13.291	✓	×	0.077	-
	19.085	10.018	✓	✓	0.111	0.022
	23.906	8.028	✓	✓	0.194	0.026
	28.874	6.614	✓	✓	0.248	0.030
	33.725	5.628	✓	✓	0.277	0.033
	38.602	4.891	✓	✓	0.278	0.034
	43.611	4.380	×	✓	-	0.032
	48.421	3.900	✓	✓	0.184	0.024
$\delta^*/D_l = 0.07$, $M_i = 0.58$						
0.250	9.633	19.954	✓	✓	0.060	0.017
	14.213	13.476	✓	×	0.083	-
	19.168	10.005	✓	✓	0.144	0.022
	23.906	8.028	✓	✓	0.201	0.026
	28.874	6.614	✓	×	0.246	-
$\delta^*/D_l = 0.03$, $M_i = 0.58$						
0.250	9.357	20.657	✓	✓	0.033	0.014
	14.015	13.792	✓	×	0.067	-
	18.822	10.157	✓	✓	0.097	0.017

Continued on next page

Table D.1 – *continued from previous page*

h/D_l	U_∞ (ms^{-1})	U^*	PIV	TP	Γ^*	DC_{60}
	23.646	8.118	✓	✓	0.231	0.021
	28.574	6.705	✓	✓	0.274	0.024
	33.451	5.676	✓	✓	0.278	0.025
	38.373	4.937	✓	✓	0.258	0.024
$\delta^*/D_l = 0.11$, $M_i = 0.58$						
0.320	0.000	∞	✓	×	0.050	-
	9.633	19.954	✓	×	0.059	-
	19.168	10.005	✓	×	0.136	-
	28.874	6.614	✓	×	0.226	-
	33.725	5.628	✓	×	0.258	-
	38.602	4.891	✓	×	0.160	-
	44.232	4.291	✓	×	0.000	-
$\delta^*/D_l = 0.11$, $M_i = 0.58$						
0.400	0.000	∞	✓	✓	0.039	0.016
	10.057	19.115	✓	✓	0.062	0.016
	14.434	13.291	✓	×	0.113	-
	19.414	9.893	✓	✓	0.167	0.026
	24.211	7.890	✓	✓	0.206	0.029
	29.433	6.518	✓	✓	0.146	0.030
	34.235	5.604	✓	✓	0.056	0.021
	39.126	4.903	✓	×	0.000	-
$\delta^*/D_l = 0.07$, $M_i = 0.58$						
0.400	9.633	19.954	✓	✓	0.069	0.016
	14.213	13.476	✓	×	0.117	-
	19.168	10.005	✓	✓	0.157	0.026
	23.893	7.997	✓	✓	0.201	0.030
	28.762	6.634	✓	×	0.134	-
	33.768	5.603	✓	×	0.066	-
$\delta^*/D_l = 0.03$, $M_i = 0.58$						
0.400	9.392	20.486	✓	✓	0.063	0.014
	14.015	13.557	✓	×	0.156	-
	18.819	10.158	✓	✓	0.185	0.022
	23.675	8.076	✓	✓	0.166	0.025
	28.561	6.625	✓	✓	0.085	0.013
	33.768	5.604	✓	×	0.000	-

Continued on next page

Table D.1 – *continued from previous page*

h/D_l	U_∞ **(**ms^{-1}**)**	U^*	PIV	TP	Γ^*	DC_{60}
$\delta^*/D_l = 0.11$, $M_i = 0.43$						
0.250	0.000	∞	✓	✓	0.068	0.003
	11.655	11.583	✓	✓	0.101	0.011
	16.145	8.362	✓	✓	0.172	0.015
	21.459	6.291	✓	✓	0.233	0.020
	31.452	4.292	×	✓	-	0.016
0.400	0.000	∞	×	✓	-	0.003
	11.681	11.557	×	✓	-	0.015
	16.256	8.304	×	✓	-	0.020

D.2 Rolling Road Experiments

h/D_l	U_∞ (ms^{-1})	U_g (ms^{-1})	U^*	PIV	TP	Γ^*	DC_{60}
	$\Delta U \approx 0m/s$						
0.25	0.000	0.000	∞	✓	✓	0.059	0.015
	9.910	10.000	19.515	✓	✓	0.059	0.013
	15.205	15.000	12.679	✓	✓	0.076	0.011
	20.295	20.000	9.499	✓	✓	0.082	0.012
	25.663	25.000	7.503	✓	✓	0.106	0.008
	30.864	30.000	6.243	×	✓	-	0.006
	$\Delta U \approx 10m/s$						
0.25	9.580	0.000	19.808	✓	✓	0.067	0.016
	15.580	5.000	12.403	✓	✓	0.080	0.020
	20.817	10.000	9.270	✓	✓	0.085	0.022
	26.130	15.000	7.381	✓	✓	0.137	0.022
	31.321	20.000	6.155	✓	✓	0.132	0.023
	36.630	25.000	5.279	×	✓	-	0.020
	$\Delta U \approx 20m/s$						
0.25	19.249	0.000	10.018	✓	✓	0.113	0.022
	26.080	5.000	7.397	✓	✓	0.178	0.024
	31.231	10.000	6.184	✓	✓	0.169	0.025
	36.633	15.000	5.269	✓	✓	0.148	0.022
	41.877	20.000	4.629	×	✓	-	0.020
	$\Delta U \approx 0m/s$						
0.4	9.834	10.000	19.034	✓	×	0.070	-
	15.102	15.000	12.684	✓	×	0.124	-

Table D.2: Test matrix for the rolling ground plane experiments (M_i = 0.58)

D.3 Crosswind

Table D.3: Test matrix under crosswind conditions

h/D_l	ψ	U_∞ (ms^{-1})	U^*	PIV	TP	Γ^*	DC_{60}
$\delta^*/D_l = 0.11$, $M_i = 0.55$							
0.250	90.000	9.917	18.339	✓	✓	0.256	0.116
		14.933	12.178	✓	✓	0.268	0.160
		20.004	9.095	✓	✓	0.288	0.217
		25.119	7.284	✓	✓	0.331	0.219
		30.223	6.077	✓	✓	0.358	0.269
		35.438	5.249	✓	✓	0.422	0.300
		40.662	4.593	✓	✓	0.507	0.388
$\delta^*/D_l = 0.03$, $M_i = 0.55$							
0.250	90.000	9.438	19.329	✓	✓	0.245	0.110
		14.544	12.540	×	✓	-	0.186
		19.692	9.379	✓	✓	0.266	0.183
		24.812	7.258	✓	✓	0.318	0.274
		29.966	6.081	×	✓	-	0.272
$\delta^*/D_l = 0.11$, $M_i = 0.55$							
0.400	90.000	9.819	18.630	✓	✓	0.158	0.093
		14.109	12.990	✓	✓	0.227	0.135
		19.964	9.241	✓	✓	0.243	0.155
		25.088	7.370	✓	✓	0.128	0.167
		30.255	6.249	×	✓	-	0.050
$\delta^*/D_l = 0.11$, $M_i = 0.43$							
0.400	90.000	10.224	14.302	✓	×	0.181	-
		15.387	9.504	✓	✓	0.225	0.177
		20.420	7.165	✓	✓	0.130	0.200
0.250	90.000	10.203	14.245	✓	×	0.252	-
		15.089	9.573	✓	✓	0.299	0.191
		20.583	7.098	✓	✓	0.339	0.227
$\delta^*/D_l = 0.11$, $M_i = 0.55$							
0.250	90.000	9.917	18.339	✓	✓	0.252	0.116
	80.000	9.523	19.414	×	✓	-	0.105
	70.000	9.482	19.392	✓	✓	0.221	0.085

Continued on next page

Table D.3 – *continued from previous page*

h/D_l	ψ	U_∞ **(**ms^{-1}**)**	U^*	PIV	TP	Γ^*	DC_{60}
	60.000	9.715	19.101	×	✓	-	0.054
	50.000	10.393	17.604	✓	✓	0.149	0.032
	30.000	9.991	18.621	✓	✓	0.100	0.018
	0.000	9.580	19.808	✓	✓	0.066	0.016

APPENDIX **E**

Vortex Characteristics Determination

The PIV results presented in this thesis comprises of over 100 PIV configurations. For each configuration 300 snapshots were acquired to provide an adequate sample of the flowfield. Over all configurations in the order of 30000-60000 vortex snapshots were analyzed. In the following, the method used to determine the vortex circulation, core size and Vatistas shape factor for every single vortex snapshot is described.

This appendix starts by giving a detailed description of the technique used to determine the vortex characteristics. In subsequent sections the effect of the integration area and resolution on the vortex parameters is demonstrated. This is followed by the issues associated with applying the technique and methods used to overcome these problems. Finally the methods used to detect and remove outliers are discussed.

E.1 Detailed Outline

The vortex core size, r_c, and Vatistas shape factor, n, were identified using the vorticity disk method[7]. The output of this method is a circumferentially averaged swirl velocity distribution as a function of radial distance, r, from the centre of the vortex. After processing the raw PIV data in Insight 3G version 8.0.5, all the data files, for each flowfield snapshot, are loaded into Tecplot 360 using the Insight 3G add-on. By default the data is constructed in rectangular zones, with the grid resolution, Δ_{rg}, typically between 0.8 and 0.9mm across all PIV datasets. In order to determine the vortex characteristics, using the vorticity disk method, each flowfield snapshot is linearly interpolated onto a structured circular zone, with its axis positioned on the vortex centre (Fig. E.1). The vortex core position is located using the peak out-of-plane vorticity, ω_z (Fig. E.1). Tracking of the vortex centre and the interpolation process were both performed in the Tecplot 360 environment, using a macro, which loops over all flowfield snapshots. Although there are caveats with using vorticity for this purpose, due to its low signal to noise ratio, ω_z was preferred because it can discriminate between positive (anti-clockwise) and negative (clockwise) rotating vortices. Other more advanced vortex identification parameters such as the swirling strength, Q and the eigenvalues of the velocity gradient tensor, λ_2[23], are less affected by noise, but cannot distinguish

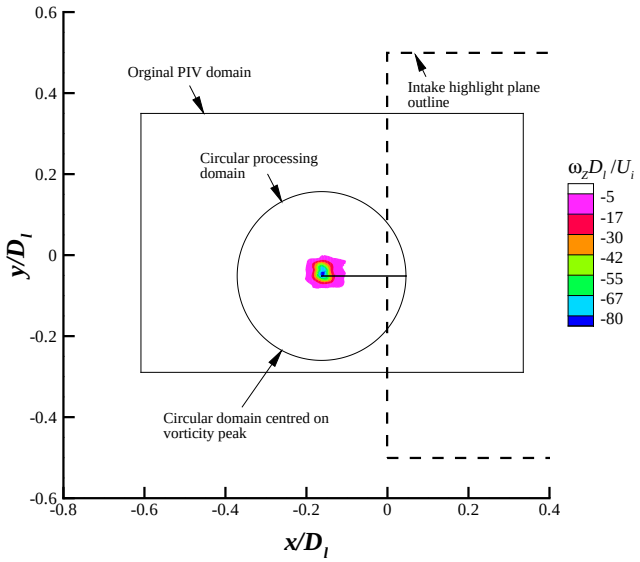

Figure E.1: Example snapshot for the crosswind ground vortex showing the original PIV measurement domain and the circular domain centred on the vorticity peak for processing the vortex parameters

between vortices of differing rotational sense. Using the vorticity therefore enables both positive and negative vortices to be identified and for their respective characteristics (such as circulation, Γ and core size, r_c) to be determined individually. Fig. E.2 shows an example flowfield snapshot under quiescent conditions in which two contra-rotating vortices are present. The positive vortex is identified by searching the peak positive out-of-plane vorticity (+ve $\omega_{z,max}$) with the negative vortex being located from the position of minimum vorticity (-ve $\omega_{z,min}$).

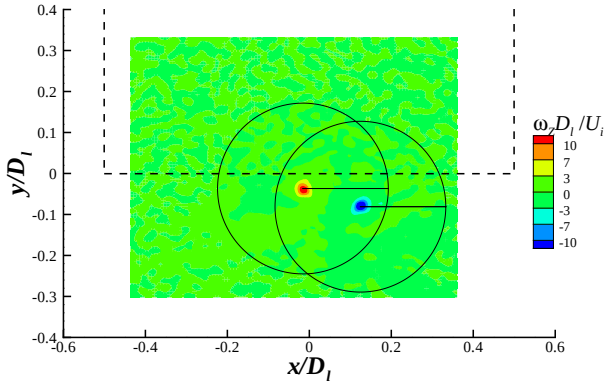

Figure E.2: Example snapshot under quiescent conditions with two contra-rotating vortices showing the original PIV measurement domain and two circular zones centred on the vorticity peak of each respective vortex for processing the vortex parameters

The radius of the circular domain, r_{max}, was fixed in size for all configurations and was equal to $25mm$ or $r_{max}/D_i = 0.25$ (Fig. E.3). The determination of the disk radius

is discussed in §E.2. The circular grid used had a total of 150 radial (I_{max}) and 261 circumferential grid points (J_{max}). J_{max} had to be an odd number and be divisible by 4 for reasons discussed in §E.4. The effect of varying the grid resolution for both headwind and crosswind configurations is demonstrated in §E.3.

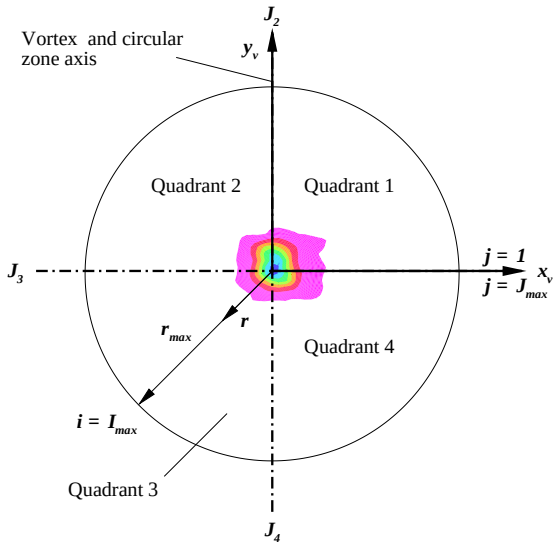

Figure E.3: Example circular domain with its centre at the vorticity peak location illustrating the domain parameters

With the vortex centre identified and data interpolated onto a circular zone centred on the vortex axis, each individual circular zone was exported from Tecplot in ASCII file format. The data was then loaded into Matlab R2007a for further analysis. Following the method described in Burley et al[7] the vorticity was integrated over circular areas with increasing radial distance, r, from the centre of the vortex (Eq. E.1.1) (i.e. from the middle of the circular zone). This gives a distribution of circulation as a function of radial distance (Fig. E.4).

$$\Gamma_i = \int \omega_z dA_{i,j} = \sum_{j=1}^{J_{max}} \omega_{i,j} \cdot A_{i,j} \qquad \text{(E.1.1)}$$

where

$$A_{i,j} = \begin{cases} \dfrac{\pi}{J_{max}} \left[\dfrac{r_{i+1,j}}{2}\right]^2 & i = 1 \\ \dfrac{\pi}{J_{max}} \left[\left(\dfrac{r_{i+1,j} - r_{i,j}}{2} + r_{i,j}\right) - \left(\dfrac{r_{i,j} - r_{i-1,j}}{2} + r_{i-1,j}\right)\right]^2 & i > 1 \end{cases}$$

For configurations when two vortices are present* (i.e. Fig. E.2), this introduces a problem because both positive (+ ve ω_z) and negative (- ve ω_z) vortices are often in-

*This applies primarily to the quiescent, headwind and rolling road configurations

side each of the respective circular domains (Fig. E.2). Therefore when integrating both positive and negative vorticity the total circulation within the circular domain, for both vortices, will be near zero which is not wanted. An example of this is shown in Fig. E.4b where the +/- ω_z line represents the result of integrating both positive and negative ω_z vorticity. The figure shows the integration for both the clockwise ($-ve$) and anti-clockwise vortices (+ ve). For both cases the vortex strength significantly reduces between a radial distance, r, of 0.015 and 0.02. As mentioned above, this is not wanted because the calculated circulation will be near zero for all cases that include two vortices. In addition the calculated circulation will depend on the relative distance between the vortices and the relative strengths. Since the space between the two vortices varies significantly between snapshots and between configurations, this will introduce inconsistencies in the results.

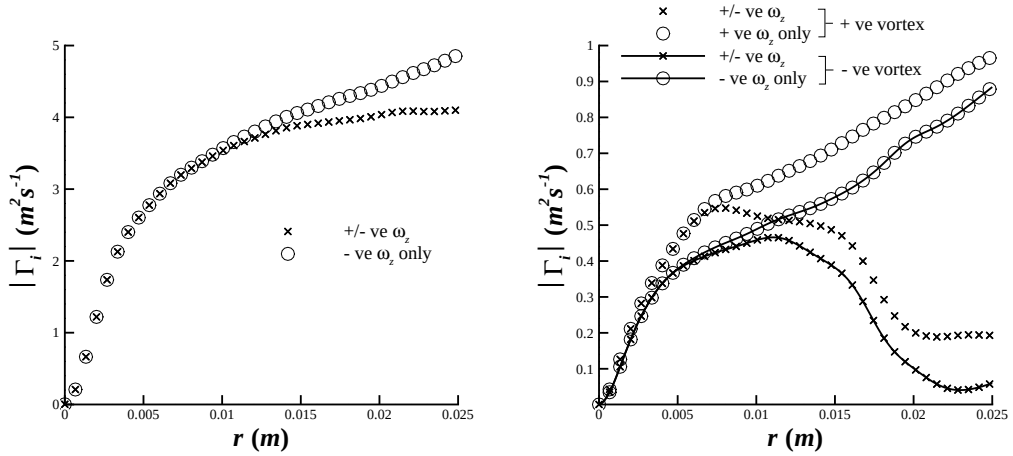

(a) Crosswind snapshot (b) Quiescent snapshot

Figure E.4: Example plot of circulation as a function of radial distance from the centre of the vortex for (a) single crosswind snapshot and (b) single quiescent snapshot for both positive (+ve) and negative (-ve) rotating vortices (see Fig. E.2) (only every 4^{th} symbol shown for clarity). This figure also compares the results for integrating both positive and negative vorticity and just integrating the dominant vorticity associated with each respective vortex

To overcome this issue only the positive vorticity is integrated for the + ve rotating vortex (as shown by the + ve ω_z line in Fig. E.4b) and vice versa for the negative vortex (i.e. the - ve ω_z line in Fig. E.4b). The result of performing this integration for both clockwise and anti-clockwise vortices is also shown in Fig. E.4b). As can be seen in the figure, the vortex circulation for both cases now increases monotonically with radial distance from the centre of the vortex. This is also not ideal as the resulting circulation therefore depends on the integration area. However since the aim of calculating the circulation is to determine the relative strength of the vortex between difference configurations, this is not an issue as long as the integration area stays constant across all configurations.

In order to be consistent between the headwind and crosswind mechanisms, only negative vorticity is integrated for all crosswind cases as only one vortex forms under such

conditions which always has negative vorticity[†] (Fig. E.1). A comparison between both integration methods is also shown for the crosswind case in Fig. E.4a and as can be seen the difference between the two is small.

For all configurations the circulation is taken as being the total integrated, positive or negative vorticity, (which one depends on the rotation of the vortex) within the whole circular domain. Therefore referring to the example in Fig. E.4, the circulation for the crosswind case is calculated to be $4.87 m^2 s^{-1}$. For quiescent conditions, the positive vortex has a calculated circulation of $0.97 m^2 s^{-1}$ whereas the negative vortex is -$0.88 m^2 s^{-1}$[‡]

$$V_\theta = \frac{\Gamma_i}{2\pi r_i} \tag{E.1.2}$$

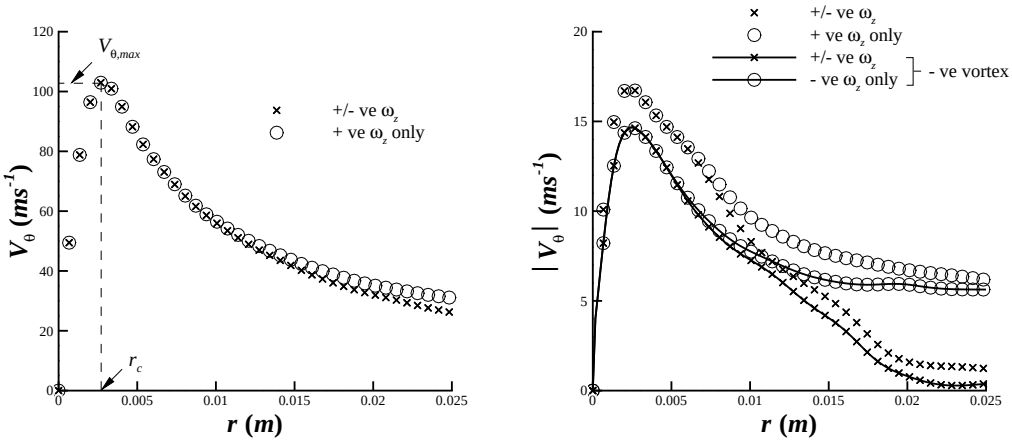

(a) Crosswind snapshot (b) Quiescent snapshot

Figure E.5: Circumferentially averaged swirl velocity against radial distance from the centre for (a) crosswind snapshot and (b) quiescent conditions for both positive and negative vortices (only every 4^{th} symbol shown)

With the distribution of circulation obtained as a function of radial distance, the swirl velocity distribution, V_θ, is then obtained by dividing the local circulation, Γ_i, at each radial position by $2\pi r$ (Eq. E.1.2). The resulting plot is shown in Fig. E.5 for both crosswind and quiescent conditions.

$$\frac{V_\theta}{V_{\theta,max}} = 2^{1/n}\left[\frac{r^*}{(1+r^{*2n})^{1/n}}\right] \tag{E.1.3}$$

[†]This is not strictly true as just before the vortex blows-away, under crosswind conditions, multiple vortices can be observed which are associated with the approaching boundary layer vorticity (see §7.2.2). However this situation only occurred for two configurations under crosswind conditions and for such cases the same processing methods were applied in comparison to that in headwind conditions

[‡]Note in Fig. E.4 the abscissa is the absolute value of circulation

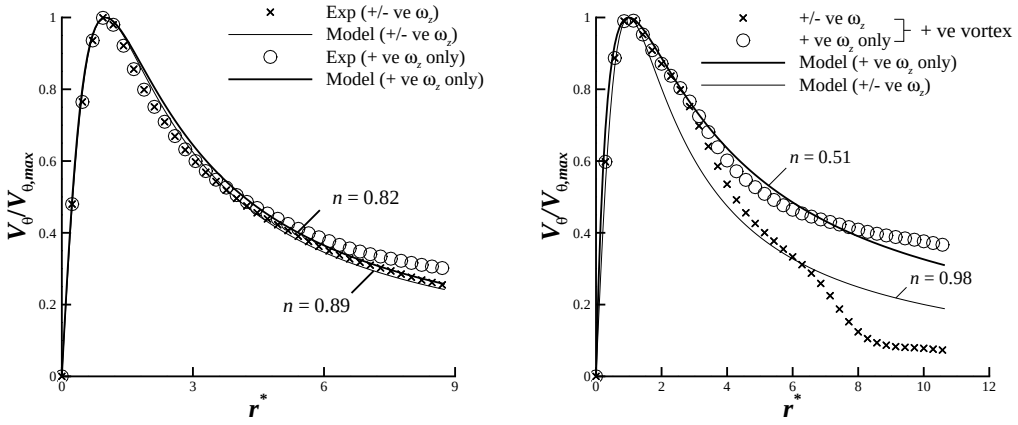

(a) Crosswind snapshot (b) Quiescent snapshot

Figure E.6: Normalised tangential velocity against non-dimensional radial distance showing experimental data for a single vortex snapshot with the model fit also included (only every 4^{th} symbol shown). For the quiescent case, results for only the positive rotating vortex is shown in the figure for clarity.

The radial position of peak swirl velocity, $V_{\theta,max}$, gives the vortex core size, r_c (Fig. E.5a). Non-dimensionalizing the swirl velocity distribution by the peak value, and the radial distance by the vortex core size enables the Vatistas shape factor, n, to be calculated using a least squares fit of the velocity distribution (Eq. E.1.3). The total individual vortex strength is obtained by integrating vorticity over the whole circular domain.

The vortex strength, Γ, core size, r_c and Vatistas shape factor, n, was determined for both positive and negative vortices (if both are present) for all flowfield snapshots (i.e. 300). The total average strength of the vortex system, $\bar{\Gamma}$, is determined by computing the average of all positive vortex strengths, $\bar{\Gamma}^+$, and all negative vortex strengths, $\bar{\Gamma}^-$ over all 300 vortex snapshots and summing the absolute magnitudes of both (Eq. 3.6.4).

$$\bar{\Gamma} = \left|\bar{\Gamma}^+\right| + \left|\bar{\Gamma}^-\right| \tag{E.1.4}$$

For the majority of crosswind configurations only a negative vortex was present, hence the total circulation is given by:

$$\bar{\Gamma} = \left|\bar{\Gamma}^-\right| \tag{E.1.5}$$

The total average non-dimensional vortex strength, Γ^*, is then calculated by dividing $\bar{\Gamma}$ by the intake velocity, U_i, and intake diameter, D_l, from the dimensional analysis presented in §3.1.1:

$$\Gamma^* = \frac{\bar{\Gamma}}{U_i D_l} \tag{E.1.6}$$

E.2 Disk Size Determination

In order to establish the size of the circular domain used for processing a number of disk sizes, r_{max}, were initially used to determine the sensitivity. In general it is desirable to make the circular zone as large as possible. However, because the measurement domain was fixed in space, the vortex was occasionally close to the edge of the area which consequently has implications on the measurement area that can be used. In addition, with multiple vortices being observed at the PIV plane for some configurations, it is preferable to ensure that the integration domain only includes the vortex of interest. As well as the above, a very large area size has significant implications on the processing time and given the amount of configurations that need to be processed, this is an important issue. To examine the effect of the domain size on the vortex characteristics four different circular zones were tested with r_{max}/D_i values of 0.15,0.25,0.35 and 0.45. In doing this, the resolution of the disk was kept constant by satisfying the following ratios:

$$\frac{r_{max}}{I_{max}} = 6 \tag{E.2.1}$$

$$\frac{J_{max}}{I_{max}} = 1.74 \tag{E.2.2}$$

Table E.1 summarizes the circular zone characteristics used in the tests. In these tests both positive and negative vorticity was integrated within the whole domain of each respective circular zone. Fig. E.7 shows the variation in circulation with radial distance from the centre of the vortex for a typical crosswind snapshot for all four zones. The general criteria used to determine the zone radius, r_{max}, was to ensure that the change in circulation for a given change in the disk size was less than 5% (Eq. E.2.3). For the example shown in Fig. E.7 the vortex circulation with radial distance reaches a plateau at a radial position, r, of approximately $0.02m$. The vortex characteristics for all the domain sizes tested are shown Table .E.1. The change from 0.15 to 0.25 (r_{max}/D_i) leads to a 5.6% increase in the circulation which therefore indicates that the 0.15 domain size is not large enough given the criteria used. However an increase in the radius from 0.25 to 0.35 corresponds only to 0.24% increase in the circulation. Hence the $r_{max}/D_i = 0.25$ was deemed large enough for processing.

$$\frac{\Delta\Gamma}{\Gamma} < 0.05 \tag{E.2.3}$$

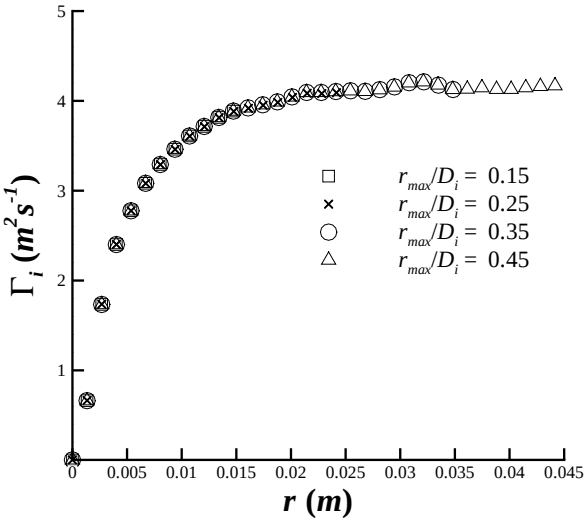

Figure E.7: Circulation as a function of radial distance from the centre of the vortex for various circular domain sizes (only every 8^{th} symbol shown for clarity)

r_{max}/D_i	I_{max}	J_{max}	Γ ($m^2 s^{-1}$)	r_c/r_i	n
0.15	90	157	3.89	0.058	0.94
0.25	150	261	4.11	0.058	0.89
0.35	210	365	4.12	0.058	0.88
0.45	270	469	4.15	0.058	0.87

Table E.1: Effect of circular domain radius, r_{max}, on the vortex characteristics for a crosswind vortex snapshot

E.3 Effect of Disk Resolution

As well as the domain size, the grid resolution was also investigated to establish its sensitivity during the interpolation process. This study was conducted using the circular domain radius of 0.25 (r_{max}/D_i). The grid resolutions in terms of the number of radial, I_{max}, and circumferential, J_{max}, grid points are summarized in Table E.2. Again the vortex circulation, Γ, is calculated by integrating both positive and negative vorticity. The sensitivity of the vortex characteristics to the grid resolution is in general very small. Since the circumferential and radial grid points are equi-spaced, the cell area increases with radial distance from the centre of the domain. At the lowest resolution tested the cell area at the edge of the domain was larger than the corresponding area for the original rectangular structured data. As a result this leads to some sensitivities in the results in comparison to the higher resolution cases (Table E.2). The vortex parameters were found to have converged with the resolution set at (I_{max}, J_{max}) = (150,261), hence this was the grid resolution chosen for the circular domain.

I_{max}	J_{max}	$\Gamma\ (m^2 s^{-1})$	r_c/r_i	n
30	53	4.18	0.034	0.54
90	157	4.12	0.054	0.89
150	261	4.11	0.058	0.89
210	365	4.11	0.058	0.89
270	469	4.11	0.058	0.89

Table E.2: Effect of circular domain resolution on the vortex characteristics

E.4 Method Limitations

As already stated above, for some configurations the vortex spatial unsteadiness was relatively large, which consequently means that the vortex is occasionally at the edge of the measurement domain (Fig. E.8a). In this case the vorticity within the portion of the circular domain that is outside the PIV measurement area is set to zero during the interpolation process. This can be seen from the contour levels in Fig. E.8b. Typically this situation happened for approximately 10-20% of all cases. To overcome this issue the ground vortex is assumed to be axi-symmetric (i.e. to have an axi-symmetric vorticity distribution). Vorticity on the opposite side of the vortex axis is mirrored to fill in the missing data (Fig. E.8c). This is mathematically expressed below using the example in Fig. E.8.

The circular zone is split into four quadrants (Fig. E.3) with the edges being defined by the grid points J_2, J_3 and J_4 (Fig. E.3 and Eq. E.4.1 - E.4.3).

$$J_2 = \frac{(J_{max} - 1)}{4} \tag{E.4.1}$$

$$J_3 = \frac{(J_{max} - 1)}{2} \tag{E.4.2}$$

$$J_4 = \frac{3\,(J_{max} - 1)}{4} \tag{E.4.3}$$

Within Matlab grid points with zero vorticity are located and data is mirrored with respect to the symmetry plane depending on the quadrant that the missing data lies in. Using the example in Fig. E.8, a point (i, j) with zero vorticity will be found in quadrant 1. From this point the equivalent position on the other side of the y-axis will be identified (i.e. in quadrant 2 for this example) and is given by the coordinate position $(i, (J_2 + (J_2 - j)))$. If this data point has a non-zero value of vorticity then its value is copied to the grid point (i, j):

$$\omega_z(i, j) = \omega_z(i, (J_2 + (J_2 - j))) \tag{E.4.4}$$

However if this data point also has zero vorticity, as is the case in Fig. E.8b, then the mirrored position with respect to the x-axis is used which in this case is in quadrant 4:

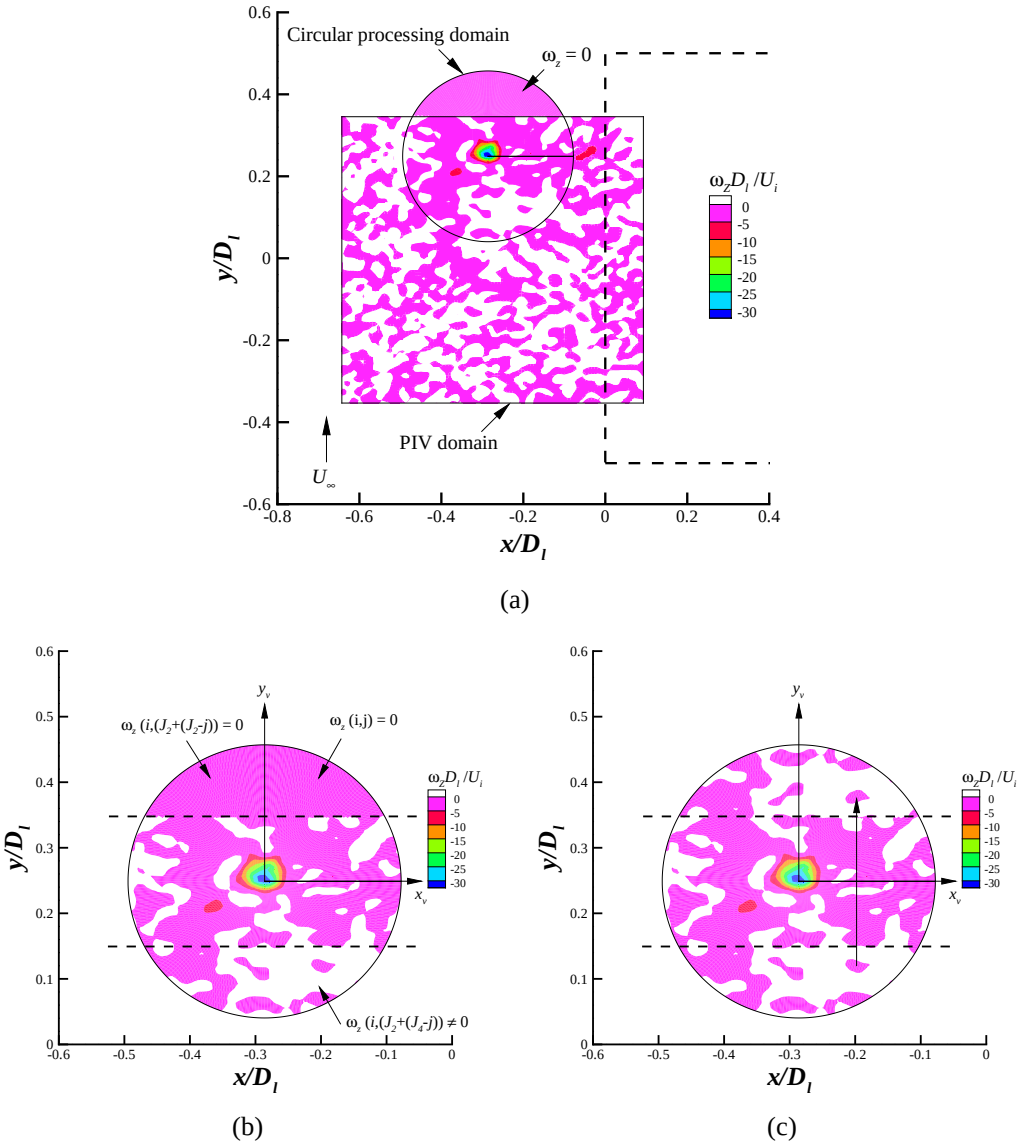

Figure E.8: Example application of the data filling method. (a)Example circular domain that is over the edge of the original PIV measurement area (b) A close-up of the circular domain with zero vorticity at the top and (c) the resulting contour plot after the filling process.

$$\omega_z(i, j) = \omega_z(i, (J_2 + (J_4 - j))) \tag{E.4.5}$$

This process is repeated for points which have zero vorticity in all four quadrants. The resulting plot is shown in E.8c. The affect of applying this method on the resulting vortex characteristics is shown in Table E.3 for the example displayed in Fig. E.8. Since the circulation for a clockwise vortex is determined by integrating all negative vorticity only, the vortex strength increases, as expected. However the data filling method has no significant impact on the core size, r_c, and Vatistas shape factor, n (Table E.3).

	$\Gamma\ (m^2 s^{-1})$	r_c/r_i	n
Without filling	2.89	0.068	0.69
With filling	3.14	0.068	0.67

Table E.3: Effect of filling data at the edge of the measurement domain

E.5 Outlier Detection

In this section the methods used to detect spurious data points within the processed vortex characteristics is demonstrated and discussed with the use of an example. Most outliers manifested themselves with either a very large vortex core radius (of a similar size to the circular domain radius), possessing a very large Vatistas model constant or being identified in an area in which a vortex could not of formed (for example underneath the intake at the edge of the measurement domain).

Two primary methods were used to detect outliers within the data:

- Within the Matlab code developed to process the vortex characteristics, a vortex formation region range was manually inputted. If a 'vortex' was detected outside this range the data was discarded and the code moved onto the next flowfield snapshot.
- Data points were also deemed to be unreliable if the least squares fit of the Vatistas vortex model with the experimental circumferentially average swirl velocity distribution was greater than 0.3. This is expressed mathematically in the following inequality:

$$\epsilon = \sum_{i=1}^{I_{max}} \left[\left\{ \frac{V_{\theta i}}{V_{\theta,max}} \right\}_{exp} - \left\{ 2^{1/n} \left[\frac{r_i^*}{\left(1 + r_i^{*2n}\right)^{1/n}} \right] \right\}_{model} \right]^2 > 0.3 \qquad \text{(E.5.1)}$$

The value of 0.3 was chosen after a number of trials in which the identified data points were manually checked. This threshold was found to adequately remove all the erroneous data points across all configurations tested. In general the average vortex circulation was not affected by the filtering, but did affect the vortex core size and Vatistas shape factor, as both of these parameters were more sensitive and resulted in unrealistically large values when no clear vortex structure was present in the flowfield. An example plot of the least squares residual of the Vatistas curve fit is given in Fig. E.9 for the positive vortex under quiescent conditions. The figure also includes the threshold, above which data points were rejected. Selected cases which passed and failed the criteria are shown in Fig. E.10, which includes the vector field and corresponding circumferentially average swirl velocity distribution.

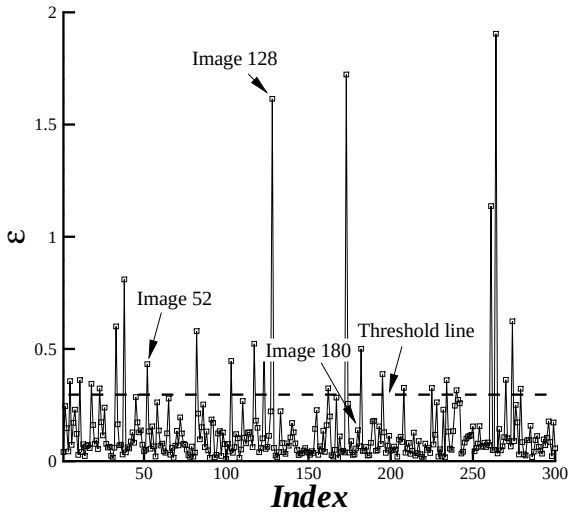

Figure E.9: Example plot of the least squares residual of the curve fit between the Vatistas vortex model and the experiments for all 300 vortex snapshots under quiescent conditions for the positive vortex (h/D_l = 0.25, M_i = 0.58, U^* = ∞). Also included in the figure is the threshold used to determine if a data point is unreliable.

E.6 Summary

In this appendix the methods used to determine the vortex characteristics from the PIV data is described in detail. This includes the vortex circulation, Γ, core size, r_c, and Vatistas shape factor, n. In addition to this, some of the issues associated with processing the results are discussed and methods implemented to overcome the problems are presented. This appendix also describes how spurious data points were identified and removed.

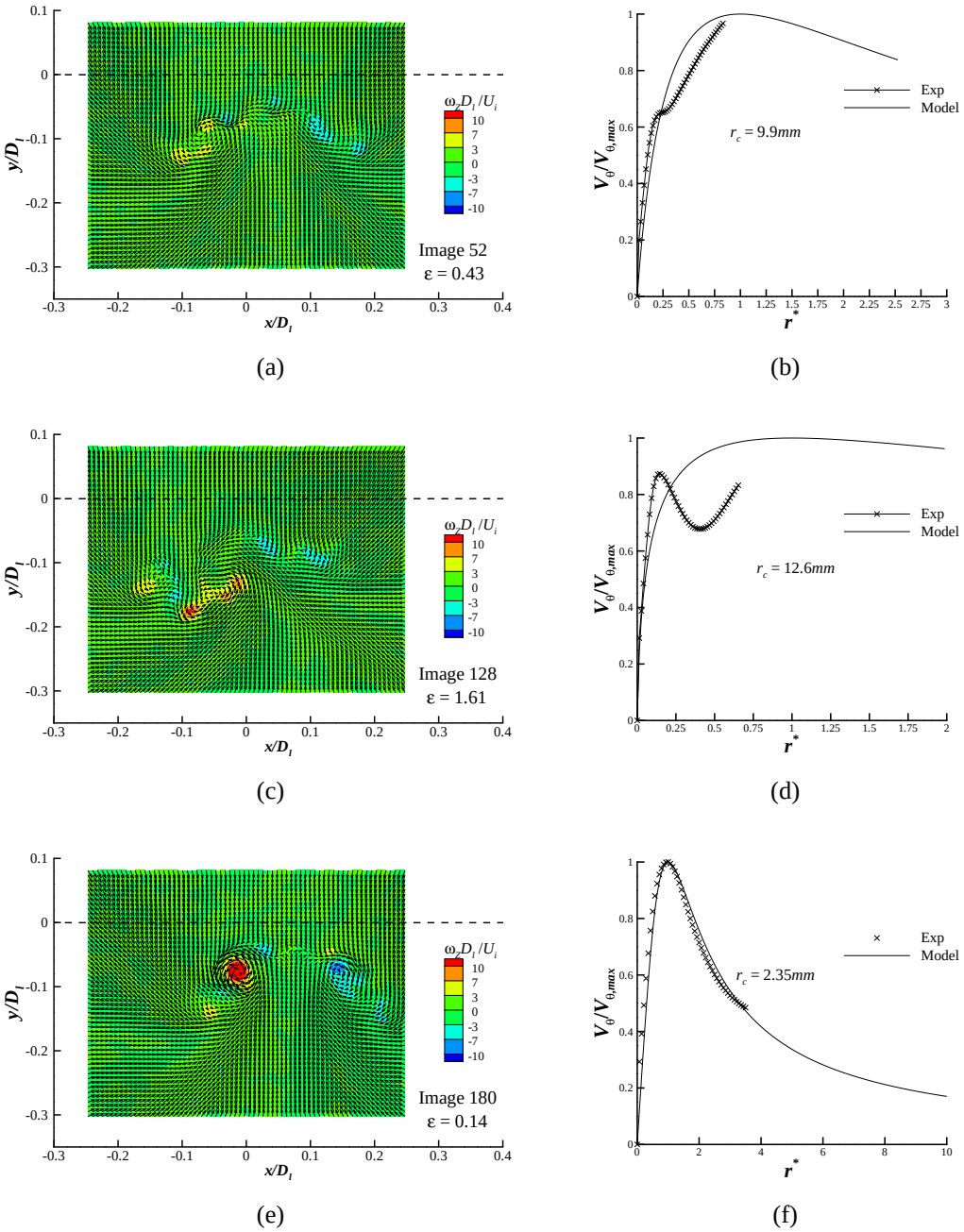

Figure E.10: Example snapshots with the corresponding circumferentially average swirl velocity distribution as a function of radial distance (Note the scales change due to the differing vortex core size) for cases which fail the threshold (b & d) and one example that passes the criteria (f).

APPENDIX **F**

Distortion Descriptors

This appendix describes the distortion descriptors considered in this thesis. Results are presented for each of the parameters using the crosswind data to demonstrate the trend of each respective descriptor with velocity ratio and non-dimensional height.

F.1 Loss Coefficient

The loss coefficient, P_L, is defined in this work as being the difference between the area weighted fan face average total pressure, $\bar{P}_f$ and the minimum average 60 degree sector pressure, $\bar{P}_{60}$ normalised by $\bar{P}_f$ (Eq. F.1.1). To illustrate the use of this parameter P_L has been determined for a range of crosswind velocity ratios at two non-dimensional heights, as shown in Fig. F.1. The corresponding total pressure plots for the non-dimensional height of 0.25 (h/D_l) are shown in §7.2.1.2.

$$P_L = \frac{\bar{P}_f - \bar{P}_{60}}{\bar{P}_f} \tag{F.1.1}$$

where

$$\bar{P}_f = \frac{1}{A}\int P dA \tag{F.1.2}$$

F.2 The DC_{60} Parameter

The distortion coefficient, DC_{60}, is defined as being the difference between the area weighted average total pressure and the minimum 60° sector pressure normalised by the average dynamic head in the intake duct, q_f (Eq. F.2.1)[47]. The definition of the parameters is illustrated in Fig. F.2. The DC_{60} trend with velocity ratio is plotted in Fig. F.3 for two different non-dimensional heights under crosswind conditions. As can be seen this parameter exhibits similar features to the loss coefficient.

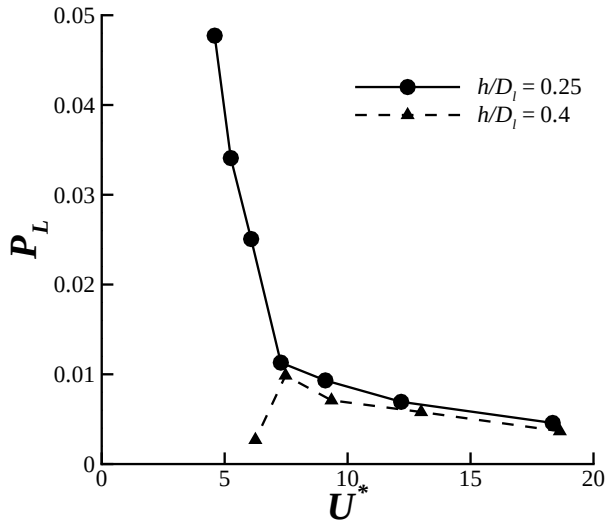

Figure F.1: Loss coefficient descriptor, P_L, as a function of velocity ratio for two non-dimensional heights under crosswind conditions (ψ = 90°)

$$DC_{60} = \frac{\bar{P}_f - \bar{P}_{60}}{q_f} \tag{F.2.1}$$

F.3 The KD_2 Index

This parameter considers circumferential distortion elements. At each radial location (i.e. for each ring pressure distribution) the difference between the ring average pressure, $\bar{P}_{ring}$, and the corresponding minimum probe pressure, $P_{min,probe}$, is determined and is then normalised by $\bar{P}_{ring}$ (Fig. F.4). This value is then multiplied by the loss extent, θ_i^-, which is the size of the low pressure region in degrees that is lower than the average ring pressure (Fig. F.4).

$$KD_2 = \sum_{i=1}^{N_{rings}} \left[\left(\frac{\bar{P}_{ring} - P_{min,probe}}{\bar{P}_{ring}} \right) \theta \right]_i \tag{F.3.1}$$

where

$$\bar{P}_{ring,i} = \frac{1}{360} \int_0^{360} P(\theta)_i \, d\theta \tag{F.3.2}$$

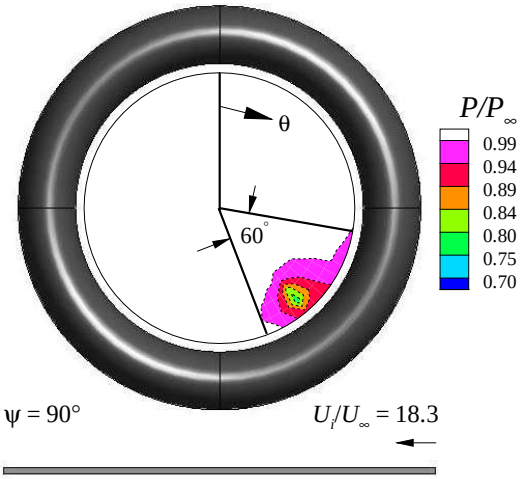

(a)

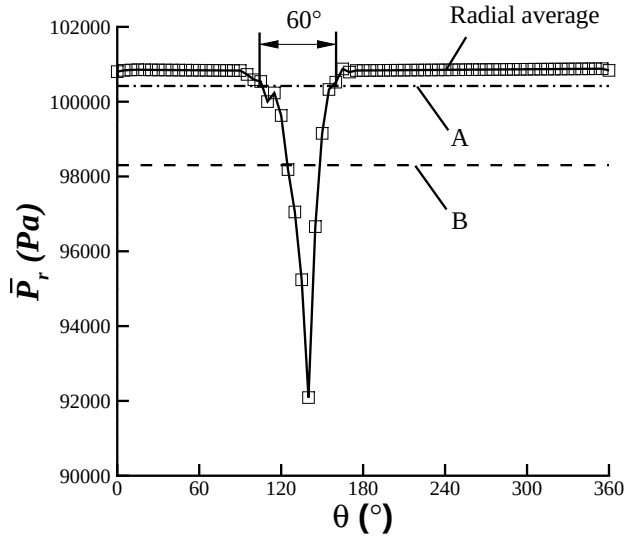

(b)

Figure F.2: Definition of DC_{60} parameters (a) example total pressure contour plot under cross-wind conditions showing the 60° sector region and (b) the radially averaged circumferential total pressure plot against theta (Note: the line marked by A is the $\bar{P}_f$ line and B is the $\bar{P}_{60}$ line)

F.4 Intensity

SAE[22] recommend a distortion descriptor for assessment relating to aerodynamic stability and performance called the Intensity (Eq. F.4.1). $\bar{P}_i$ is the ring average pressure (Eq. F.3.2, Fig.F.6a) while $\bar{P}_{low,i}$ is the average pressure of the low-pressure region (Eq. F.4.2, Fig. F.6a).

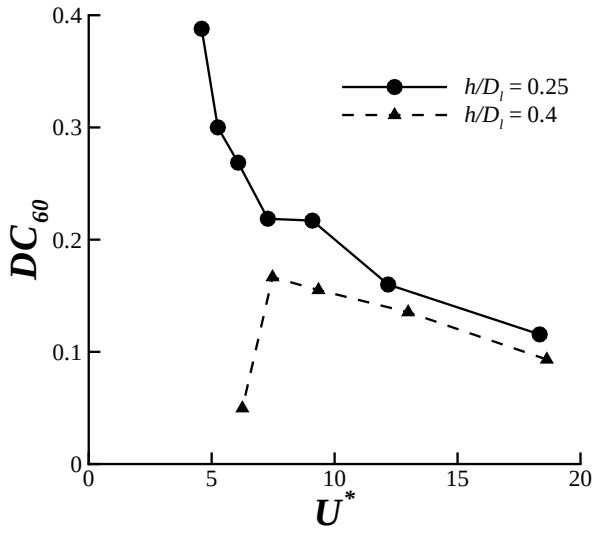

Figure F.3: DC_{60} against velocity ratio for two non-dimensional heights under crosswind conditions

$$Intensity = \sum_{i=1}^{N_{rings}} \left(\frac{\bar{P} - \bar{P}_{low}}{\bar{P}} \right)_i \tag{F.4.1}$$

where

$$\bar{P}_{low,i} = \frac{1}{\theta_i^-} \int_{\theta_{1i}}^{\theta_{2i}} P(\theta)_i \, d\theta \tag{F.4.2}$$

with

$$\theta_i^- = \theta_{2i} - \theta_{1i} \tag{F.4.3}$$

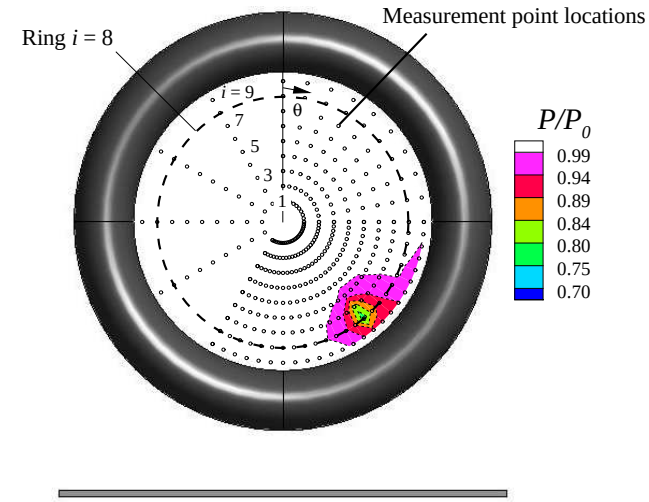

(a)

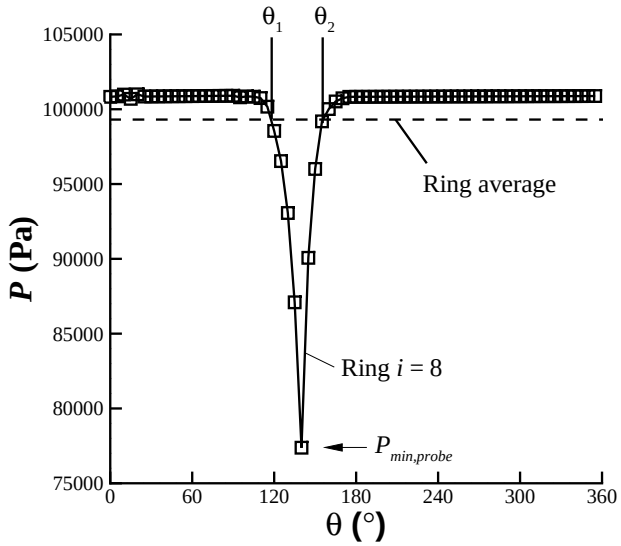

(b)

Figure F.4: (a) Illustration of ring definition and index system (b) an example ring pressure distribution for i=8 ring location (i.e. through the centre of the vortex) illustrating the ring average pressure, $\overline{P}_{ring,i}$, and the minimum pressure, $P_{min,probe}$

F.5 Summary

A number of distortion descriptors have been introduced and applied to the current problem. The loss coefficient and DC_{60} are sector descriptors whereas the KD_2 and the Intensity are based on circumferential distortion elements. Despite the differences all parameters exhibit the same trends.

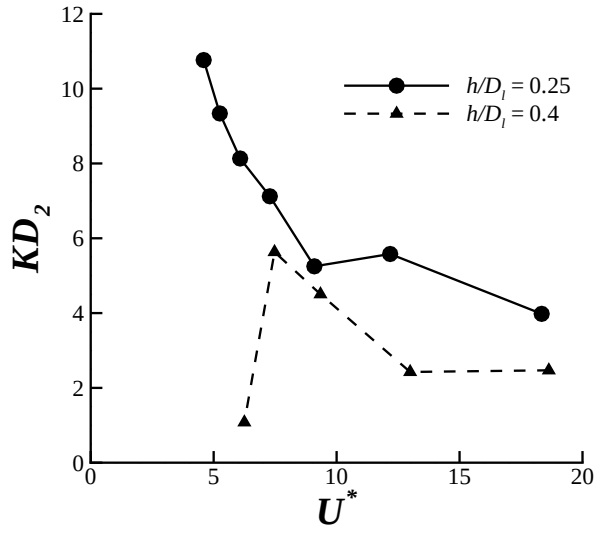

Figure F.5: The KD_2 index as a function of velocity ratio for two non-dimensional heights under crosswind conditions

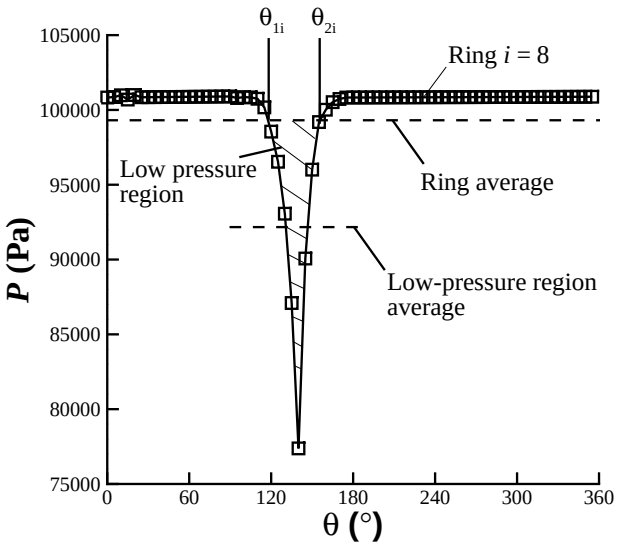

(a)

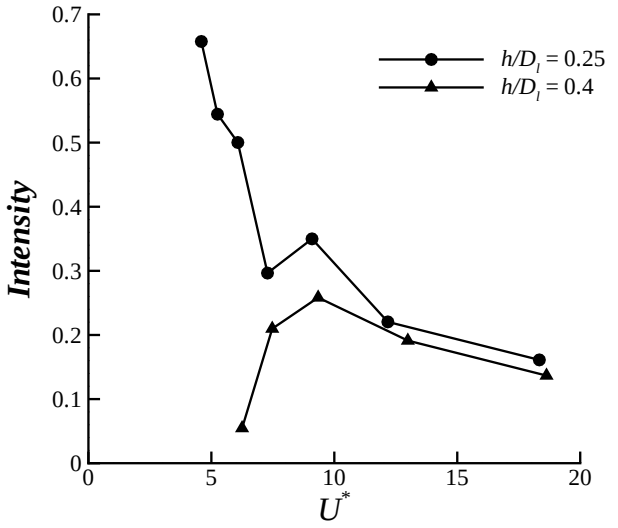

(b)

Figure F.6: (a) Typical ring pressure distribution through the centre of the vortex (see Fig. F.4a for ring location) illustrating the ring average pressure ($\bar{P}_{ring}$), the low-pressure region and the low-pressure region average pressure, $\bar{P}_{low}$ and (b) A plot of intensity as a function of velocity ratio for two non-dimensional heights under crosswind conditions

APPENDIX **G**

Uncertainty Analysis

The uncertainties associated with the intake height (h/D_l), tunnel velocity (U_∞), intake velocity (U_i), and also an estimation of the velocity error of the PIV results is given in this appendix. The latter error estimation is derived using synthetic images presented in Raffel[41]. All other uncertainties were derived following the methods proposed by Taylor[57]

G.1 Intake Ground Clearance

The intake ground clearance was set by placing blocks of a known height underneath the intake. The variable height strut was manually adjusted to match the clearance between the lowest point of the outer intake surface and the ground with the block height. In total three non-dimensional heights were investigated and were equal to 0.25, 0.32, and 0.4 (h/D_l). The clearance between the lowest point of the outer intake surface to the ground plane, h_c, for each height-to-diameter ratio was 20, 32 and 38 *mm* respectively. For $h_c = 20$ *mm* the height was measured using a 20 *mm* block, whereas for $h_c = 32$ *mm* the clearance was set using a combination of a 30 *mm* block and two 1 *mm* blocks. In contrast for $h_c = 38$ *mm* an amalgamation of a 20, 15, and three 1 *mm* blocks were implemented.

The relationship between, h_c, and h is given by Eq. G.1.1:

$$h = h_c + \frac{D}{2} \tag{G.1.1}$$

The intake height, h, is then non-dimensionalised by the intake highlight diameter, D_l. In this appendix the intake height-to-diameter ratio will be denoted by h^*:

$$h^* = \frac{h}{D_l} \tag{G.1.2}$$

G.1.1 Error Sources

Sources of uncertainty in the ground clearance are:

1. Uncertainties in the block heights
2. The human error in setting h_c
3. Uncertainty in the intake highlight diameter size, D_l
4. Uncertainty in the intake outer diameter dimension, D

The block heights were manufactured from a CNC machine and therefore the uncertainty is expected to approximately 0.005 *mm* for each block. However, the human error in setting the height is expected to be considerably larger at 0.5 *mm*. It is therefore assumed that the uncertainty in h_c is solely due to the human error factor. Hence $\delta h_c = 0.5$ *mm*. The uncertainty in the intake outer diameter, δD, is also expected to be 0.5 *mm*. Following Taylor[57] the uncertainty in h given by δh can be estimated as follows:

$$\begin{aligned} \delta h &= \sqrt{(\delta h_c)^2 + (\delta D)^2} \\ &= \sqrt{(0.5)^2 + (0.5)^2} \\ &= 0.707mm \end{aligned} \tag{G.1.3}$$

Hence for the lowest intake non-dimensional height of 0.25 (h/D_l) the uncertainty can be calculated as follows:

$$\frac{\delta_{h^*}}{h^*} = \sqrt{\left(\frac{\delta h}{h}\right)^2 + \left(\frac{\delta D_l}{D_l}\right)^2} \tag{G.1.4}$$

$$= \sqrt{\left(\frac{0.707}{20}\right)^2 + \left(\frac{0.5}{120}\right)^2} \tag{G.1.5}$$

$$= 3.6\% \tag{G.1.6}$$

Following the same process for the larger ground clearance of 0.4 the uncertainty is estimated to be 1.9%

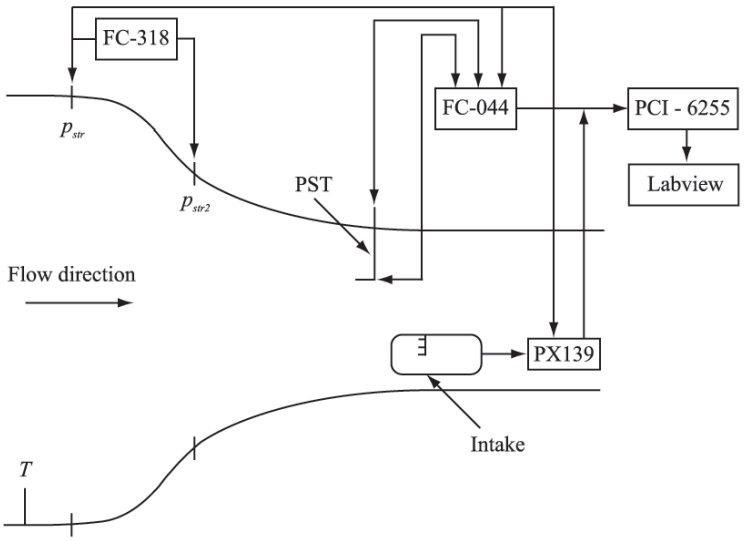

Figure G.1: Schematic of the pressure system used in all the experiments

G.2 Pressure System and Associated Measurements

A schematic of the pressure system used in all experiments is shown in Fig. G.1. The system comprises of 40 PX139-005D4V differential pressure transducers, three Furness FC-044 transducers and one FC-318 differential pressure transducer. The PX139s are used to measure both the static and total pressures within the intake duct. The reference pressure for the intake measurements (i.e. for the PX139s) is the tunnel static rings pressure, p_{str} (Fig. G.1). This pressure is the arithmetic average of four equispaced static pressure measurements around the circumference of the tunnel in the contraction at the location marked by p_{str} in Fig. G.1. In addition a Furness Controls FC-044 pressure transducer is used to measure the reference pressure, p_{str}, against ambient pressure, P_{amb} and also the tunnel static and total pressures in the working section via the pitot static tube (PST, Fig. G.1). Therefore by noting the ambient pressure before each run the absolute pressure can be determined within the intake. All channels from the PX-139s and the FC-044 were passed through a National Instruments PCI-6255 16-bit DAQ card which converts all signals from all channels into digital. Data acquisition was controlled using Lab View version 8.5 and the sampling frequency and period was set at 600 *Hz* and 5 *s* respectively for all tests.

G.2.1 Determination of Tunnel Speed

During tests the tunnel speed, U_∞, was set by measuring the difference between the ring static pressures in the contraction, using a Furness Controls FC-318 differential pressure transducer (Fig. G.1). This pressure is then multiplied by a tunnel calibration, k_{tun}, to determine the dynamic pressure, q_∞, in the working section (Eq. G.2.1). The density is calculated by measuring the temperature, T, inside the settling chamber of

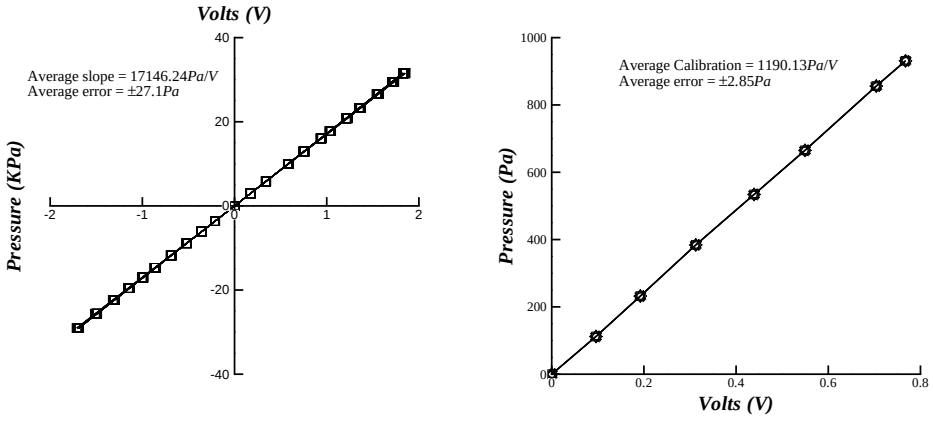

(a) (b)

Figure G.2: Calibration curves for (a) all 40 PX139-005D4V transducers and (b) all FC-044 transducers

Transducer	s/n	Range (Pa)	Supply Voltage (V)	Error (% Full-scale)
PX139	005D4V	34474	5	0.1%
FC-044	960738	2500	12	0.3%
	960740	2500	12	0.3%
	960739	2500	12	0.3%
FC-318	0603242	981	12	0.3%

Table G.1: Transducer characteristics used in the experiments

the tunnel (Fig. G.1) and the atmospheric pressure, P_{amb} (Eq. G.2.2).

$$q_\infty = (p_{str2} - p_{str}) \times k_{tun} \tag{G.2.1}$$

$$\rho_\infty \approx \frac{P_{amb}}{RT_0} \tag{G.2.2}$$

The tunnel velocity can therefore be calculated as follows:

$$U_\infty = \sqrt{\frac{2q_\infty}{\rho_\infty}} \tag{G.2.3}$$

The above method of calculating the tunnel velocity was only used as guidance during tests. This is because the calibration factor only applies for an empty tunnel and the ambient pressure is used to determine the density. The tunnel velocity quoted in text is that measured from the pitot static tube in the working section. As explained above the pressures from the pitot-static tube are measured using the FC-044 transducer which

Measurement	Transducer	Value
$P_\infty - P_{amb}$	T1	413.480 Pa
$p_\infty - P_{amb}$	T2	-79.093 Pa
T	-	289 K
P_{amb}	-	98204 Pa

Table G.2: Typical measurement values for the calculation of tunnel velocity at 30 ms^{-1}

uses the ambient pressure, P_{amb}, as the reference pressure. Hence the tunnel velocity is determined by first calculating the dynamic pressure, q_∞, as follows:

$$q_\infty = (P_\infty - P_{amb}) - (p_\infty - P_{amb}) \tag{G.2.4}$$

The density is therefore calculated using Eq. G.2.5:

$$\rho_\infty \approx \frac{p_\infty}{RT_0} \tag{G.2.5}$$

The tunnel velocity is then calculated using Eq. G.2.3 above.

G.2.1.1 Error Sources

For the pressure system the error sources comprise of the following factors:

1. Calibration error of the transducers, δ_{cal}
2. Resolution error of the transducers, δ_{res}
3. Accuracy of the transducers quoted by the manufacturers, δ_{te}
4. Uncertainty in ambient pressure, P_{amb}
5. Uncertainty in total temperature, T_0

G.2.1.2 Uncertainty in Tunnel Speed

An uncertainty band for the tunnel velocity, U_∞, is calculated for the median speed investigated which was 30 ms^{-1}. The typical measured pressures for this tunnel speed are summarized in Table G.2.

Given the above sources of error, the uncertainty in the transducer reading, δ_T, can be calculated using the following relationship:

$$\delta_T = \sqrt{(\delta_{cal})^2 + (\delta_{res})^2 + (\delta_{te})^2} \tag{G.2.6}$$

The calibration error, δ_{cal}, is calculated from the calibration curve (Fig. G.2) for the specific transducer that was used and is called the *y*-error. This was calculated in Microsoft Excel using the LINEST function. Since the determination of the tunnel speed uses two transducers, T1 and T2 (Table G.2) the associated uncertainties are as follows:

$$\begin{aligned} \delta_{cal,T1} &= 2.854Pa \\ \delta_{cal,T2} &= 1.180Pa \end{aligned} \tag{G.2.7}$$

The resolution error, δ_{res}, is determined from the number of bits the DAQ card has and the voltage range that it operates in. In these experiments the DAQ card implemented has 2^{16} bits with a voltage range of $12V$. Hence the minimum voltage that the DAQ card can resolve is:

$$V_{min} = \frac{12}{2^{16}} = 0.000183V$$

Converting to pressure using the calibration of the transducers gives:

$$\delta_{res,T1} = 0.223Pa$$

The transducer error is the error quoted by the manufacturers and is typically a percentage of the full-scale range. For FC-044 transducers used to determine the tunnel velocity the range is 2500 *Pa* and the quoted error is 0.3% of the full range. Hence

$$\delta_{te,T1} = \delta_{te,T1} = 7.5Pa$$

$$\begin{aligned} \delta_{T1} &= \sqrt{(\delta_{cal,T1})^2 + (\delta_{res,T1})^2 + (\delta_{te,T1})^2} \\ &= \sqrt{(2.854)^2 + (0.223)^2 + (7.5)^2} \\ &= 8.028Pa \end{aligned} \tag{G.2.8}$$

As a fractional uncertainty this is:

$$\frac{\delta_{T1}}{P_{T1}} = \frac{8.028}{413.480} = 0.0194$$

In a similar fashion:

$$\delta_{T2} = 7.595Pa$$

$$\frac{\delta_{T2}}{P_{T2}} = \frac{7.595}{79.093} = 0.096$$

The static pressure, p_∞, is calculated using the pressure reading from the T1 transducer and the ambient pressure. The ambient pressure for this particular example is 98204 *Pa* (Table G.2) and the associated uncertainty, $\delta_{P_{amb}}$, is 5 *Pa*. Hence:

$$\begin{aligned}\delta_{p_\infty} &= \sqrt{(\delta_{T2})^2 + (\delta_{P_{amb}})^2} \\ &= \sqrt{(7.595)^2 + (5)^2} \\ &= 9.093Pa\end{aligned} \tag{G.2.9}$$

$$\frac{\delta_{p_\infty}}{p_\infty} = \frac{9.093}{98124.907} = 0.0000927$$

In terms of the density, ρ_∞, the uncertainty, δ_{ρ_∞} can be estimated as follows:

First ρ_∞ is calculated:

$$\rho_\infty = \frac{p_\infty}{RT} = 1.183kgm^3$$

Given that, $\delta_T = 0.5\ K$:

$$\frac{\delta_{\rho_\infty}}{\rho_\infty} = \sqrt{\left(\frac{\delta_{p_\infty}}{p_\infty}\right)^2 + \left(\frac{\delta_T}{T}\right)^2} \tag{G.2.10}$$

$$= \sqrt{(0.0000927)^2 + (0.00173)^2} \tag{G.2.11}$$

$$= 0.00173 \tag{G.2.12}$$

The dynamic pressure is given by the difference in the pressure transducer readings. Hence the uncertainty, δ_{q_∞}, is given by:

$$\delta_{q_\infty} = \sqrt{(\delta_{T1})^2 + (\delta_{T2})^2} \tag{G.2.13}$$

$$= \sqrt{(8.028)^2 + (7.595)^2} \tag{G.2.14}$$

$$= 11.052Pa \tag{G.2.15}$$

Hence given that $q_\infty = 492.573\ kgm^5s^{-2}$

Measurement	Transducer	Value
$p_i - p_{str}$	T1	-19914 Pa
$p_{str} - P_{amb}$	T2	-2.176 Pa
T	-	290 K
P_{amb}	-	96952 Pa
$\bar{P}_f$	T1	96857.676 Pa
$\bar{p}_i$	T1,T2	77035.460 Pa

Table G.3: Typical measurement values for the calculation of the intake velocity, U_i

$$\frac{\delta_{q_\infty}}{q_\infty} = \frac{11.052}{492.573} = 0.0224$$

The uncertainty in the tunnel velocity can then be calculated using the following:

$$\frac{\delta_{U_\infty}}{U_\infty} = 0.5\sqrt{\left(\frac{\delta_{\rho_\infty}}{\rho_\infty}\right)^2 + \left(\frac{\delta_{q_\infty}}{q_\infty}\right)^2} \tag{G.2.16}$$

$$= 1.1\% \tag{G.2.17}$$

G.2.2 Determination of Intake Velocity

The intake velocity was determined by placing the intake far from the ground and measuring the average static pressure and area weighted average total pressure inside the intake duct. The average static pressure, $\bar{p}_i$, was measured by connecting 12 equi-spaced static pressure ports around the intake circumference together to give an arithmetic average (see Fig. 3.1a for static pressure port locations). The average total pressure, $\bar{P}_i$, was determined using four total pressure rakes equi-spaced and rotating the intake twice to give 108 total pressure measurements within the intake duct. A summary of typical measurement values for the determination of the intake velocity is given in Table G.3.

The intake static pressure determined from the sum of the two transducer readings and the ambient pressure:

$$\begin{aligned} p_i &= P_{T1} + P_{T2} + P_{amb} \\ &= -19914 + 2.176 + 96952 \\ &= 77035.460Pa \end{aligned} \tag{G.2.18}$$

$$PR_i = \frac{\bar{P}_f}{\bar{p}_i} \tag{G.2.19}$$
$$= \frac{96858}{77035}$$
$$= 1.257$$

Given that T_{0i} is 290 K and for air $\gamma = 1.4$ the static temperature can be calculated using the pressure ratio, PR_i:

$$T_i = \frac{T_{0i}}{PR_i^{(\gamma-1)/\gamma}} \tag{G.2.20}$$
$$= \frac{290}{(1.257)^{2/7}} \tag{G.2.21}$$
$$= 271.6K \tag{G.2.22}$$

The density within the intake duct can then therefore be calculated:

$$\rho_i = \frac{\bar{p}_i}{RT_i} \tag{G.2.23}$$
$$= \frac{77035}{287 \times 271.6}$$
$$= 0.988 Kgm^3$$

The intake velocity is then calculated using the energy equation:

$$U_i = \sqrt{2C_P\,(T_{0i} - T_i)} \tag{G.2.24}$$
$$= \sqrt{2 \times 1005\,(290 - 271.6)}$$
$$= 192.1 ms^{-1}$$

The mass flow within the intake duct is calculated given that the intake area, A_i, is calculated using the intake inner radius, r_i, which is equal to 0.05 m:

$$\dot{m} = U_i A_i \rho_i \tag{G.2.25}$$
$$= 192.1 \times \pi\,(0.05)^2 \times 0.988$$
$$= 1.49 kgs^{-1}$$

The intake Mach number can also be computed given that the speed of sound is equal to $\sqrt{\gamma RT_i}$:

$$\begin{aligned} M_i &= \frac{U_i}{\sqrt{\gamma RT_i}} \\ &= \frac{192.1}{\sqrt{1.4 \times 287 \times 271.6}} \\ &= 0.582 \end{aligned} \tag{G.2.26}$$

G.2.2.1 Uncertainty in Intake Velocity

Determination of the intake velocity implements 37 PX139 transducers and one Furness Controls FC-044 differential pressure transducer. Similar to the tunnel velocity uncertainty analysis the calibration slope and associated error are all approximately the same for the PX139 transducers, therefore an average y-error is taken.

The calibration error for the PX139s transducers, $T1$, and the FC-044, $T2$, is as follows:

$$\delta_{cal,T1} = 27.1Pa \tag{G.2.27}$$

$$\delta_{cal,T2} = 2.85Pa \tag{G.2.28}$$

For the resolution error for the two types of transducers is:

$$V_{min,T1} = \frac{5}{2^{16}} = 0.000076V \tag{G.2.29}$$

$$V_{min,T1} = \frac{12}{2^{16}} = 0.000183V \tag{G.2.30}$$

Converting to pressure using the calibration of the transducers gives:

$$\delta_{res,T1} = 1.314Pa \tag{G.2.31}$$

$$\delta_{res,T2} = 0.223Pa \tag{G.2.32}$$

The transducer error for the FC-044 transducer is 0.3% of the maximum pressure range, whereas for the PX139s the error is 0.1% of the maximum pressure. Hence:

$$\delta_{te,T1} = 34.474Pa$$

$$\delta_{te,T2} = 7.5Pa$$

$$\begin{aligned}\delta_{T1} &= \sqrt{(\delta_{cal,T1})^2 + (\delta_{res,T1})^2 + (\delta_{te,T1})^2} \\ &= \sqrt{(27.1)^2 + (1.314)^2 + (34.474)^2} \\ &= 43.860Pa\end{aligned} \tag{G.2.33}$$

As a fractional uncertainty this is:

$$\frac{\delta_{T1}}{P_{T1}} = \frac{43.860}{19914} = 0.0022$$

In a similar fashion:

$$\delta_{T2} = 8.028Pa \tag{G.2.34}$$

$$\frac{\delta_{T2}}{P_{T2}} = \frac{4.106}{2.176} = 3.690$$

The static pressure in the intake duct, p_i, is determined from Eq. G.2.19. Given that the uncertainty in the ambient pressure, δ_{P_amb}, is 5 Pa hence the uncertainty in p_i is given by:

$$\begin{aligned}\delta_{p_i} &= \sqrt{(\delta_{T1})^2 + (\delta_{T2})^2 + (\delta_{P_amb})^2} \\ &= \sqrt{(43.860)^2 + (8.028)^2 + (5)^2} \\ &= 44.868Pa\end{aligned} \tag{G.2.35}$$

As a fractional uncertainty this is:

$$\frac{\delta_{p_i}}{p_i} = \frac{44.868}{77035.460} = 0.00058$$

For the fan face average pressure, the uncertainty in the position of the probes and areas that each probe is associated with is ignored. Since the probes are equi-spaced in the radial direction from the intake centre, the area associated with each probe, A_p increases. The uncertainty of each total pressure reading, δ_P, is given by Eq. G.2.33. With three different circumferential positions being measured within the intake, the number of probe measurements at each radial location, N_p, is 12 (since 4 rakes were implemented). An estimate for the uncertainty in $\bar{P}_f$ is determined by multiplying

A_p	$A_p\delta_p$	$A_p\delta_p N_p$	$\left(A_p\delta_p N_p\right)^2$
4.729E-06	2.074E-04	2.489E-03	6.194E-06
2.695E-05	1.182E-03	1.418E-02	2.012E-04
3.534E-05	1.550E-03	1.860E-02	3.460E-04
4.843E-05	2.124E-03	2.549E-02	6.498E-04
6.152E-05	2.698E-03	3.238E-02	1.049E-03
7.461E-05	3.273E-03	3.927E-02	1.542E-03
8.770E-05	3.847E-03	4.616E-02	2.131E-03
1.008E-04	4.421E-03	5.305E-02	2.814E-03
1.139E-04	4.995E-03	5.994E-02	3.593E-03
1.005E-04	4.409E-03	5.291E-02	2.800E-03
		$\sqrt{\sum\left(A_p\delta_p N_p\right)^2}/A_i$	15.662 *Pa*

Table G.4: Calculation of the uncertainty in the area weighted average fan face pressure, $\bar{P}_f$

each area, A_r, by the uncertainty in the probe reading, δ_p and the number of probes, N_p (Table G.4). All resulting values are then squared and summed together and divided by the total area of intake duct, A_i, to give an uncertainty $\delta_{\bar{P}_f}$ (Table G.4).

From Table G.4 the uncertainty in $\bar{P}_f$ denoted by $\delta_{\bar{P}_f}$ is 15.662 *Pa*. In terms of a fractional uncertainty this is:

$$\frac{\delta_{\bar{P}_f}}{\bar{P}_f} = \frac{15.662}{96857.676} = 0.000162$$

The uncertainty in the pressure ratio is therefore given by:

$$\begin{aligned}\frac{\delta_{PR_i}}{PR_i} &= \sqrt{\left(\frac{\delta_{\bar{P}_f}}{\bar{P}_f}\right)^2 + \left(\frac{\delta_{p_i}}{p_i}\right)^2} \\ &= \sqrt{(0.000582)^2 + (0.000162)^2} \\ &= 0.000604\end{aligned} \tag{G.2.36}$$

In terms of the intake static pressure, given that the uncertainty in the tunnel total temperature, δ_{T_0}, is 0.5 *K*, then:

$$\begin{aligned}\frac{\delta_{T_i}}{T_i} &= \sqrt{\left[\left(\frac{\gamma-1}{\gamma}\right)\frac{\delta_{PR_i}}{PR_i}\right]^2 + \left(\frac{\delta_{T_0}}{T_0}\right)^2} \\ &= \sqrt{(3.5\times 0.000604)^2 + (0.00172)^2} \\ &= 0.00273\end{aligned} \tag{G.2.37}$$

The intake velocity is then calculated using Eq. G.2.25 and the error estimate can therefore be given by first calculating the uncertainty in the temperature difference $(T_0 - T_i)$ here denoted as ΔT:

$$\begin{aligned} \delta_{\Delta T} &= \sqrt{(\delta_{T_0})^2 + \sqrt{(\delta_{T_i})^2}} \\ &= \sqrt{(0.5)^2 + \sqrt{(0.741)^2}} \\ &= 0.894K \end{aligned} \tag{G.2.38}$$

As a fractional uncertainty this is:

$$\frac{\delta_{\Delta T}}{\Delta T} = \frac{0.891}{18.365} = 0.0487$$

Hence the uncertainty in the intake velocity is therefore given by:

$$\frac{\delta_{U_i}}{U_i} = 0.5\frac{\delta_{\Delta T}}{\Delta T} = 2.4\%$$

G.3 PIV Velocity Error

The overall measurement accuracy in PIV involves many different contributing factors. These factors include how the experiment was set-up (for example the laser sheet alignment with the calibration plate) to how the images are evaluated (for example how the size of the interrogation area affects the measurement accuracy).

The total error associated with a single vector, ϵ_{tot} can be decomposed into two groups; the sum of the bias errors, ϵ_{bias}, and the random errors, ϵ_{rms}:

$$\epsilon_{tot} = \epsilon_{bias} + \epsilon_{rms} \tag{G.3.1}$$

G.3.1 Bias Errors

Typically three point Gaussian peak approximators are implemented for peak detection and displacement estimation in the correlation plane. When using this technique bias errors can occur if the particle image diameter, d_τ, is less than one pixel, resulting in the displacements estimates being biased towards integer values. This phenomenon is known in the literature as peak-locking. For the experiments in this thesis the particle image diameter was typically around 1.5-2 pixels in diameter therefore peak locking is not expected to have occurred.

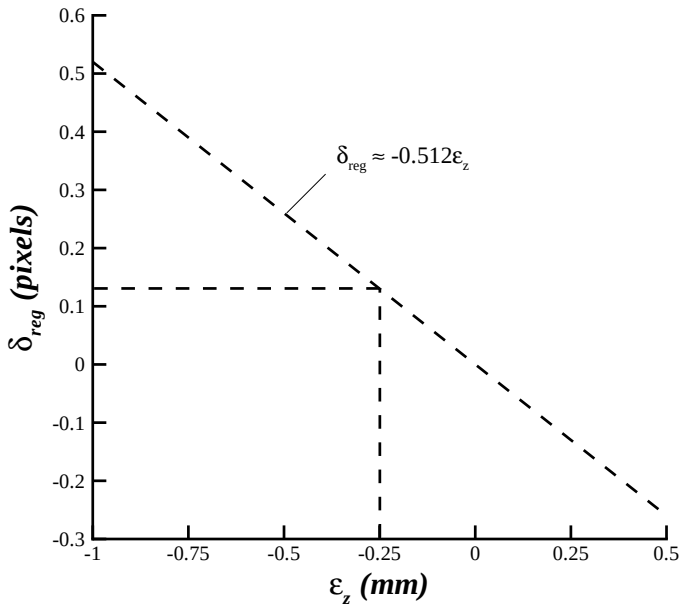

Figure G.3: Registration error, δ_{reg}, as a function of the degree of misalignment of the light sheet with the calibration plate (data after Petracci et al[38])

An additional source of error, which is expected to be the largest single contributor to the error in the velocity measurement, is the misalignment of the laser sheet with the calibration plate. Petracci et al[38] quantified this so-called registration error source using synthetic images of a pipe flow. In their analysis the camera orientations are at +/-45° to the light sheet, the light sheet thickness, Δz_{ls}, is 1 *mm*, the f-stop is 4 and the magnification is 0.22, all of which are very similar to the values used in the experiments within this thesis. In addition the interrogation window size used in the processing was 32×32 which is again comparable to this work. In the simulations the light sheet is traversed with respect to the reference position in the calibration target and the error is recorded. The results have been extracted from Petracci et al[38] and are shown in Fig. G.3. It is expected that the misalignment of the light sheet thickness with the calibration plate was no larger than 0.25 *mm* throughout the experiments applicable to this research. Hence this leads to a registration error, δ_{reg}, at worst of 0.13 pixels.

G.3.2 RMS Errors

Huang[20] identifies a number of sources that contribute to the RMS uncertainty of the PIV velocity measurement. These are as follows:

- Poor particle seeding
- Strong velocity gradients
- Out of plane motion
- Non-uniformity reflection of particles at different angles and orientations
- Nonlinear, non-uniform response of the cameras
- Camera's dark current noise
- Seeding size
- Optimizing particle image diameter
- Optimizing particle image shift between pulses
- Particle image density
- Image quantization levels
- Background noise (such as a external light sources)

The non-linear and non-uniform response of the camera in general has a very minor effect and is therefore ignored. Also the non-uniform reflection of particles at different locations and angles is very complicated and can therefore not be quantified[20].

Poor particle seeding, strong velocity gradients, and out of plane motion generally effect the correlation peak, resulting in a weak signal. This can result in the noise peak being detected rather than the actual displacement peak. This results in outlier vectors which are easily detected and removed after the correlation. In this thesis the deformation grid algorithm was implemented which accounts for strong velocity gradients. Out of plane loss of pairs was avoided by ensuring that particles do not move by more than 1/3 of the light sheet thickness between the laser pulses during the experiments[28].

One approach, adopted by Raffel et al[41], to assess measurement precision in PIV measurements is to uses synthetic particle image recordings. By varying a single parameter at a time each uncertainty source can be assessed against the known answer to provide an uncertainty band. Within Raffel et al's analysis a three point Gaussian peak approximator and FFT correlation engine were used in the analysis which is applicable to this research. The effect of particle image diameter, interrogation window size, particle image displacement, seeding, quantization levels and background noise have been assessed independently. Similar to an approach used in Raffel et al[40] the diagrams presented Raffel et al[41] for each uncertainty source are used to determine an approximate uncertainty for the displacement estimate for each camera.

Particle Image Diameter

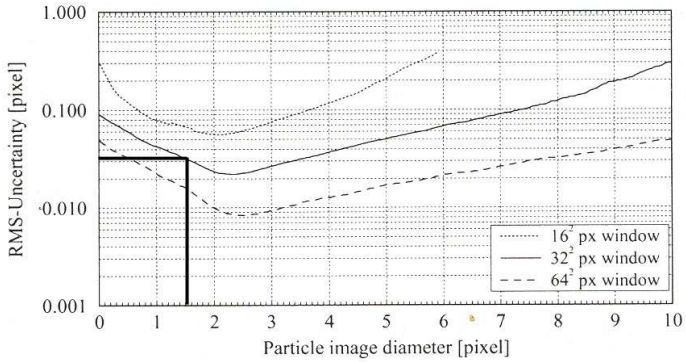

Figure G.4: Optimizing particle image diameter[41]

Fig. G.4 shows the effect of particle image diameter, d_τ, on the measurement precision. In the experiments performed in this thesis the particle image diameter was approximately 1.5 to 2 pixels in diameter and the final interrogation window used was 32×32. Hence using Fig. G.4 the uncertainty as a result of the particle image diameter, δ_{d_τ} is approximately 0.03 pixels.

Particle Image Displacement

Fig. G.5 displays the effect of the particle image shift on the RMS uncertainty for different interrogation window sizes and different particle image diameters. The post-processing method used in this thesis implements a multi-pass procedure which en-

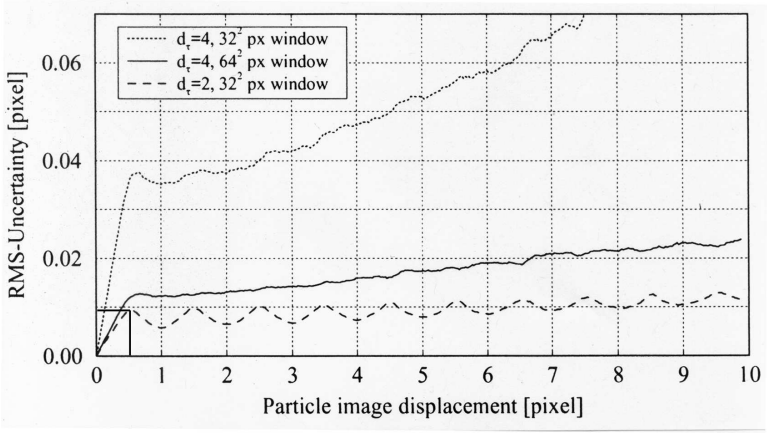

Figure G.5: Effect of particle image displacement on the measurement uncertainty[41]

ables the interrogation windows to offset between passes, according the displacement field estimated from the previous pass. This increases the number of particle image pairs detected and also increases the detectability of the correlation peak. By implementing such a procedure the particle image shift is expected to be no more than 0.5 pixels. In the experiments the particle diameter, d_τ, was between 1.5 and 2 pixels and the final interrogation window size was 32×32. Hence the uncertainty due to the particle image displacement, δ_{pid}, is expected to be approximately 0.01 pixels.

Particle Seeding

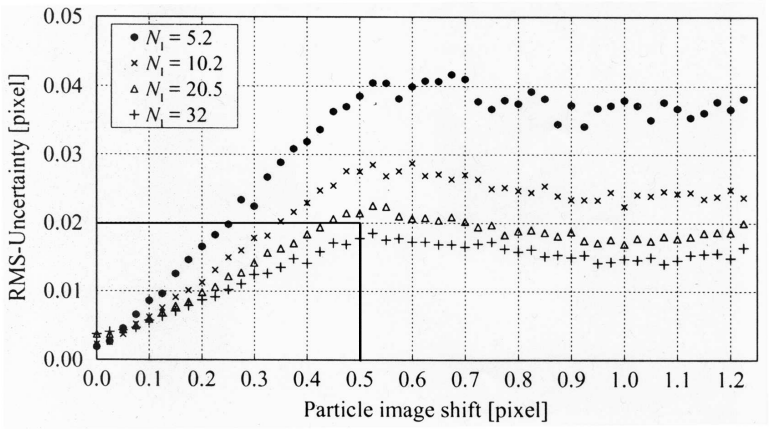

Figure G.6: Measurement uncertainty for a single exposure/double frame PIV as a function of particle image shift for different particle densities[41]

Fig. G.6 shows the effect of particle image shift against uncertainty for various image densities (note with window offsetting being implemented, the particle image shift is expected to be no greater than 0.5 pixels). In the experiments related to this thesis the interrogation area was 32×32 pixels in size and typically there was approximately 15-20 particle images within each region. This would result in a maximum uncertainty

level due to the seeding, δ_{ps}, of approximately 0.02 pixels.

Quantization Levels

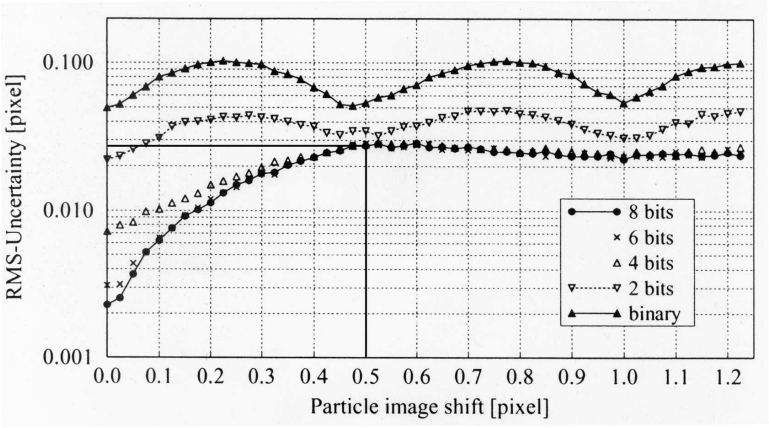

Figure G.7: Effect of image quantization levels on the measurement uncertainty[41]

The effect of image quantization levels on the measurement uncertainty is shown in Fig. G.7. The cameras implemented in this thesis were 12-bits. Hence using Fig. G.7 the uncertainty is expected to be at worst 0.03pixels.

Background Noise

In terms of background noise Fig. G.8 illustrates the effect of this aspect on the RMS-uncertainty. In the simulations normal-distributed (white) noise at a specified fraction of the image dynamic range was linearly added to each pixel[41]. In the experiments background noise can be introduced due to unwanted reflections, as well as addition light sources. It is expected that the background noise levels were no larger than 5% during tests therefore the uncertainty, δ_{BN}, as a results of this is expected to be no larger than 0.03 pixels.

G.3.3 Uncertainty Estimation

$$\begin{aligned}\delta_{peak} &= \sqrt{\delta_{d_\tau}^2 + \delta_s^2 + \delta_{PID}^2 + \delta_{QL}^2 + \delta_{BN}^2} \\ &= \sqrt{0.03^2 + 0.01^2 + 0.02^2 + 0.03^2 + 0.03^2} \qquad = 0.057px\end{aligned} \tag{G.3.2}$$

$$\begin{aligned}\delta_{tot} &= \sqrt{\delta_{peak}^2 + \delta_{peak}^2 + \delta_{reg}^2} \\ &= \sqrt{0.057^2 + 0.057^2 + 0.13^2} \qquad = 0.15px\end{aligned} \tag{G.3.3}$$

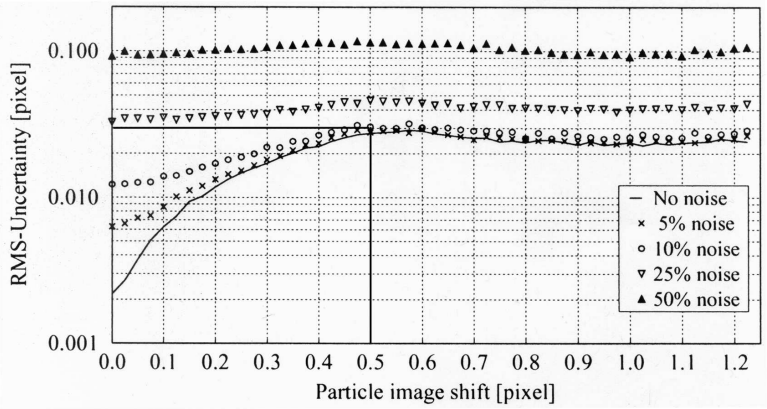

Figure G.8: The effect of background noise on the RMS-uncertainty for varying particle image shift distances[41]

To obtain an uncertainty band for the measured velocity δ_{tot} needs to be converted into a displacement in physical space. For the cameras used in experiments the CCD size was 15 *mm* with 2048pixels which leads to 7.324×10^{-6} $m/pixel$. Since the uncertainty estimate is 0.15pixels, this leads to a displacement uncertainty of 1.1×10^{-6} m. Typically the measurement area was approximately 110×110 *mm* with a spatial resolution of 0.86 *mm*. This gives a magnification factor of 15/110 or 0.136. Hence the displacement error in physical space, δ_x, is equal to 8.057×10^{-6} m. For the experiments the pulse separation time was on average 5 μs hence the uncertainty in the velocity can be calculated as follows:

$$\delta_u = \frac{\delta_x}{\Delta t} = \frac{9.131 \times 10^{-6}}{5 \times 10^{-6}} = 1.611 ms^{-1} \tag{G.3.4}$$

For an average velocity, U_{av}, of approximately 50 ms^{-1} close to the core of the vortex across all configurations the relative error is therefore:

$$\frac{\delta_u}{U_{av}} = \frac{1.611}{50} = 3.2\% \tag{G.3.5}$$

To obtain an uncertainty estimate for the out-of-plane vorticity, ω_z, first an error band for the velocity gradient, $\partial u/\partial y$, is computed as given by Eq. G.3.8 where Δx is the grid resolution.

$$\delta_{\partial u/\partial y} = \frac{1}{2\Delta x}\left[\sqrt{\delta_u^2 + \delta_u^2}\right] \tag{G.3.6}$$

$$= 1326 s^{-1} \tag{G.3.7}$$

Since the uncertainty in the velocities is the same an error band for the out-of-plane vorticity is then given by the following:

$$\delta\omega_z = \sqrt{\left(\delta_{\partial u/\partial y}\right)^2 + \left(\delta_{\partial v/\partial x}\right)^2} \qquad = 1875 s^{-1} \qquad \text{(G.3.8)}$$

Since the circulation was calculated by integrating the vorticity within a circular domain, the area of each cell increases with radial distance from the centre of the circular zone. As described in Appendix E, the circular zone used had 150 radial (I_{max}) and 261 circumferential (J_{max}) grid points. The uncertainty in the circulation was therefore calculated by multiplying δ_{ω_z} by the area of the cell at each radial location, A_i and by the number of circumferential grid points, J_{max} (Eq. G.3.10 where i is a radial index from the centre of the circular zone).

$$\delta_\Gamma = \sqrt{\sum_{i=1}^{Imax} \left[A_i \delta_{\omega_z J_{max}}\right]^2} \qquad \text{(G.3.9)}$$

$$= 0.3 m^2 s^{-1} \qquad \text{(G.3.10)}$$

G.4 Summary

Measurement	Uncertainty
h/D_l	1.9-3.6%
U_∞	1.1%
U_i	2.4%
u, v, w	3.2%
ω_z	1875 s^{-1}
Γ	0.3 $m^2 s^{-1}$

Table G.5: Summary of uncertainties in selected variables